Investigation of a Novel Heat Pipe Solar Collector/CHP System

By

Xudong Zhao, BEng, MSc

Thesis submitted to the University of Nottingham

for the degree of Doctor of Philosophy

June 2003

Contents

Abstract

The European Union has an ongoing commitment to reducing CO_2 emission as highlighted by its agreement at the Kyoto Summit. One approach to achieving these reductions would be to develop alternative energy sources for major energy demanding sectors. In the EU, about 40% of all energy consumed is associated with buildings and of this, about 60% is utilised in the housing sector. A major part of the energy demand of buildings could be met by utilising renewable energy sources, e.g., solar energy.

Existing large-scale plants for power generation prevent efficient utilisation of the waste hot water produced. This means that to meet electricity demand, vast quantities of fossil fuels are burnt releasing unwanted pollutants (e.g., CO_2 and NO_x) into the atmosphere. Over the last decade, small-scale CHP plants have been introduced for many applications with proven environmental and economic benefits. In addition, solar energy has been used to generate electricity and provide hot water in conjunction with the CHP plants.

Investigation of a hybrid heat pipe solar collector/CHP system was carried out in this research. The system is powered by solar and gas energy as well as the boiler waste heat to provide electricity and heating for residential buildings. Compared to the relevant system configurations, this system has the following innovative features:

- The solar collector was integrated with exhaust flue gas channels that allowed both solar energy and waste heat from exhaust gas to be utilised.
- Heat pipes as high efficiency heat transfer devices were incorporated in the collector panel. Both miniature and normal heat pipes were investigated, and this resulted in two types of collectors, e.g., thin membrane heat pipe solar collector, and hybrid heat pipe solar collector, to be produced for this application.
- A compact, lightweight turbine was applied in this system.
- Novel refrigerants, including n-pentane and hydrofluoroethers (HFEs), were employed as the working fluids for the CHP system.

Use of the system would save primary energy of approximately 3,150kWh per year compared to the conventional electricity and heating supply systems, and this would result

in reduction of CO_2 emission of up to 1.5 tonnes. The running cost of the proposed system would also be lower.

The research initially investigated the thermal performance of several heat pipes, including micro/miniature heat pipes, normal circular and rectangular heat pipes, with/without wicks. An analytical model was developed to evaluate the heat transport capacity for these heat pipes. A miniature heat pipe with parallelepiped channel geometry was proposed. The variation of heat transport capacity for either micro/miniature or normal heat pipes with operation temperature, liquid fill level, inclination and channel geometry were investigated.

Investigation of the operating characteristics of the selected heat pipes, e.g., two miniature and one mini heat pipes, and two normal heat pipes, was then carried out using both the numerical technique and experimental testing. It was found that the results from tests were in good agreement with the numerical predictions when the test conditions were close to the simulation assumptions.

The research work further involved the design, modelling, construction and tests of two innovative heat pipe solar collectors, namely, the thin membrane heat pipe solar collector and the hybrid heat pipe solar collector. A computer model was developed to analyse the heat transfer in the collectors. Two collector efficiencies, η and η_1, were defined to evaluate their thermal performance, which were all indicated as the function of a general parameter $(t_{mean}-t_a)/I_n$. Effects of the top cover, manifold as well as flue gas temperature and flow rate (for hybrid collector only) on collector efficiencies were investigated using the computer model developed. Laboratory tests were carried out to validate the modelling predictions and experimentally examine the thermal performance of the collectors. Comparison was made between the modelling and testing results, and the reasons for error formation were analysed.

The research then considered the issues of the micro impulse-reaction turbine, which was another part of the integrated system. The structure configuration, coupling pattern with the generator as well as internal geometry contour of the turbine were described. The velocity, pressure and turbulent kinetic energy of the flow in the turbine were determined using numerical CFD prediction. In addition, experimental tests were carried out using a prototype system. The results of CFD simulation and testing show good agreement. This

indicates that CFD can be used as a tool of optimizing turbine geometry and determining operating conditions.

The research finally focused on the integrated system which brought the heat pipe solar collector, boiler and micro turbine together. The individual components, configurations and layout of the system were illustrated. Theoretical analysis was carried out to investigate thermodynamic cycle and heat transfer contained in the combined system, which is based on the assumption that the system operated on a typical Rankine cycle powered by both solar and gas energy. Tests for the prototype system was carried out to realistically evaluate its performance. Two types of turbine units were examined; one is an impulse-reaction turbine, and the other is a turbo-alternator. The turbo-alternator was found to be too small in capacity for this system thereby affecting its output significantly. The micro impulse-reaction turbine was considered a better option. A typical testing showed that the majority of heat required for the turbine operation came from the boiler (7.65kW), and very little (0.23kW) from the solar collector. The gas consumption was 8.5kW. This operation resulted in an electricity output and domestic hot water generation, which were 1.34kW and 3.66kW respectively. The electrical efficiency was 16% and the thermal efficiency was 43%, resulting in an overall efficiency of 59%.

Increasing the number of the collectors used would result in reduced heat output from the boiler. This would help in improving system performance and increasing efficiencies. In this application, number of collectors used would be 4 as the flue gas flow rate would only be sufficient to provide 4 to 5 such collectors for heat recovery.

The research resulted in the proposal of another system configuration. The innovative concept is illustrated in Chapter 8, and its key technical issues are discussed.

Acknowledgement

I would like to thank my supervisor, Professor S. B. Riffat to whom I am indebted for his unlimited support and assistance with my research work. I should also thank my second supervisor, Dr. P. S. Doherty, for his technical instructions and dedicated involvement throughout the whole process. Thanks to the European Commission (EC) for its financial support for this project.

My special thanks to my family, particularly my wife; who encouraged me and shared quite many of the house works throughout my studies. I am also grateful to my colleagues and working partners, especially Dr. Rabah Bonkanouf, Prof. Armando Oliveira, Prof. Clito Afonso, Dr. Abraham Dayan, Dr. Song Lin, Mr Trevor Griffiths, Mr Fred Best, Mr Jorge Facão, Mr Joaquim Matos, for their continued support. I would like to thank the technicians of the School for their tolerance and co-operation.

Nomenclature

Chapter 2

Symbol	Term	Unit
α	Half of the angle of the sharp corner in the miniature 'parallelepiped' heat pipe	degree
w	Half the width of the liquid-vapour interface	m

Chapter 3

Symbol	Term	Unit
A	Cross-sectional area	m^2
C, C_1, C_2	Coefficients of vapour phase resistance calculation	
C_p	Specific heat of liquid at constant pressure	kJ/kg.°C
d	Diameter	m
d_i	Equivalent diameter of the cross section	m
f_v	Frictional resistance coefficient	
g	Gravitational acceleration	m/s^2
G	Minimum filled liquid mass	kg
K	Coefficient for liquid phase resistance calculation	
k_{eff}	Effective thermal conductivity of the wicks	W/m.°C
h_{fg}	Latent heat of vaporization	J/kg
k_l	Thermal conductivity of liquid	W/m.°C
k_s	Shape factor of the heat pipe channel geometry	
l_a	Length of adiabatic section	m
l_c	Length of condensation section	m
l_e	Length of evaporation section	m
l_{eff}	Effective length of the heat pipe	m
r_{ce}	Capillary radius	m
r_{hl}	Hydraulic radius of liquid cross section	m
r_{hv}	Hydraulic radius of vapour cross section	m
$r_{h,w}$	Hydraulic radius of the triangle grooved wicks with liquid	m
r_i	Equivalent radius of the cross section	m
r_n	Critical radius of bubble generation	m
r_v	Equivalent radius of the vapour area in the cross section	m

R	Universal gas constant, 8317	J/kg.K
Re	Reynolds number	
R_v	Water vapour constant	J/kg.K
M_v	Mach number of vapour flow	
P	Pressure	Pa
p_{cl}	Capillary pressure	Pa
q_c	Heat input	W
$q_{b,m}$	Boiling limit for heat transport	W
$q_{e,m}$	Entrainment limit for heat transport	W
q_{max}	Maximum heat transport capacity	W
$q_{s,m}$	Sonic limit for heat transport	W
$q_{v,m}$	Viscous limit for heat transport	W
T	Absolute temperature	K
Δp_{ag}	Axial hydrostatic pressure drop	Pa
Δp_{cl}	Net capillary pressure difference	Pa
$\Delta p_{c,m}$	Maximum capillary force	Pa
Δp_l	Viscous pressure drop occurring in the liquid phase	Pa
Δp_{rg}	Radial hydrostatic pressure drop	Pa
Δp_v	Viscous pressure drop occurring in the vapour phase	Pa
θ	Wetting angle of liquid-vapour surface	degree
ϕ	Angle of inclination relative to horizontal surface	degree
ρ	Density	kg/m^3
σ	Surface tension	N/m
γ	Specific heat ratio	
μ	Dynamic viscosity	$N.s/m^2$

Subscripts

v	Vapour
l	Liquid
s	Solid

Chapter 4

Symbol	Term	Unit
A	Cross-sectional area	m^2
C_p	Specific heat of liquid at constant pressure	kJ/kg.K
d	Diameter	m
g	Gravitational acceleration	m/s^2
h_{fg}	Latent heat of vaporization	J/kg
j	Free molecular flow mass flux of evaporation	$kg/m^2.s$
M	Molecular weight	kg/kmol
ms	Average mass flow rate in the element	kg/s
P	Pressure	Pa
P_{cl}	Capillary pressure	Pa
q_c	Heat input	W
$q_{\infty c}$	Heat transfer rate on the vapour-liquid interface in the element	W
R	Universal gas constant, 8317	J/kg.K
T	Absolute temperature	K
t	Temperature	°C
u	Axial velocity	m/s
v	Radial velocity	m/s
$W_{\infty c}$	Perimeter of the vapour-liquid interface	m
$\Delta m_{\infty c}$	Evaporation-condensation rate in the liquid-vapour interface of the element	kg/s
Δms	Difference of mass flow rates between the two sections of the element	kg/s
Δp_{sg}	Axial hydrostatic pressure difference	Pa
Δp_{cl}	Net capillary pressure difference	Pa
Δp_{fl}	Friction pressure loss in the liquid phase	Pa
Δp_{fv}	Friction pressure loss occurring in the vapour phase	Pa
Δp_l	Viscous pressure drop in the liquid phase	Pa
Δp_{ml}	Pressure loss due to momentum change in the liquid phase	Pa
Δp_{mv}	Pressure loss due to momentum change occurring in the vapour phase	Pa
Δp_{rg}	Radial hydrostatic pressure difference	Pa
Δp_v	Viscous pressure drop in the vapour phase	Pa
Δp_{vl}	Difference of the vapour and liquid pressure in the element	Pa

Δq	Heat increase in an element unit at Δti time interval in transient state	W
Δt	Temperature increase during the time interval	°C
Δti	Time interval used in the iteration	s
Δu	Axial velocity difference between the two sections of the element	m/s
Δv	Radial velocity difference between the two sections of the element	m/s
μ	Dynamic viscosity	$N.s/m^2$
ν	Kinematic viscosity	m^2/s
θ	Wetting angle of liquid-vapor surface	degree
ρ	Density	kg/m^3
σ	Surface tension	N/m
ϕ	Angle of inclination relative to horizontal surface	degree

Subscripts

v	Vapour
l	Liquid
s	Solid
0	Inlet of the element
1	Outlet of the element

Chapter 5

Symbol	Term	Unit
A_c	Cross-sectional area of the flue gas channel	m^2
A_{con}	Contact area between heat pipes and condenser manifold	m^2
A_d	Area of the surface of the collector bottom chamber	m^2
A_g	Area of the top cover	m^2
A_s	Area of the absorber surface	m^2
C_{pa}	Specific heat of air at constant pressure	J/kg.°C
C_{pl}	Specific heat of the cooling liquid at constant pressure	J/kg.°C
C_{ps}	Specific heat of the flue gas at constant pressure	J/kg.°C
c_t	Correction factor in relation to flue gas temperature	
d_e	Equivalent diameter of the flow gas channel	m
D_h	Hydraulic diameter of the condenser manifold cross-section	m

Fv	Frictional resistance coefficient of the vapour flow in the heat pipe	
h_1	Convection heat transfer coefficient of the inner surface of the top cover	$W/m^2.°C$
h_2	Convection heat transfer coefficient of the outer surface of the top cover	$W/m^2.°C$
h_m	Convection heat transfer coefficient between flue gas and the enclosure wall	$W/m^2.°C$
I_n	Global solar irradiation	W/m^2
J	Correction factor in relation to the heat resistance of the vapour flow	
k_{con}	Thermal conductivity of the manifold wall	W/m.°C
k_e	Thermal conductivity of the wicked space	W/m.°C
k_f	Thermal conductivity of the bottom metal cover	W/m.°C
k_g	Thermal conductivity of the top cover	W/m.°C
k_h	Thermal conductivity of the cooling liquid	W/m.°C
k_i	Thermal conductivity of the insulation layer	W/m.°C
k_p	Thermal conductivity of the heat pipe wall	W/m.°C
k_v	Thermal conductivity of the vapour flow	W/m.°C
L	Volume flow rate of the flue gas	m^3/s
L_a	Length of the adiabatic section of the heat pipe	m
L_c	Length of the condensation section of the heat pipe	m
L_e	Length of the evaporation section of the heat pipe	m
m	Mass flow rate of the cooling liquid	kg/s
m_s	Mass flow rate of flue gas	kg/s
n	Number of the heat pipes included	
Nu_f	Nusselt number of the flue gas	
Nu_o	Nusselt number of the cooling liquid	
Pr_f	Prandtl number of the flue gas	
Q_{abs}	Overall heat absorbed by the top cover	W
Q_{abs1}	The primary heat absorbed by the top cover	W
Q_{abs2}	The additional heat absorbed by the top cover	W
Q_{con}	Heat transfer between all the heat pipes and the cooling liquid	W
$Q_{con,i}$	Heat transfer between the heat pipe (No. i) and the cooling liquid	W
$Q_{cover\text{-}absorber}$	Heat transfer between the top cover and absorber	W
$Q_{down,oss}$	Downward heat loss through the surface of the bottom chamber	W
Q_{gas}	Potential energy of the flue gas in relation to the environment	W
$Q_{gas\text{-}heat\text{-}obtain}$	Heat obtained from the flue gas by the absorber	W

$Q_{gas\text{-}heat\text{-}loss}$	Heat loss from the flue gas to the environment	W
$Q_{hp,i}$	Heat transfer of a single heat pipe (No. i)	W
$Q_{incident}$	Heat striking the absorber surface	W
Q_{lim}	Limit of heat transport capacity of a single heat pipe	W
Q_{max}	Limit of heat transport capacity of the collector	W
Q_{obt}	Heat obtain of the absorber plate	W
Q_{ref}	Heat reflected to the environment by the top cover	W
$Q_{up,loss}$	Upward heat loss through the top cover	W
r_i	Radius of the evaporation section of the heat pipe (inner surface)	m
r_{ic}	Radius of the condensation section of the heat pipe (inner surface)	m
r_o	Radius of the evaporation section of the heat pipe (outer surface)	m
r_{oc}	Radius of the condensation section of the heat pipe (outer surface)	m
r_v	Radius of the vapour column in the evaporation section of the heat pipe	m
r_{vc}	Radius of the vapour column in the condensation section of the heat pipe	m
R	Overall heat resistance of the heat pipe	$m^2.°C/W$
Re_f	Reynolds number of the flue gas	$m^2.°C/W$
$R_{p.c}$	Condenser wall heat resistance	$m^2.°C/W$
$R_{p.e}$	Evaporator wall heat resistance	$m^2.°C/W$
R_v	Heat resistance of the vapour flow in the heat pipe	$m^2.°C/W$
R_w	Heat resistance of the condenser saturated wicks	$m^2.°C/W$
$R_{w.e}$	Heat resistance of the evaporator saturated wicks	$m^2.°C/W$
t_a	Temperature of the surrounding air	°C
t_{ci}	Temperature of the inner surface of the top cover	°C
t_f'	Flue gas inlet temperature	°C
t_f''	Flue gas outlet temperature	°C
t_{gc}	Temperature in the centre area of the top cover	°C
t_{i-1}	Cooling liquid temperature before the No. i heat pipe	°C
t_i	Cooling liquid temperature after the No. i heat pipe	°C
t_{mean}	Cooling liquid average temperature	°C
t_s	Temperature of the absorber surface	°C
t_{w2}'	Temperature of the downward enclosure wall of the flue gas channel	°C
T_f	Absolute temperature of flue gas (average)	°C
$T_{p.c}$	Outer surface absolute temperature of the condensation section of a heat pipe	°C

$T_{p.e}$	Outer surface absolute temperature of the evaporation section of a heat pipe	°C
T_v	Absolute temperature of vapour flow in the heat pipe	°C
T_w	Absolute temperature of the flue gas enclosure wall (average)	°C
Δt_{m1}	Average calculation temperature difference between flue gas and absorber	°C
Δt_{m2}	Average calculation temperature difference between flue gas and downward enclosure wall	°C
α_s	Solar absorptivity of the absorber surface	
α_g	Solar absorptivity of the top cover	
σ	Bolzman Constant, 5.67e-8	$W/m^2.K^4$
ξ_g	Emittance of the top cover	
ξ_s	Emittance of the absorber surface	
τ_g	Transmittance of the top cover	
ρ_a	Density of air	kg/m^3
ρ_s	Density of the flue gas	kg/m^3
ρ_v	Density of vapour flow	kg/m^3
η	Solar efficiency of the collector	
η_l	Overall efficiency of the collector (for hybrid solar collector only)	
δ_{con}	Thickness of the manifold wall	m
δ_f	Thickness of the metal cover of the bottom chamber	m
δ_g	Thickness of the top cover	m
δ_i	Thickness of the insulation material	m

Chapter 6

Symbol	Term	Unit
h_1	Enthalpy of the refrigernat vapour at the inlet of the turboine (ideal)	J/kg.K
h_2	Enthalpy of the refrigernat vapour at the outlet of the turboine (ideal)	J/kg.K
m	Mass flow rate of the refrigerant	kg/s
m_e	Mass flow rate of the refrigerant passing through a channel	kg/s
n	Number of flow channels required	
W	Power output of the turbine	W

Chapter 7

Symbol	Term	Unit
A_{abs}	Absorber area of each solar collector	m^2
C_p	Specific heat of hot water	J/kg.°C
h_1	Enthalpy of the refrigerant at the outlet of the pump	J/kg
h_2	Enthalpy of the refrigerant at the inlet of the turbine	J/kg
h_3	Enthalpy of the refrigerant at the outlet of the turbine	J/kg
h_4	Enthalpy of the refrigerant at the inlet of the pump	J/kg
I_n	Global solar irradiation	W/m^2
m_{flow}	Mass flow rate of the boiler hot water	kg/s
m_r	Mass flow rate of the refrigerant	kg/s
n	Number of solar collectors	
Q_{con}	Energy available for heating	W
Q_e	Energy available for electricity generation	W
Q_{flue}	Potential energy of the flue gas in relation to the environment	W
Q_{gas}	Gas energy consumed by the boiler	W
Q_h	Heat power for hot water	W
Q_{ref}	Heat gain of the refrigerant from the heat sources	W
Q_{sol}	Heat from the solar collector	W
Q_{sup}	Heat supply of the heat sources	W
t_{flow}	Boiler flow temperature	°C
t_{return}	Boiler return temperature	°C
W	Power output	W
η_1	Overall efficiency of the solar collector	
η_{boiler}	Boiler heat efficiency	
η_{con}	Condenser heat efficiency	
η_e	Electricity efficiency of the hybrid solar collector/CHP system	
η_h	Heat efficiency of the hybrid solar collector/CHP system	
η_{hr}	Efficiency for heat exchange between the hot water and refrigerant	
η_m	Efficiency factor of the turbine	
η_{total}	Total efficiency of the hybrid solar collector/CHP system	

List of Figures

Chapter 4

Chapter 6

Chapter 7

Appendix

List of Tables

Chapter 6

Chapter 7

Chapter 1. Introduction

1.1 Background

The European Union has an ongoing commitment to reducing CO_2 emission as highlighted by its agreement at the Kyoto Summit. One approach to achieving these reductions would be to develop alternative energy sources for major energy demanding sectors. In the EU, about 40% of all energy consumed is associated with buildings and of this, of which about 60% is utilised in the housing sector. A major part of the energy demand of buildings could be met by utilising renewable energy sources, e.g., solar energy. The annual mean global solar irradiation reaching a south facing surface of a house located at the centre of the EU latitude range is typically approximately 2.0 kWh/(m^2.day). This energy could be exploited for heating and power generation.

Existing large-scale plants for power generation are usually located far away from centres of population; this prevents efficient utilisation of the waste hot water produced. Moreover, current technology limits these power stations to a maximum efficiency of about 40% and after transportation of electricity via the national grid, there is only about 35% of the original energy remaining at the point of use. This means that to meet current electricity demand, vast quantities of fossil fuels are burnt releasing unwanted pollutants (e.g., CO_2 and NO_x) into the atmosphere.

Over the last decade, small-scale CHP plants (below 100kWe) have been introduced for many applications with proven environmental and economic benefits (Evans R. D., 1990; Smith, 1994). The success of this market has been mainly due to inexpensive gas and deregulation of the electricity industry. The trend for smaller CHP installation could lead to a potentially large market for domestic CHP (D-CHP). Currently the smallest commercially available unit is 38kWe. In the U.S., 5kWe diesel-fuelled D-CHP units are available from Intelligent, but these are unsuitable for the U.K. individual domestic application as their electrical output is too high. No unit has been developed for the U.K. domestic application, which would require an electrical rating in the region of 1-2kWe. A previous analysis (Jennekens M., 1989) has shown that even with low-energy housing and poor plant utilisation, a 15% reduction in domestic CO_2 emissions can be easily achieved by using a small-scale CHP system.

Use of renewable solar energy in conjunction with conventional energy sources to meet electricity, heating requirements of buildings would reduce pollutant emissions and offer savings in running cost to users. As reserves of fossil fuels diminish, there will be increasing pressure to use renewable energy sources, and it is in the immediate interest to identify and develop technologies which can harness these sources to reduce dependence on fossil fuel combustion. Solar energy has been used to generate electricity and several studies (McNelis B., 1992; Naylor A.I., 1982; Underwood C.P., 1995) have investigated use of power from photovoltaic cladding on buildings for heating, ventilation and air conditioning (HVAC) plants. Unfortunately, photovoltaic technology has low efficiency and high capital cost and, as solar energy is intermittent, some means must be incorporated to store surplus electricity and release it again when it is needed.

Solar energy could also be used to generate electricity using a Rankine cycle in which a turbine or an engine is employed to convert thermal energy into mechanical energy. Sawyer S. L. (1991) described the Enreco organic Rankine cycle engine which was developed as part of solar pond technology to generate electricity from brine at 80°C. Other studies concerning the application of solar energy and Rankine cycles for power generation were described in a review paper by Spencer L. C. (1989).

The aim of this research is to develop a novel hybrid solar/gas CHP system to provide electricity and heating for buildings. This system is powered by a solar collector, and supplemented by a natural gas boiler for periods when solar radiation is low. Use of the hybrid solar/gas system would result in significantly reduced CO_2 emissions to the environment. The hybrid solar/gas system could employ "ozone-friendly" refrigerants such as water, methanol, n-pentane or hydrofluoroethers (HFEs) and the anticipated cost of production is low since inexpensive construction materials (e.g. copper or aluminium) could be used. The building, energy, chemical and manufacturing industries would benefit from the outcome of this research.

The research is novel in the following ways:

i) The solar collector was integrated with exhaust gas flue channels to provide an efficient and robust heat supply system.

ii) Isothermal heat pipe panels, composed of either 'miniature' or 'normal' heat pipes, were used to achieve a high efficiency solar collector.

iii) A compact and lightweight micro-turbine was used for power generation.

iv) New refrigerants, such as n-pentane or hydrofluoroethers (HFEs), were examined as the working fluids for the novel CHP system.

1.2 Description of the research

The CHP system utilised novel and integrated design concept for optimising system performance, size, reliability and costs. It was based on the integration of a heat pipe solar collector, boiler and micro-turbine in one unit. The solar collector could be made in the form of a flat plate heat pipe. This consisted of a sealed unit internally covered with a heat pipe panel, composed of either miniature or normal heat pipes (wicked or wickless), and contained a refrigerant. A boiler was mounted to supply additional heat when solar radiation is low or unavailable. The exhaust gas from the boiler was directed through the channels which were fitted beneath the heat pipe panel to enhance heat transfer. The solar collectors and the boiler in combination provided hot water at 110°C to 120°C, and the hot water used to heat a secondary fluid, either n-pentane or HFE7100, using a generator, a super-heater and a separator, as shown in Figure 1-1. Both n-pentane and HFE7100 are refrigerants which have low boiling points, i.e., 35°C and 60°C respectively, and can be converted to a pressured, superheated vapour when heated in the super-heater and the generator. The vapour was used to drive the turbine to generate electricity, causing its pressure and temperature to fall, and would exit the turbine as a superheated vapour, or mixture of vapour and liquid. The low pressure vapour (or mixture) would be used to produce domestic hot water by passing it through the heat exchangers to allow heat exchange between the refrigerant and chill water.

Two types of solar collectors have been investigated for integration with the proposed system. These are the thin membrane heat pipe solar collector and hybrid heat pipe collector.

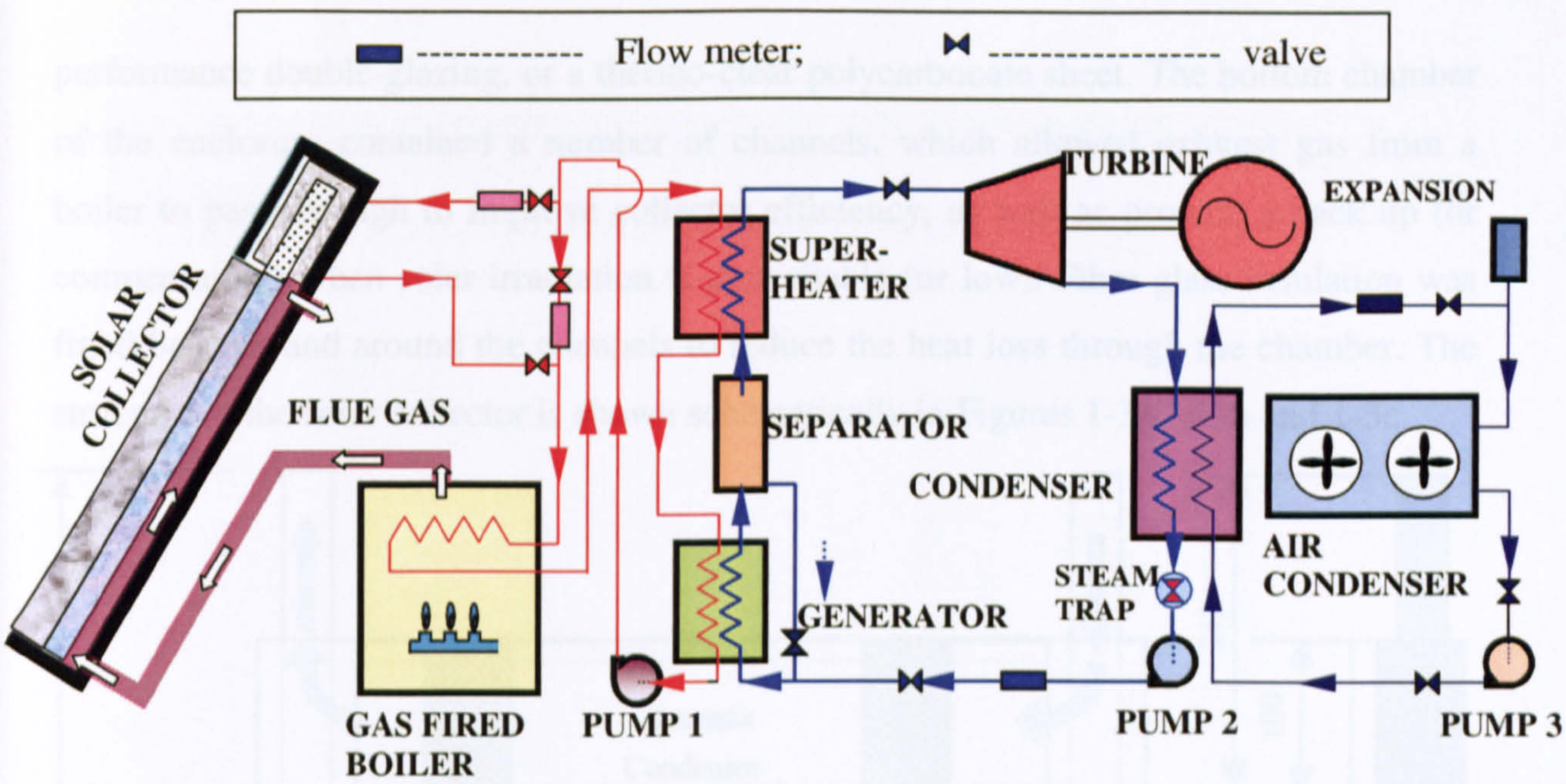

Figure 1-1. Schematic diagram of the hybrid solar collector/CHP system

The thin membrane heat pipe collector mainly comprised of an evacuated housing and an absorber located inside, a reservoir at the bottom end of the collector and a condenser panel on the top end of the collector. There were 2 additional absorbers (narrow strip panel) attached on the main absorber body where solar irradiation was concentrated with the lens on the outer cover, hence called 'super heat pipes'. A micro-pore insulation material, attained with an aluminium/foam plastic tray, was fitted beneath the absorber panel to reduce downward heat loss. A clear acrylic cover was fitted on the top of the evacuated housing, building up an enclosed space where a vacuum was to be maintained to eliminate convection/conduction heat loss. The main body of the collector comprised two plates separated by a thin evaporation gap. The plates were 'spot' welded together creating mini-channels (ribs) that were parallel along the width of the absorber. Each mini-channel was considered to be a single micro (or called 'miniature') heat pipe. The micro heat pipes connected the evaporator section to the condensation section of the collector enabling the flow of refrigerant vapour and condensed liquid refrigerant. The structure of the collectors is shown schematically in Figures 1-2.

Hybrid heat pipe collector mainly comprised of a heat pipe panel, an insulated bottom chamber and a top cover. The panel included 20 heat pipes that are either wicked or wickless structure. The casings were constructed from aluminum frames, comprising an insulated bottom chamber and a top cover. The top cover was an insulated, high

performance double-glazing, or a thermo-clear polycarbonate sheet. The bottom chamber of the enclosure contained a number of channels, which allowed exhaust gas from a boiler to pass through to improve collector efficiency, as well as provide a back up (or compensation) when solar irradiation is unavailable (or low). Fibre-glass insulation was fitted beneath and around the channels to reduce the heat loss through the chamber. The structure of the solar collector is shown schematically in Figures 1-3a, 1-3b and 1-3c.

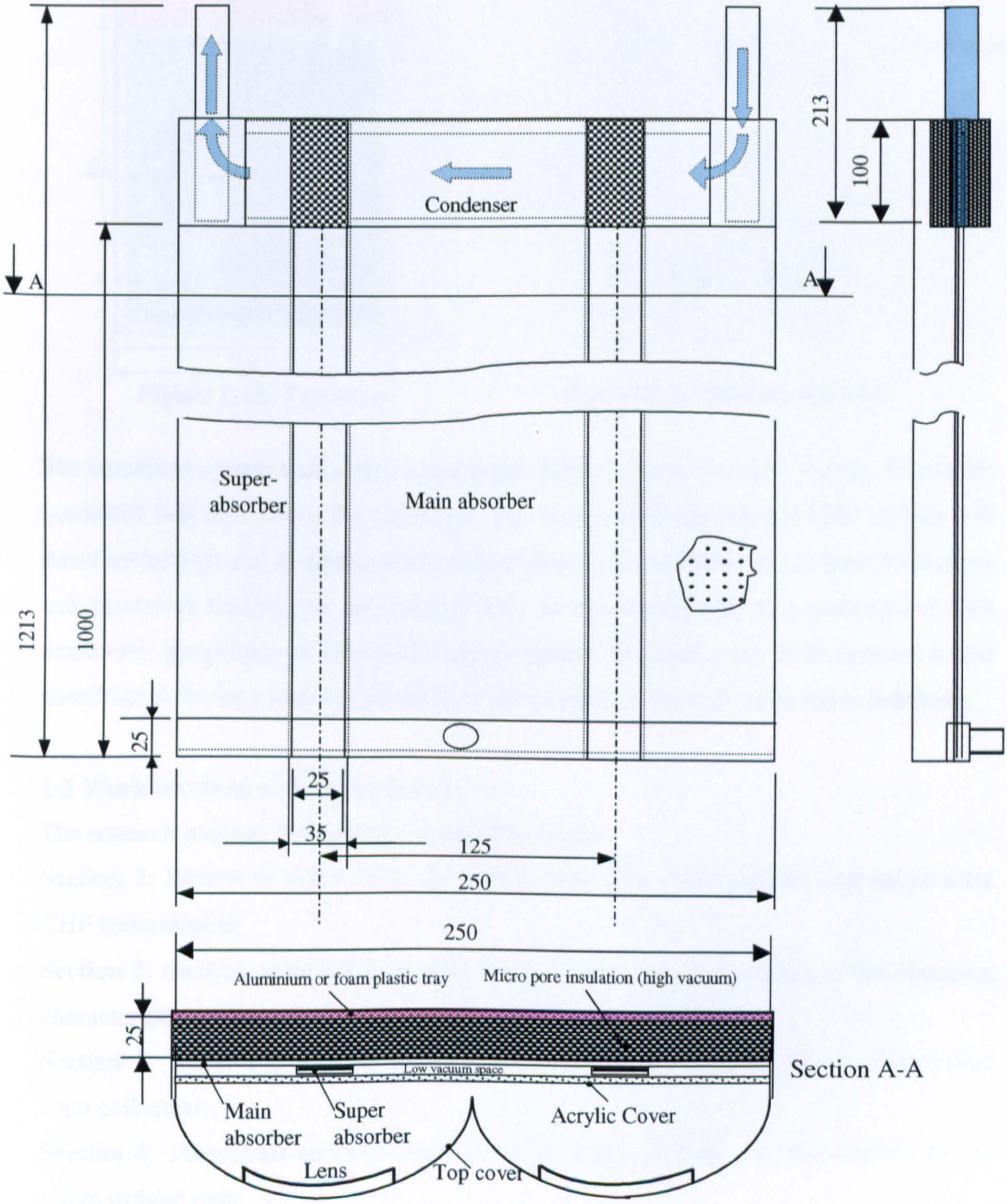

Figure 1-2. Schematic diagram of the 'normal' thin membrane heat pipe solar collector

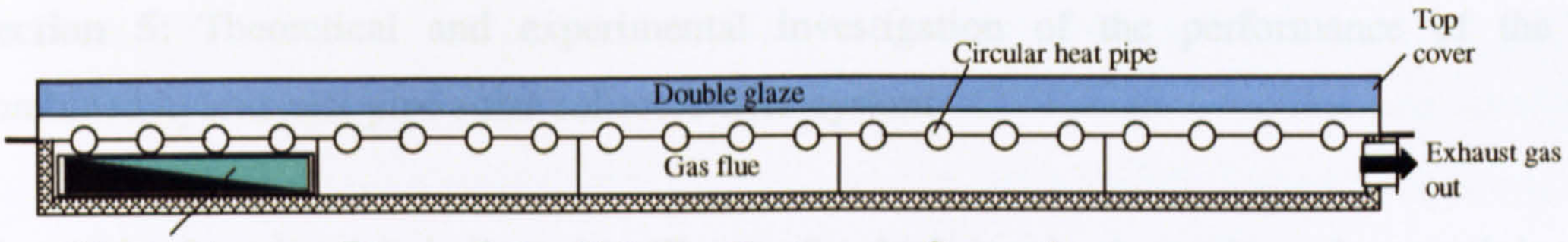

Figure 1-3a. Solar collector configuration

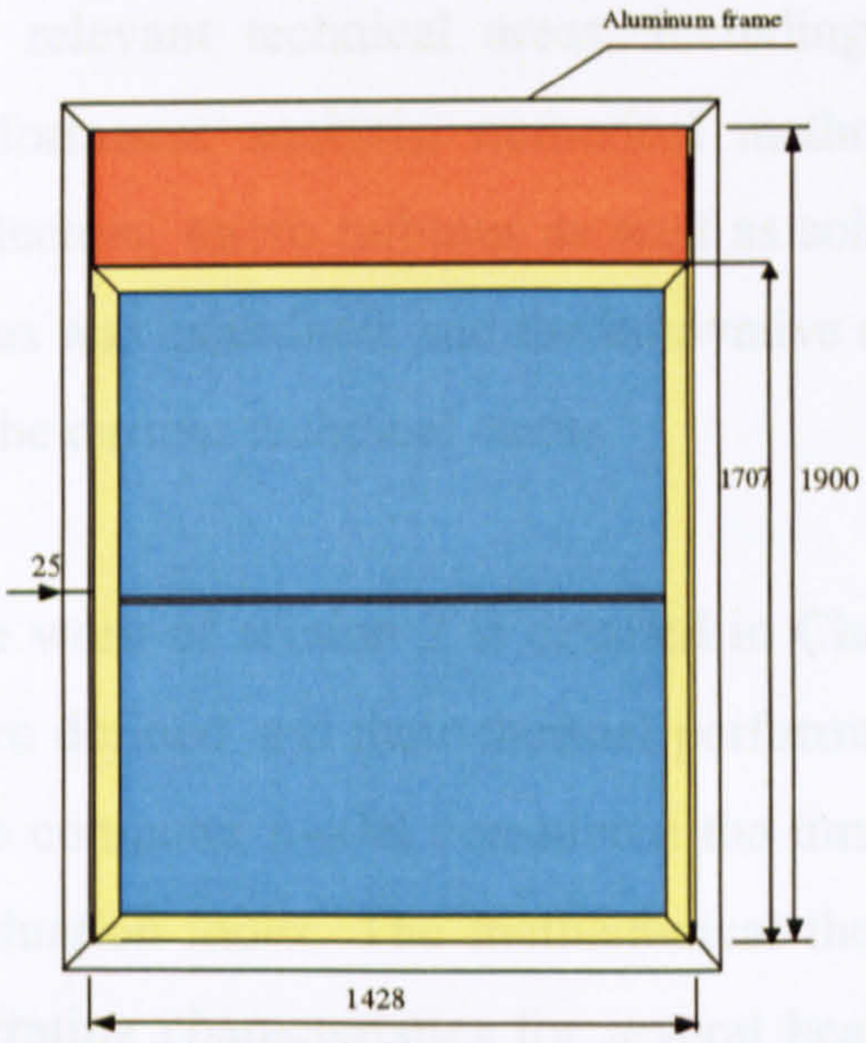

Figure 1-3b. Top cover

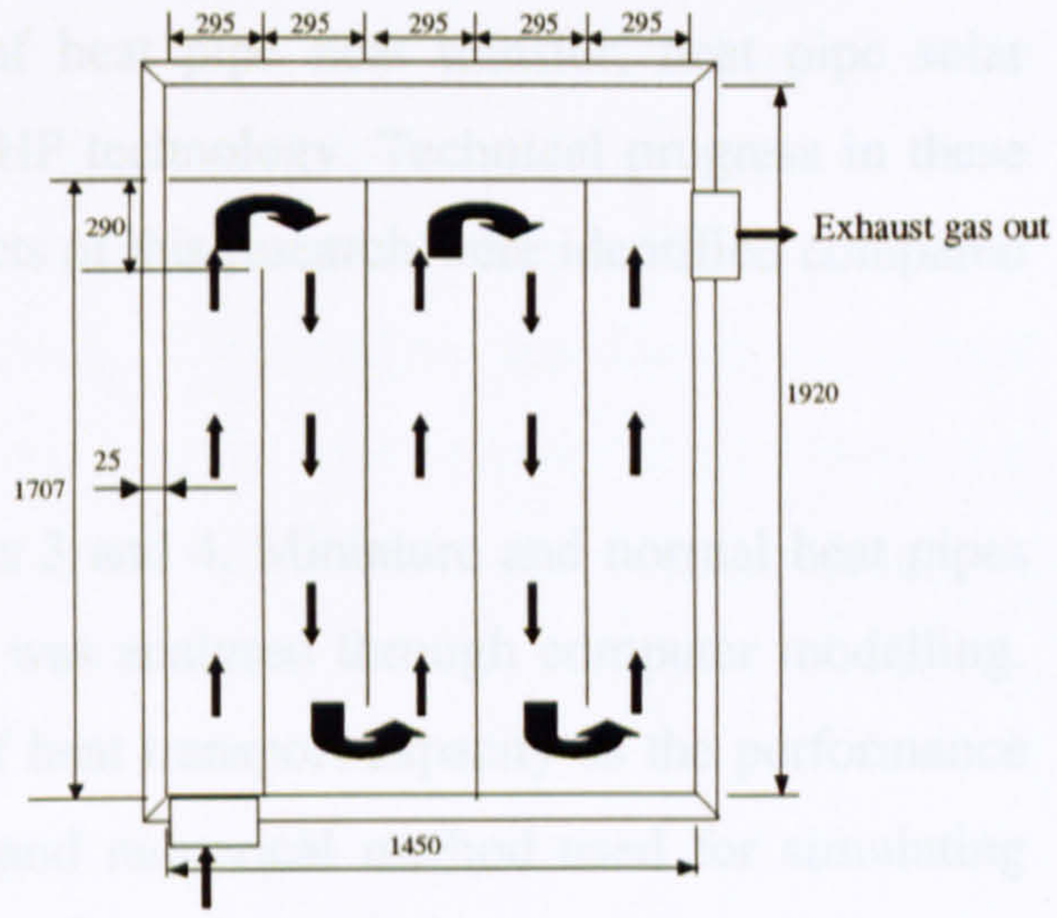

Figure 1-3c. Bottom chamber

The combined system will utilise a renewable energy source, i.e., solar energy, to provide combined heat and power for buildings. The energy efficiency of the CHP system will therefore be high and its development would allow consumption of fossil fuels for heating and power for buildings to be reduced. This in turn would lead to a reduction of CO_2 emissions. Integration of renewable energy system in small-scale CHP systems would contribute to the long-term sustainability of the heating, power and construction industries.

1.3 Work involved with the research

The research includes following 5 technical sections:

Section 1: Review of research of heat pipes, heat pipe solar collector and micro solar CHP technologies;

Section 2: Analysis of heat pipe thermal performance, and investigation of the operating characteristics of heat pipes by numerical/experimental methods;

Section 3: Theoretical and experimental investigation of the performance of heat pipe solar collectors;

Section 4: Theoretical and experimental investigation of flow and heat transfer in the micro turbine unit;

Section 5: Theoretical and experimental investigation of the performance of the combined hybrid heat pipe solar collector/CHP system.

The work of section 1 is indicated in Chapter 2, which involved a review of research in the relevant technical areas, including heat pipe technology and heat pipe thermal performance analysis, numerical methods of heat pipe heat transfer, heat pipe solar collectors, micro turbines as well as solar CHP technology. Technical progress in these areas was examined, and the innovative aspects of this research were identified compared to the current technical status.

The work of section 2 is detailed in Chapters 3 and 4. Miniature and normal heat pipes were defined and their thermal performance was analysed through computer modelling. The computer model considered the limits of heat transport capacity as the performance evaluation index. The mathematical theory and numerical method used for simulating operating characteristics for several heat pipes, including micro (miniature) and normal heat pipes, were introduced. Based on the theory and method, a numerical computer modelling was developed to simulate the flow and heat transfer in any of the heat pipes described above. Results obtained were discussed. To validate the numerical prediction, experiment was carried out to measure heat transfer and temperature variation for a long 'wicked' and a short 'wickless' heat pipe. Comparison between testing results and numerical predictions indicates that the numerical model is able to predict heat transfer occurring in the heat pipes at a reasonable accuracy.

The work of section 3 is detailed in Chapter 5. Two types of heat pipe solar collectors used for this application were designed, and the geometry and sizes of the heat pipes contained in the collectors were determined by using the analytical and numerical models above. A computer model used for analysing heat transfer in the collectors was developed, which could give collector efficiency, and temperature variation over the absorber and condenser areas, by solving a few coupled heat transfer equations. Two prototype solar collectors were constructed, and the rigs were built to test the performance of these collectors. Test results were compared to the modelling predictions enabling validation/modification of the computer model.

The work of section 4 is indicated in Chapter 6. Two micro turbines used for this application were introduced. These are the micro impulse-reaction turbine and turbo-alternator, which could generate electricity by operating with the selected working fluids, including water, n-pentane, HFEs and R141b. CFD numerical prediction was carried out by assuming a number of inlet and outlet conditions and using the FLUENT code. The simulation results allowed the percentage of un-blocked flow area to be determined for different working fluids and different inlet/outlet conditions, and the optimum working fluid and operation conditions to be found. To validate the CFD prediction as well as demonstrate the thermal and power performance of the turbine, experiment was carried out by using n-pentane as the working fluid and keeping inlet pressure at 5.14 bar(a) and outlet pressure at 1.15 bar(a). Experimental results were found to be in good agreement with the numerical predictions.

The work of section 5 is indicated in Chapter 7. A prototype hybrid heat pipe solar collector/CHP system was constructed. Theoretical investigation of the thermal and power performance of the prototype was carried out to evaluate electrical, heat and overall efficiency of the system. Testing of the prototype was then carried out. The results obtained are used to assess real performance of the combined system. These were also compared to theoretical predictions to validate/modify the analytical model. Saving on fossil fuel consumption and reduction of CO_2 emission were analysed compared to the traditional method of heat and power supply.

A number of conclusions derived from the research were arisen in Chapter 8. The merits of the proposed system were highlighted, and the problems encountered with the research were illustrated. Opportunities for further study on this topic were also discussed.

Chapter 2. Review of Research of Heat Pipes, Heat Pipe Solar Collectors and Micro CHP Technologies

2.1 Heat Pipes and Heat Pipe Thermal Performance Analysis

Heat pipes are simple heat transfer devices, having high, effective thermal conductivity and capable of transporting large amount of heat over considerable distances. Because of the simplicity of design and ease of manufacture and maintenance, these devices have found applications in a wide variety of areas, including energy conversion systems, cooling of nuclear reactors and electronic equipment as well as space apparatus, particularly the solar energy system involved in this analysis (Abhat A., 1982; Riffat S. B. et al, 2000; Riffat S. B., 2000).

Heat pipes make use of the evaporation of a suitable working fluid, transport of the latent heat of vaporization, condensation of the vapour and back flow of the condensate to the area where evaporation takes place (Dunn and Reay, 1982). The means of transporting the condensate from the condensation zone to the evaporation zone is the major distinction between the different designs of heat pipes. Different forces can be utilized, e.g., capillary (surface tension) forces, gravitation, acceleration (centrifugal) forces, thermally induced pressure differences or some combination of these.

Heat pipes can be designed and constructed with various cross-sectional areas and geometries as small as 0.6 mm x 0.6 mm and 25 mm in length (micro heat pipes), or 2mm in diameter and 1m in length (mini heat pipes) (Riffat et al, 2002), and as large as 100m in length (Takaoka M. et al, 1985). All heat pipes have an evaporator and condenser section where the working fluid evaporates and condenses respectively. Many heat pipes also have a transport or adiabatic section, which separates the evaporator and condenser sections by an appropriate distance intended to satisfy the heat pipe limitations and the design constraints of the application. A given heat pipe may have multiple evaporators, condensers and adiabatic sections. A working fluid usually circulates due to the influence of capillary forces in a wick.

However, gravitational, centrifugal, electrostatic, and osmotic forces can also be used to return the liquid from the condenser to the evaporator.

Various types of heat pipes can be made to suit for different applications. Seven typical heat pipe configurations, namely, gravity-assisted wickless heat pipe (two-phase closed thermosyphon), capillary-driven heat pipe, annular heat pipe, flat-plate heat pipe, rotating heat pipe, leading edge heat pipe, gas-loaded heat pipe, capillary pumped loop heat pipe and mono groove heat pipe, are shown in Figs. 2-1 to 2-8 (Faghri A., 1995). Heat pipe containers are generally circular cylinders for simplicity of design and manufacturing. However, other shapes such as rectangular (flat plate heat pipes), parallelepiped, micro/miniature, conical (rotating heat pipes), and nose-cap (leading edge heat pipes) geometries have also been investigated for special applications.

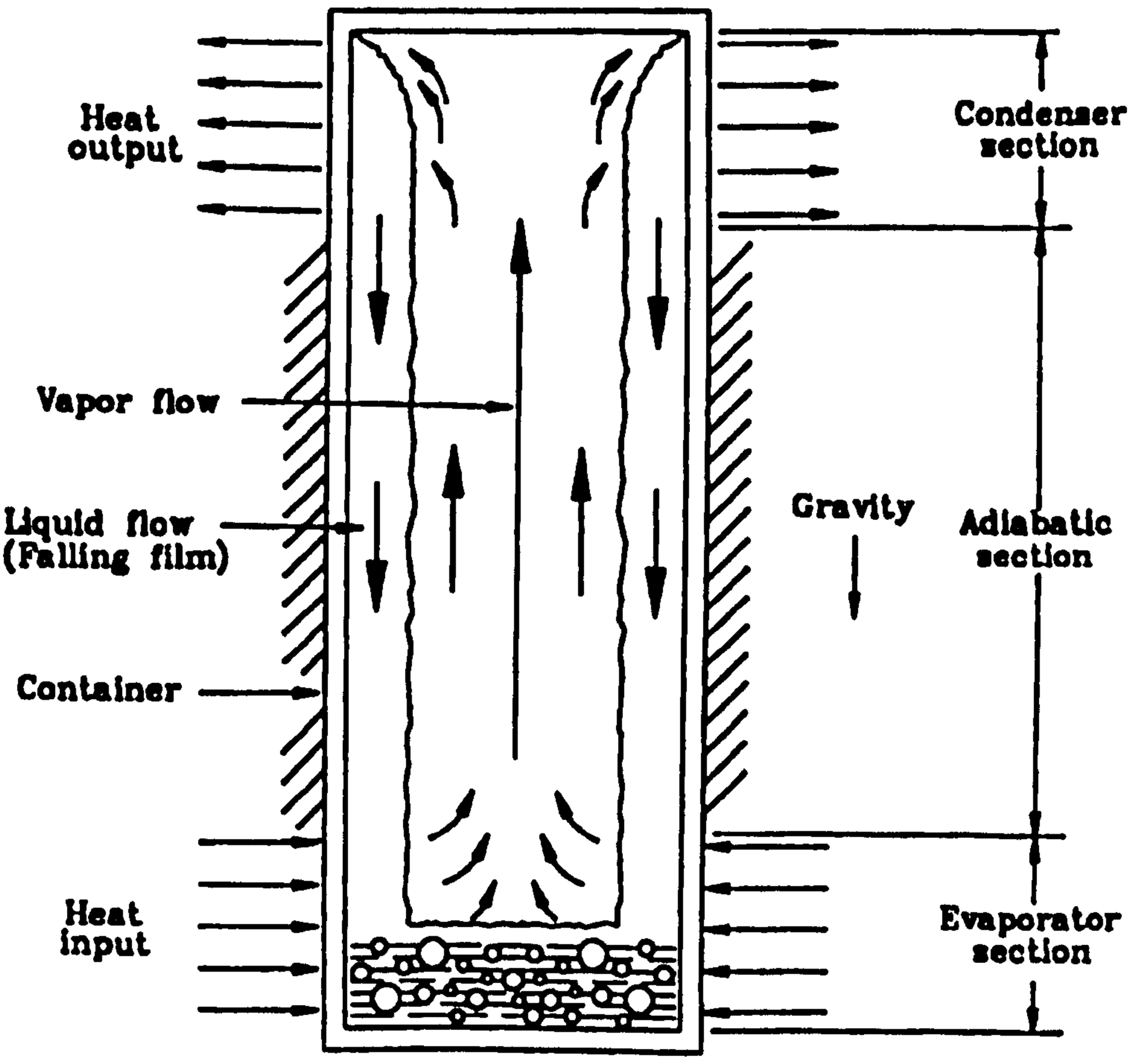

Figure 2-1 Gravity assisted wickless heat pipe (two-phase closed thermosyphon)

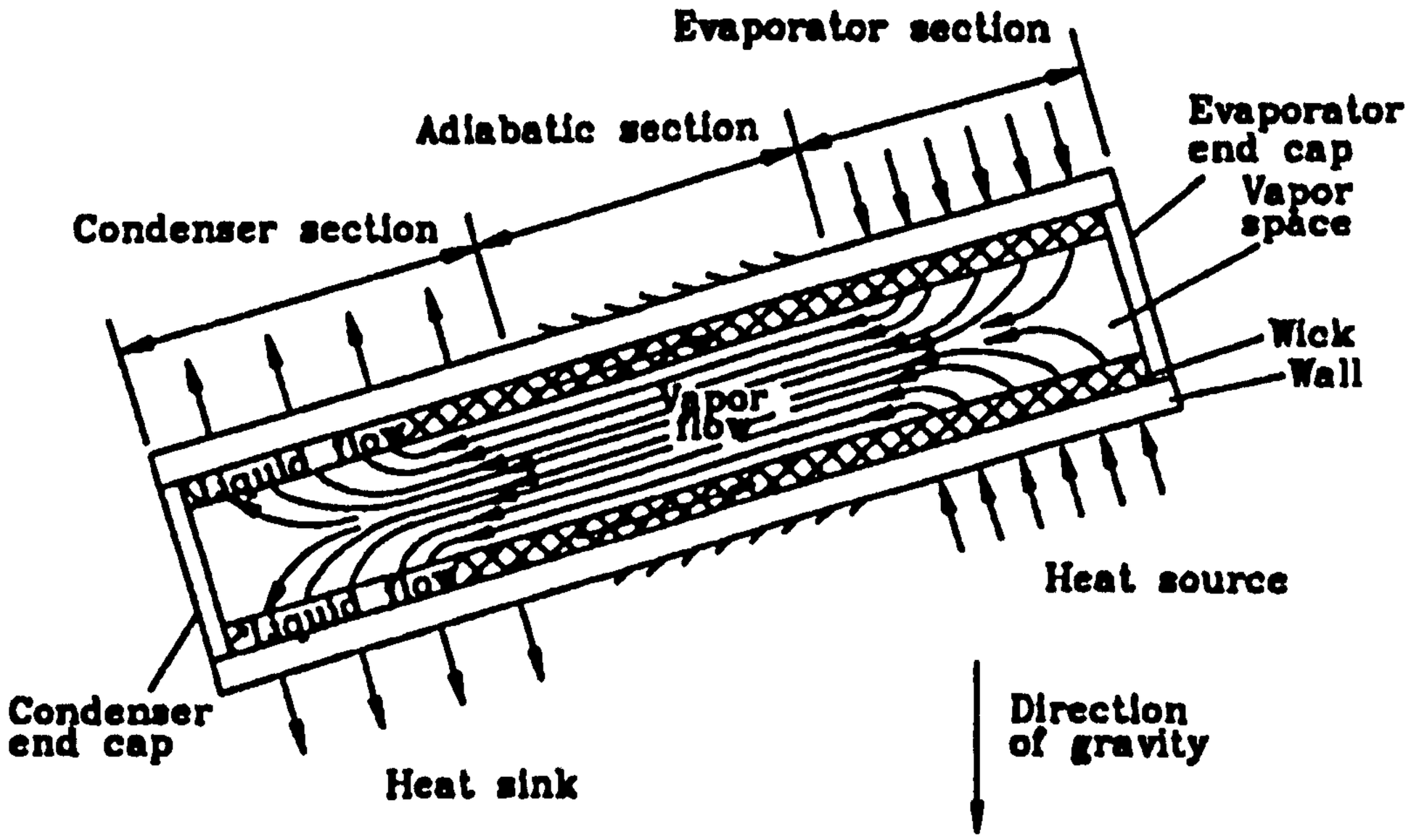

Figure 2-2 Conventional capillary-driven heat pipe

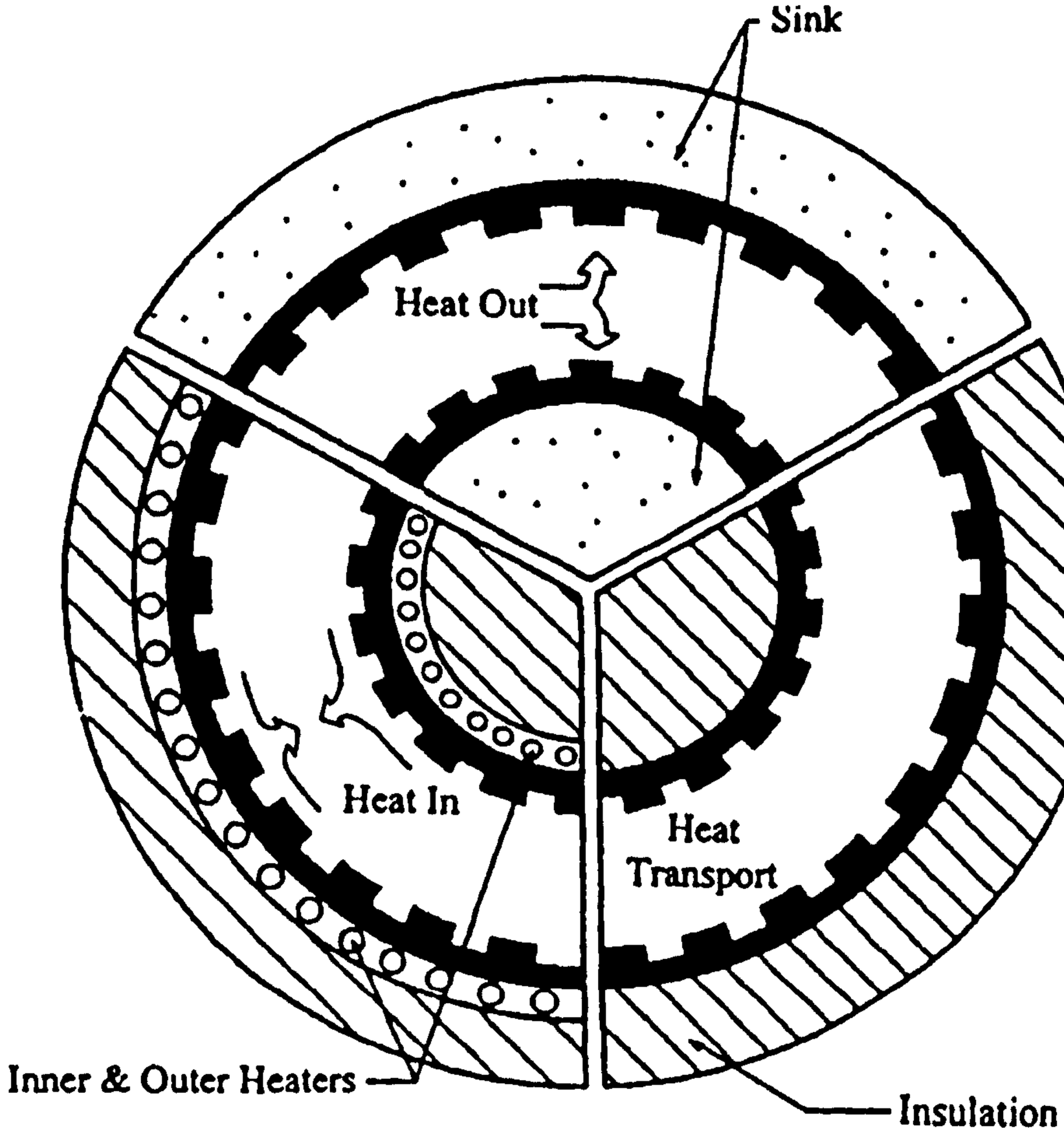

Figure 2-3. Concentric annular heat pipe design

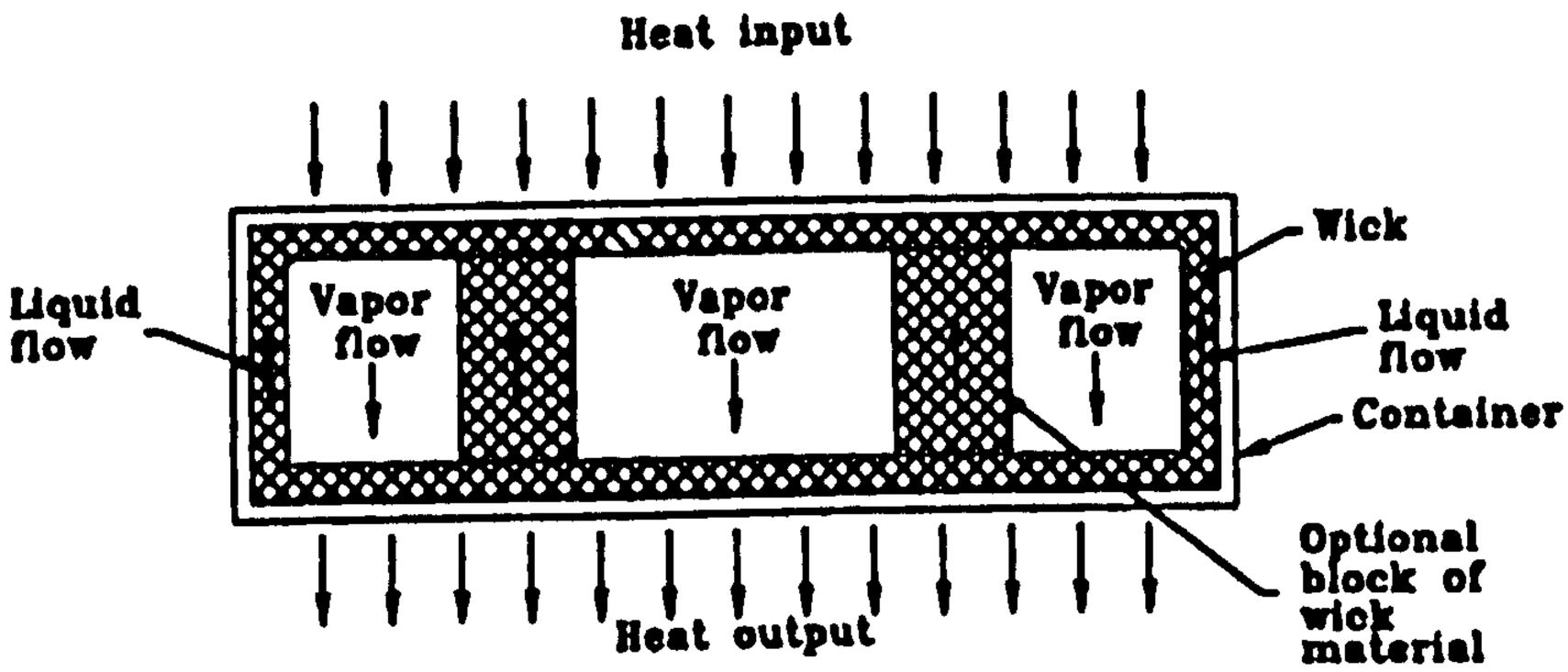

Figure 2-4. Flat-plate heat pipe

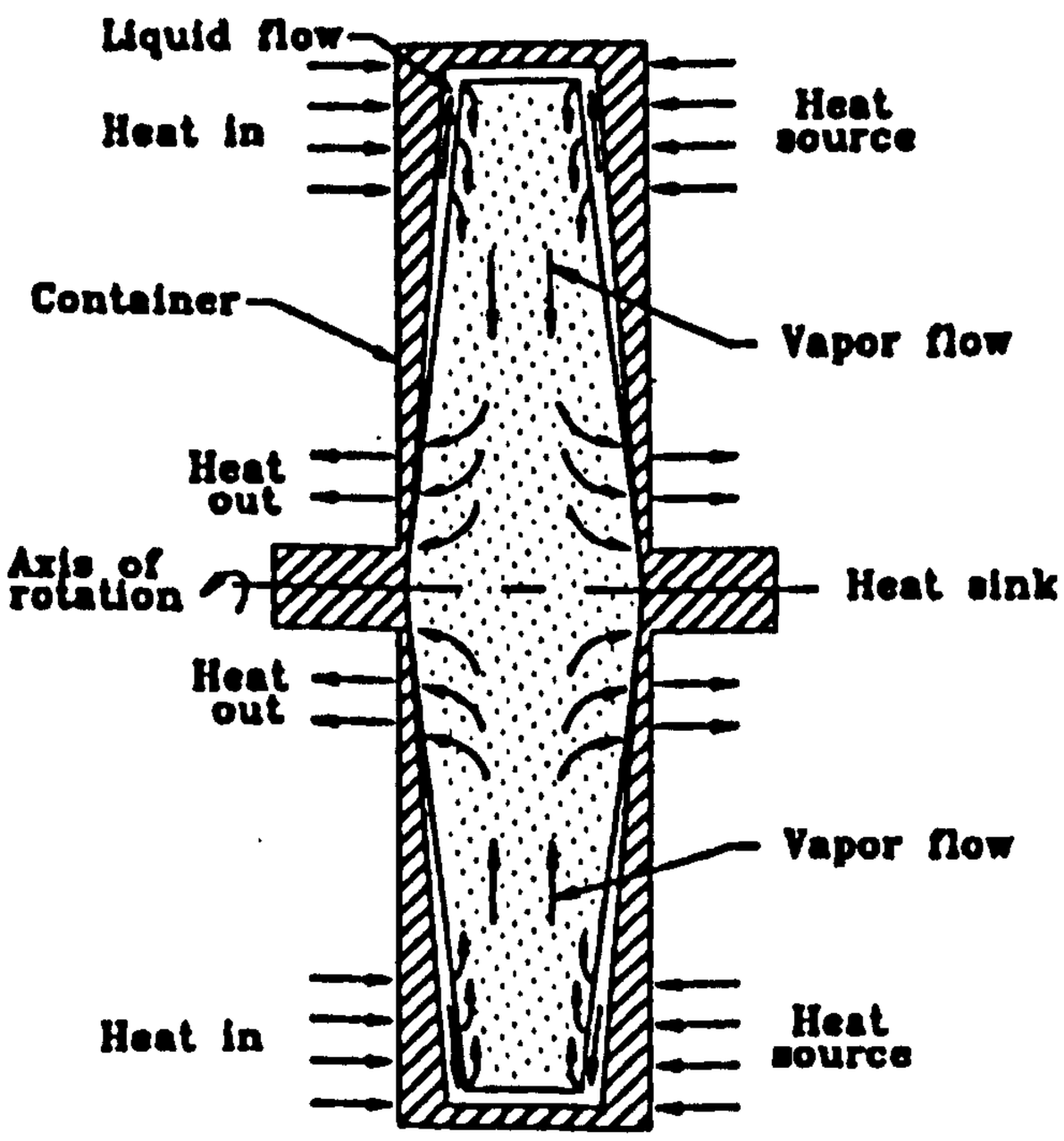

Figure 2-5. Rotating heat pipe (radial flow)

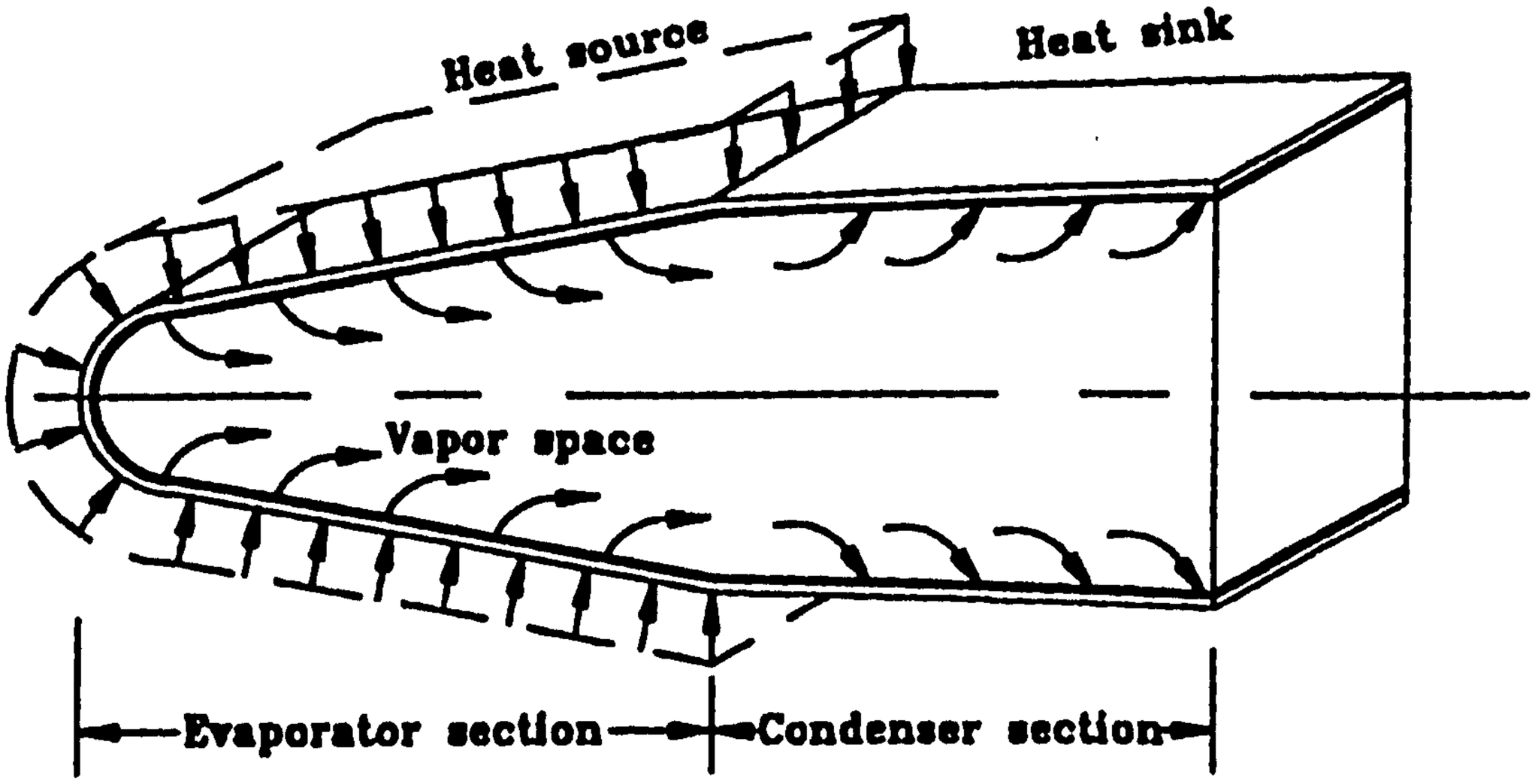

Figure 2-6. Conceptual design of a leading edge heat pipe

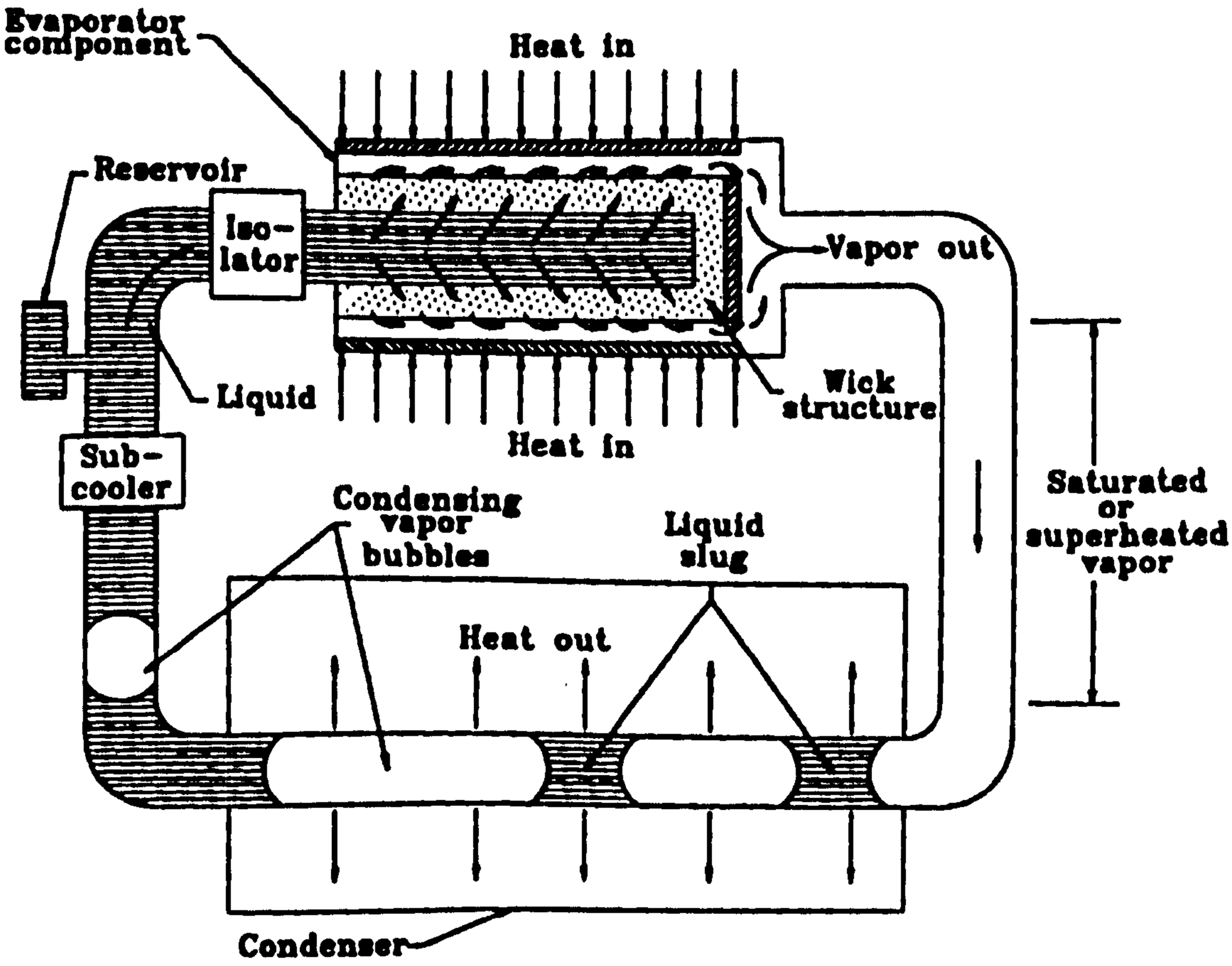

Figure 2-7. Capillary pumped loop heat pipe (CPL)

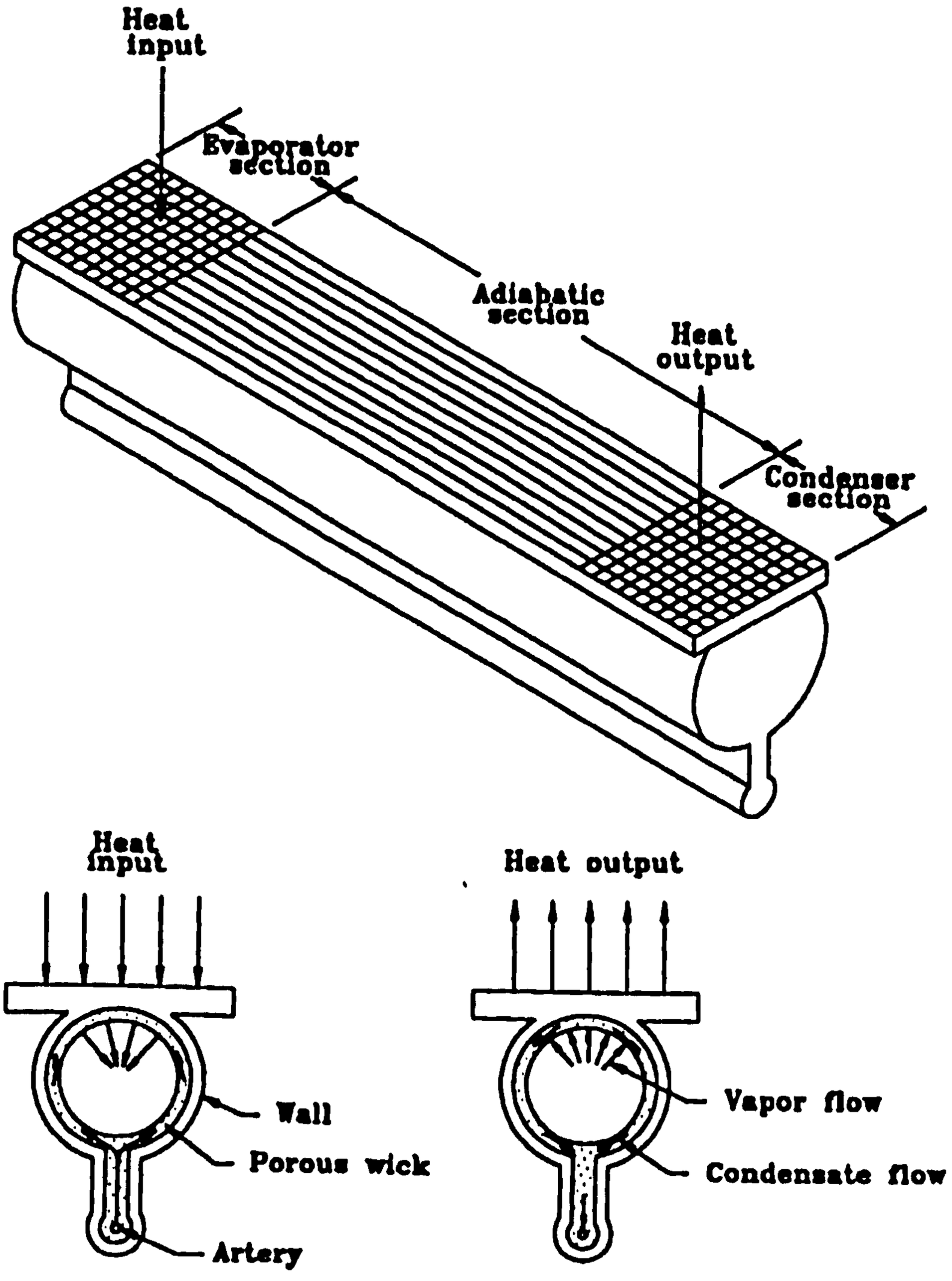

Figure 2-8. Monogroove heat pipe

'Miniature' or 'micro' heat pipes are two types of heat pipes particularly used for small space heat transfer, such as heat transfer in micro-electronic equipment and aerospace apparatus. A 'micro' heat pipe is defined as a heat pipe that is so small that the mean curvature of the vapour-liquid interfaces is necessarily comparable in magnitude to the reciprocal of the hydraulic radius of the total flow channel (Cotter, 1984). In practical terms, a 'micro' heat

pipe is a 'wick-less', non-circular channel with an equivalent diameter of 0.1 to 1 mm. The cross section geometry of a 'micro' heat pipe is usually a concave trapezoid with tapered triangular channels in each of the four corners (Babin B. R., Peterson G. P. and Wu D., 1989), as shown in Figure 2-9. Capillary action plays a major role in the operation of a 'micro' heat pipe. A 'miniature' heat pipe is similar to a 'micro' heat pipe in most aspects, but has a relatively larger equivalent diameter, which is in the range 1 to 3mm.

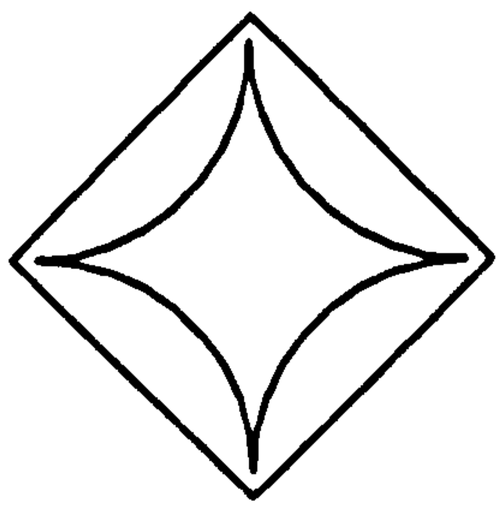

Figure 2-9. A typical micro heat pipe

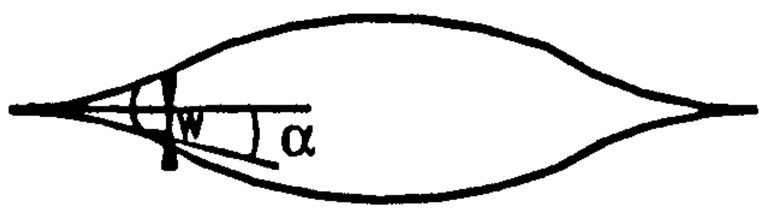

Figure 2-10. A special 'miniature' heat pipe

A special 'miniature' heat pipe was used as the basic component of a thin membrane heat pipe solar collector. The heat pipe differs from traditional 'miniature' pipes in that it has a parallelepiped channel geometry with two sharp corners in opposite, as shown in Figure 2-10. The sharp corners are slim enough to hold liquid block and produce a capillary force, and the capillary force plays an important role on returning liquid. In addition, since the heat pipe was arrayed with a certain inclination in relative to horizon. gravitational force also played a role on returning the liquid as well.

For any heat pipe, the maximum heat transport capacity is governed by five limits, namely, sonic limit, the entrainment limit, the boiling limit, the viscous limit and the capillary limits. These limits could be calculated by using the techniques presented in Dunn and Reay (1982) and Babin et al (1990), and the critical limit would be the minimum value calcuated. For a gravity heat pipe, filled liquid mass also influences its heat transfer to a certain extent, representing an additional limit which could be calculated by the method presented by Zhuang J. et al (1989).

The formulas for limits of heat transport capacity are normally applied to normal heat pipes with circular cross-section. For 'micro' or 'miniature' heat pipes, some new problems may arise and hence a special consideration would be required. One of these is the larger viscosity and entrainment effect between the vapour and liquid phases, which would cause higher flow resistance and poorer heat transfer. To cope with the situations of both micro/miniature and normal heat pipes, it is increasingly desirable to develop an extensive analytical model, which takes a few factors, including the influence of heat pipe geometry on flow, as well as capillary effect caused by the sharp corners of the micro/miniature heat pipes, into account.

2.2 Numerical Methods of Heat Pipe Heat Transfer

Over the past 30 years, extensive studies have been conducted in order to provide a thorough understanding of the heat pipe operation and appropriate design schemes for practical applications. As a result, numerous methods, covering a variety of aspects of heat pipe operations, have been developed (Faghri, A., 1995).

Previous experimental studies, concentrating on a variety of heat pipe aspects, have provided useful insights into heat pipe operations, set references for validation of theoretical models, and provided databases for design purposes. Moreover, many theoretical analyses have incorporated empirical or semi-empirical correlation to simplify the models and the solution process.

Most previous theoretical studies developed numerical methods to solve governing equations of the heat pipe operation. These numerical models ranged from lumped analysis to quasi-one-dimensional vapour flow to conjugated three-dimensional vapour flow and heat pipe wall heat conduction. A review of numerical models and solution methods for various heat pipe operations including steady state, continuum transient and frozen start-up has been carried out by Faghri (1995). Generally, previous theoretical models consisted of a set of highly nonlinear partial differential equations. To obtain solutions to these equations, numerical techniques such as finite-difference and finite-element methods have to be

incorporated, and significant programming efforts and computational time are required (Colwell and Modlin, 1992).

Bowman and Hitchcock (1988) and Issacci et al. (1991) developed two-dimensional transient models of vapour flow in heat pipes and showed that a one-dimensional treatment is inadequate since it could not predict accurately the radial heat and mass transfers or the pressure drop. Such vapour flow models provided valuable information on vapour flow dynamics.

Ivanovsky et al (1982) and Tilton et al (1986) suggested that during steady state or slow transients, heat pipe operation could be adequately described by using heat balance principle in various heat pipe regions. Following this observation, Chang and Colwell (1985), Tilton et al (1986), Faghri and Chen (1989) and Cao and Faghri (1990) solved the two-dimensional heat conduction equations for the wall and liquid-wick region, which were thermally coupled to either a one- or two-dimensional vapour flow model. Faghri and Chen (1989) used their steady-state model to evaluate the effects of axial conduction, vapour compressibility and viscous dissipation on the operation of water and sodium heat pipes. Cao and Faghri (1990) also modeled the start-up of heat pipes from the frozen state. Different start-up periods were considered, including free molecular and continuum vapour flow conditions. Continuum flow was modeled using the two-dimensional compressible Navier-Stokes equations, while the rarefied flow was simulated using turbulent diffusion model.

Tilton et al (1986), Cao and Faghri (1990) and other investigators mentioned above neglected both the liquid flow and the hydrodynamic coupling of the liquid and vapour phase by assuming the wick to be a pure conducting medium with an effective thermal conductivity. Later, Faghri and Buchko (1991) included the effect of liquid flow in the wick by treating this region as a saturated and isotropic porous medium, but computed the pressure profiles along the heat pipe independently. Such decoupling of the liquid and vapour momentum equations can result in an error when calculating the liquid flow rates and vapour pressure.

Ransom and Chow (1987), Doster and Hall (1989) and Seo and El-Genk (1989) incorporated liquid flow and thermal compressibility, hydro-dynamically coupled the liquid and vapour phases, and predicted the vapour volume distribution in the wick. They used the capillary relationship of Pascal to relate the phase pressures, and the radius of curvature of the liquid meniscus at the liquid-vapour (L-V) interface was geometrically related to vapour volume fraction in the wick. Such information is needed for predicting the capillary and dry-out limits during transient operation of the heat pipe.

Although Ransom and Chow (1987), Doster and Hall (1989) and Seo and El-Genk (1989) have incorporated the effects of liquid flow and thermal compressibility, their models, except that of Doster and Hall, lacked the capability of predicting the liquid pooling at the end of the condenser. Such pooling occurred due to the thermal expansions of the liquid phase during startup transients of heat pipe charged with excess liquid (Merrigan M. A. et al, 1986). The pooling model of Doster and Hall dealed with local variation of the liquid fraction in the wick region to differences in evaporation/condensation rates and thermal expansion of the liquid. However, it did not determine when and where a 'net point' appears in the heat pipe nor its propagation with time toward the end of the condenser as the heat pipe continued to heat up (a 'net point' was where the liquid-vapour interface became flat and the vapour and the liquid pressures are equal). Similarly, the pool model of Doster and Hall did not handle the accumulation and receding of the liquid pool with time during the heat-up and cool-down transients of the heat pipe, respectively.

The model of Ransom and Chow (1987), Doster and Hall (1989) and Seo and El-Genk (1989) also treated the vapour flow using either a one-dimensional, transient approximation or a quasi-steady state approach, which may not be justified during rapid start-up or shut-down transients of heat pipes. At start-up, when a heat pipe was operating at low vapour density and high vapour velocity, large radial temperature gradients may develop in the wall, liquid-wick and vapour regions, and hence a two-dimensional treatment of the vapour flow

was required (Deverall J. E. et al, 1970).

Heat Pipe Transient Analysis Model was developed, and the model predictions were compared with the experimental data of Huang et al (1993) for a horizontal water heat pipe. An analysis was performed to determine the transient behavior and axial distributions of liquid and vapour pressure, the radius of curvature of liquid meniscus at the liquid-vapour interface, and liquid pooling and recession following step function heat-up and cool-down transients of the water heat pipe.

The complicated mathematical expressions and numerical schemes in those studies above are useful in accurate analysis, but sometimes may 'mask' the real physics from a designer's point of view. For most practical applications, it is usually not desirable or necessary to get into such details. Therefore, a simple and practicable model for the heat pipe analysis would be more attractive.

2.3 Heat Pipe Solar Collectors

Solar collectors transform solar radiant energy into heat energy. There are several types of solar collector available for practical application, including evacuated tubes, flat plate solar collectors and parabolic dish collectors.

Heat pipes are devices of high thermal conductance, which transfer thermal energy by two-phase circulation of fluid, and can easily be integrated into most types of solar collector. The basic difference in thermal performance between a heat-pipe solar collector and a conventional one lies in the heat-transfer processes from the absorber tube wall to the energy-transporting fluid flow. For a heat pipe collector, the process is evaporation-condensation-convection, while for conventional solar collectors, heat transfer occurs only in the absorber plate. Thus, solar collectors with heat pipes have a lower thermal mass, resulting in a reduction of start-up time.

A feature that made heat pipes an attractive for solar collectors is their ability to operate like a thermal-diode, i.e., the flow of the heat is in one direction only. This minimizes heat loss from the transporting fluid, e.g., water, when incident radiation is low. Furthermore, when the maximum design temperature of the collector is reached, additional heat transfer can be prevented. This would prevent over-heating of the circulating fluid, a common problem encountered in many applications of solar collectors (Bienert and Wolf, 1976; DeVriers et al, 1980).

Integration of heat pipes also provides the advantage of high heat transfer in the latent form. Heat pipes are self-contained devices and can be for collection and transfer of energy in solar collectors. Collectors used for heating of liquids may incorporate the evaporator section of the heat pipe, under pressure in the flat plate of the solar collector, and the condenser section would be inserted in the storage tank containing the liquid to be heated. The system therefore needs no piping or fittings between the storage tank and the collector, and this reduces both the cost and the heat loss of the system. If the working fluid of the heat pipes was chosen to have a low freezing point, the collector may offer freeze protection (Ismail and Abogderah, 1998).

One of the first studies of heat pipes in solar applications was carried out by Bienert and Wolf (1976). In this case, the evaporator end of a heat pipe was inserted in a flat-plate collector, and the condenser protruded into a water manifold attached to the upper end of the collector. Their results were neither conclusive nor optimistic. Since then numerous studies have been carried out, and these could be placed into an rerview according to the time order. Franken (1979) presented an analysis and calculation of the thermal resistance of heat pipe solar collector. Ortabasi and Fehlner (1979) analysed the performance of a concentrated vacuum tube solar collector which used a heat-pipe for the heat transfer to the circuit of the heating fluid, which circulated between the collector and the tank. DeVries and Kamminga (1980) gave a comparison for fluid circulation control between a heat pipe planar collector and a conventional one. Ernst (1981) conducted a theoretical and experimental investigation of a

cost-effective solar collector using heat pipes with evacuated tubes. Bairamov and Toiliev (1981) described the operation of a solar system using a thermosyphon heat-pipe and analysed its performance in relation to a typical thermosyphon system. Emphasis was given to the absence of a reverse flow and to the elimination of problem associated with the circulation of heat transfer fluid (corrosions, stability of heat transfer fluid, freeze protection, etc). Ribot and McConnell (1983) performed a testing and analysis of a typical evacuated heat pipe solar collector, which gave a testing efficiency of 50% above. Lu and Guo (1984) investigated fundamental thermal performance of solar collectors, especially for the heat pipe themselves. Ramsey (1986) found that the collector efficiencies would be on the order of 50% or more if the heat pipe panel was coated with a high performance coating material and equipped with single-axis tracking parabolic trough concentrators. Terpstra et al (1987) described a system with a heat-pipe in which there was no wick and the flow of the condensed liquid was accomplished by gravity. At the collector outlet, vapour was brought together with liquid and they were condensed in an auxiliary heat exchanger in the upper part of the system. Zanardi (1989) studied a heat pipe parabolic solar collector and obtained efficiency of about 50 percent. Ismail and Abogderah (1991, 1992[a], 1992[b]) published some partial results related to heat pipe solar collectors. El-nasr (1993) investigated the thermal performance of a wickless heat pipe solar collector on the basis of heat-transfer analysis using R-11, acetone, or water as working fluid at different charging pressures. The effects of angle of inclination and the effect of liquid fill on performance of the wickless heat pipe solar collector were also investigated in this study. Bong et al. (1993) investigated the performance of an array of flat-plate heat pipe collectors. The array had been in operation for several years, to serve a solar-powered air-conditioning system. Balzar et al. (1996) presented results from the tests performed in a solar cooker, which operated through the use of vacuum tubes with an incorporated heat-pipe. Ismail and Abogderah (1998) presented a comparative analysis between theoretical results and experimental figures in a pumped system, in which a heat-pipe was used for the heat transfer from the collecting surface to the tank-collector circuit. Theoretical calculations were carried out for both the collector and the heat pipe, which were slightly tilted as the condenser was fitted on the upper part. Chun et al (1999)

developed a solar domestic hot water system using heat pipes. Some other major design parameters examined in the study included: types of heat pipe (presence of a wick), coating materials for the evaporator section and the shape of storage unit for maximum thermal stratification. Hussein et al. (1999) examined the transient thermal behaviour of a wickless heat-pipe flat plate collector with regard to solar radiation and various geometrical characteristics of the collector. Riffat et al (2000) carried out the performance testing of a few different types of liquid flat plate collectors. Mathioulakis et al (2002) investigated the performance of a new solar hot water system with an integrated heat pipe.

Most previous work focused on the investigation of the thermal performance of various types of heat-pipe solar collector, including evacuated tube, flat plate and parabolic, by using analytical, numerical or experimental methods. Of existing collector designs, evacuated tube and flat plate collectors are most widely used and the former is usually found to be most efficient for high temperature operations. Flat plate heat pipe solar collectors, on the other hand, have their own set of advantages including simpler structure, lower cost, easier manufacture and simple operation.

The lower efficiency of flat plate collectors is mainly due to the heat loss via the cover surface due to convection and conduction. Standard flat plate collectors have efficiencies of typically less than 50% (Riffat et al, 2000), while evacuated devices have efficiencies of about 50-80% (Ribot and McConnell, 1983; Ramsey, 1986; Zanardi, 1989). It would be desirable to develop a new structure for flat plate collectors that would overcome heat loss problems and allow a high efficiency to be achieved.

In the research, two novel structures of flat-plate collectors were designed. One is the thin membrane heat pipe solar collector, and the other is hybrid solar heat pipe collector. They were all designed to generate high temperature water, used to drive a micro turbine to produce electricity and hot water for residential use (Riffat et al, 2000; Riffat, 2000). To find a suitable structure and configuration layout, the miniature and normal heat pipes, as the

basic elements of the collectors, were investigated using analytical, numerical and experimental methods, which are described in Chapters 3 and 4. An analytical model for efficiency calculation and energy balance of flat plate solar collectors was developed, which was used to simulate the thermal performance of these two collectors. Laboratory tests were made as well to test the thermal performance of the collectors. Theoretical and experimental results were compared to validate/modify the prediction of the analytical model and examine the real performance of the collectors under operation.

2.4 Micro Steam Turbines

A steam turbine is defined as a form of heat engine in which the energy of the steam is transformed into kinetic energy by means of expansion through nozzles, and the kinetic energy of the resulting jet is in turn converted into force doing work on rings of blading mounted on a rotating part.

The usual turbine consists of four fundamental parts (Church Edwin F. et al, 1982): the rotor which carries the blades or buckets; the stator consisting of cylinder and casing, which are often combined and within which the rotor turns; the nozzles or flow passages for the steam, which are generally fixed to the inside of the cylinder; and the frame or base for supporting both the stator and the rotor, the latter being carried in bearings. Cylinder, casing, and frame are often combined, particularly in small turbines. Accessories necessary for the successful continuous commercial operation are a controlling or governing system for adjusting energy supply to the turbine to suit the load to be carried and for maintaining constant speed, a lubricating system, piping for steam supply and exhaust, and a condensing system.

Steam turbines may be classified in different ways. With respect to form of steam passage between the blades, the turbines may be categorized into three different styles, namely, impulse, reaction/parsons and combination impulse and reaction. An impulse turbine is defined as a system in which all steam expansion takes place in fixed nozzles and none occurs in passage among moving blades. A simple-impulse turbine is shown schematically in

Figure 2-11. A reaction or Parsons turbine is one in which the steam decreases in pressure and expands while it is passing through the moving blades as well as in its passage through the fixed nozzles, as illustrated in Figure 2-12. A combined impulse-reaction turbine is shown in Figure 2-13, where a velocity-stage impulse wheel precedes the reaction stages. This is the usual combination in all central-station turbines except certain machines which handle very large quantities of steam, where the two-row wheel may be omitted.

Micro turbines offer a number of potential advantages compared to normal turbines for small-scale power generation (Pilavachi P. A., 2002). For example, compact size and low-weight per unit power leading to reduced civil engineering costs, a small number of moving parts, lower noise, multi-fuel capabilities as well as opportunities for low emissions (in the CHP context).

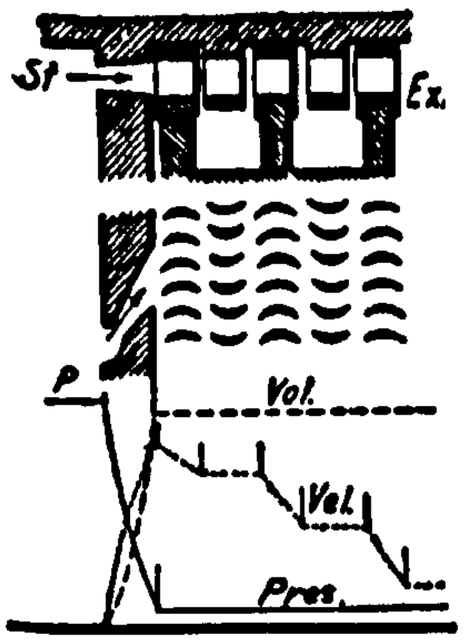

Figure 2-11. A simple impulse turbine

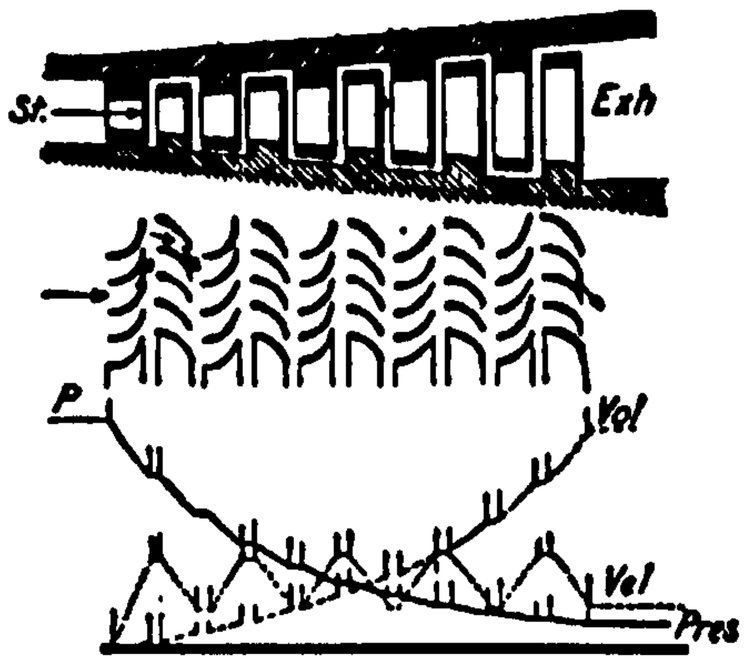

Figure 2-12. A reaction (Parsons) turbine

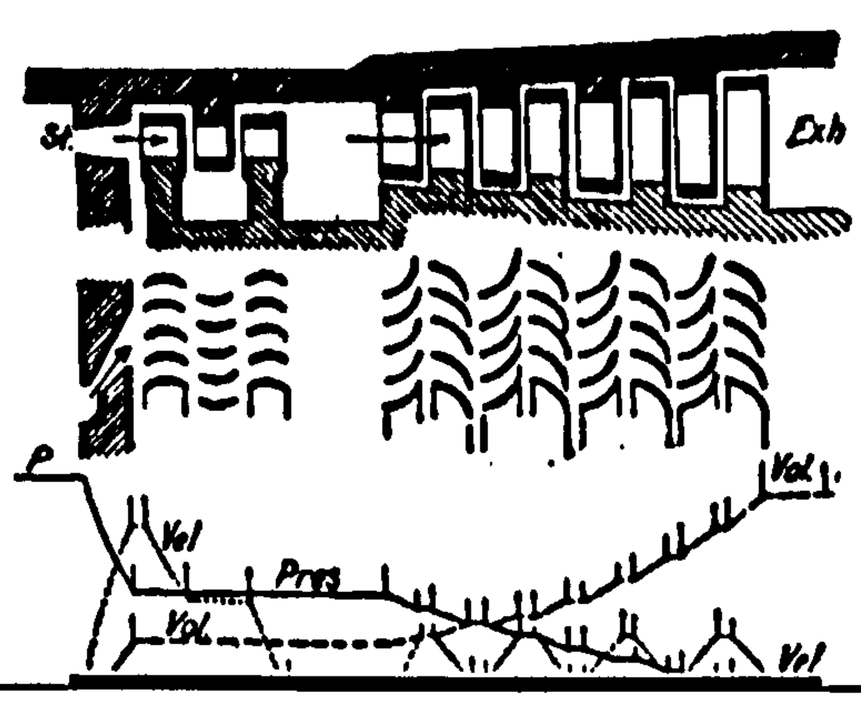

Figure 2-13. Combination of impulse and reaction turbine

Most micro turbines are driven by natural gas. However, some other fuels, such as diesel, landfill gas, industrial off-gases and ethanol, are also available for operation of the turbines. This type of turbine is called micro gas turbine.

Currently the smallest commercially available turbine is 38kWe, which is driven by natural

gas. In the U.S., 5kWe diesel-fueled turbines are available from intelligent (FEW P. C. et al, 1997). There is no report for commercial application for a micro steam turbine less than 50kWe output. However, a specially designed impulse-reaction steam turbine with 1.5-3kWe outputs has been developed and used in a prototype CHP system (Oliveira A. C. et al, 2002).

2.5 Solar CHP technology

Combined heat and power (CHP) systems use energy more efficiently than that generated and delivered to the national grid by conventional methods. Conventional power stations generate electricity and reject the heat as a waste. This wastage together with losses in the transmission of electricity results in poor overall efficiency and high electricity costs.

CHP schemes are a more efficient means of generation as they can produce electricity for local use and thus minimise the distribution losses. They also allow the heat output from the generation plant to be used for space or process heating. In applications where there is a combined heating and electricity requirement a very efficient means of energy usage is produced compared to the conventional method of providing heating and electricity. This is detailed in Figure 2-14a & 2-14b, which shows the primary energy consumed by a conventional scheme compared with a CHP scheme to satisfy the same heating and electrical demand. From this it may be seen that the conventional system shown uses 60% more primary energy than the CHP scheme (Prosser and Maidment, 1998).

It has brought about growing interests in research and development of CHP technologies over the past decades. These covered a variety of aspects, including strategies of CHP technology development, theoretical simulation of the system performance, determination of the sizes and economic analysis, as well as likely applications in markets. A review of previous studies focusing on specific subjects of CHP technology is given below:

Pilavachi P. A. (2002) overviewed the power generation with gas turbine and combined heat and power (CHP) system. It also presented the European Union strategy for developing gas

turbines and CHP systems. Methods to improve the performance of the several types of gas turbine cycle would be a major objective in the coming years. The targets would be combined cycle efficiencies above 60%, industrial gas turbine system efficiencies of at least 50% and small gas turbine efficiencies above 35% and designs for the use of fuels with less than 25% heating value of that of natural gas. The main CHP targets would be the reduction of the overall costs and the development of biomass-fired systems of above 40kW.

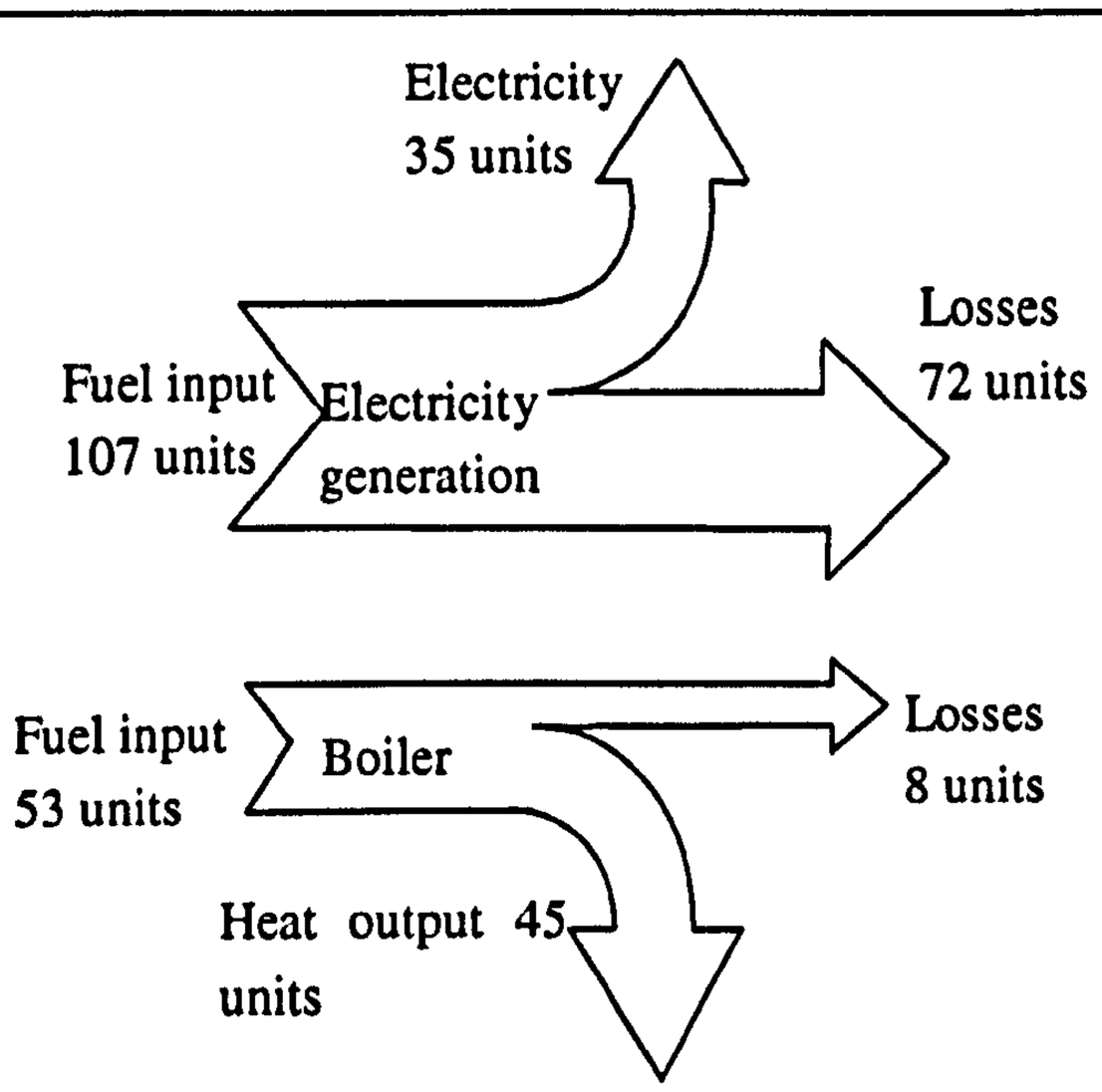

Figure 2-14a. Conventional heat and power application

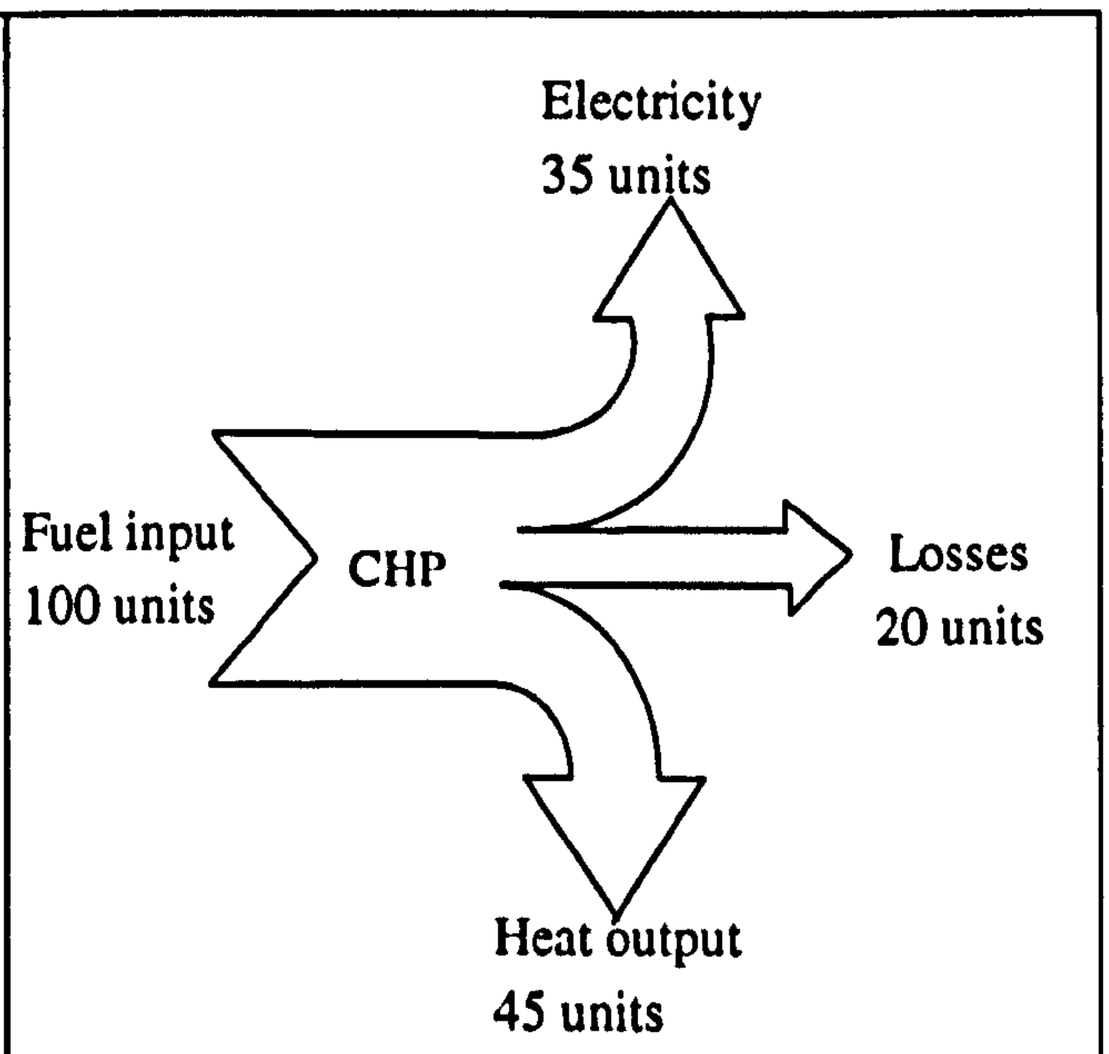

Figure 2-14b. Combined heat and power application

Olivier Le Corre et al (2002) proposed a unified comparison method for the calculations of thermodynamic efficiencies applied to combined heat and power (CHP) plants. Two new dimensionless indices, namely, heat structure index and electric power structure index, were introduced, and they were used to estimate the influence of technical and economical features on the profitability of a CHP plant. A case of a CHP installation using internal combustion engine was treated as a practical application.

Alfred Ongiro Alfred et al (1996) developed a steam power plant thermodynamic model using ASPEN Plus shell. The model was validated using field data from two units, one with a capacity of 105Mwe and the other 150Mwe. The model was then modified and used to

evaluate the thermodynamic feasibility of servicing a small (less than 20MWt) thermal load in addition to generating electricity.

Blakemore F. B. et al (1995) discussed a novel decision-making approach (option appraisal) of the CHP system. This incorporated the items, such as costs and benefits, that may not have direct monetary value. The existence of economics of scale for CHP units was considered over the full range of outputs encountered in commercial and industrial situations. Capital costs per kWe of output were minimized at about 1Mwe. Maintenance costs may also form a minimum depending upon the maintenance package agreed. In the application studied by the authors, the optimum choice using option appraisal was found to be the best solution for four of the six desiderata considered, but was not the largest CHP unit nor the lowest capital cost per output option.

Maidment and Tozer (2002) reported the application of CHP scheme in supermarkets. In these commercial building, the seasonal demand for heat resulted in limited utilisation of the CHP equipment, and subsequently, limited primary energy savings achieved. To increase the utilisation time, it was proposed that heat generated by the CHP unit could be used to power an absorption refrigeration system providing cooling for refrigerated cabinets. The application of an integrated CHP/absorption scheme or combined cooling, heat and power (CCHP) in the supermarket was investigated.

Small-scale CHP systems have become increasing popular over recent years. This is mainly due to inexpensive gas and deregulation of electricity industry. Smith et al (1995) reported the technical, economic and environmental performance of a 40kWe CHP plant, located within Queens Building at De Montfort University. Conventional analysis gave the overall efficiency as 77% with a 7.1 year payback period. By examining the thermal and casual gains, a novel alternative analysis gave an effective plant efficiency of 104%. Environmental analysis shows that the CHP-generated energy produced half the carbon dioxide emissions of separately imported electricity and heat from a boiler plant. The scheduling of plant

utilisation had an effect on thermal efficiency due to thermal capacity.

FEW P. C. et al (1997) introduced an innovative domestic co-generation system, which was based on the integration of a CHP with heat pump cycle. Preliminary analysis had shown the potential of a domestic scale hybrid CHP/HP plant in term of energy utilization, economic viability and emission reduction. The incorporation of the heat pump would give a CHP/HP plant very high effective efficiency, hence significantly reducing carbon dioxide emission and fuel costs. By allowing surplus electrical generation to be used by the heat pump, the engine could still run efficiently while satisfying very low domestic electrical requirements. The incorporated heat pump gave a high degree of flexibility in meeting domestic energy requirements, including cooling applications, as the heat to power ratio of a CHP/HP plant could be varied over a wide range. This system would be installed into a property for field evaluation as the work of the next stage.

Small-scale CHP systems have been further developed to work in conjunction with a renewable energy, such as solar energy. This would result in significant reduction in pollutant emissions and saving of running cost. The system may also be combined with an absorption/adsorption or ejector cycle to produce cooling while providing heat and power. A number of studies in relation to this technical topic are indicated as follows:

A new flat plate solar hybrid system with heating and cooling was developed by Li M. et al (2002). This system used a normal flat plate water heat collector absorber, which was immersed into the adsorbent bed. Experiment results showed a very effective heat and mass transfer achieved within both adsorption and absorption process. The COP of the system was 0.11 and the heat efficiency was about 0.45. This achievement illustrated a good way of utilisation of solar energy.

Xu Feng et al (2000) proposed a combined power/cooling system which used ammonia-water mixture as the working fluid. The system was a combination of Rankine and

absorption refrigeration cycle, and hence able to produce power and cooling simultaneously. Initial simulation results showed that the cycle could achieve high thermal efficiencies for heat source temperature around 400K, which could be obtained easily from geothermal sources, flat plate and low concentration solar collector, waste heat from other cycles, to name a few. Using flat plate or low concentration solar collectors in this cycle could reduce the cost of a solar thermal power plant from $3500/kW to less than $2000/kW (based on year 2000 price). If a solar thermal power plant based on this cycle was combined with a natural gas combustion turbine (especially if natural gas was used as a backup fuel), which costed around $500 to $700/kW, the combined cost would be in the range of about $1200 to $1500/kW, which could make solar thermal power cost competitive.

Sun Dawen (1997) described a novel solar-driven refrigeration and air-conditioning system, which was a combination of an ejector and vapour compression cycle. Water was used as the refrigerant in the ejector sub-cycle and HFC-134a in the vapour compression sub-cycle. The study showed that the combined cycle was: (i) a potentially high performance system with a potential increase in system COP by more than 50% over the conventional cycles; (ii) a 'green' system that conforms to all foreseeable ozone preserving regulations and reduces 'green house' effect; and (iii) a cost effective system with low maintenance.

Angelino Gianfranco et al (1998) evaluated the merits of organic-fluid mixtures as the working media for Rankine power cycles. Non-isothermal phase change both at high and low temperature represented the main advantage with respect to pure fluids. StanMix, a computer code using the Wong and Sandler (WS) mixing rules, was integrated into a commercial package, and employed for cycle analysis and optimisation. Heat recovery and geothermal applications using mixtures of siloxanes and hydrocarbons, respectively, were illustrated. It was demonstrated that optional selection of working-fluid composition was a powerful tool for an efficient organic Rankine cycle (ORC) design.

R.A.HAJ KHALIL et al (1997) investigated the potential of using a solar pond for the

generation of electricity in Jordan. A solar pond power plant model was presented to simulate and optimize such a system under the Jordanian climate conditions. A Rankine cycle analysis was carried out using an environmentally friendly working fluid, Refrigerant 134a. It was found that using a solar pond for the generation of electricity in Jordan had the potential, with the cost of 0.234JD/kWh (1997) when using a pond of surface area of 1.5km^2, to generate 5Mwe.

A novel hybrid solar/gas system intended to provide cooling/heating and electricity generation for buildings was developed by Oliveira A. C. et al (2002). The system was based on the combination of an ejector heat pump cycle with a Rankine cycle. It was driven by solar energy and supplemented by a gas burner. The system also used an environmentally friendly refrigerant, i.e., n-pentane, to have minimal impact on the environment. Results of the computer modeling, prototype tests and economic analysis were reported. It showed cooling capacities up to 5kW and electrical output up to 1.5kW could be achieved.

2.6 Summary

A thorough review in relation to the selected technical subjects, e.g., heat pipe technology and heat pipe thermal performance analysis, numerical methods of heat pipe heat transfer, heat pipe solar collectors, micro turbines as well as solar CHP technology, was carried out. These subjects are all related to this research as each of those is part of the areas the project involved, and therefore, a better understanding of the technical progress in these areas is necessary.

In section 2.1, the concepts of heat pipes were illustrated and the development of this technology was reviewed. The varieties of heat pipes used for different applications were summarised. Emphases were focused on two types of heat pipes, i.e., micro and miniature ones. A special miniature heat pipe was proposed, which would be used as the basic element of a heat pipe solar collector. Methods used for calculating limits of heat transport capacity of normal heat pipes were listed. The review shows that a more versatile analytical model covering the situations of both micro/miniature and normal heat pipes is desirable.

In section 2.2, various numerical methods and mathematical expressions used for the simulation of fluid flow and heat transfer in a heat pipe were reviewed. Different treatments on the flow of vapour and liquid/wick areas and heat transfer between vapour and liquid phases, and that caused by heat pipe wall conduction were discussed. It was pointed out that the mathematical expressions and numerical schemes seemed to be rather complex in engineering applications, and therefore, a simple numerical model for heat pipe heat transfer analysis is desirable.

In section 2.3, the concepts of solar collectors and heat pipe solar collectors were described, and the advantages of heat pipe solar collectors were highlighted. The progress on this technical area was reviewed. It was found that most of the previous works focused on the investigation of thermal performance of different types of heat pipe solar collectors by using analytical, numerical or experimental methods. The aim was to improve collector efficiency

through developing the optimum structures and finding suitable operating conditions. A flat plate heat pipe collector is inferior to an evacuated tubular heat pipe collector in heat efficiency, but it has its own advantages. It would be desirable to develop a new structure for flat plate collector that would overcome the currently existed problem, i.e., lower efficiency, and allow a high efficiency to be achieved.

In section 2.4, the concepts of steam turbines were indicated. Development of micro turbines, particularly micro steam turbines, was introduced. There is no report so far for commercial application for a micro steam turbine less than 50kWe. However, a specially designed impulse-reaction steam turbine with 1.5-3kW outputs has been used in a prototype CHP system.

In section 2.5, benefits of CHP scheme were identified compared to conventional method of providing heat and electricity. Current status of CHP technology was indicated. Emphases were focused on small-scale CHP systems, particularly those working with solar energy and combined with adsorption/absorption or ejector refrigeration cycle.

Chapter 3. Heat Pipes and Heat Pipe Thermal Performance Analysis

3.1 Micro/miniature Heat Pipes and Normal Heat Pipes

Cotter (1984) defined a 'micro' heat pipe as 'a heat pipe so small that the mean curvature of the vapour-liquid interfaces is necessarily comparable in magnitude to the reciprocal of the hydraulic radius of the total flow channel'. In practical terms, a 'micro' heat pipe is a 'wick-less', non-circular channel with an equivalent diameter of 0.1 to 1 mm.

For this Ph.D work, the 'micro' heat pipes arrayed at a certain inclination, and hence they are gravitational 'micro' heat pipes (also called 'micro' closed two-phase thermosyphon) in which gravity played a significant role. Further investigation into the heat pipes found that the expression 'gravitational micro heat pipe' is not correct since each heat pipe has an equivalent diameter of about 2mm, which is beyond the sub-millimeter range. It is therefore more precise to call them 'miniature gravitational heat pipes' (Groll and Rosler , 1992).

The geometrical shape of the heat pipe channel is a critical factor affecting the performance of the heat pipe. The channel geometry of a micro/miniature heat pipe is usually a concave trapezoid with tapered triangular channels in each of the four corners (Babin et al, 1989), as shown in Figure 2-9. Capillary action plays a major role for the operation of this kind of micro/miniature heat pipe.

A special channel geometry was investigated in this research. This geometry is parallelepiped that has two very sharp opposite corners (Riffat et al, 2002), as shown in Figure 2-10. The sharp corners are slim enough to hold liquid block and would be able to produce a capillary force, and the capillary force played an important role on returning the liquid. In addition, because the heat pipe was arrayed at a certain inclination relative to horizontal, gravity force also played a role on returning the liquid.

This special heat pipe was compared to a circular heat pipe of the same equivalent diameter. The circular heat pipe was operated only by a gravitational force, instead of the combination of capillary and gravitational force, and hence has different operation characteristics from the

miniature pipe. In addition, the circular heat pipe also differs from normal circular heat pipe in that it has a very small diameter, 1-3mm, which is same as the equivalent diameter of the miniature heat pipe. To identify this from the normal circular heat pipes and the miniature heat pipes, this pipe was termed 'mini' heat pipe.

Compared to micro, miniature or 'mini' heat pipes, 'normal' heat pipes have larger channel diameter (or equivalent), above 2mm, and relatively longer length. They could be made into different channel geometries, but most are circular or rectangular. The inner surface of the heat pipes may be fitted with wicks, which are used to produce capillary force to aid the operation of the heat pipes; but some are wickless, which are operated by gravitational force.

3.2 Analytical Model Set-up – Limits of Heat Transport Capacity

The formulae for limits of heat transport capacity for circular channel heat pipes have been developed. These formulaes could be used to calculate heat transport capacities of the heat pipes with other channel geometries by introducing the equivalent diameter d_i, which is expressed as follows;

$$d_i = \sqrt{4A/\pi} \qquad (3\text{-}1)$$

Whereby A is the cross-sectional area of the heat pipe. However, this calculation would cause an error since it does not consider the influence of channel geometry to fluid flow and heat transfer. In fact, this influence is un-negligible when conducting an accurate calculation. Babin et al (1990) Introduced the concept of shape factor, which is used to correct the errors that may arisen from shape of channel geometry, as shown in Table 3-1.

Table 3-1. Valuse of the shape factor for heat pipe calculation

Shape	Circle	Regular hexagon	Square
k_s	1.000	0.964	0.883

There have been no reports in relation to the shape factor of the parallelepiped channel geometry. However, a value similar to that of the square geometry, such as 0.85, could be applied. This is because; firstly, there is no significant difference between the square channel

and the parallelepiped channel, except for the sharp corners which are only existed in the parallelepiped one; and secondly, although the sharp corners result in increased friction (entrainment) resistance between the liquid and vapour flows, they create a capillary force in a return which would promote fluid flow and heat transfer. As a result, the overall effect would be a compromised situation.

For the miniature heat pipes, some problems may arise due to the additional capillary effect, and the larger flow resistance caused by the sharp corners. These will be considered in the calculation of the capillary limit.

For any heat pipe, the maximum heat transport capacity is governed by five limits; namely, the sonic limit, the entrainment limit, the boiling limit, the viscous limit and the capillary limits. Using the techniques presented in Dunn and Reay (1982) and Babin et al (1990), and considering the influence of channel geometry on heat transfer, these limits may be expressed as:

Sonic Limit

$$q_{s,m} = k_s A_v \rho_v h_{fg} (\gamma R_v T_v / (2(\gamma+1))^{1/2} \tag{3-2}$$

Entrainment Limit

$$q_{e,m} = k_s A_v h_{fg} (\sigma \rho_v / (2 r_{h,w}))^{1/2} \tag{3-3}$$

Boiling Limit (or Dry Out Limit)

$$q_{b,m} = \frac{2\pi d_{eff} k_{eff} T_v}{h_{fg} \rho_v \ln(r_i / r_v)} (\frac{2\sigma}{r_n} - \Delta p_{c,m}) k_s \tag{3-4}$$

Viscous Limit

$$q_{v,m} = \frac{k_s r_v^2 h_{fg} \rho_v p_v A_v}{16 \mu_v l_{eff}} \tag{3-5}$$

Capillary Limit

$$\Delta p_{cl} \geq \Delta p_{rg} + \Delta p_{ag} + \Delta p_l + \Delta p_v \qquad (3\text{-}6)$$

Due to the influence of gravity on the heat pipes investigated, the heat transport capacity is also governed by the filled liquid mass. Zhuang (1989) expressed this parameter as follows:

$$G = (0.8l_c + 0.8l_e + l_a)\left(\frac{3\mu_l \rho_l \pi^2 d_i^{\,2}}{k_l h_{fg} g}\right)^{1/3} q_c^{\,1/3} \qquad (3\text{-}7)$$

For wickless 'mini' or 'normal' heat pipes, there are no capillary pressure differences along the pipe length, i.e., $\Delta p_{cl}=0$. In addition, the entrainment limit may be expressed in a different way, as shown below (Zhuang, 1989).

$$q_{e,m} = k_s f_1(\phi) C_w^{\,2} \frac{\pi d_i^{\,2.5}}{4} \frac{h_{fg}\sqrt{g\rho_v(\rho_l - \rho_v)}}{[1 + (\rho_v/\rho_l)^{0.25}]^2} \qquad (3\text{-}8)$$

$C_w=0.725$

$$f_1(\phi) = \left(\frac{\phi}{180} + \sqrt{\sin 2\phi}\right)^{0.65} \qquad (3\text{-}9)$$

For the micro/miniature gravitational heat pipes or the wicked normal heat pipes, the net capillary pressure difference Δp_{cl} is calculated by using LaPlace-Young equation and assuming that during steady state operation the capillary radius of the curvature in the condenser section approaches infinity. This assumption allows the capillary pressure difference, Δp_{cl}, to be defined as a function of the surface tension σ, the wetting angle θ, and the radius of curvature of the liquid-vapour interface in the evaporator, r_{ce}.

$$\Delta p_{cl} = (2\sigma / r_{ce})\cos\theta \qquad (3\text{-}10)$$

The corner regions of the micro/miniature heat pipe may be approximated to a triangle, shown in Figure 2-10, and hence the capillary radius may be found as:

$$r_{ce} = w/\cos(\alpha+\theta) \tag{3-11}$$

Where, w is half the groove width and is dependent on the position along the pipe length and the fluid properties. α is equal to half the included angle of the geometry.

For wicked heat pipes, the capillary radius may be expressed in different ways, depending on wick structure, which are outlined in Table 3-2 (Zhuang, 1989).

Table 3-2. Capillary radius for different wick structures

Wick structure	**Effective capillary radius r_{ce}**	**Nomenclature**
Cylinder hole	$r_{ce}=r$	r: radius of cross section of cylinder
Rectangular groove	$r_{ce}=W$	W: width of rectangular groove
Triangle groove	$r_{ce}=W/\cos\beta$	W: width of rectangular groove; β: 1/2 of depth angle
Parallel wires	$r_{ce}=W$	W: distance between adjacent wires
Mesh (1 layer)	$r_{ce}=(W+d)/2$	W: distance between adjacent mesh wires; d: diameter of the mesh wire
Sintered metal fibre	$r_{ce}=d/(2(1-\varepsilon))$	d: diameter of metal fiber wire ε: ratio of void
Sintered particle	$r_{ce}= 0.41r_s$	r_s: radius of sintered particle

For any kind of heat pipe, the radial and axial hydrostatic pressure drops Δp_{rg}, Δp_{ag} are the result of the gravitational forces and may be expressed as:

$$\Delta p_{rg} = -\rho_l g d_v \cos\phi \tag{3-12}$$

$$\Delta p_{ag} = -\rho_l g l_p \sin\phi \tag{3-13}$$

The liquid pressure drop, Δp_l, may be found by evaluating the shear forces at the liquid-solid and liquid-vapour interfaces. These forces inhibit the return of the liquid through the wall areas and may be computed by integrating the pressure gradient over the length of the heat pipe. For constant heat addition and heat rejection, this yields:

$$\Delta p_l = -(\frac{\mu_l}{KA_l h_{fg} \rho_l}) l_{eff} q_c \qquad (3\text{-}14)$$

$$K = r_{hl}^2 / 8 \qquad (3\text{-}15)$$

$$l_{eff} = 0.5 l_e + l_a + 0.5 l_c \qquad (3\text{-}16)$$

Due to the compressibility of the vapour phase and the mass addition and removal in the evaporation and the condensation section, determination of the vapour pressure drop, Δp_v, in the heat pipes is complicated. Because of the large difference in the density between the liquid and vapour phases, the velocity of the vapour phase must be significantly higher than the velocity of the liquid phase. Hence, the pressure gradient due to variation in the dynamic pressure, which is due to velocity and density changes, must also be considered when evaluating the vapour pressure drop. Chi (1976) gave the following expression for the vapour pressure drop:

$$\Delta p_v = (\frac{C(f_v \, \mathrm{Re}_v)\mu_v}{2(r_{h,v})^2 A_v \rho_v h_{fg}}) l_{eff} q_c \qquad (3\text{-}17)$$

In addition, this pressure gradient also partly results from the frictional drag in the heat pipes.

The friction factor, f_v, and the constant, C, can be determined once the local axial Reynolds number and Mach number are defined. These expressions are given below.

$$\mathrm{Re}_v = \frac{2(r_{h,v}) q_c}{A_v \mu_v h_{fg}} \qquad (3\text{-}18)$$

$$M_v = \frac{q_c}{A_v \rho_v h_{fg} (R_v T_v \gamma)^{0.5}} \qquad (3\text{-}19)$$

Kraus and Bar-Cohen (1983) gave the expressions for f_v and C, for different sets of conditions, as follows:

$\mathrm{Re}_v \le 2300, \quad M_v \le 0.2$ (3-20)

$(f_v \mathrm{Re}_v) = 16, \quad C=1.00$

$\mathrm{Re}_v \le 2300, \quad M_v \succ 0.2$ (3-21)

$(f_v \mathrm{Re}_v) = 16$

$$C = C_1 = (1 + (\frac{\gamma - 1}{2}) M_v{}^2)^{0.5}$$

$\mathrm{Re}_v > 2300, \quad M_v \le 0.2,$ (3-22)

$(f_v \mathrm{Re}_v) = 0.038$

$$C = C_2 = (\frac{2\gamma_{hv} q_c}{A_v h_{fg} \mu_v})^{0.75}$$

$\mathrm{Re}_v > 2300, \quad M_v > 0.2$ (3-23)

$(f_v \mathrm{Re}_v) = 0.038$

$C = C_1 C_2$

The algorithm used in the analytical model is described as follows:

(i) Equations 3-18 and 3-19 define the Reynolds and Mach numbers as functions of the heat transport capacity, q_{max}. Hence, the model initially assumes that the vapour flow within the heat pipe is laminar (i.e., $\mathrm{Re} \le 2300$ and $M_v \le 0.2$).

(ii) The individual pressure drops are calculated by using Eqs. 3-12, 3-13, 3-14 and 3-17.

(iii) The individual pressure drop values are used in equation 3-6 to obtain the capillary limit, and the other limits of heat transport were obtained from Equations 3-2 to 3-5.

(iv) The values obtained from Equations 3-2 to 3-6 are compared and the minimum is assumed to be the heat transport capacity, q_{max}.

(v) This value is substituted into Equations 3-18 and 3-19. The initial assumption of laminar flow is checked, by comparing the Reynolds and Mach numbers against Equations 3-20 to 3-23.

(vi) The correct equation for Reynolds and Mach number is then used. An iterative procedure from step (ii) is then initiated until the differences in the values of Reynolds and Mach numbers between the consecutive two iterations approach the predefined small values.

(vii) The final value of q_{max} is taken as the limit of heat transport capacity.

3.3 Validation of the Analytical Modeling

To validate the suitability and accuracy of the model used for a heat pipe, comparison was carried out between the modeling results and published experimental data for a micro heat pipe.

Two test pipes were constructed [Babin B. R. et al, 1990], one made of silver and the other copper. They were both charged with 0.032g of distilled, deionized water and were evacuated. In addition, two uncharged test pipes, one each of copper and silver, were tested to determine the amount of heat conducted through the wall to establish a baseline for evaluating the improvement in performance due to the vaporization and condensation of the working fluid.

Figure 3-1 illustrates the geometry of the heat pipes investigated. The shape factors and the sizes of the heat pipe are indicated in Tables 3-3. The limits of heat transport capacity, including capillary, sonic, entrainment, viscous limits, were calculated using the model, and the results were illustrated in Figure 3-2. The simulation results of capillary pressure, liquid pressure and vapour pressure are shown in Figure 3-3.

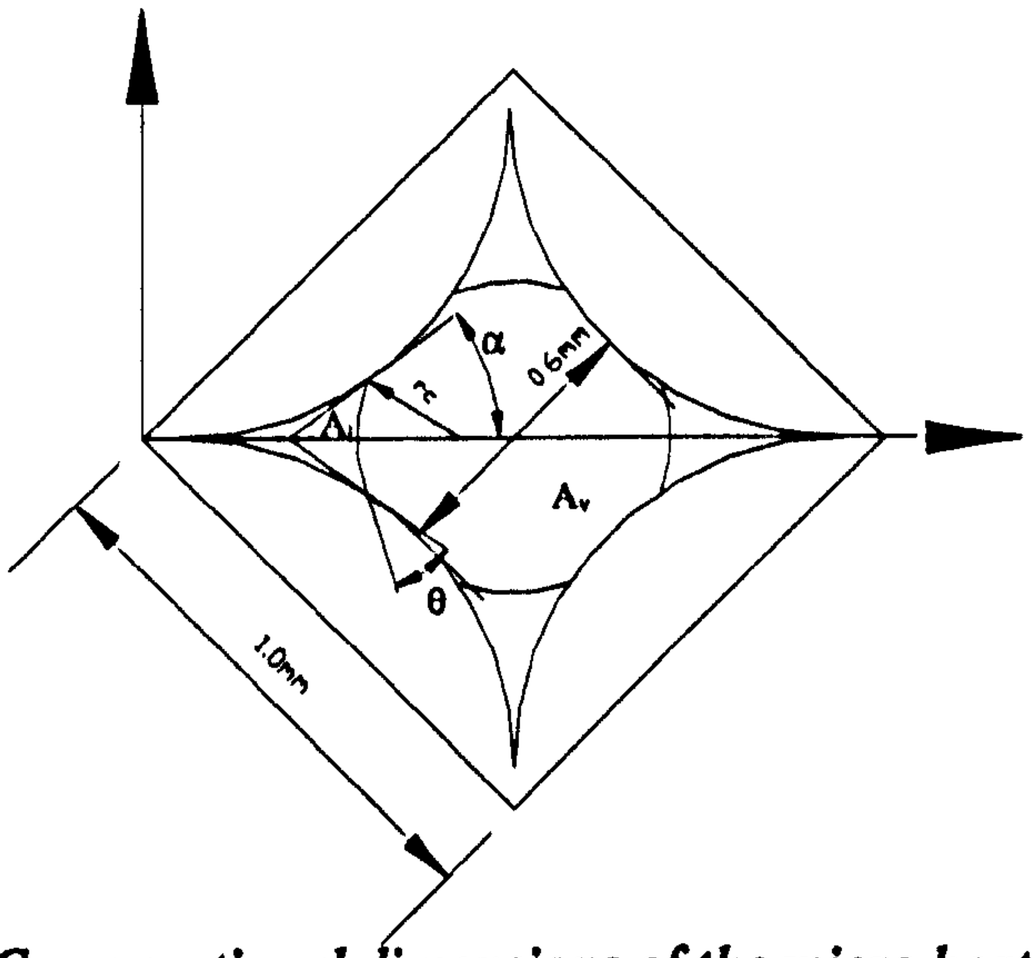

Figure 3-1.Cross-sectional dimensions of the micro heat pipe

Table 3-3. Micro heat pipe dimensions

Length, m	0.05
Length of condenser, m	0.0127
Length of evaporator, m	0.0127
w, m	0.000133
α, rad	0.5854
K_l'	0.6
K_v'	0.975

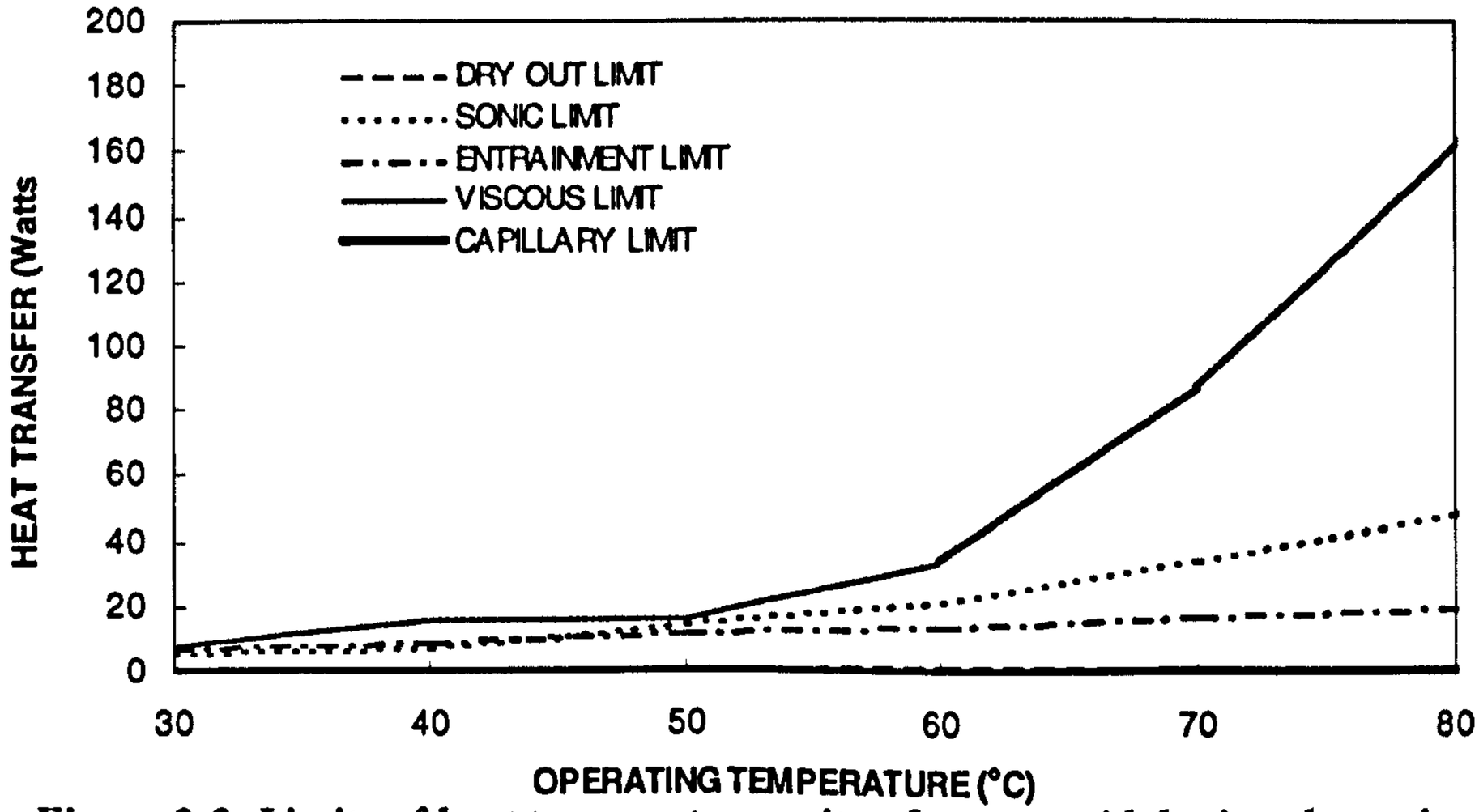

Figure 3-2. Limits of heat transport capacity of a trapezoidal micro heat pipe with water at a horizontal orientation

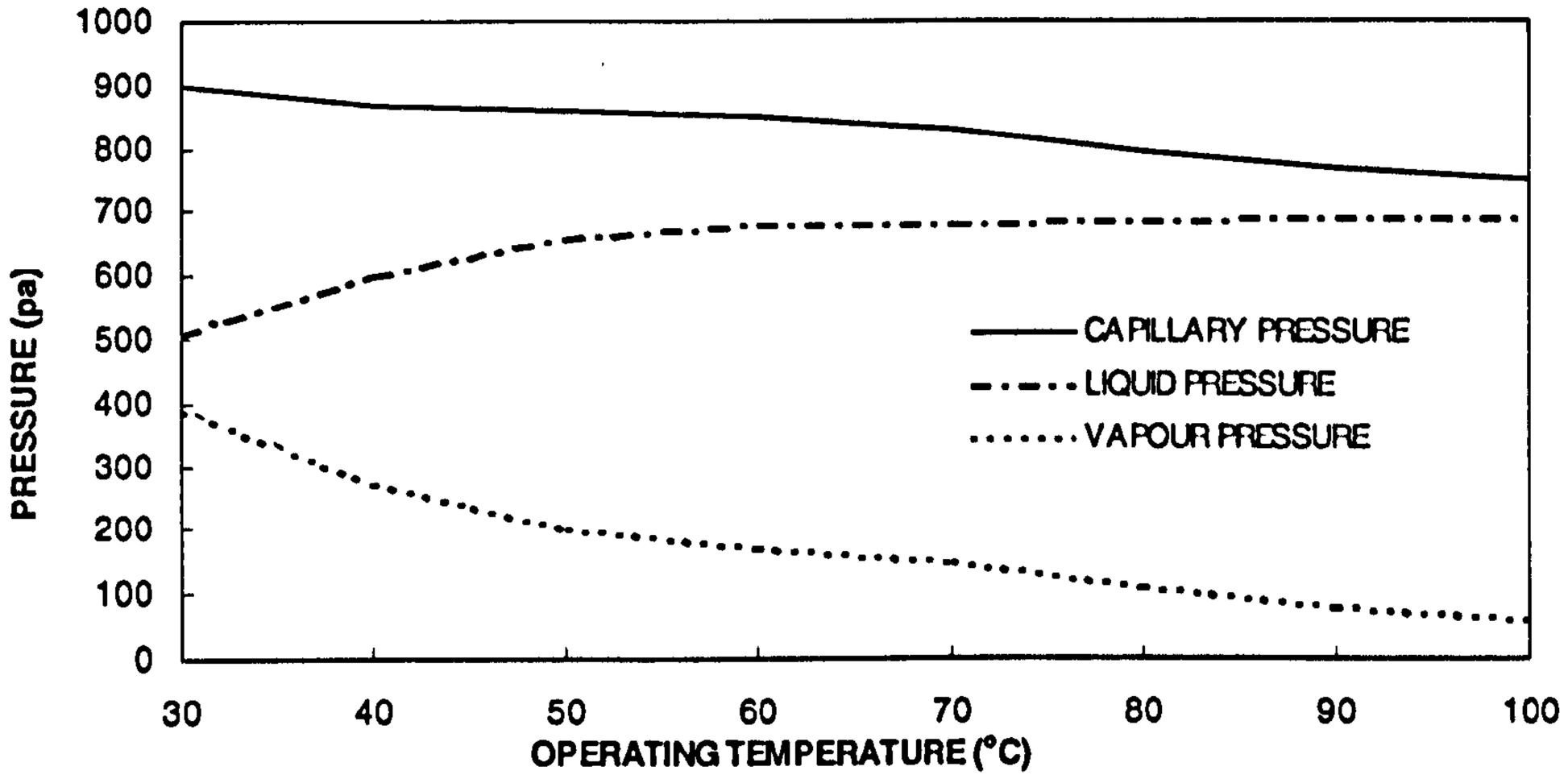

Figure 3-3. Evaluation of the pressure component as a function of the operating temperature for the trapezoidal heat pipe with water at a horizontal orientation

Figure 3-4 illustrates the results obtained for a copper heat pipe of the dimensions described above, operating in a horizontal orientation and charged with 0.0032g of water. The heat pipe was evaluated at a total of six operating temperatures, 30.8°C, 39.5 °C, 43.8 °C, 51.6 °C, 58.9 °C and 67.6°C, one operating temperature for each set of test points. As shown, the thermal conductance of the pipe decreased rapidly with respect to the evaporator temperature and asymptotically approached a constant value somewhat above the value obtained for an uncharged pipe. With the exception of the slightly decreasing difference between the ultimate conductance value of the test pipe and the conductance of the uncharged pipe, this behavior is precisely what would be expected for a heat pipe in which the evaporator is slowly drying out. Increases in the input power initially caused the liquid meniscus to recede into the liquid channels located in the corners of the heat pipe. This resulted in a decrease in the radius of curvature of the liquid-vapour meniscus, a corresponding decrease in the cross-sectional area of the liquid, and hence, a slight increase in the evaporator temperature. The receding of the meniscus continued with increasing power, until dry-out of the evaporator occurs.

The slightly decreasing difference between the ultimate conductance value of the test pipe and the conductance of the uncharged pipe resulted from an increase in the effective size of

the evaporator. Prior to dry-out, all the vaporization occurs in the evaporator region. Once dry out begins, the temperature of the heat pipe wall in the adiabatic section increases and a small part of the adiabatic section began to act as an evaporator. As the power continued to increase, the dry-out in the evaporator spread and the portion of the adiabatic section that behaved as an evaporator expanded. In the extreme case where complete dry-out of the evaporator section occurs, a large portion of the adiabatic section may behave as an evaporator and may even begin to dry out at the end farthest from the condenser.

Figure 3-5 illustrated the results for the various test points obtained for a silver heat pipe of the same dimensions, charged with 0.0032 g of water. The test conditions were similar; however the operating temperature at which the silver heat pipe was evaluated were 31.8°C, 32.3°C, 42.0°C, 52.5°C, and 62.8°C. As shown, the trends and tendencies were all similar to those of the copper pipe tested.

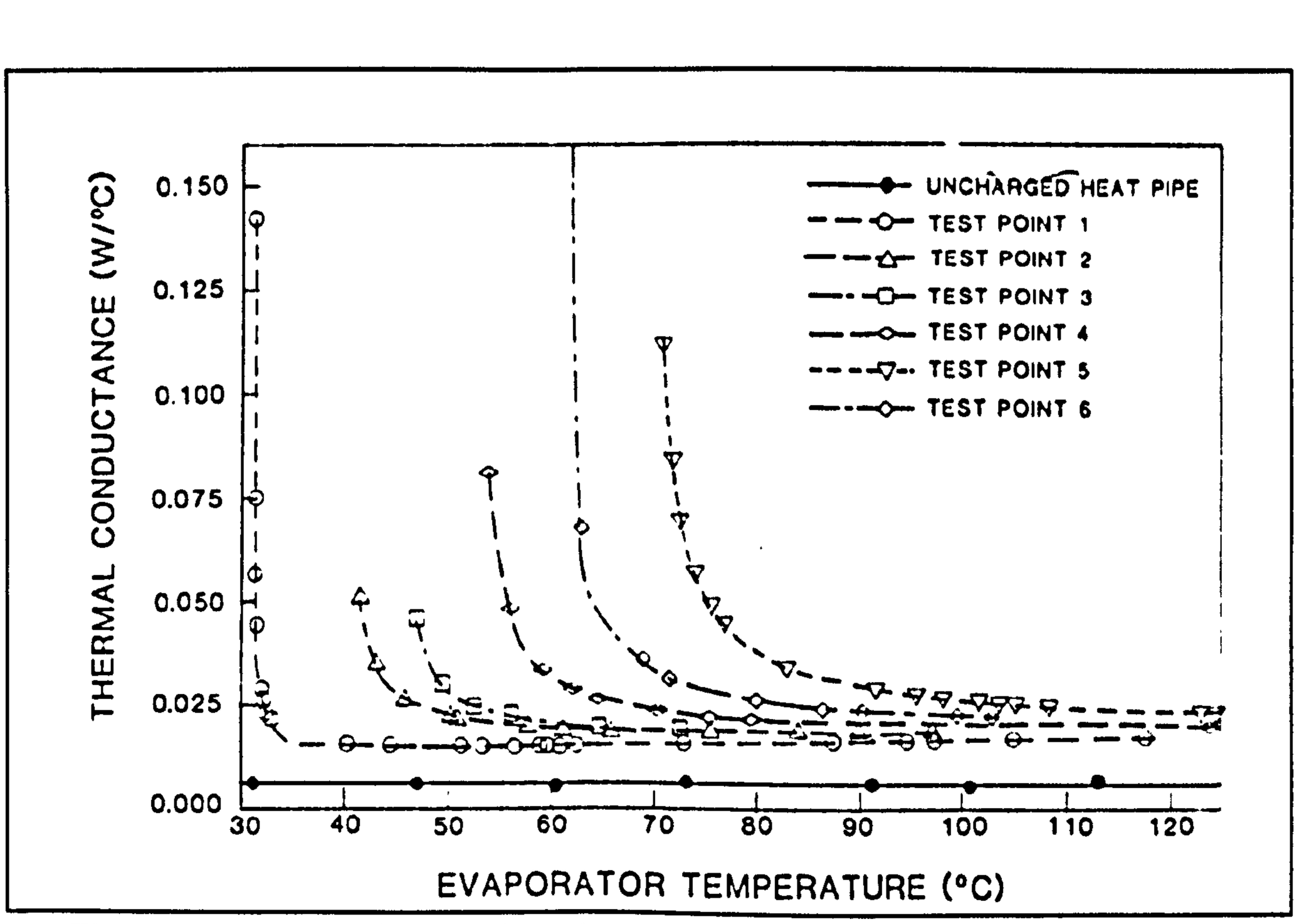

Figure 3-4. Measured thermal conductance of a trapezoidal micro heat pipe as a function of the evaporator temperature (copper, 0.032 g charge)

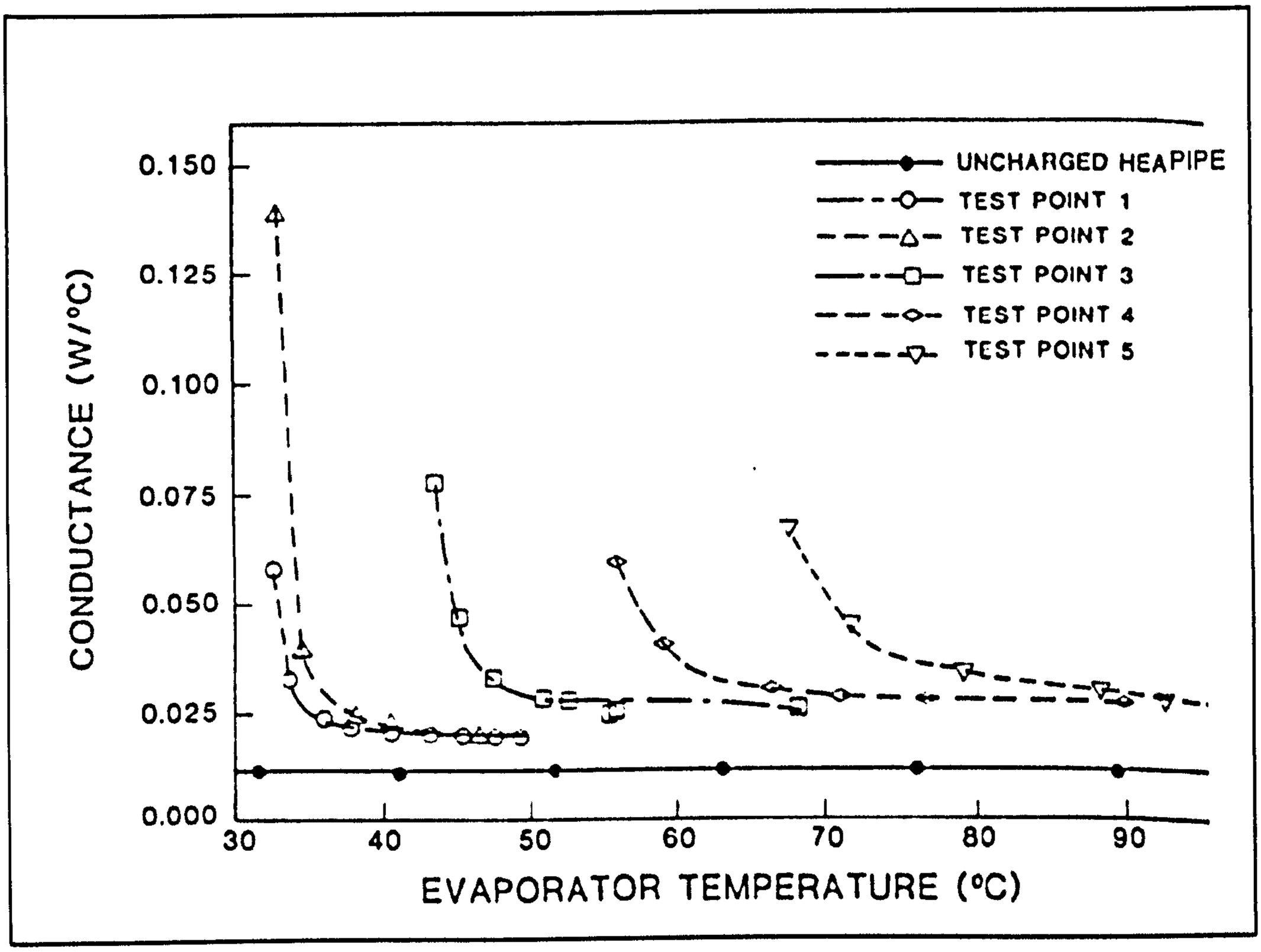

Figure 3-5. Measured thermal conductance of a trapezoidal micro heat pipe as a function of the evaporator temperature (silver, 0.032 g charge)

In order to compare the experimental results with those predicted by the analytical model, it was necessary to develop a method for determining the point at which dry-out begins. The experimental data presented in Figs 3-4 and 3-5 clearly display a change in the operation of the two test pipes as the operation temperature and power levels were increased. After reviewing the experimental data, an attempt was made to identify and quantify better the onset of dry-out. Because, as discussed previously, there was no clear cut division between the evaporator and condenser, this proved to be quite difficult.

Several strategies were completed, including development of a mathematical method for determining the maximum curvature for each operating temperature. The final approach used

was to select a region on both sides of the point of maximum curvature, that is a range around the point at which the most rapid change of the conductance occurs with respect to evaporator temperature. This range was assumed to be the region over which dry-out occurred. The initial point, which will be referred to as the onset of dry-out, was identified as that point where the slope of a line tangent to the curve was 60 deg. The termination of dry-out was assumed to occur at that point where slope of the tangent line was 30 deg. Although this would appear to be a large range, in reality it is probably reasonably close to the actual behavior, since dry-out is a gradual process and unlike the sonic or boiling limit, develops quite slowly.

Figures 3-6 and 3-7 illustrate the results of this process and compare the measured input power to the heat pipe evaporator, with the maximum heat transfer capacity predicted by the model for the copper and silver test pipes, respectively. As shown, at low operating temperatures, this model over-predicts the experimentally determined maximum heat transport capacity by approximately 15 percent for both the copper and silver test pipes. Between operating temperatures of 40 and 60, the model predicts dry-out with a reasonable degree of accuracy, and above 60 the model slightly under-predicts dry-out.

In overall, the steady-state experimental results provide experimental verification of the trapezoidal micro heat pipe concept and indicate that the analytical model can be used to predict accurately the level of performance. Since variations in the way the dry-out phenomenon is defined can significantly increase or decrease the experimentally determined values, the discrepancy between the measured and predicted values may in part be due to the technique used to define dry-out. As a result, the perceived accuracy of the models is strongly dependent upon the way dry-out is defined. To resolve this problem, it is necessary to understand the dry-out phenomenon better and define more clearly when it begins and how it proceeds.

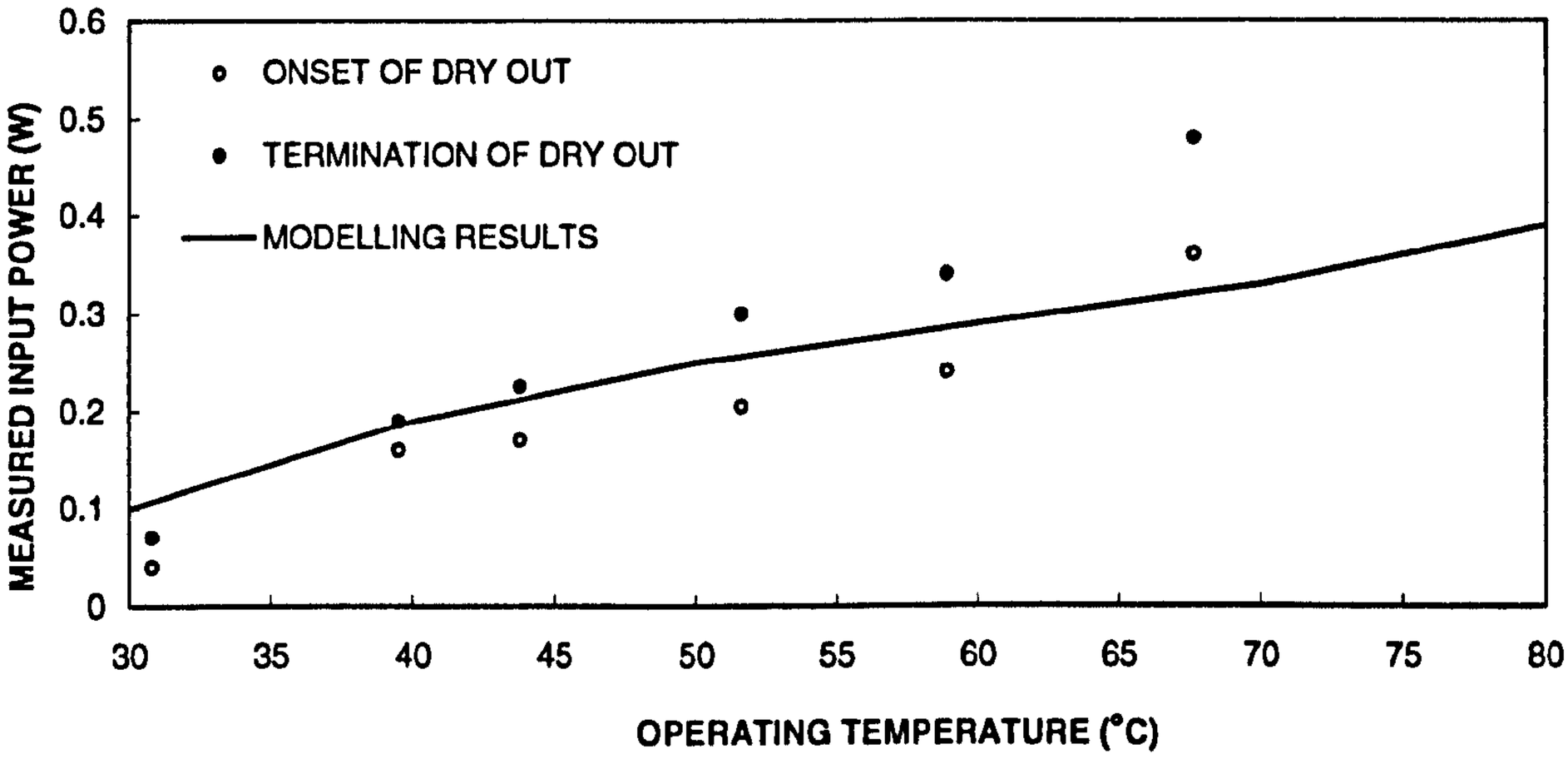

Figure 3-6. Comparison of the maximum heat transport capacity of a trapezoidal micro heat pipe as a function of the operating temperature (copper, 0.0032 g charge)

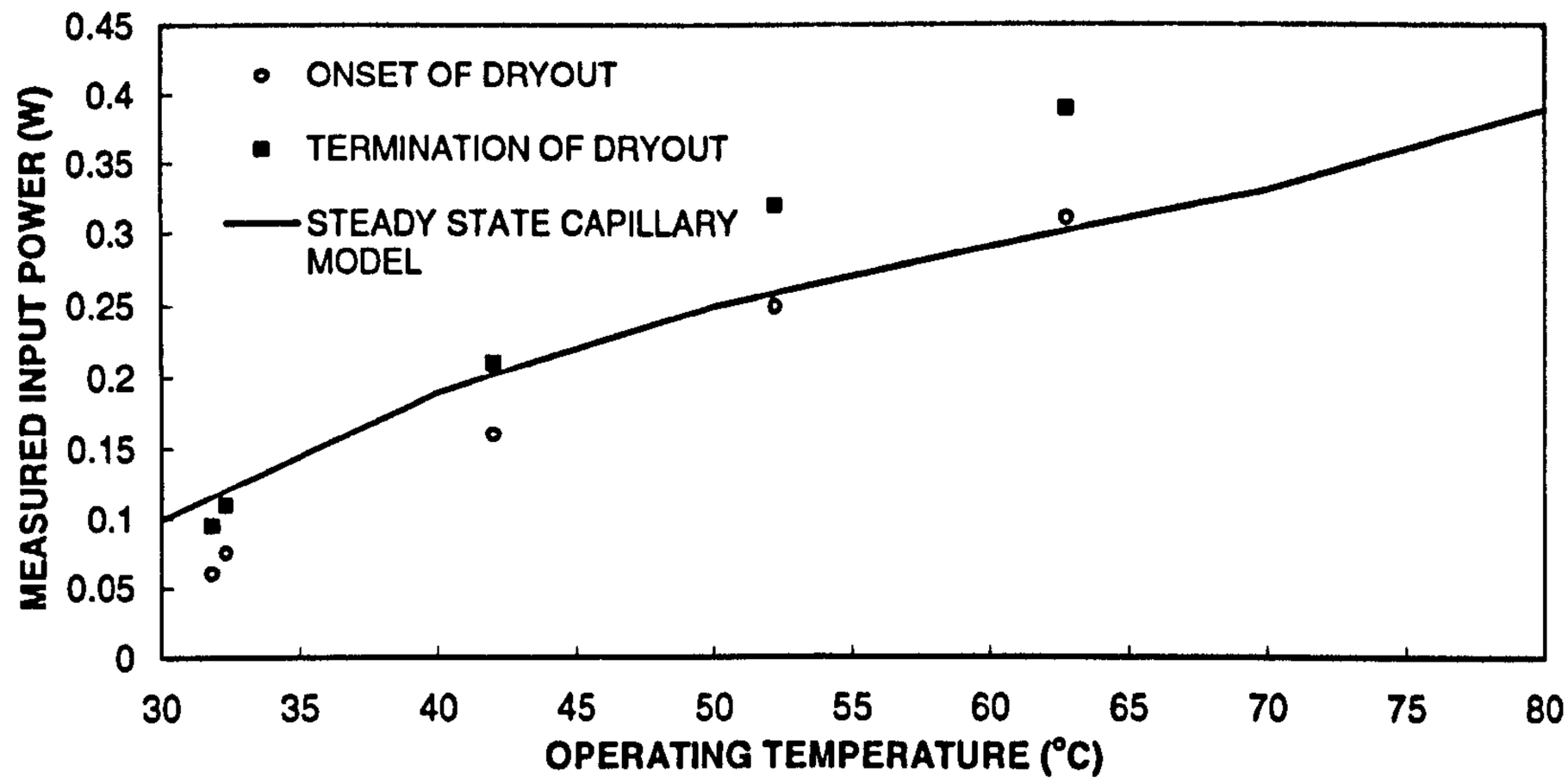

Figure 3-7. Comparison of the maximum heat transport capacity of a trapezoidal micro heat pipe as a function of the operation temperature (silver, 0.032 g charge)

3.4 Discussion of the Modelling Results

3.4.1 Comparison of the Thermal Performance of the Miniature and Mini Heat Pipes

Figure 3-8 illustrates the geometry and dimensions of the two miniature heat pipes and one mini heat pipe investigated. The heat pipes have the same overall length, evaporator length and condenser length of 1100, 1000 and 100 mm respectively, which are the exact dimensions of the real heat pipes used in the thin membrane heat pipe solar collector. The cross-sectional areas of the heat pipes are 3.14 mm^2 each. The mini heat pipe has a circular cross-section with the diameter of 2mm. The two parallelepiped miniature heat pipes have dimensions of length and width as follows:

Table 3-4. Dimensions of the miniature heat pipe channels

	CASE 1	CASE 2
Length (a) - mm	9.97	6.28
Width (b) - mm	0.63	1.0

The analytical model was initially used to determine the limits of heat transport capacity and the critical limit for the miniature and mini heat pipes as a function of operating temperature, inclination and liquid fill level. The investigation initially assumed that the heat pipe operated at inclination of 60deg, liquid fill level of 0.25m and temperature of 150°C, which was in consistent with the testing conditions of the heat pipe operation in the collector application. The subsequent investigation allowed two of the three parameters (inclination, liquid fill level and temperature) constant and one variable in order to analyse the influence of the each parameter to heat transport capacity.

Since the thin membrane heat pipe solar collector was designed to allow a 60deg inclination, the heat pipe was assumed to operate at this inclination. Since a gravity-assisted heat pipe was suggested to fill to 1/3 to 1/4 of the evaporation length to prevent dry-out and enable the maximum heat transfer during the operation [Zhuang J. et al, 1989], the heat pipe was assumed to be filled to 1/4 of the evaporation length (0.25m). Furthermore, the operating temperature was initially set at 150°C to comply with the design requirement for the heat pipe operation.

Influence of operating temperature

Figures 3-9 and 3-10, respectively, show the variations of the limits of heat transport capacity with working temperature for the miniature and mini gravitational heat pipes simulated. These results were obtained by assuming the heat pipes to be inclined at 60deg to the horizontal, and filled to the same liquid fill level (0.25m). It was found that:

- The entrainment limit is the dominant limit for the two miniature heat pipes.
- As can be seen from Figure 3-9, increasing the width 'b' of the miniature channel from 0.63 to 1mm and decreasing the length 'a' from 9.97 to 6.28mm, whilst keeping the cross-sectional area the same, resulted in increase of the capillary limit and decrease of the entrainment limit. Consequently, the critical limit decreases. This shows the miniature heat pipe with the smaller width (Case 1) has a better thermal performance than the miniature heat pipe with the larger width (Case 2).
- The entrainment is the dominant heat transport limit for the mini heat pipe studied, as shown in Figure 3-10.
- Figures 3-9 and 3-10 show that the miniature heat pipes result in larger heat transport limits and hence perform better than the mini heat pipes of the same cross-sectional area.

Influence of inclination to the horizontal

Figures 3-11 and 3-12 show the variations of the limits of heat transport capacity with inclination for the miniature and mini gravitational heat pipes. The results were obtained by assuming the operating temperature to be 150°C and liquid fill level to be 0.25m.

- Figure 3-11 shows that the critical limit increases as inclination is increased from 0 to 30 degrees for the miniature heat pipe Case 1. Beyond 30 degrees inclination, the critical limit remains constant. A similar behaviour is observed for the miniature heat pipe Case 2 whereby the critical limit increases with increase in inclination from 0 to 20 degrees, and remains constant beyond this value. This behaviour is largely due to the capillary limit being the dominant factor at inclinations below 30deg for Case 1, and below 20deg for Case 2. At higher inclinations, the entrainment limit becomes the dominant factor

affecting the critical heat transport of the miniature heat pipes, which remains constant when inclination varies.

- At inclinations below 30deg, the miniature heat pipe Case 2 has higher heat transport limit than the miniature heat pipe Case 1. At higher inclinations, miniature heat pipe Case 1 has a better thermal performance.
- The critical limit for the mini gravitational heat pipe increases with the inclination, as shown in Figure 3-12.

Influence of liquid fill level

Figures 3-13 and 3-14 show the variations of the limits of heat transport capacity with liquid fill level for the miniature and mini gravitational heat pipes. The results assumed the operating temperature to be 150°C and the heat pipes to be inclined at 60 degree to the horizontal.

- Figure 3-13 shows that for both miniature heat pipe Case 1 and Case 2, the critical limit increases when the liquid fill level is varied up to 0.2m. Beyond 0.2m, there is a slight increase in the critical limit. At liquid fill levels below 0.2m, the dry out limit is the most significant factor affecting heat transport of the heat pipes. As shown in Figures 3-6, this factor increases significantly with liquid fill level. At higher liquid fill levels (0.2m-0.8m) the entrainment limit becomes the dominant factor, which increases slightly with liquid fill level.
- In the case of the mini gravitational heat pipe (Figure 3-14), the critical limit increases with liquid fill level when it is below 0.1m due to the effect of the dry out limit, and beyond a liquid fill level of 0.1m the entrainment limit becomes the most significant factor affecting heat transport capacity of the heat pipe, which remains constant at the liquid fill range.

TEXT BOUND INTO

THE SPINE

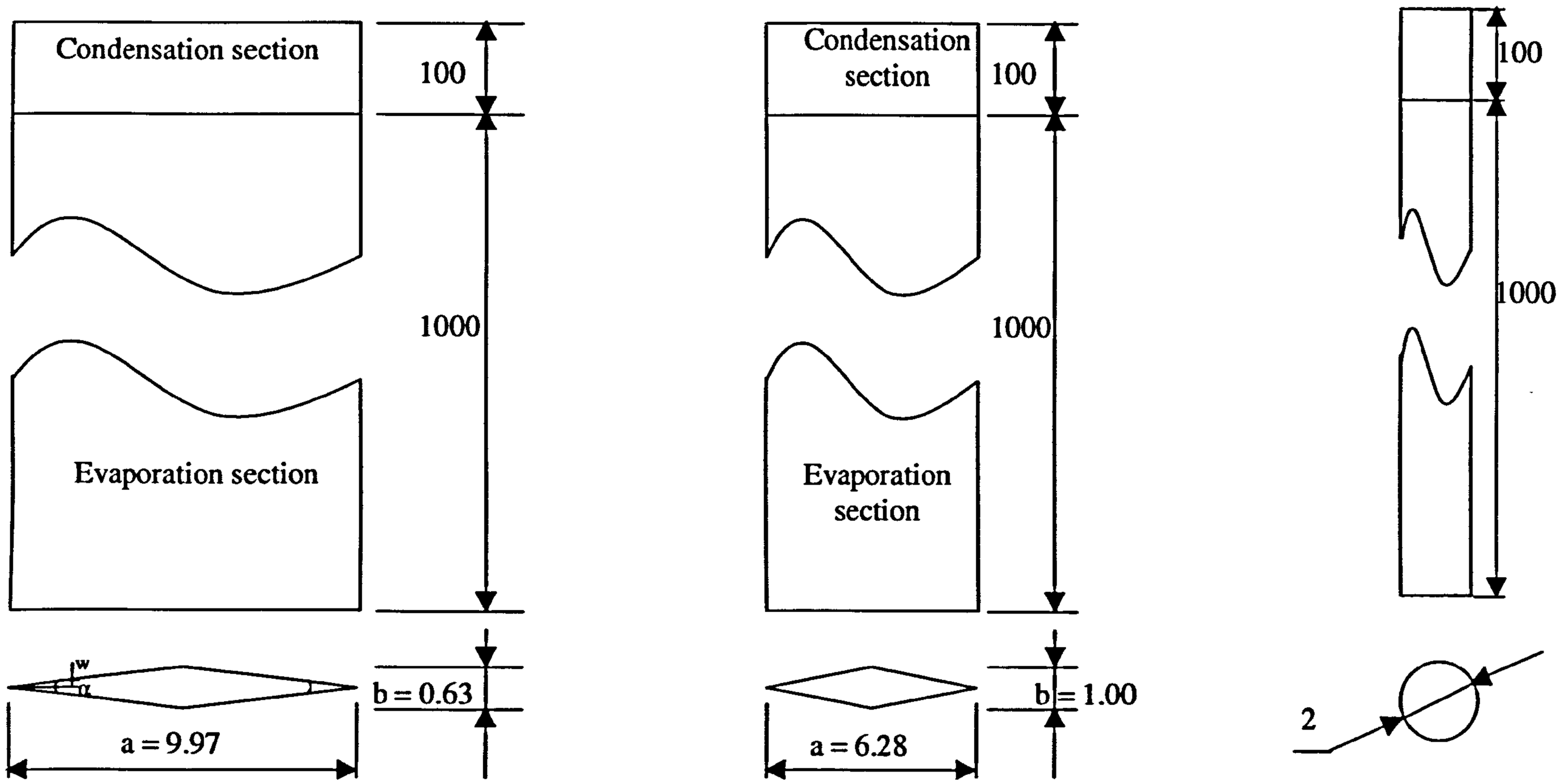

'Miniature' heat pipe – Case 1 **'Miniature' heat pipe – Case 2** **'Mini' heat pipe**

Figure 3-8. Geometry illustration of the 'miniature' and 'mini' heat pipes

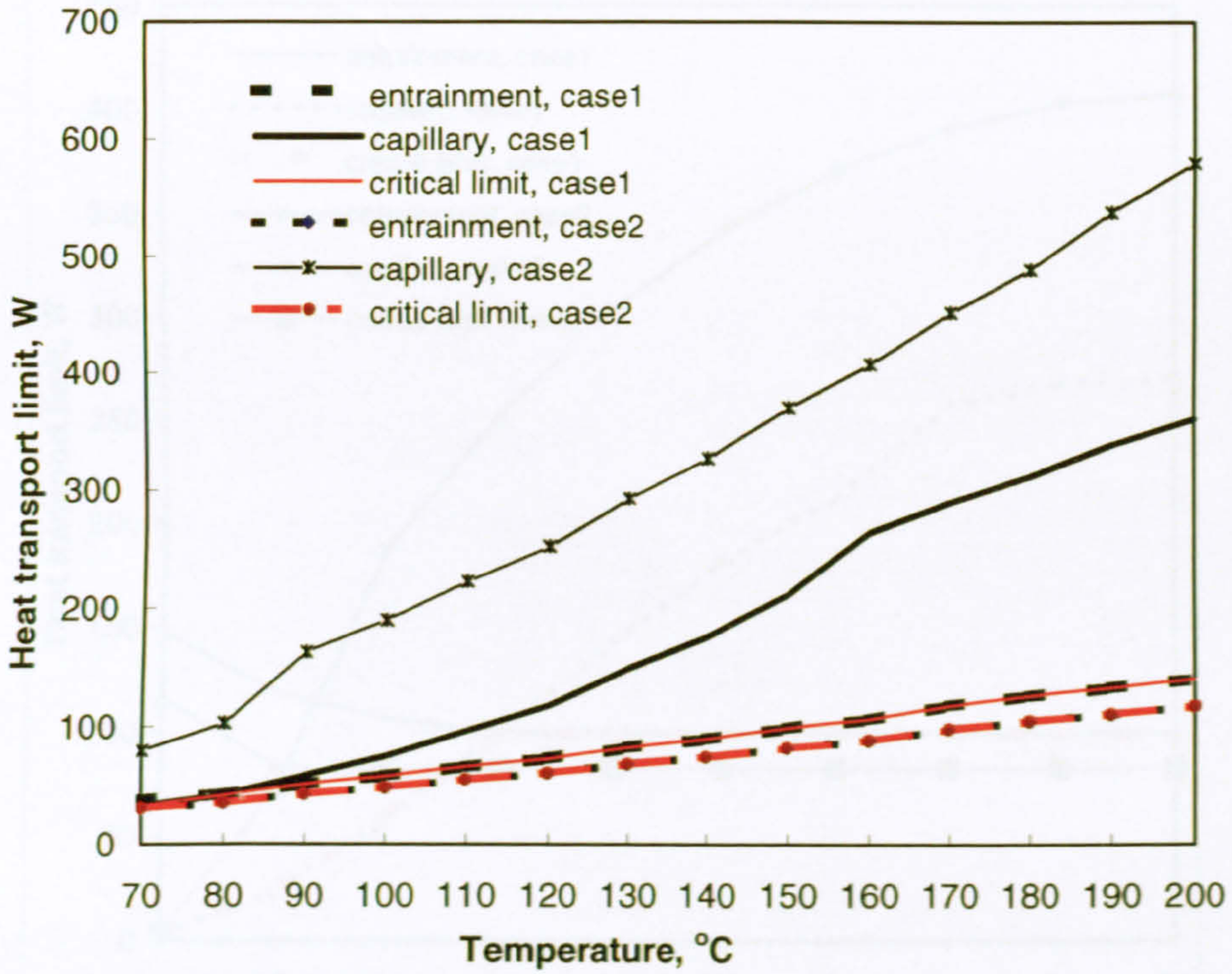

Figure 3-9. Variation of the limits of heat transport capacity with operating temperature (miniature heat pipes)

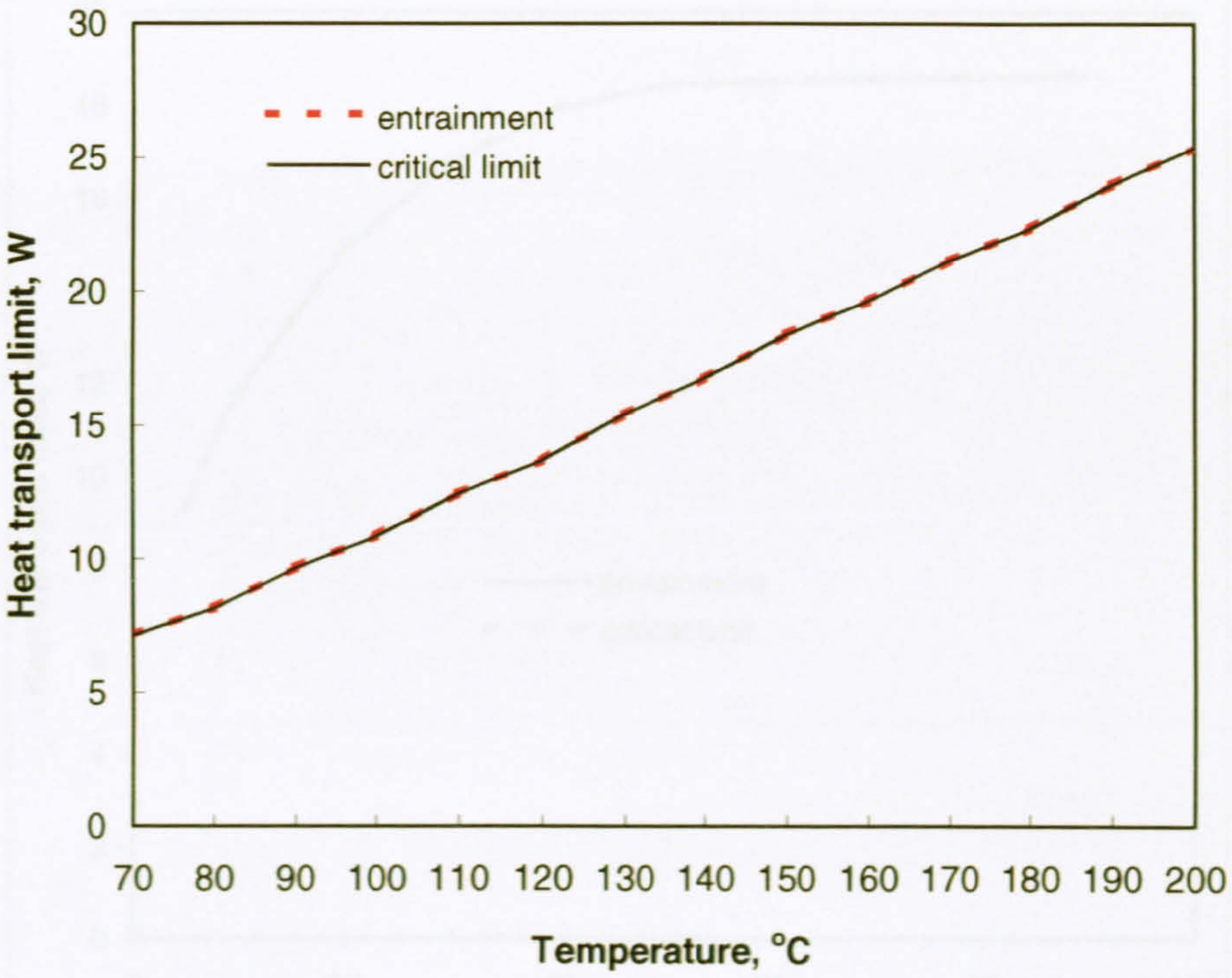

Figure 3-10. Variation of the limits of heat transport capacity with operating temperature (mini heat pipes)

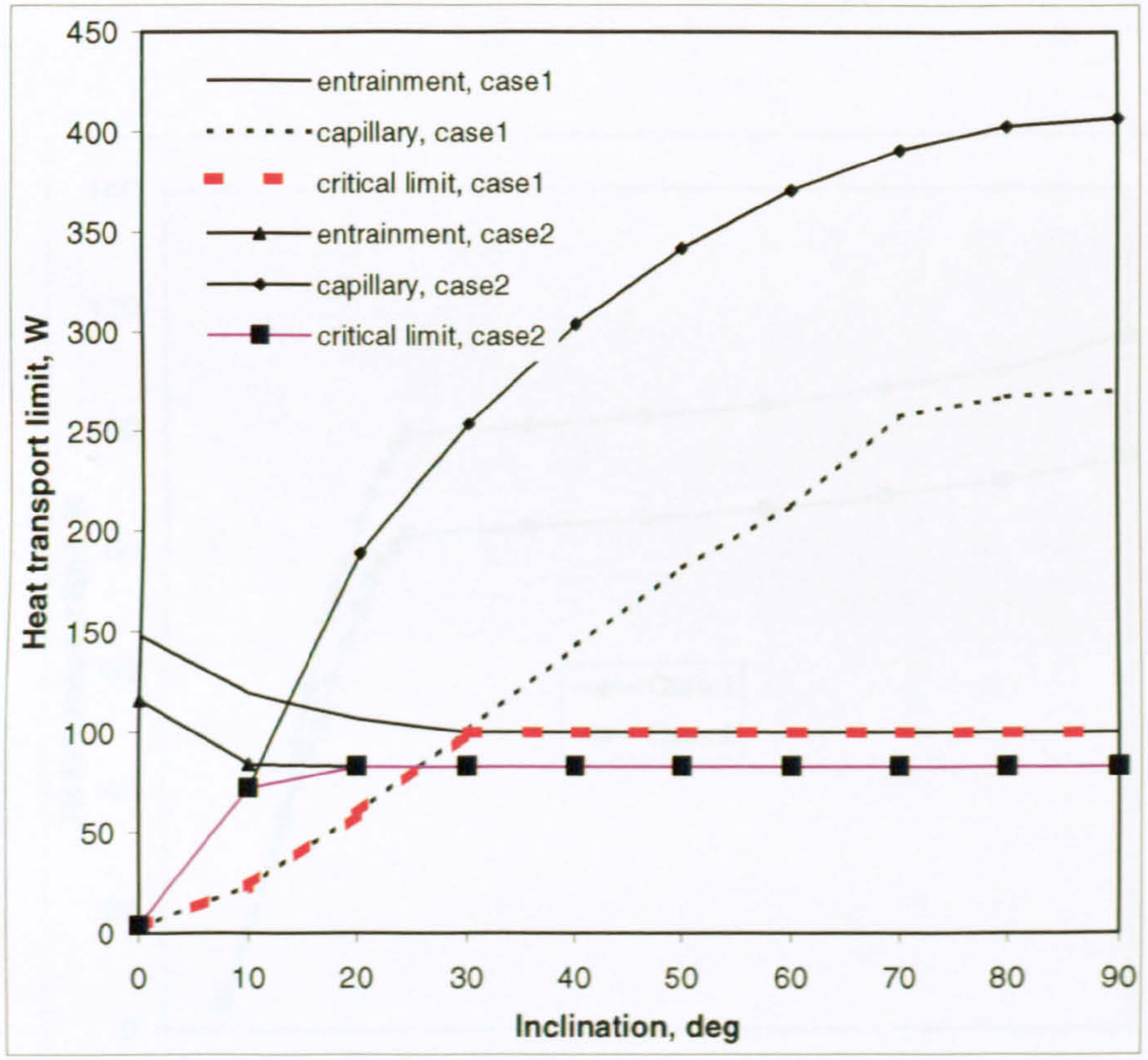

Figure 3-11. Variation of the limits of heat transport capacity with pipe inclination (miniature heat pipes)

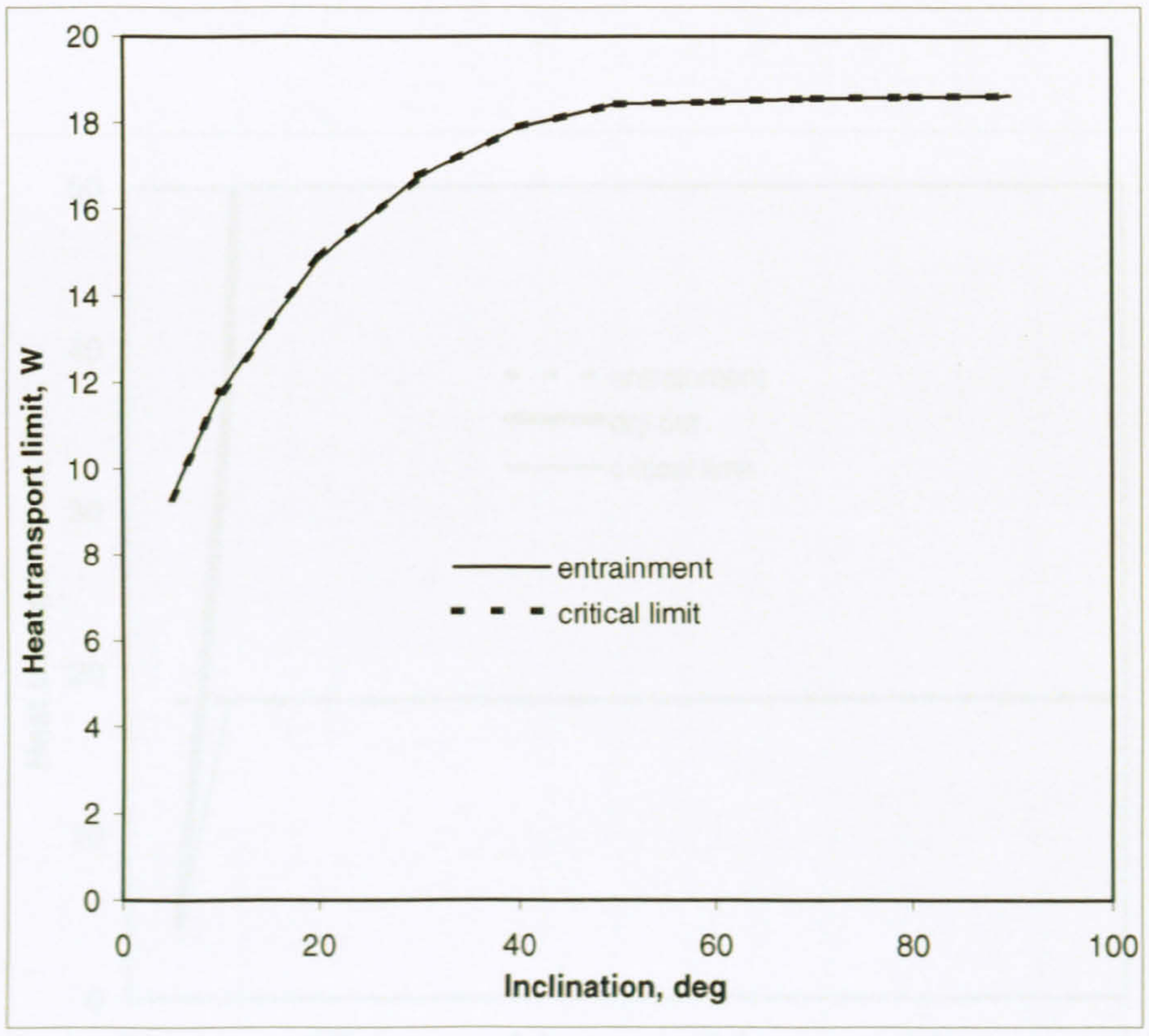

Figure 3-12. Variation of the limits of heat transport capacity with pipe inclination (mini heat pipes)

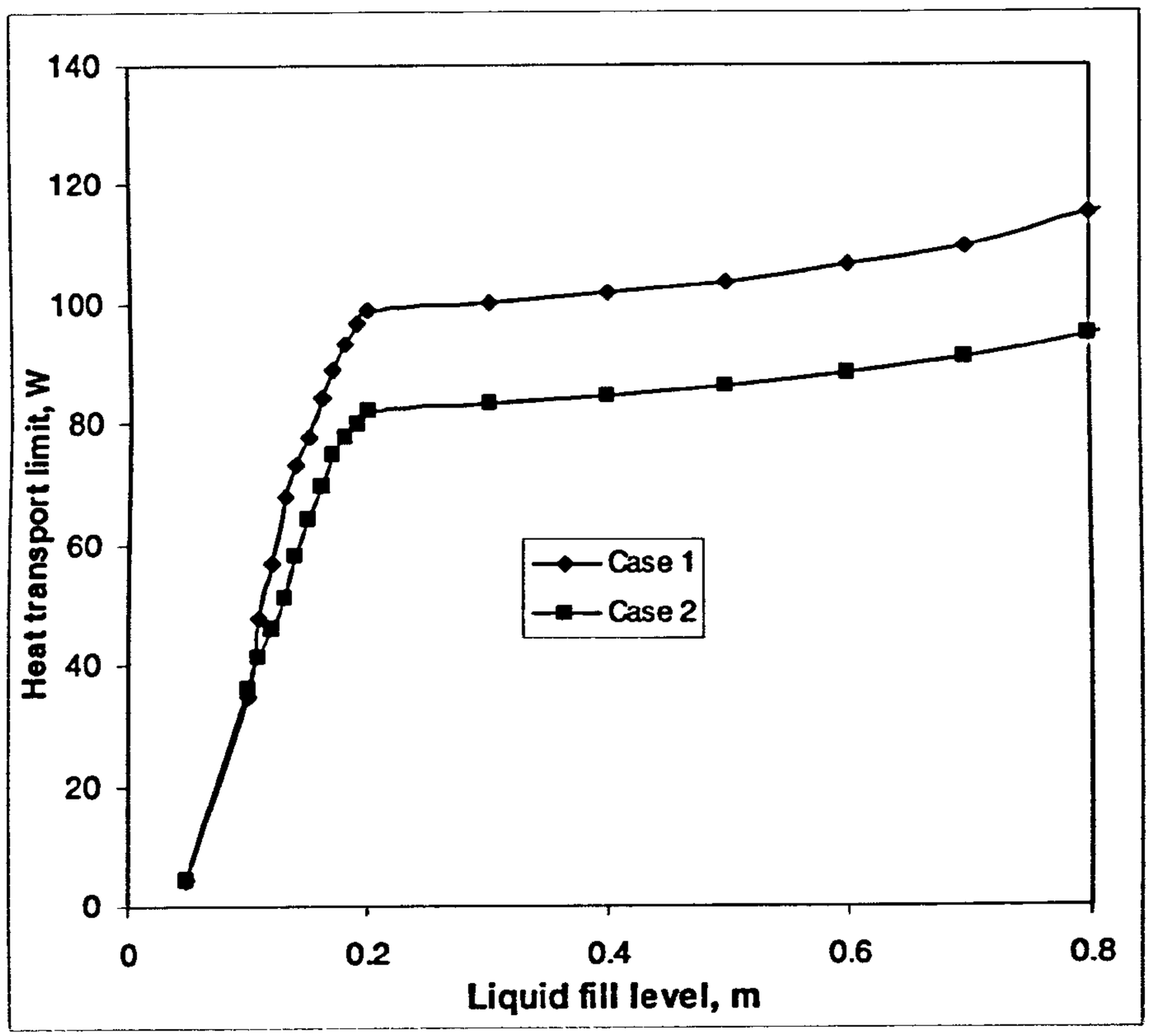

Figure 3-13. Variation of the limits of heat transport capacity with liquid fill level (miniature heat pipes)

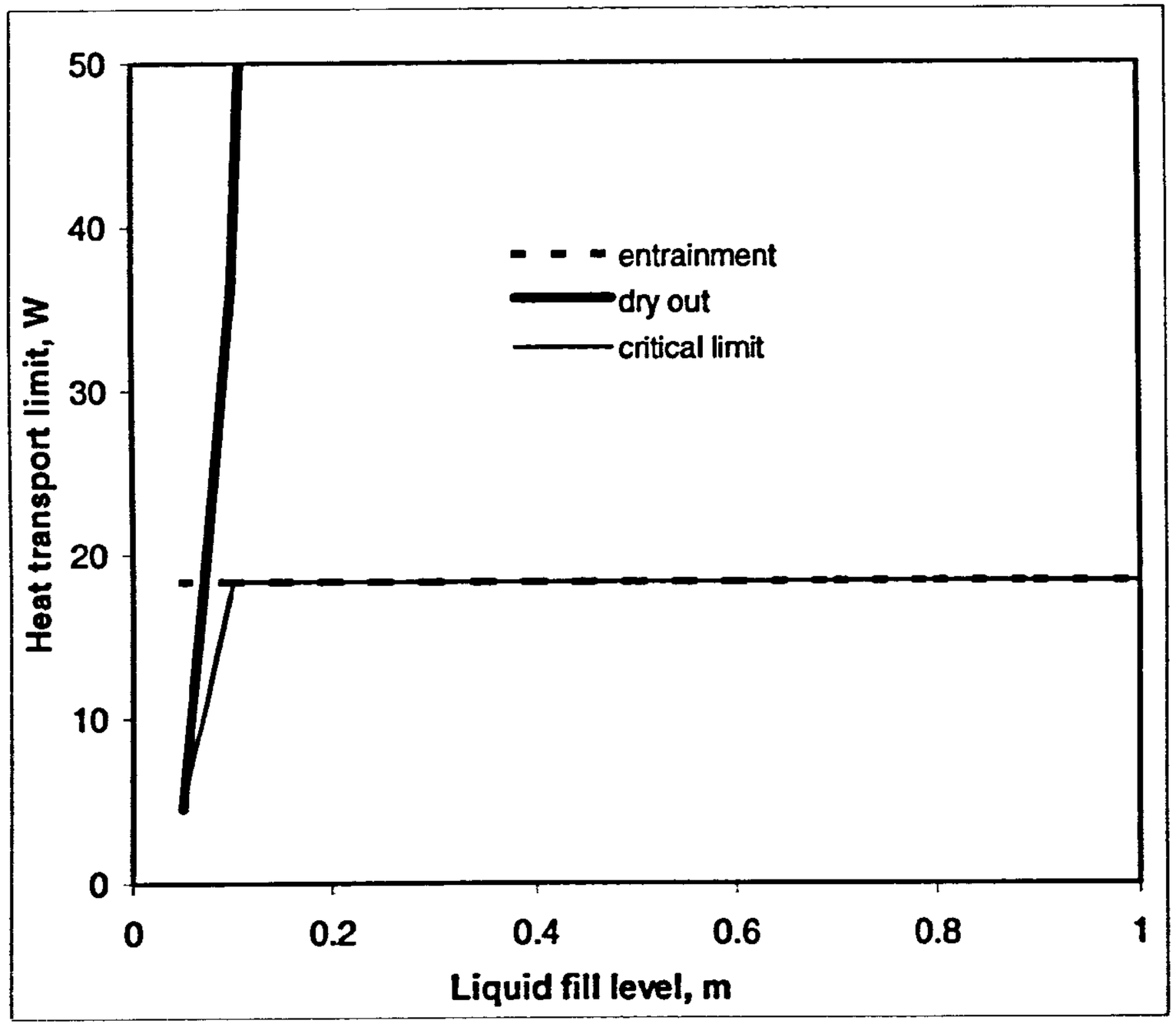

Figure 3-14. Variation of the limits of heat transport capacity with liquid fill level (mini heat pipes)

3.4.2 Comparison of the Thermal Performance of the Normal Rectangular and Circular Heat Pipes, with/without Wicks

The analytical model was also used to predict the thermal performance of the normal heat pipes, with circular and rectangular channel geometries, with/without wicks. The dimensions of the cross section vary in a wide range, as shown in Table 3-5. However, the lengths of the heat pipes remain the same as the real heat pipes used in the hybrid heat pipe solar collector, i.e., 1970mm, of which 1700 mm as the evaporation section, 200mm as the condensation section, and 70mm as the adiabatic section. For either the wicked or the wickless structure, the dimensions of the heat pipes are the same.

Table 3-5. Dimensions of the normal heat pipe channels

Channel geometry	Dimensions						
Circular (diameter, mm)	6	7	8				
Rectangular (width x height, mm x mm)	5.652 x5	7.693 x 5	10.048 x 5	25 x 5	50 x 5	100 x 5	500 x 5

The limits of heat transport capacity and the critical limit for the heat pipes were determined using the analytical model, which are indicated as a function of operating temperature, inclination and fill level. They were compared to each other in order to sort out the favourite channel geometry, dimensions and operating conditions. The investigation initially assumed that the heat pipe operated at inclination of 30deg, liquid fill level of 0.425m and temperature of 120°C, which was in consistent with the real conditions of the heat pipe operation in the collector application.

Since the heat pipe solar collector was intended to be installed at a roof with a 30deg slope, the heat pipe was assumed to operate at this inclination. Since a gravity-assisted heat pipe was suggested to fill to 1/3 to 1/4 of the evaporation length to prevent dry-out and enable the maximum heat transfer during the operation [Zhuang J. et al, 1989], the heat pipe was assumed to be filled to 1/4 of the evaporation length. Furthermore, the operating temperature was initially set at 120°C to comply with the design and testing conditions of the heat pipe operation.

Influence of operating temperature

A circular and wickless heat pipe was selected to investigate influence of operating temperature to heat transport capacity. The results were obtained by assuming the heat pipes to have a diameter of 7mm, to be inclined at 30deg to the horizontal, and filled to the same liquid fill level (0.5m), which are shown in Figure 3-15. The entrainment limit was found to be the dominant limit for the heat pipe, which increases with the working temperature at an approximately linear trend. To enhance the heat transfer of a heat pipe, a good way is to operate it at a higher temperature. Further investigation showed that other heat pipes had the same trend as this heat pipe, see Appendix 1.

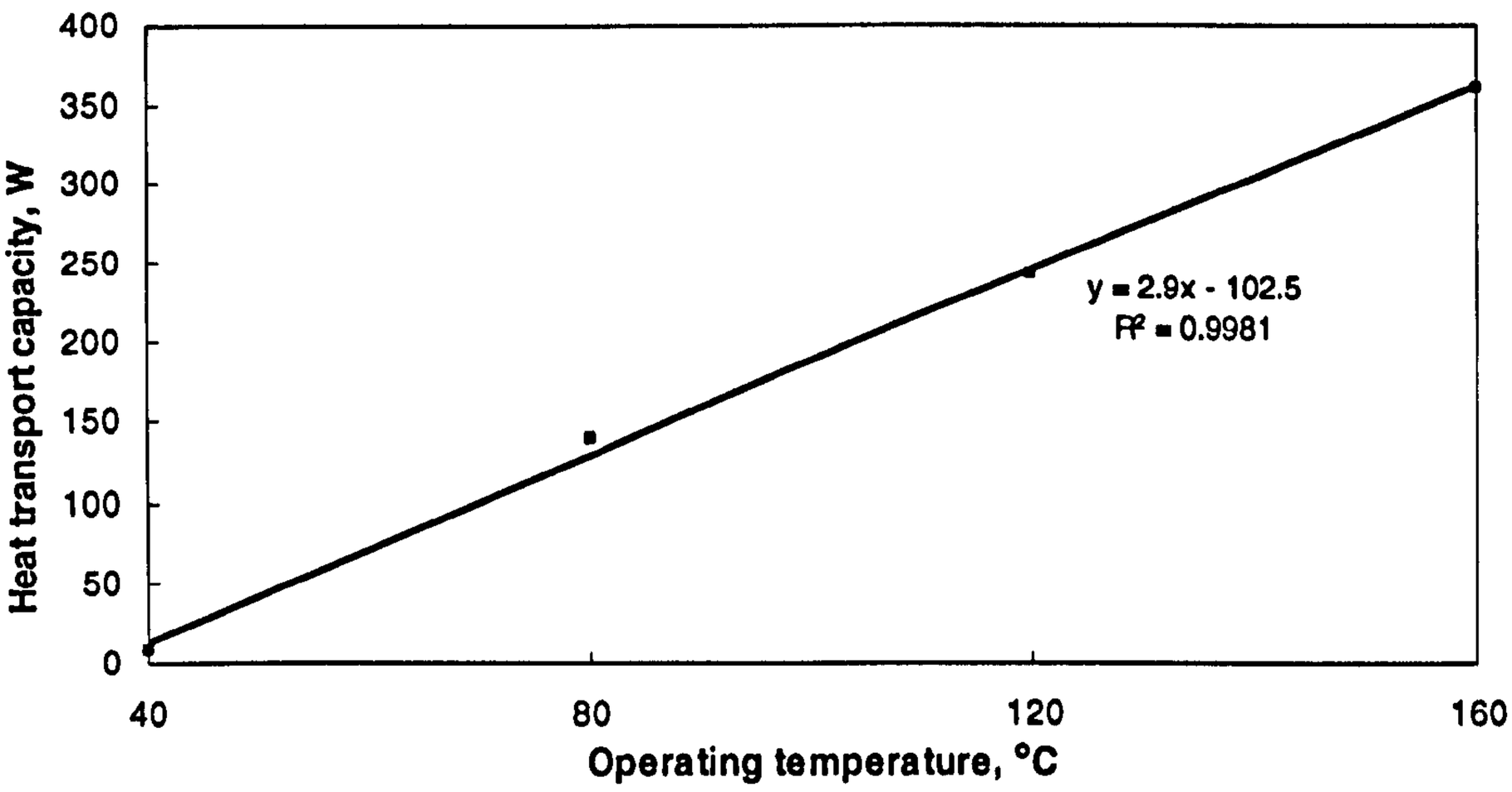

Figure 3-15. Variation of heat transport capacity with operating temperature – circular, wickless heat pipe

Influence of inclination

The same heat pipe was used to investigate influence of inclination to heat transport capacity. These results were obtained by assuming the pipe operated at the same temperature (200°C) and filled to the same liquid fill level (0.5m), which are shown in Figure 3-16. It was found that the entrainment limit is still the dominant limit for a circular/wickless heat pipe, which increases with the inclination.

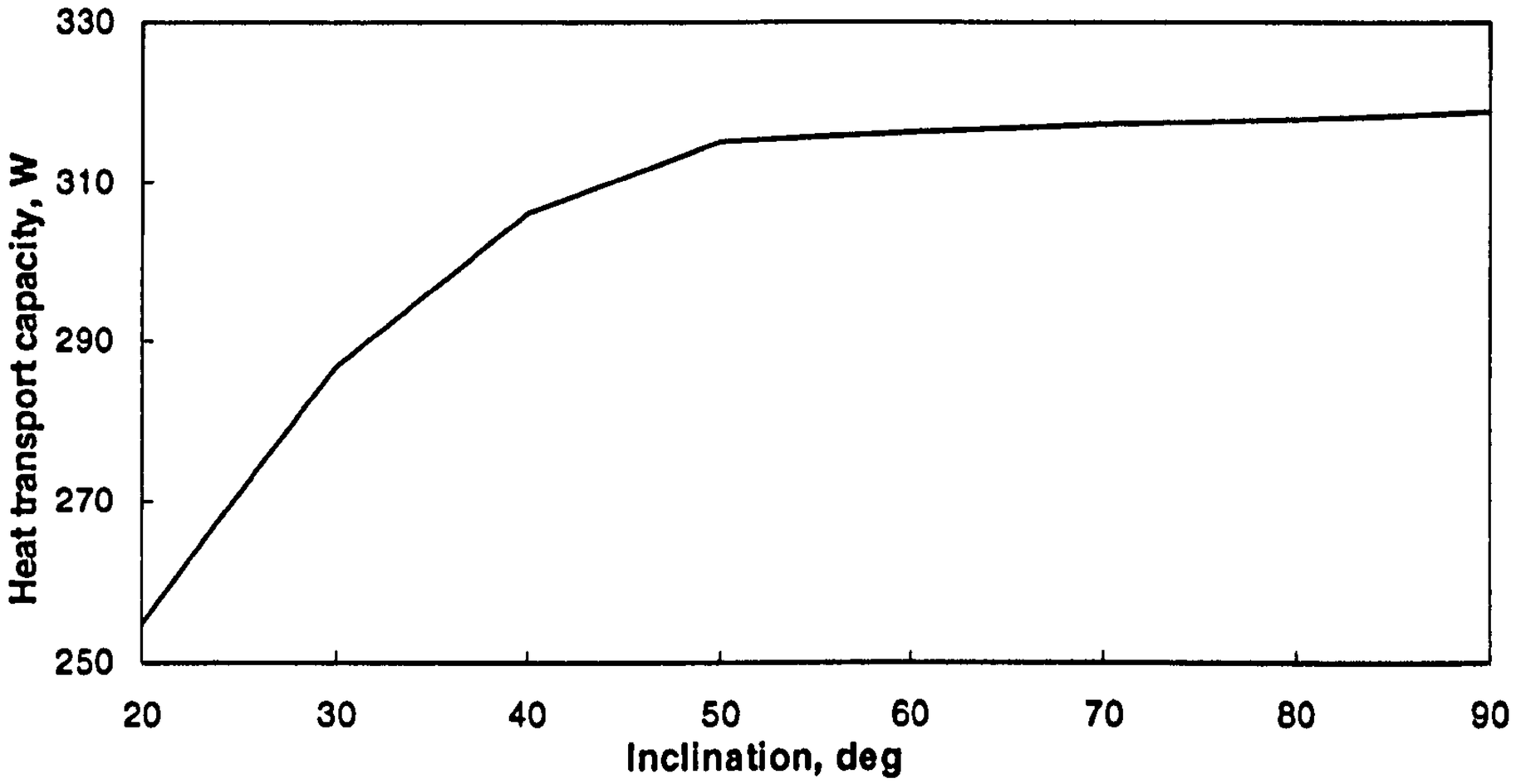

Figure 3-16. Variation of heat transport capacity with inclination – circular, wickless heat pipe

Influence of liquid fill level

The same heat pipe was used to investigate influence of liquid fill level to heat transport capacity. It was found that the entrainment limit is the dominant limit for the heat pipe, which remains constant at any liquid fill level, above 0.1m, and the dry-out limit is the dominant limit when the liquid fill level is below 0.1, which increases with the level.

Influence of heat pipe dimensions

The variation of the limits of heat transport capacity with diameter of the circular/wickless heat pipes is shown in Figure 3-17. These results were obtained by assuming the pipe operated at the same temperature (200°C), to be mounted at the same inclination (30deg) and filled to the same liquid fill level (0.5m). It was found that the entrainment limit is the dominant limit for a circular/wickless heat pipe, which increases with the diameter.

For the rectangular heat pipes investigated, the heights remain the same, i.e., 5mm, but the widths vary in a wide range of dimensions, from 5mm to 500mm. The variation of the limits of heat transport capacity with width of the rectangular heat pipes is shown in Figure 3-18. These results were obtained by assuming the pipe operated at the same temperature (200°C), to be mounted at the same inclination (30deg) and filled to the same liquid fill level (0.5m). It

was found that the entrainment limit is the dominant limit when the width is less than 25mm, but boiling limit becomes the dominant limit when the width is more than 25mm. Overall, the critical heat transport limit increases linearly with width of the heat pipes.

Provided that a number of rectangular heat pipes were fitted tightly in an area of 500mm width and 1900mm length to construct a flat plate solar absorber, i.e., a heat pipes group, then quantity of the heat pipes included would be totally dependent on the width of the heat pipes selected. The overall heat transport capacity of the heat pipes group is also dependent on the width of the pipes. Relationship between overall heat transport capacity of the heat pipes group, quantity of the heat pipes and width of the heat pipes is shown in Figure 3-19. It was found that the heat transport capacity of the heat pipes group achieves the maximum value when using 20 heat pipes with the width of 25mm. This happened because the entrainment and boiling limits of the heat pipe are the same at the given operating conditions, which results in the best heat transfer for the combined heat pipes group.

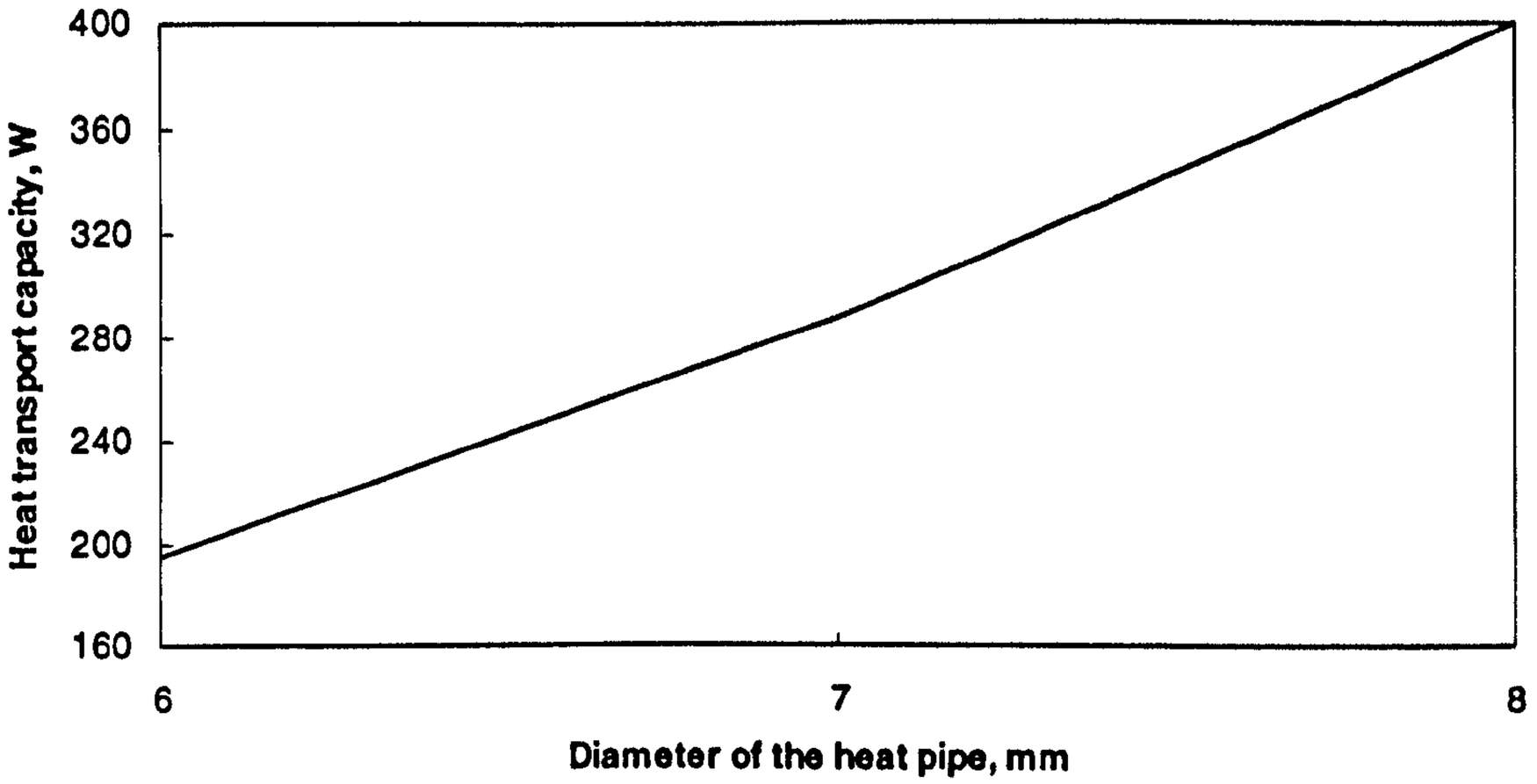

Figure 3-17. Variation of heat transport capacity with diameter – circular, wickless heat pipse

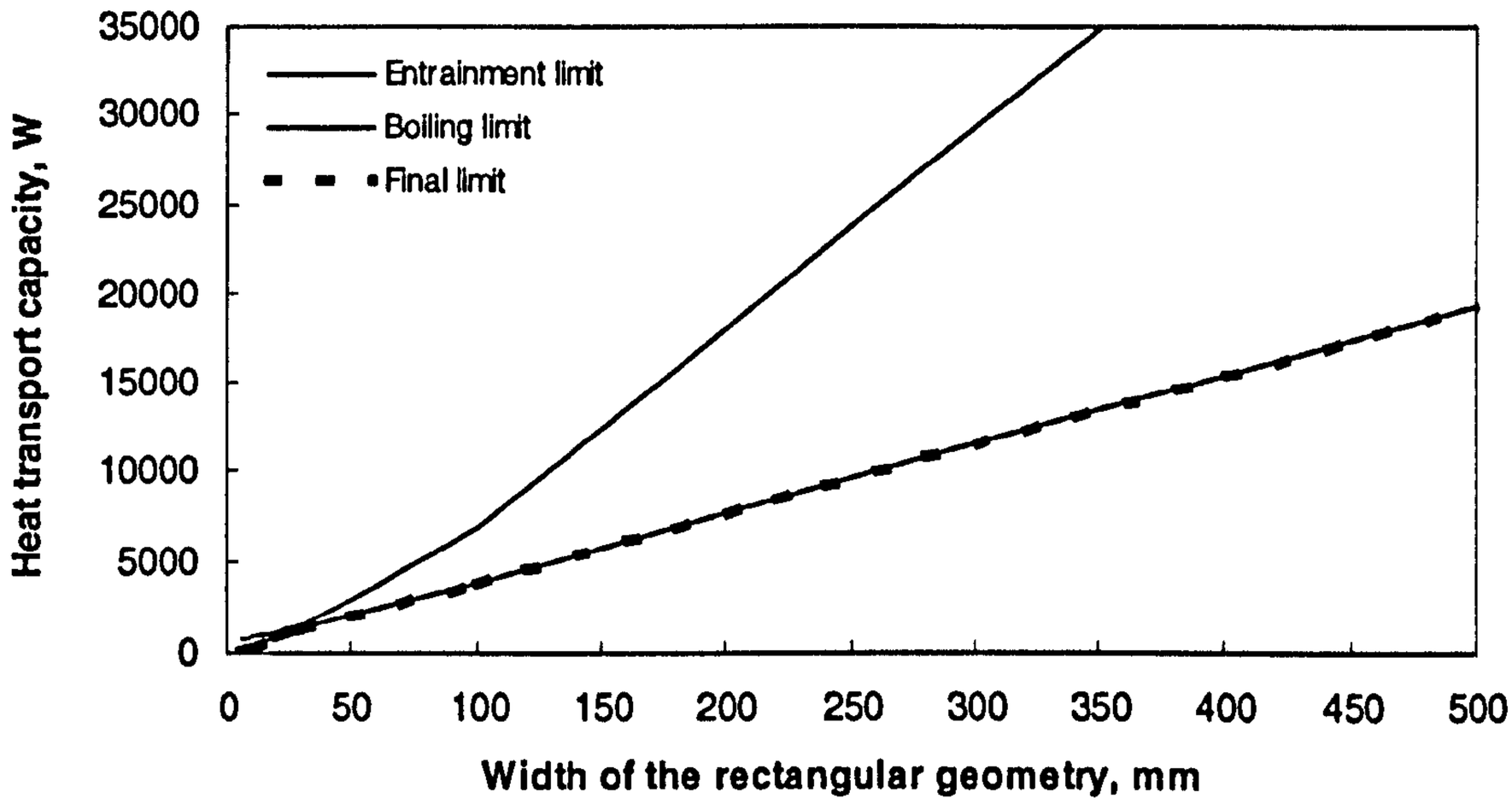

Figure 3-18. Variation of heat transport capacity with heat pipe width – rectangular, wickless heat pipes

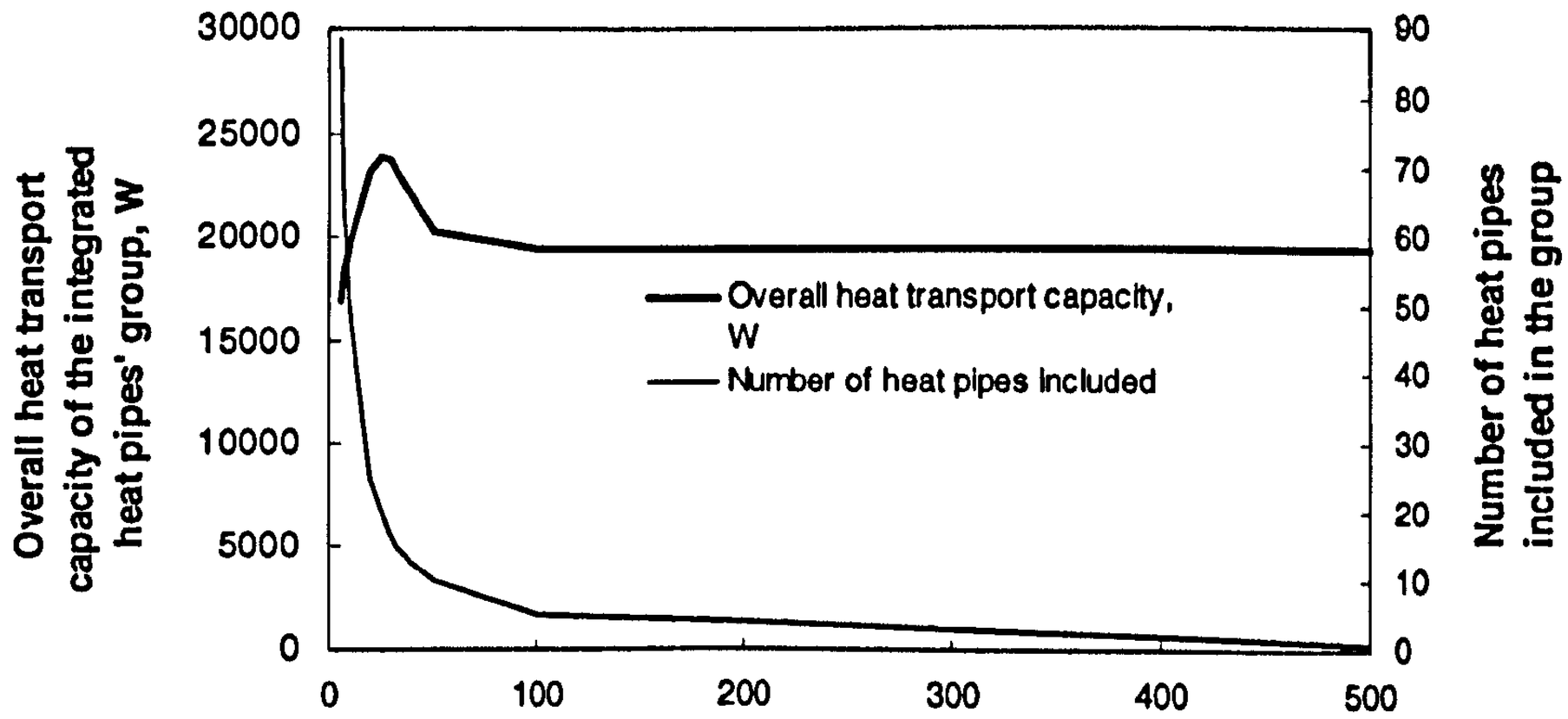

Figure 3-19. Relationship between overall heat transport capacity of the heat pipes group, quantity of the heat pipes and width of the heat pipes

Influence of heat pipe channel geometry

Influence of heat pipe channel geometry to heat transport capacity was investigated by comparing the circular/wickless heat pipes with diameter of 6mm, 7mm and 8mm and the rectangular/wickless heat pipes with the same equivalent diameter, i.e., heat pipes with sizes of 5.652mm x 5mm, 7.693mm x 5mm, and 10.048mm x 5mm. The results were obtained by assuming the pipe operated at the same temperature (200°C), to be mounted at the same inclination (30deg) and filled to the same liquid fill level (0.5m), which are shown in Figure 3-20. The entrainment limit was found to be the dominant limit for both circular and rectangular heat pipes (wickless), and a circular heat pipe has higher heat transport capacity than the rectangular one with the same equivalent diameter.

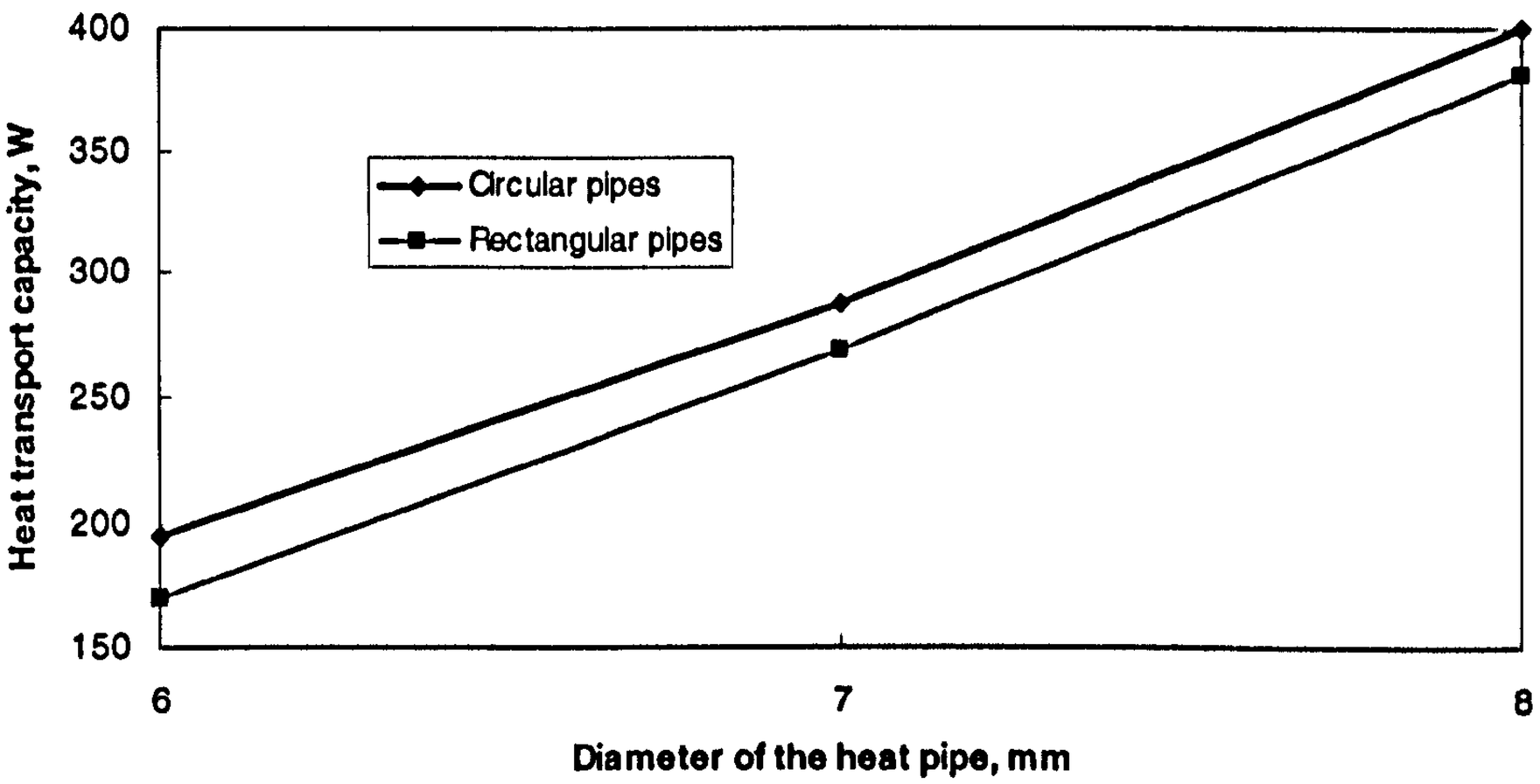

Figure 3-20. Comparison of heat transport capacities of circular and rectangular heat pipes

Influence of wick structure

Influence of wick structure to heat transport capacity was investigated by comparing the circular/wickless heat pipes with diameter of 6mm, 7mm and 8mm and the circular/wicked pipes with the same diameters. The results were obtained by assuming the pipe operated at the same temperature (200°C), to be mounted at the same inclination (30deg) and filled to the same liquid fill level (0.5m), which are shown in Figure 3-21. It is found that the entrainment limit is the dominant limit for wickless heat pipes, and the capillary limit is the dominant

limit for wicked pipes. A circular/wickless heat pipe has higher heat transport capacity than the circular/wicked pipe of the same equivalent diameter.

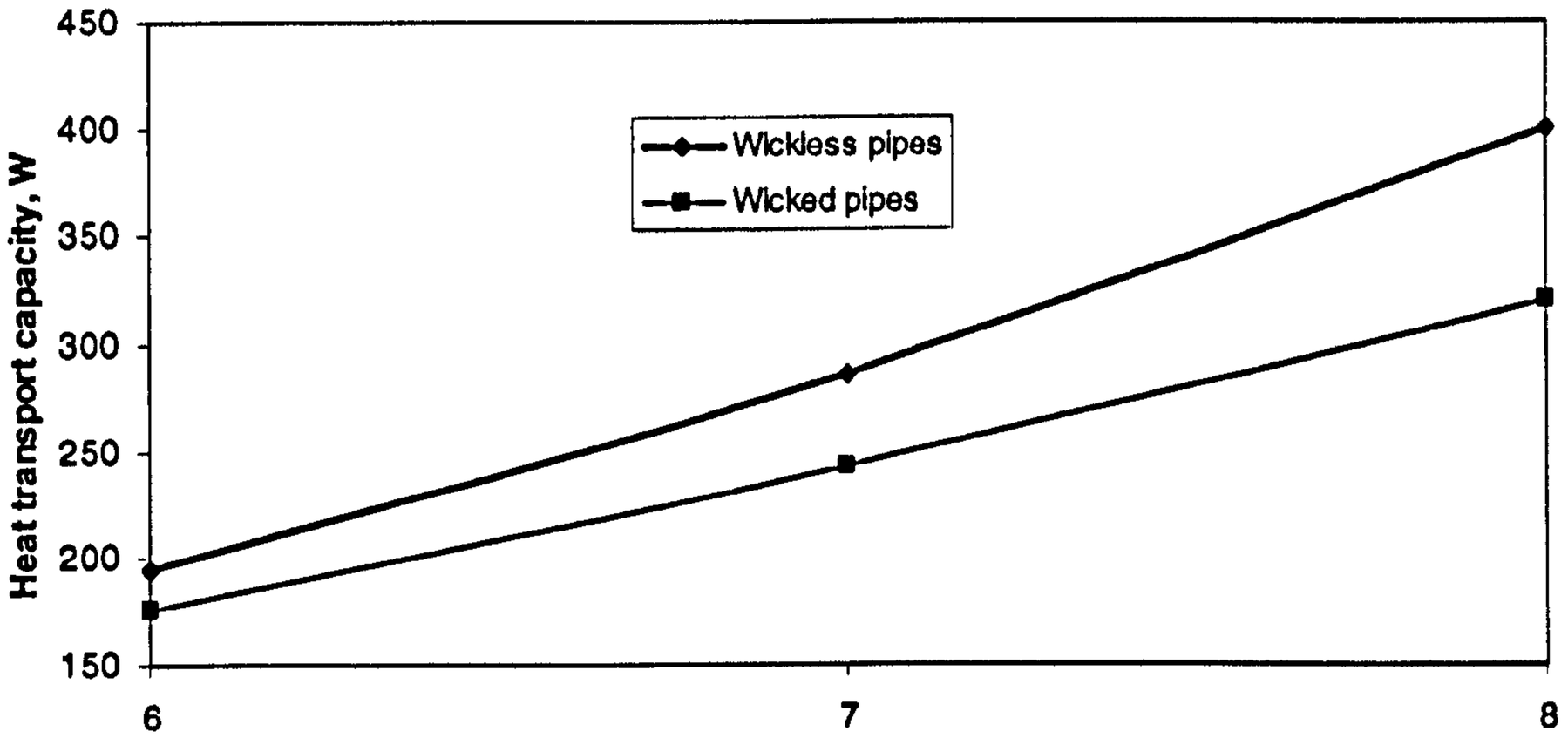

Figure 3-21. Comparison of heat transport capacities of wickless and wicked heat pipes

3.5 Summary

A number of heat pipes, namely, miniature heat pipes, normal circular and rectangular heat pipes, with/without wicks, were illustrated in this Chapter. These pipes are intended to be used as the components of the heat pipe solar collectors, which will be investigated in the following chapters.

An analytical model was developed to evaluate the thermal performance of any type of heat pipe. The maximum heat transport capacity is taken as the index evaluating heat transfer capability of a heat pipe, which is governed by six limits, i.e., the sonic limit, the entrainment limit, the boiling limit, the viscous limit, the capillary limit and the filled liquid mass limit. The physical phenomena and mathematical theory involved with the process were indicated, and a FORTRAN program was developed based on the analysis above.

The model was initially used to analyse the thermal performance of the miniature and mini heat pipes indicated above. It was found that:

- The maximum heat transport capacities of the miniature or the mini heat pipes increase with the increase of operating temperature.
- The maximum heat transport capacities of the miniature heat pipes increase with the increase of liquid fill level. However, the maximum heat transport capacity of the mini heat pipe increases initially with the liquid fill level when it is below 0.1, but remains constant when the level is above 0.1.
- The maximum heat transport capacity of the miniature heat pipe increases with the increase of the heat pipe inclination when the inclination is below 30 deg. Beyond 30 deg, its maximum heat transport capacity remains constant. However, the maximum heat transport capacity of mini heat pipe increases with the increase of heat pipe inclination.
- The maximum heat transport capacities of the miniature and mini heat pipes increase with the increase of the heat pipe inclination.
- For the two miniature heat pipes, the one with smaller width (Case 1) has a better thermal performance than that with larger width (Case 2). The miniature heat pipes perform better than the mini heat pipe if they have the same cross-sectional area.
- The entrainment limit is the dominant limits for both the miniature and mini heat pipes.

The model was then used to analyse the thermal performance of the normal circular/rectangular heat pipes, with or without wicks. It was found that:

- For any type of 'normal' heat pipe, the maximum heat transport capacity increases with the increase of operating temperature.
- For any type of 'normal' heat pipe, the maximum heat transport capacity remains constant when the liquid fill level is above 0.1.
- For any type of 'normal' heat pipe, the maximum heat transport capacity increases with the increase of the inclination.

- For any type of heat pipe, the maximum heat transport capacity increases with the increase of channel dimensions (diameter or equivalent diameter). For a flat plate solar panel with dimensions of 1900mm (length) x 500mmm (width), which is made of the selected rectangular heat pipes indicated above, the optimum width of an individual heat pipe is 25mm.
- The maximum heat transport capacity of a circular heat pipe is larger than that of the rectangular heat pipe of the same equivalent diameter, despite their wick structure.
- The maximum heat transport capacity of a wickless heat pipe is larger than that of the wicked heat pipe of the same dimensions. The entrainment limit is the dominant limit for a wickless heat pipe, and the capillary limit is the dominant limit for a wicked pipe.

Chapter 4. Numerical and Experimental Investigation of Heat Transfer in the Selected Heat Pipes

4.1 Numerical Model Set-up - Mathematical Theory and Numerical Method

A numerical model was developed based on the analysis of the previous methods. The model allowed a few simplified assumptions to be made, but still able to provide a reasonable accuracy for practical application. In this model, vapour flow was treated in different ways for different heat pipes. For a micro/miniature heat pipe, vapour flow was treated as a one-dimensional problem. This is because the vapour cross-sectional area is so small that the variations of vapour parameters (velocity, pressure and temperature etc) along radial direction becomes negligible. However, for a normal heat pipe, vapour flow was treated as a two-dimensional problem. This is because the vapour cross-sectional area is relatively large, which would result in a remarkable variation of vapour parameters along the radial direction. In that case, using one-dimensional model would cause an unacceptable discrepancy.

Heat transfers through liquid and wall regions were computed by solving a one-dimensional heat conduction equation. This is rational because of the following two reasons: firstly, the heat transfer in a heat pipe is mainly conducted by evaporation and condensation of vapour flow, and secondly, heat input across the evaporator area and heat output across condenser area are evenly distributed, which result in an even temperature distribution around the evaporator and condenser areas. As a result, heat conduction through wall and liquid region is mainly directed toward radial direction, rather than axial direction.

Flow in the liquid region was treated as a one-dimensional problem. This is because the liquid in a heat pipe is evenly distributed around the periphery of heat pipe inner wall, which would form a very thin liquid film. The film is so thin (about 0.1mm) that the variation of liquid parameters across the film becomes negligible.

Liquid and vapour flows were correlated by using a set of governing equations, including those for thermal compressibility, hydro-dynamical, capillary, and geometrical relation. Finite-difference method was employed to carry out numerical analysis for the equations, and the FORTRAN language was used to develop a computer program.

4.1.1 Mathematical Theory

Miniature and Mini Heat Pipes

As indicated above, vapour flow in a miniature/mini heat pipe could be treated as a one-dimensional flow. The flow could be analysed by coupling the governing equations with those of liquid flow, and of heat conduction for the heat transfer across wall and liquid regions.

The high thermal conductivity of heat pipes is the result of the continued evaporation and condensation process occurring within the heat pipe. For this reason, the determination of evaporation and condensation rates plays a key role in evaluating heat pipe operating characteristics. In this model, an expression for the free molecular flow mass flux of evaporation, j, presented by Collier (1981) and later used by Colwell and Chang (1984), was employed:

$$j = [\frac{M}{2\pi R(t+273)}]^{0.5}(p_s - p_v) \tag{4-1}$$

When p_s is greater than p_v, j is positive and the liquid evaporated. When p_s is less than p_v, j is negative and the vapour condensed. In the development of the numerical model, the evaporation-condensation rate was assumed to be proportional to the liquid-vapour interface area in each section of the heat pipe, i.e.,

$$\Delta m_{ec} = jW_{ec}\Delta x \tag{4-2}$$

For a given latent heat, h_{fg}, the rate of heat removed or absorbed in any section can be

determined from:

$$q_{ec} = h_{fg}\Delta m_{ec} \tag{4-3}$$

For a miniature heat pipe (or a wicked 'normal' heat pipe) to operate properly, the capillary pressure difference, plus gravity difference, must be sufficient to overcome the liquid and vapour pressure losses. However, for a mini heat pipe (or a wickless heat pipe) to operate properly, gravity difference is the sole force used to overcome the liquid and vapour pressure losses.

Capillary pressure is expressed as

$$p_{cl} = 2\sigma\cos\theta / r_{ce} \tag{4-4}$$

Since both p_{cl} and r_{ce} are functions of length position x, then

$$\frac{dp_{cl}}{dx} = \frac{-2\sigma\cos\theta}{r_{ce}^{\,2}}\frac{dr_{ce}}{dx} \tag{4-5}$$

Expressing this over a finite interval yields:

$$\Delta p_{cl} = (-2\sigma\cos\theta / r_{ce}^{\,2})\Delta r_{ce} \tag{4-6}$$

Gravity pressure differences include axial and radial pressure differences. They are expressed respectively as follows:

$$\Delta p_{ag} = -\rho_l g \sin\phi\Delta x \tag{4-7}$$

$$\Delta p_{rg} = -2\rho_l g \cos\phi\Delta r_v \tag{4-8}$$

The pressure losses of liquid and vapour are expressed as

$$\Delta p_{vl} = \Delta p_{fv} + \Delta p_{mv} + \Delta p_{fl} + \Delta p_{ml} \tag{4-9}$$

The pressure losses result from liquid and vapour friction, and the momentum changes occurring in any one section along the heat pipe. The pressure losses due to friction for laminar flow may be expressed as:

$$\Delta p_{fv} = (2\mu_v \Delta x u_{v)} / r_{hv}{}^2 \tag{4-10}$$

$$\Delta p_{fl} = (2\mu_l \Delta x u_l) / r_{hl}{}^2 \tag{4-11}$$

The total pressure drop due to the momentum change may be expressed as:

$$\Delta p_{ml} = (u_l \Delta ms_l + ms_l \Delta u_l + \Delta ms_l \Delta u_l) / A_l \tag{4-12}$$

$$\Delta p_{mv} = (u_v \Delta ms_v + ms_v \Delta u_v + \Delta ms_v \Delta u_v) / A_v \tag{4-13}$$

For steady state model the energy equation may be written as:

$$q_{in} = q_{out} \tag{4-14}$$

$$q_{in} = ms_0 h_{fgv0} + ms_1 h_{fgl1} + q \tag{4-15}$$

$$q_{out} = ms_1 h_{fgv1} + ms_0 h_{fgl0} \tag{4-16}$$

$$q = q_{ec} \tag{4-17}$$

For transient state model the energy equation may be written as:

$$q_{in} = q_{out} + q_r \tag{4-18}$$

$$q_r = \int \rho_l A_l C_{pl} \Delta t_l dx + \int \rho_v A_v C_{pv} \Delta t_v dx + \int \rho_s A_s C_{ps} \Delta t_s dx \tag{4-19}$$

The continuity equation may be written as:

$$\int \rho_v A_v dx + \int \rho_l A_l dx = constant \tag{4-20}$$

The total volume and area inside the heat pipe may be defined and expressed, respectively, as:

$$vol = vol_l + vol_v \tag{4-21}$$

$$A = A_l + A_v \tag{4-22}$$

Both the miniature and the mini heat pipes consist of three basic sections, i.e., the evaporation section, the adiabatic section and the condensation section. Each section has a different set of boundary conditions, and as a result, needs to be treated independently.

Evaporation Region: The single boundary condition used in the evaporation section was the time dependent heat flux. For a specific input heat flux, the saturation pressure at a given location could be obtained by using a combination of the mass flux expression given in Eq. 4-2 and the energy conservation equations given in Eq. 4-14 and Eq. 4-18.

For steady state condition:

$$P_s = \frac{q_{ec}}{(M / 2\pi R T_l)^{1/2} \Delta x W_{ec} h_{fg}} + P_v \tag{4-23}$$

$$q_{in} = ms_0 h_{fgv0} + ms_1 h_{fgl1} + q \tag{4-24}$$

For transient state condition:

$$q_{in} = q_{ec} + \Delta q_l + \Delta q_s + \Delta q_v \tag{4-25}$$

$$\Delta q_s = (C_{ps} \rho_s A_s \Delta x \Delta t_s) / \Delta t \tag{4-26}$$

$$\Delta q_l = (C_{pl}\rho_l A_l \Delta x \Delta t_l)/\Delta t \quad (4\text{-}27)$$

$$\Delta q_v = (C_{pv}\rho_v A_v \Delta x t_v)/\Delta t \quad (4\text{-}28)$$

Since t_l is a function of p_s, Eqs. (4-25 - 4-28) are coupled and can be solved using an iterative method with relaxation to obtain values for t_l, q_{cc}, Δq_l and Δq_s. Since the difference between the boundary and liquid temperatures Δt_{sl} is proportional to the input heat flux, the boundary temperature can be obtained by adding Δt_{sl} to t_l .

Adiabatic Region: The single boundary condition used in the adiabatic section was the time independent heat flux. For a zero input heat flux, pressure and energy balance at a given location could be expressed as follows:

For steady state condition:

$$P_s = P_v \quad (4\text{-}29)$$

$$q_{in} = ms_0 h_{fgv0} + ms_1 h_{fgl1} \quad (4\text{-}30)$$

For transient state condition:

$$q_{in} = \Delta q_l + \Delta q_s + \Delta q_v \quad (4\text{-}31)$$

$$\Delta q_s = (C_{ps}\rho_s A_s \Delta x \Delta t_s)/\Delta t \quad (4\text{-}32)$$

$$\Delta q_l = (C_{pl}\rho_l A_l \Delta x \Delta t_l)/\Delta t \quad (4\text{-}33)$$

$$\Delta q_v = (C_{pv}\rho_v A_v \Delta x t_v)/\Delta t \quad (4\text{-}34)$$

Condensation Region: In the condensation section, the boundary temperature of the heat pipe was assumed to be constant, resulting in governing equations similar to those used in the evaporation section.

Rearranging Eq. 4-23, gave:

$$q_{ec} = h_{fg} W_{ec} \Delta x (\frac{M}{2\pi R T_l})^{1/2} (p_s - p_v) \tag{4-35}$$

For steady state condition,

$$q_{out} = q + ms_1 h_{fgv1} + ms_0 h_{fgl0} \tag{4-36}$$

For transient state condition

$$q_{out} = q + ms_1 h_{fgv1} + ms_0 h_{fgl0} + \Delta q_l + \Delta q_s + \Delta q_v \tag{4-37}$$

Normal heat pipes

Most of the equations above can also be used to analyse the flows in a normal heat pipe, including the governing equations for liquid flow, and those for heat conduction through wall and liquid regions. However, the governing equations for vapour flow are different. The vapour flow can be assumed to be a steady, incompressible, axisymmetric (for circular pipes) and laminar flow for simplification (Attili Basem S., 1994). The radial velocity through liquid-vapour interface is a constant either in the evaporation section or in the condensation section. The variation of pressure only happens along the axial direction rather than the radial direction.

The equations governing laminar vapour flow in a circular heat pipe are:

Axial momentum equation:

$$u\frac{\partial u}{\partial x} + v\frac{\partial u}{\partial r} = \frac{-1}{\rho}\frac{dp}{dx} + v(\frac{\partial^2 u}{\partial r^2} + \frac{1}{r}\frac{\partial u}{\partial r}) \tag{4-38}$$

Continuity equation:

$$\frac{\partial u}{\partial x}+\frac{1}{r}\frac{\partial (vr)}{\partial r}=0 \qquad (4\text{-}39)$$

The boundary conditions are

(a) $u(0, r) = c_0$; $u(1, r) = 0$

(b) $v(0, r) = v(1, r) = 0$

(c) $v(x, 0) = 0$

(d) $\partial u/\partial r\ (x,0) = 0$

(e) $u(x, r_0) = 0$

(f) $v(x, r_0) = c$

Where c is a constant and in the evaporation section, $c > 0$ (injection); in adiabatic section, $c = 0$; and in the condensation section, $c < 0$ (suction). Of which (a) and (b) are end wall conditions, (c) and (d) are axial conditions, (e) is the non-slip condition and (f) is side wall condition.

All of the equations above provided a clear mathematical expression for the physical phenomena occurring in the selected heat pipes. The numerical analysis was carried out based on the mathematical theory.

4.1.2 Numerical Method

Miniature and mini heat Pipes

The finite-difference scheme was used to carry out numerical analysis and solution solving for the one-dimensional vapour flow model. The grid distribution and mesh network were designed, which is shown schematically in Figure 4-1. Both vapour and liquid were treated as one-dimensional flows, and the flow parameters vary only along the axial direction. The governing equations were applied to sections, grids and control volumes in a sequence order, which started from the control points and surfaces on the interface of liquid and vapour, and the boundary of liquid and wall. The grid size was set as 1mm in this

simulation. The error limit was set to 0.5%.

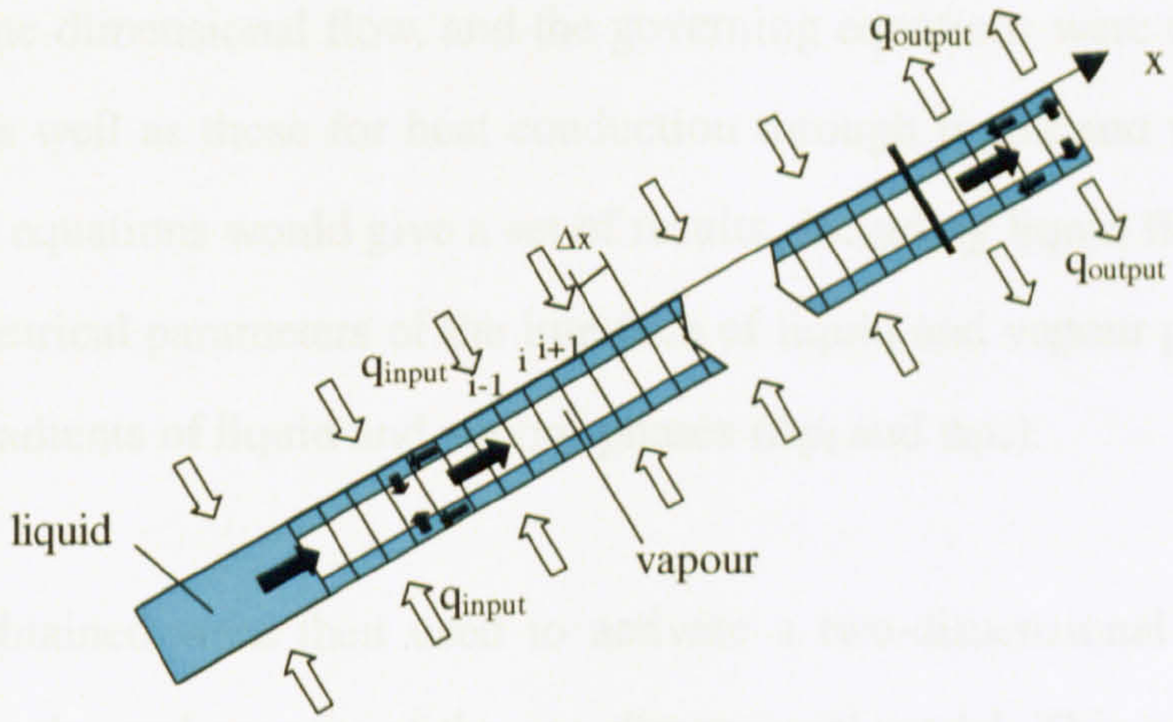

Figure 4-1. Schematic diagram showing grid distribution, mesh network and heat/fluid flow in a miniature or mini heat pipe

Normal heat pipes

The finite-difference scheme was also used to carry out numerical analysis and solution solving for the two-dimensional vapour flow model. The grid distribution and mesh network were slightly different from that of a miniature heat pipe because vapour was treated as a two-dimensional flow, as shown schematically in Figure 4-2. The grid size was set as 5mm in axial direction and 1mm in radial direction.

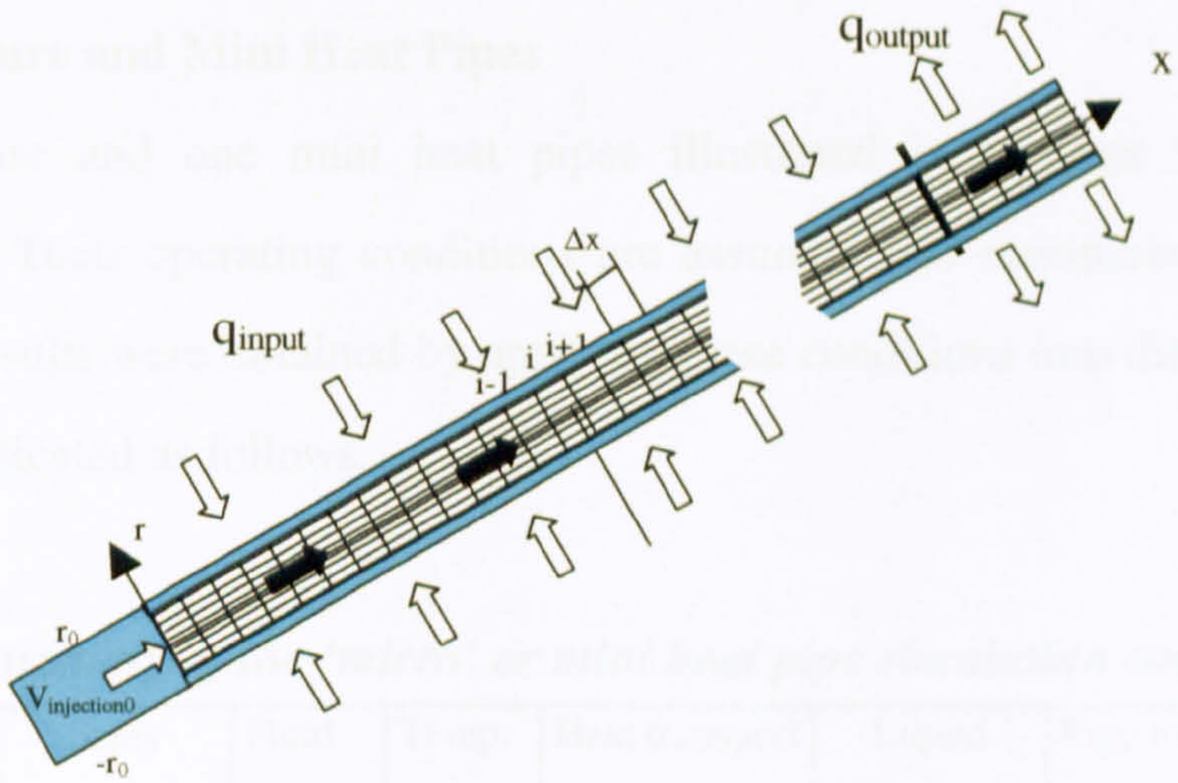

Figure 4-2. Schematic diagram of grid distribution, mesh network and heat/fluid flow in a normal heat pipe

Given a section of heat pipe along the flow as the simulated element, vapour was initially treated as a one-dimensional flow, and the governing equations were coupled with those of liquid flow, as well as those for heat conduction through liquid and wall regions. Solving the correlated equations would give a set of results, including liquid flow parameters (u_l, p_l, a_l etc), geometrical parameters of the interface of liquid and vapour phases(r_v etc), as well as pressure gradients of liquid and vapour phases (Δp_l and Δp_v).

The results obtained were then used to activate a two-dimensional vapour flow model, which acted as the replacement of the one-dimensional model. This would give another set of results, including vapour flow parameters within the heat pipe space (u_v and v_v), as well as the refined vapour pressure gradient (Δp_v').

The values of Δp_v and Δp_v' were compared, and the term of (Δp_v'-Δp_v)/ Δp_v' was defined as the calculation error, pe. If the absolute value of pe is larger than 0.5%, then the iteration in this element continues by replacing Δp_v with Δp_v'. Otherwise, the iteration in this element stops and the subsequent iteration moves onto the next section of the heat pipe.

4.2 Numerical Investigation of the Selected Heat Pipes

4.2.1 Miniature and Mini Heat Pipes

Two miniature and one mini heat pipes illustrated in Chapter 3 (Figure 3-1) were investigated. Their operating conditions are assumed and summarized in Table 4-1. The simulation results were obtained by applying these conditions into the numerical operation, which are indicated as follows.

Table 4-1. Summary of the 'micro' or mini heat pipe simulation conditions

Type of the pipe	Sizes mm x mm	Fluid	Temp. °C	Heat transport W	Liquid level, mm	Pipe material/ thickness	Inclination deg
Miniature 1	9.97 x 0.63	Water	150	10	250	Copper (0.5mm)	60
Miniature 2	6.28 x 1	Water	150	10	250	Copper (0.5mm)	60
Mini	2mm (dia)	Water	150	10	250	Copper (0.5mm)	60

Variation of liquid and vapour cross-sectional areas

Figures 4-3 and 4-4 present an indication of the complex behaviour of the liquid and vapour flow pattern in the heat pipes. As vapour condenses in the condensation section of the heat pipe, the volume of condensed liquid increases and is returned to the evaporation section. As liquid flows along the inner wall down to the bottom, it vaporizes partly due to absorbing the heat striking on the outer surface, and hence volume (or mass) flow rate reduces along the flow direction. As a result, the liquid cross-sectional area increases with height position above the reservoir in the evaporation section, and decreases with the height in the condensation section. Meanwhile, the vapour cross-sectional area varies at an opposite trend. Figure 4-3 shows little difference in the fluid flow pattern of the miniature heat pipes simulated. However, the flow pattern of the mini heat pipe follows a steeper trend.

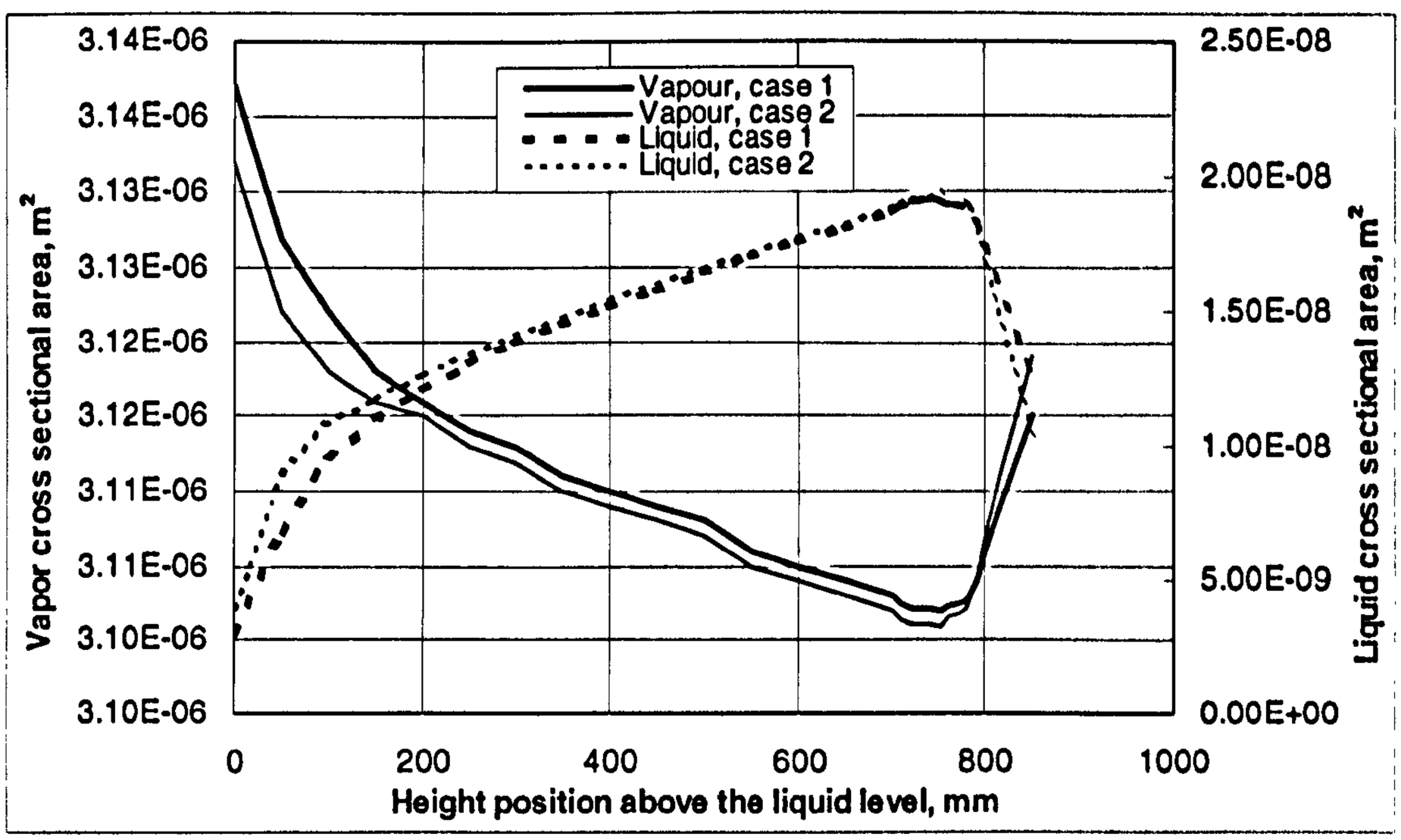

Figure 4-3. Variation of vapour and liquid cross-sectional areas with height position – the miniature heat pipes

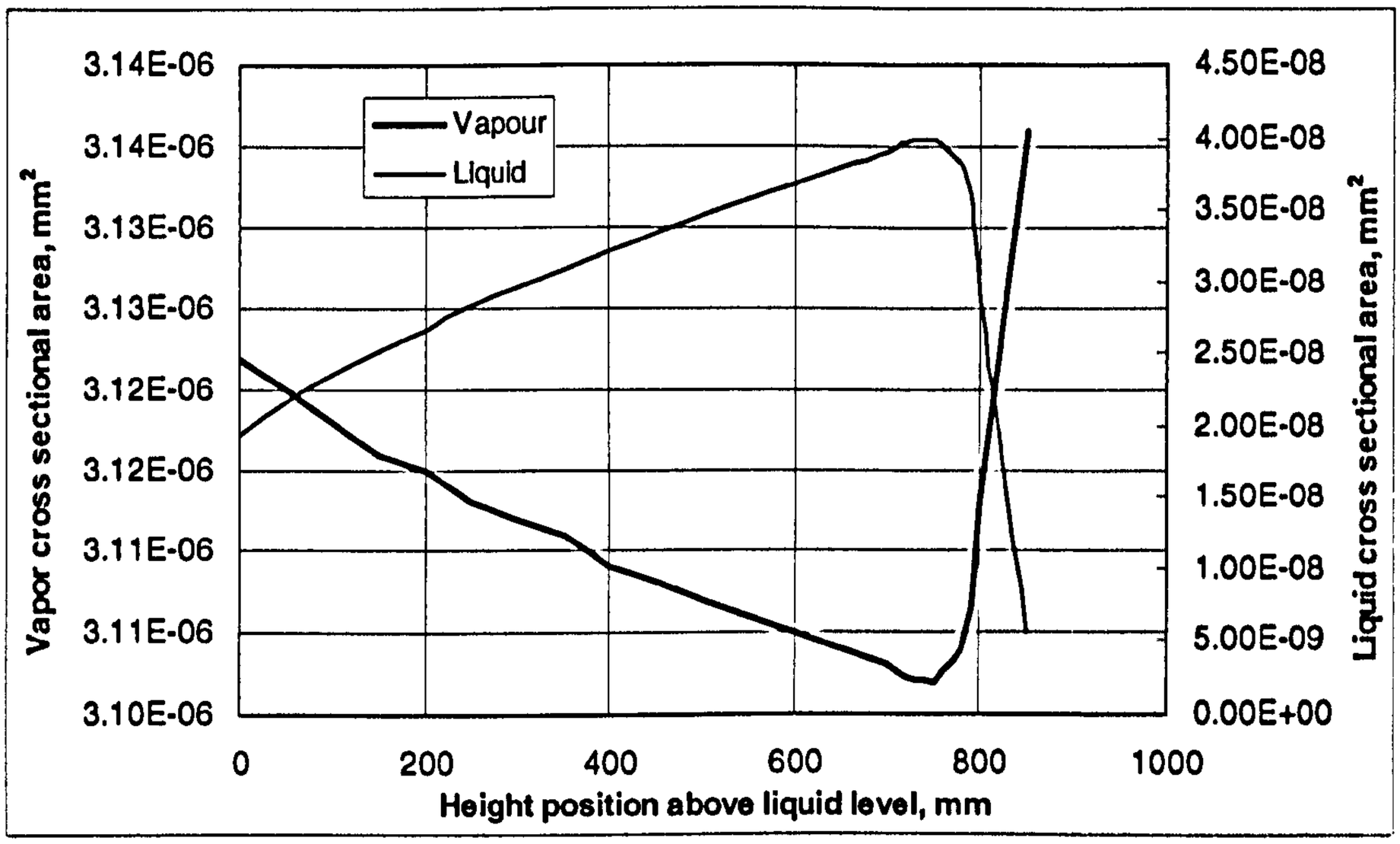

Figure 4-4. Variation of vapour and liquid cross-sectional areas with height position – the mini heat pipe

Variation of vapour and liquid pressures

The relationship of liquid and vapour pressures with height position above the filled liquid level are shown in Figures 4-5 and 4-6. The total vapour-liquid pressure difference is an important factor which affects the operation of a heat pipe. With the miniature heat pipes, the total pressure difference is shown to be significantly larger at the bottom of the evaporator section and decreased with height position above the reservoir fill level. The behaviour of the mini heat pipe shows the total pressure difference to increase from reservoir to condensation section. It is observed from Figures 4-5 and 4-6 that the vapour-liquid pressure differences in the miniature heat pipes are much larger than that for the mini heat pipe. This is mainly due to the geometrical shape of the miniature heat pipes, which causes higher flow resistances within the heat pipes. Figure 4-5 also shows that by increasing the width 'b' of the miniature heat pipe (for Case 2) the flow resistance within the heat pipe is reduced thereby resulting in reduced pressure differences.

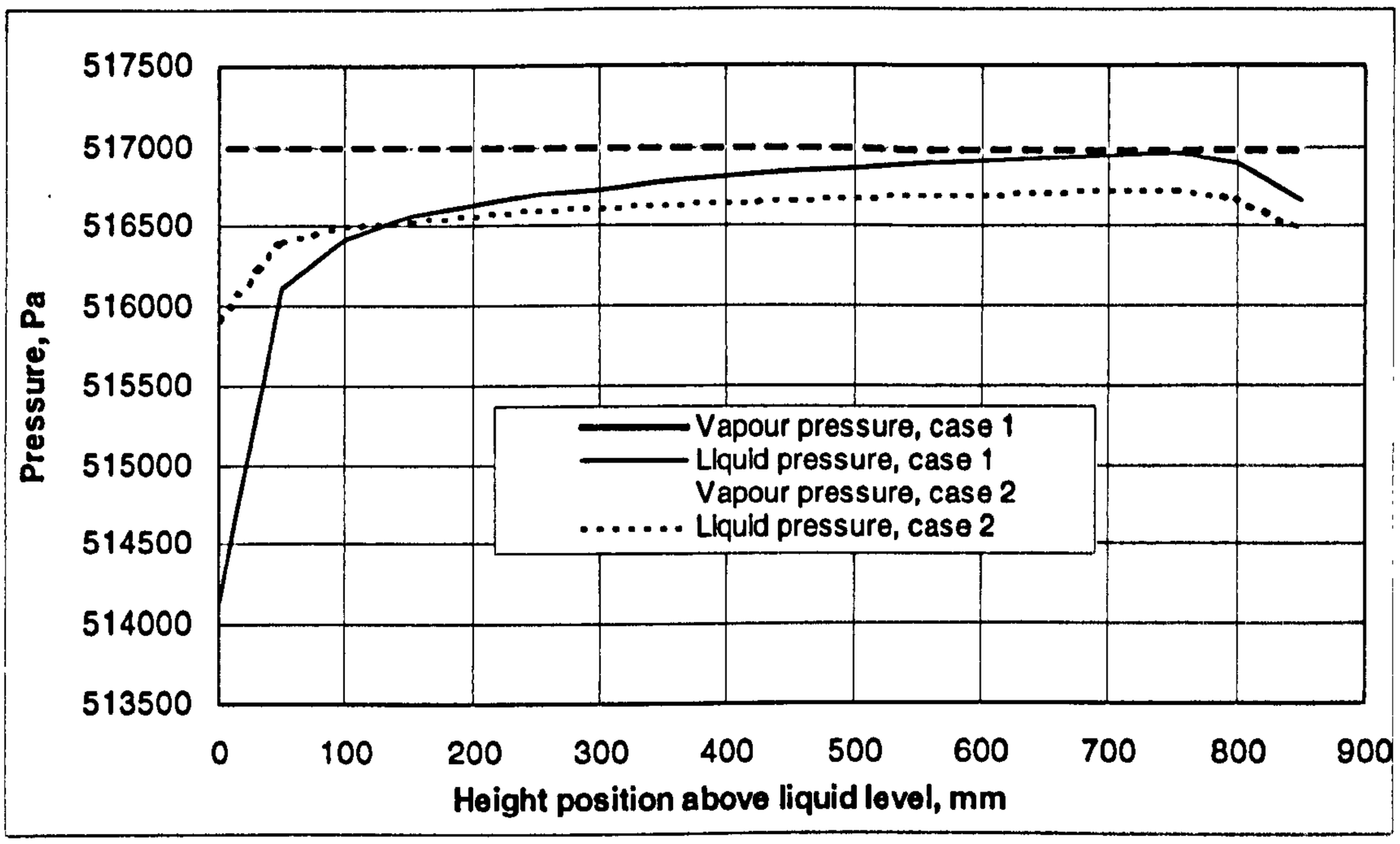

Figure 4-5. Variation of liquid and vapour pressures with height position – the miniature heat pipes

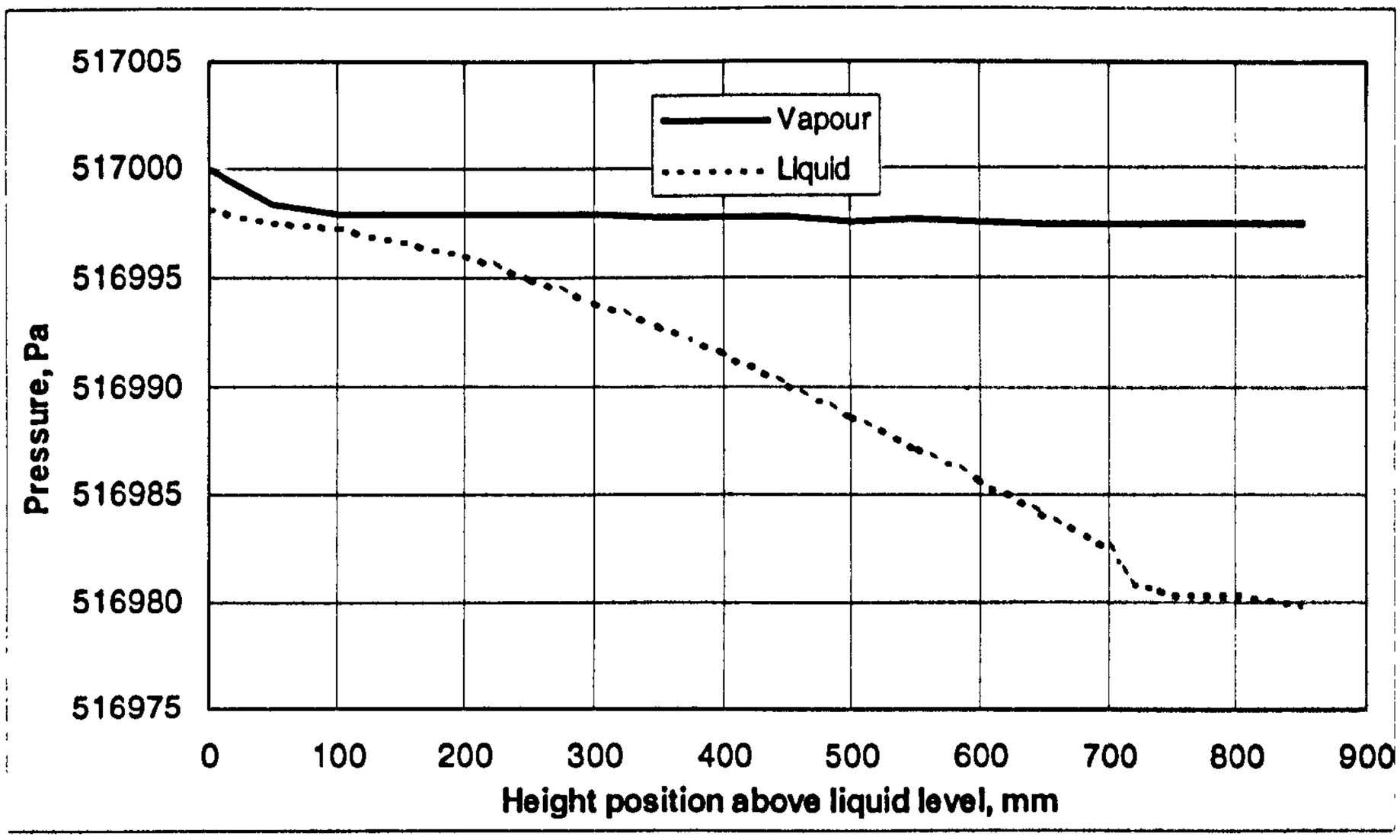

Figure 4-6. Variation of liquid and vapour pressures with height position – the mini heat pipe

Variation of vapour, liquid and wall temperatures

Variations of vapour, liquid and wall temperatures with height position above the liquid fill level are shown in Figures 4-7 and 4-8. The results show little difference in vapour and liquid temperatures for both miniature and mini heat pipes. The temperature difference

between the heat pipe inner wall and the liquid/vapour area for the mini heat pipe is +/-0.01°C compared to +/-0.4°C for the miniature heat pipe, Case 1 and +/-1.2 °C for the miniature heat pipe, Case 2. The higher temperature difference existeing in the miniature heat pipe, Case 2 is due to the liquid cross-sectional area for Case 2 being slightly larger than that for case1. For both miniature and mini heat pipes, the temperature difference betweem the inner and outer walls is about 0.001°C under the operation conditions assumed.

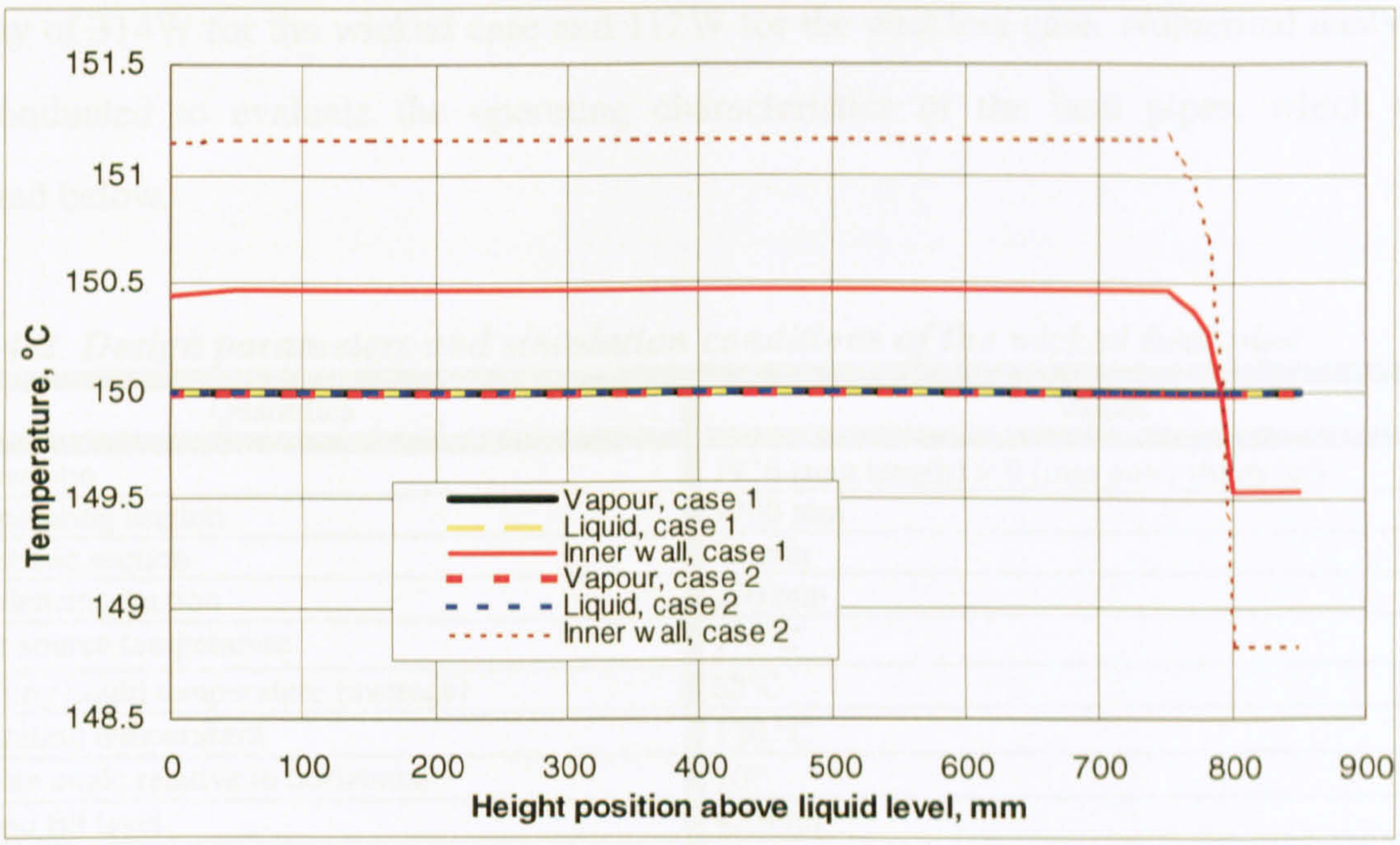

Figure 4-7. Variation of liquid, vapour and wall temperatures with height position – the miniature heat pipes

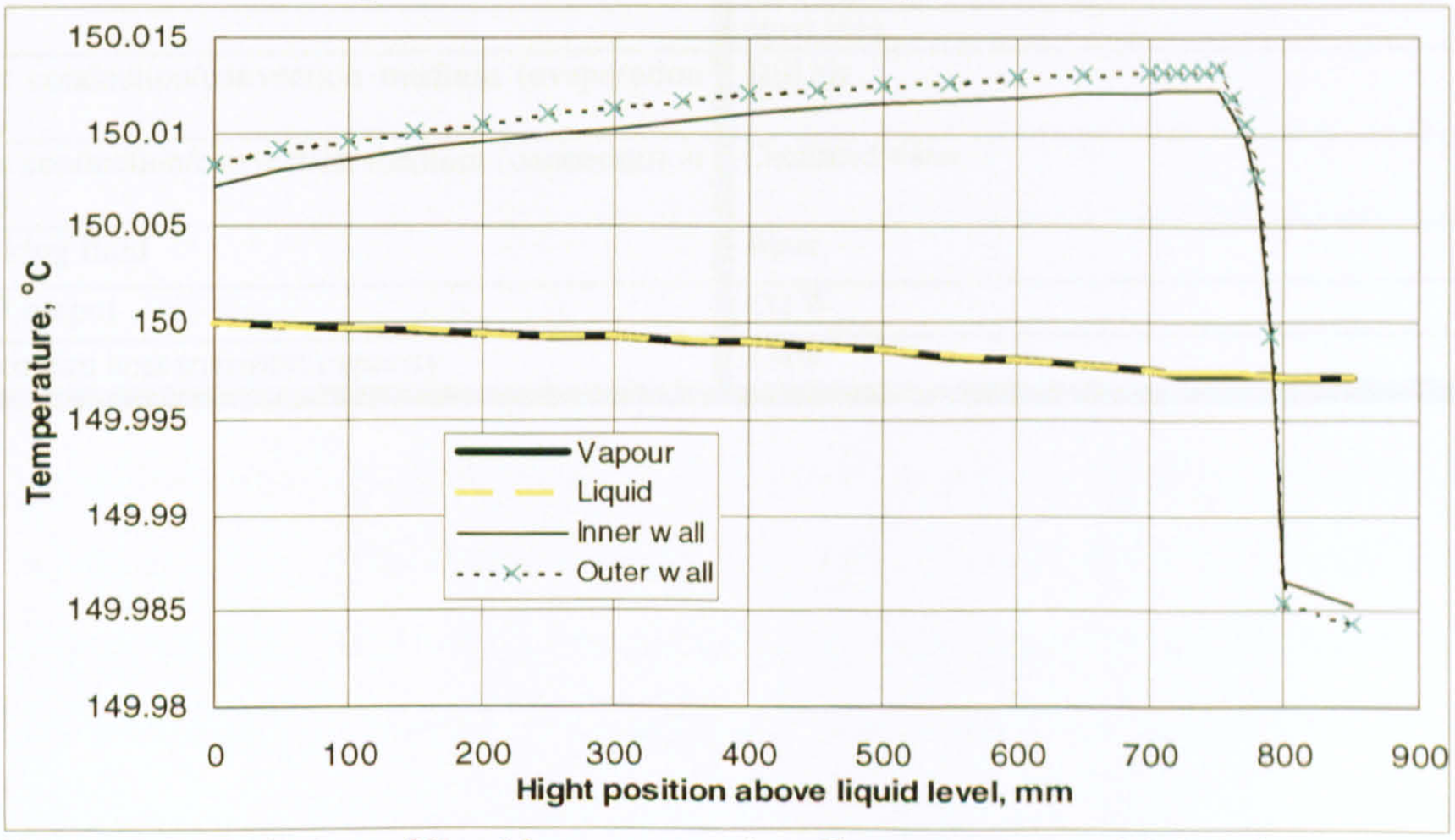

Figure 4-8. Variation of liquid, vapour and wall temperature with height position – the mini heat pipe

4.2.2 Normal Heat Pipes

Two normal heat pipes were investigated; one is a 1.97m long heat pipe, which was internally fitted with 2 wraps of copper screen meshes, as the wicks, and the other is a 0.5m long wickless (gravitational) heat pipe. For both wicked and wickless heat pipes, the design parameters and simulation conditions were all determined purposely to follow up the experimental constraints, which are detailed in Table 4-2 and Table 4-3 respectively. The calculations using the analytical model of Chapter 3 gave the maximum heat transport capacity of 314W for the wicked case and 112W for the wickless case. Numerical analysis was conducted to evaluate the operating characteristics of the heat pipes, which are indicated below.

Table 4-2. Design parameters and simulation conditions of the wicked heat pipe

Quantities	Values
Dimension	1970 (mm length) × 8 (mm outer diameter)
Evaporating section	1700 mm
Adiabatic section	70 mm
Condensing section	200 mm
Heat source temperature	170°C
Cooling liquid temperature (average)	68°C
Operating temperature	120 °C
Incline angle relative to horizontal	20°
Liquid fill level	425mm
Pipe material/ thickness	Copper, 0.376mm
Wick structure	Copper, screen, 2 wraps, 150 mesh count, 0.06mm wire diameter, 0.109mm×0.109mm aperture size, 42% open area.
Heat conduction/convection medium (evaporation section)	Still air
Heat conduction/convection medium (condensation section)	Circulated water
Working fluid	Water
Heat output	132 W
Maximum heat transport capacity	314W

Table 4-3. Design parameters and simulation conditions of the wickless heat pipe

Quantities	Values
Dimension	500 (mm length) × 8 (mm outer diameter)
Evaporating section	330 mm
Adiabatic section	25 mm
Condensing section	145 mm
Heat source temperature	85°C
Cooling liquid temperature (average)	45°C
Operating temperature	80 °C
Incline angle relative to horizontal	90°
Liquid fill level	80mm
Pipe material/ thickness	Copper, 0.5mm
Heat conduction/convection medium (evaporation section)	Hot water, 85°C
Heat conduction/convection medium (condensation section)	Circulated water
Working fluid	Water
Heat output	60 W
Maximum heat transport capacity	112W

Variation of liquid and vapour flows

Figures 4-9, 4-10, 4-11 and 4-12 indicate the behaviour of the liquid and vapour flows within the wicked and wickless heat pipes. Two pipes show very similar trend on flow characteristics. In the condensation section, vapour velocity decreases along the flow direction (upward), and liquid velocity increases along the flow direction (downward), due to a dramatic condensation. Even so, liquid cross-sectional area still increases along the liquid flow direction (downward), resulting in the decrease of vapour cross-sectional area. This is because liquid flow is not fast enough to remove condensed liquid promptly.

In the adiabatic section, liquid and vapour cross-sectional areas, as well as flow velocities, remain constant along the flow direction. This is because no heat transfer occurred in this area due to a high insulation level.

In the evaporation section, vapour and liquid flows behave in contrast with that in the condensation section. On the interface of the evaporation section and the adiabatic section, liquid volume achieves its maximum value, resulting in the maximum liquid cross-sectional area and the minimum vapour cross-sectional area. Along the liquid flow direction (downward), some of the liquid absorbs heat striking on the heat pipe outer surface and is

vaporized, and the other keeps the flow trend along the pipe inner wall. The velocity of liquid flow, as well as the liquid cross-sectional area, decrease along its flow direction (downward), due to the decrease of liquid volume. Consequently, vapour cross-sectional area decreases along the flow direction (upward).

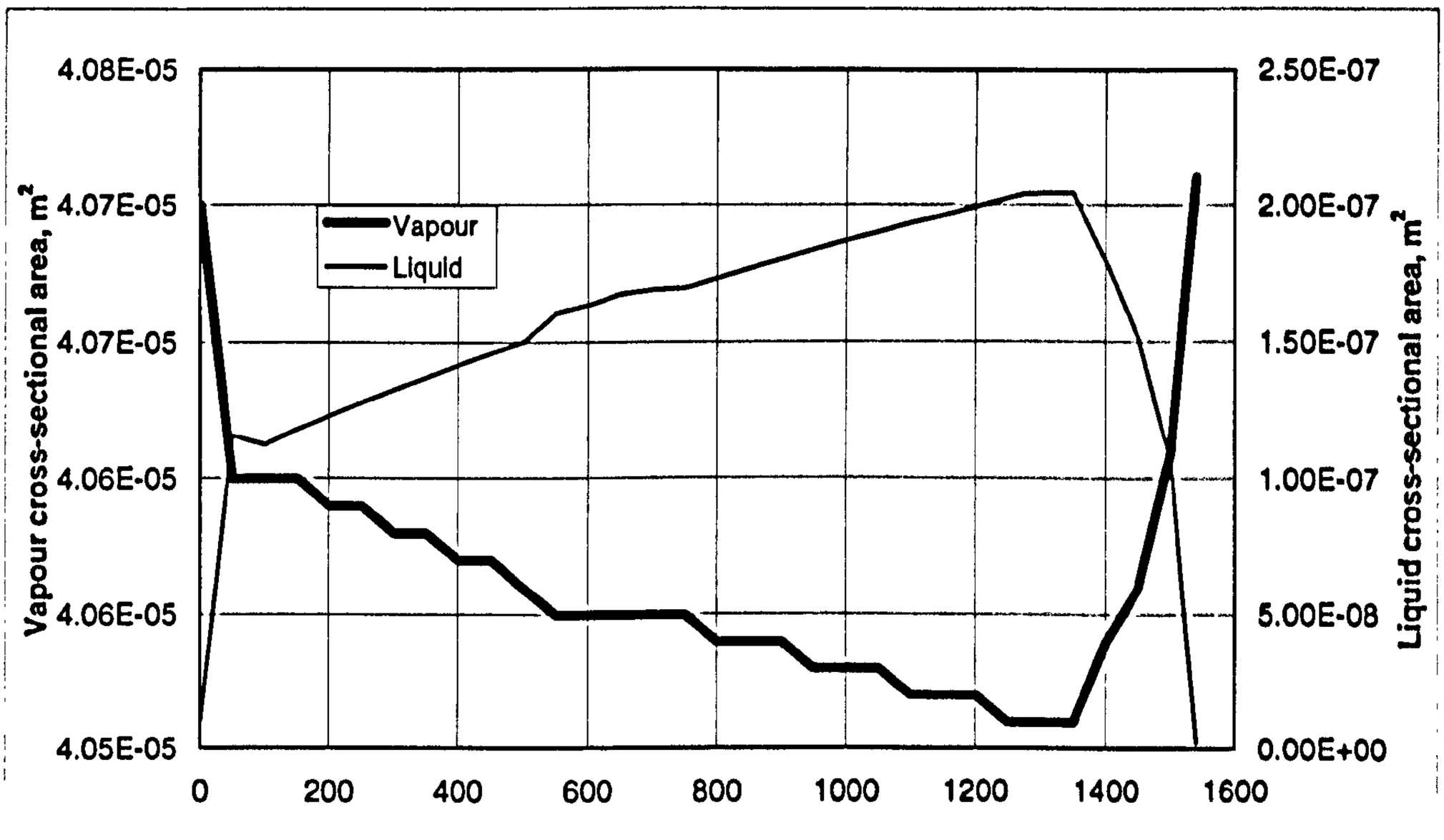

Figure 4-9. Variation of vapour and liquid cross-sectional areas along the height above the filled liquid level-the wicked heat pipe

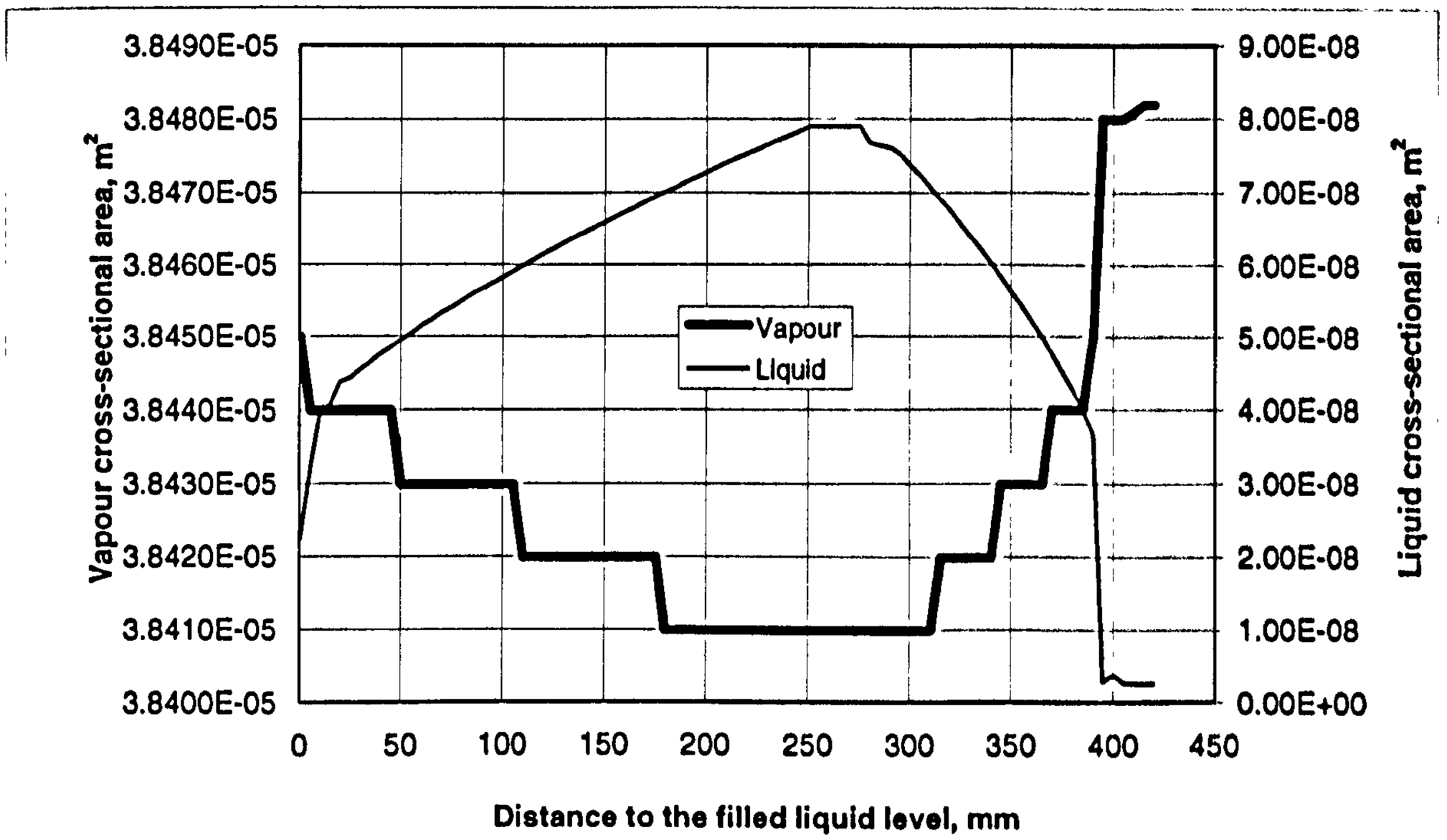

Figure 4-10. Variation of vapour and liquid cross-sectional areas along the height above the filled liquid level-the wickless heat pipe

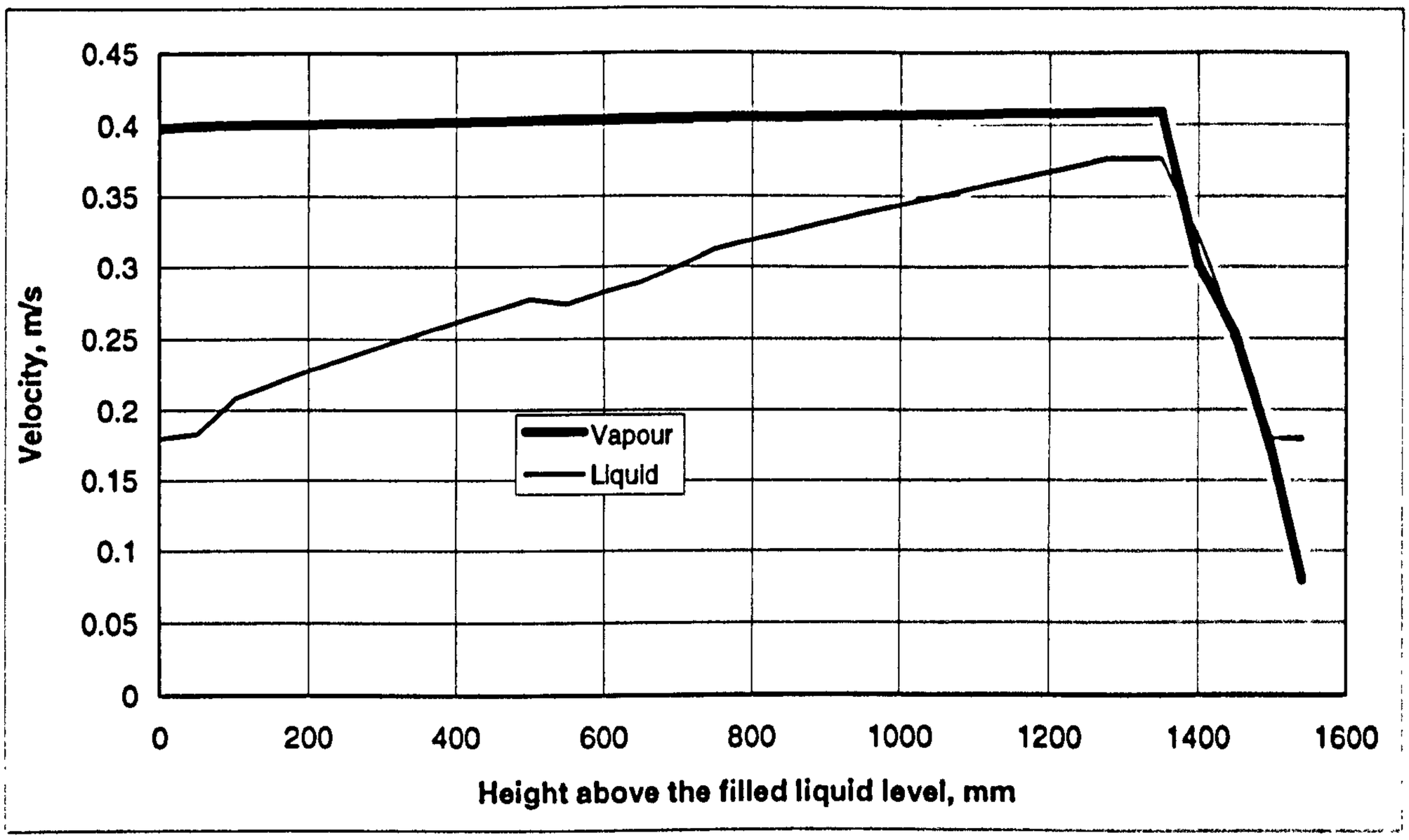

Figure 4-11. Variation of vapour and liquid velocities (axial/average) along the height above the filled liquid level – the wicked heat pipe

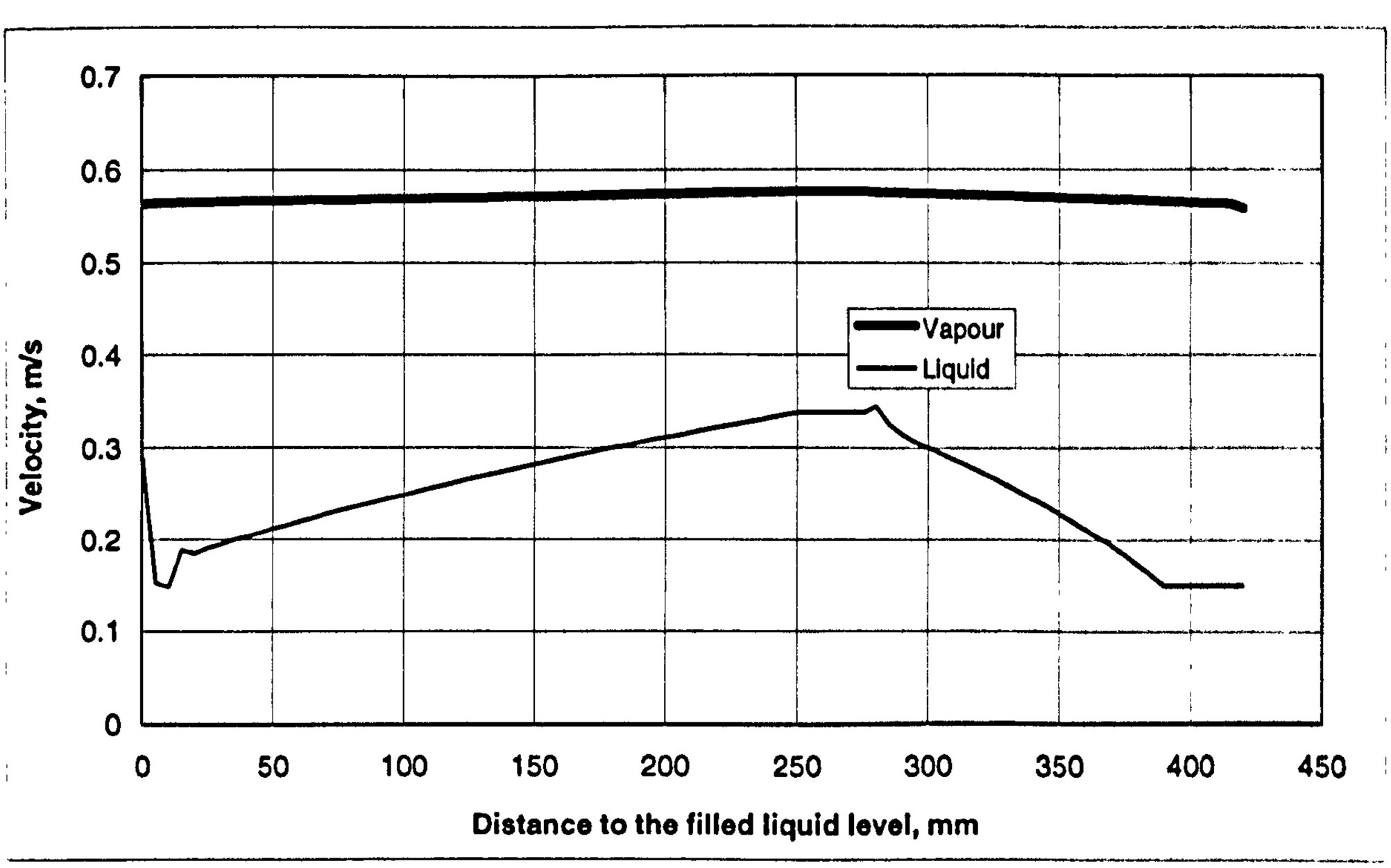

Figure 4-12. Variation of vapour and liquid velocities (axial/average) along the height above the filled liquid level – the wickless heat pipe

Figures 4-13 and 4-14 show the variation of axial vapour velocities with height position above the filled liquid level for the wicked and wickless pipes. Both pipes also show

similar trend for vapour velocity profiles. In the same cross section, the axial velocity is higher in the central area, and lower in the boundary area. The variation of the velocity across radial direction shows a parabolic shape. Along the height position, the axial velocity increases slightly in the evaporation section, remains constant in the adiatic section, but decreases significantly in the condensation section due to a relatively shorter condensing distance.

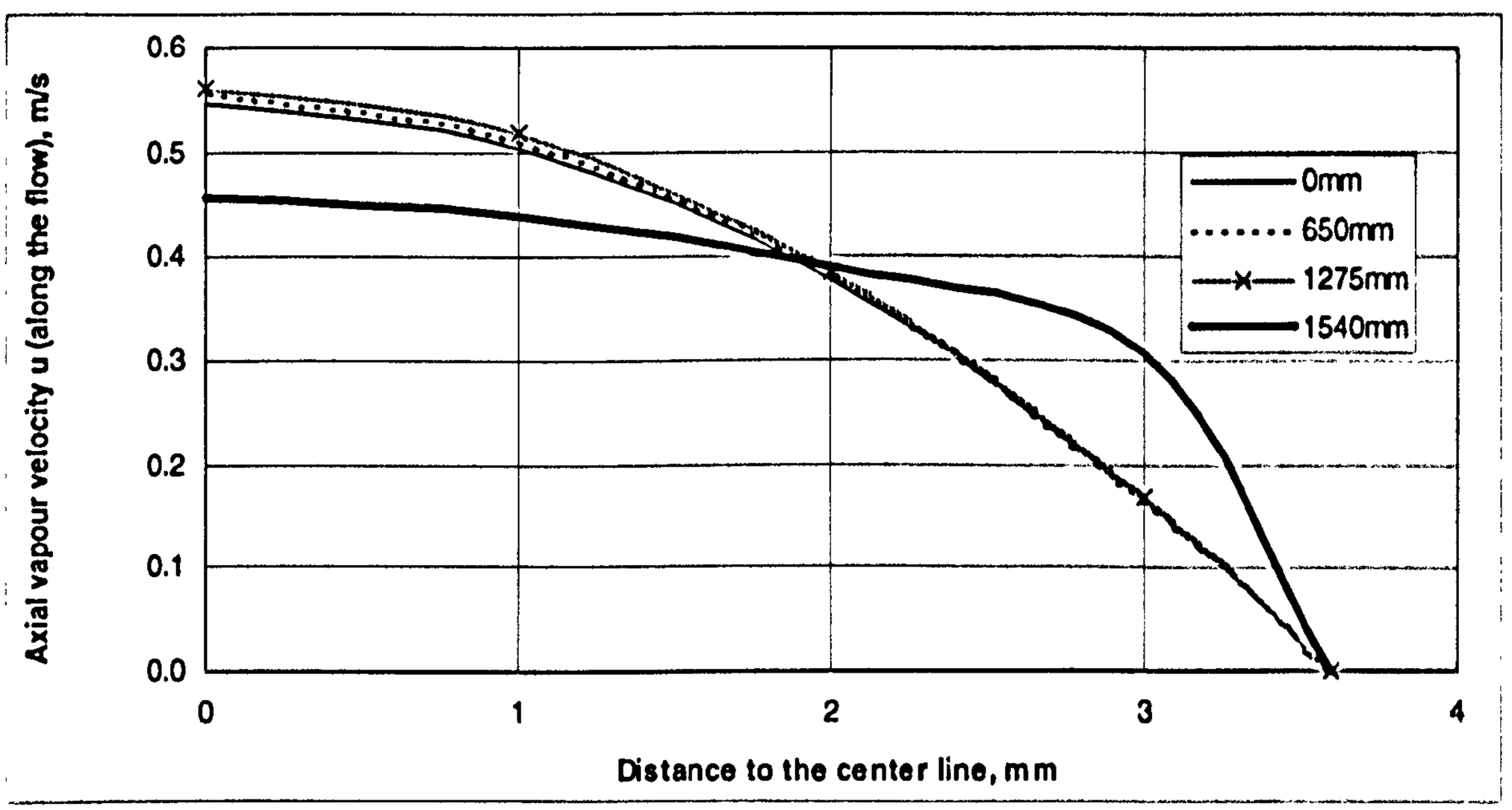

Figure 4-13. Variation of axial vapour velocity across the radial direction - the wicked heat pipe

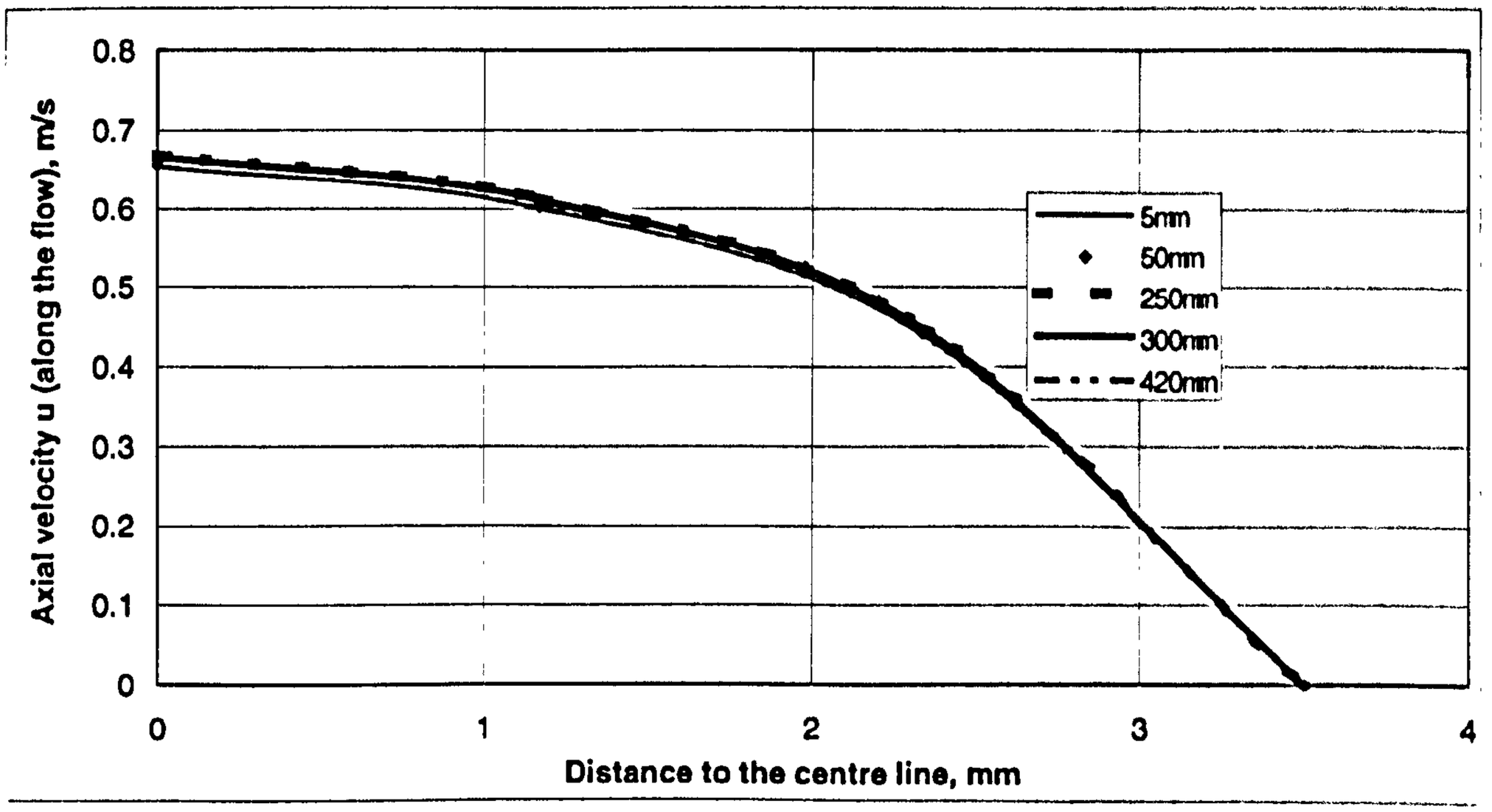

Figure 4-14. Variation of axial vapour velocity across the radial direction - the wickless heat pipe

Figures 4-15 and 4-16 shows the variation of radial vapour velocity along radial direction at different height positions (above the filled liquid level). In the evaporation section, the radial flow velocity is negative and its absolute value decreases gradually from the periphery to the centre area, which means an inward flow exists due to a constant injection from the interface of liquid/vapour phases. In the adiabatic section, the radial flow velocity is zero, which means no radial flow exists due to absence of injection/ejection on the interface of liquid/vapour phases. In the condensation section, the radial velocity becomes postive and its absolute value increases gradually from the central area to the periphery, which means an outward flow exists due to a constant ejection from the interface of the liquid/vapour phases.

However, a slight difference exists between the wicked and wickless pipes. The wickless one has a higher vapour velocity than the wicked one. This is because the wickless pipe has a relatively smaller cross-sectional area, and a larger heat intensity on per unit of absorbing surface.

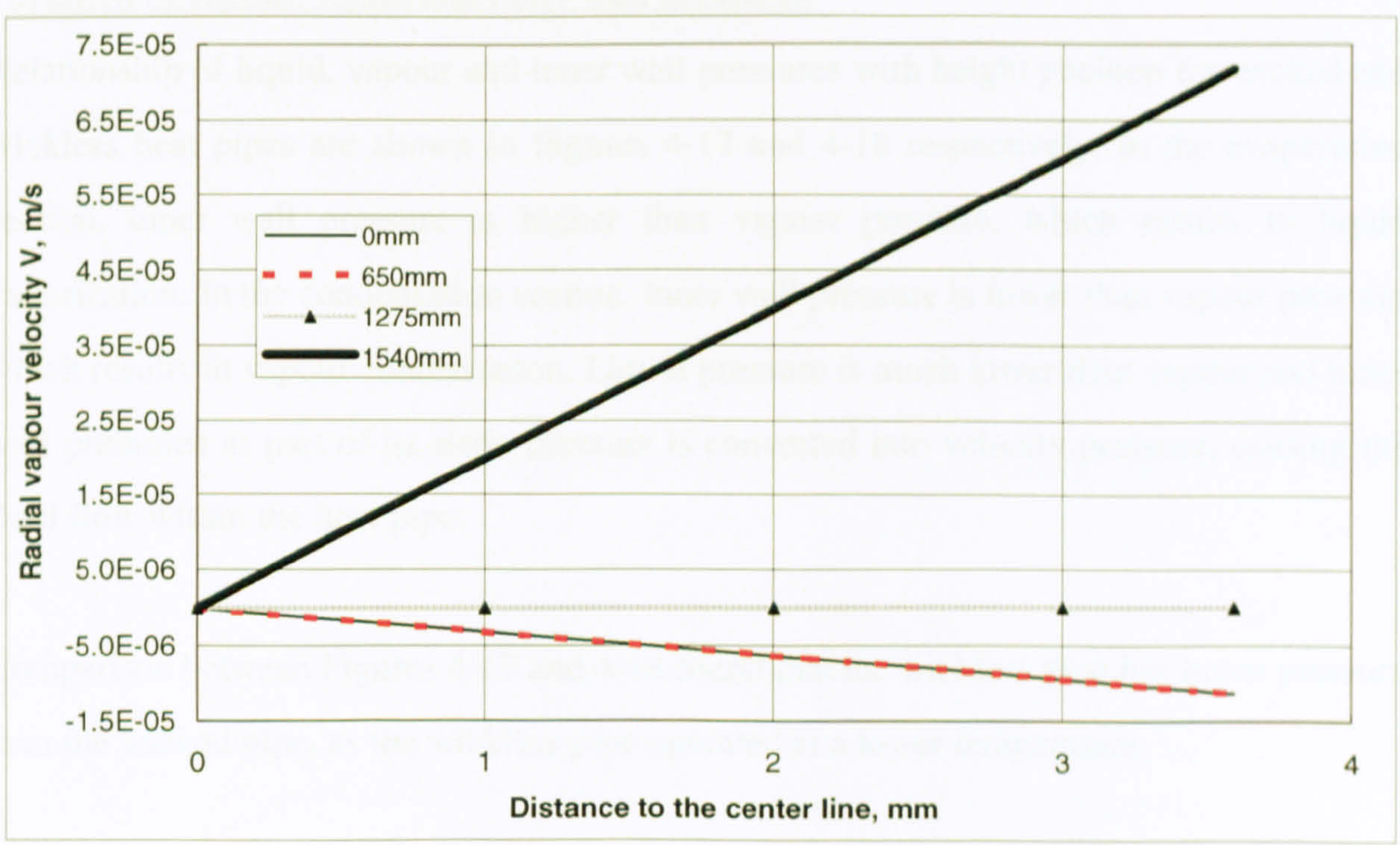

Figure 4-15. Variation of radial vapour velocity across radial direction – the wicked heat pipe

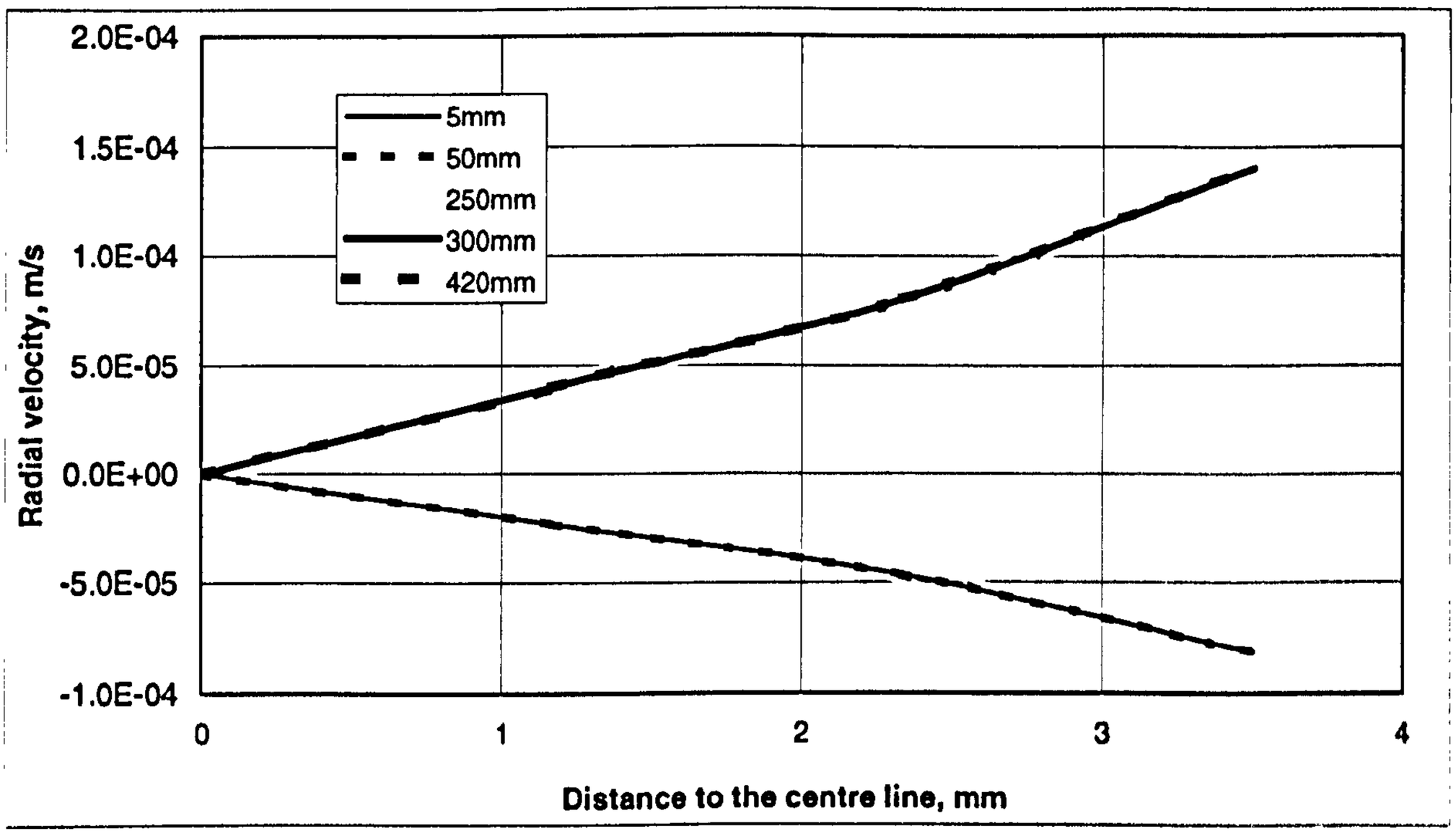

Figure 4-16. Variation of radial vapour velocity across radial direction – the wickless heat pipe

Variation of vapour, liquid and inner wall pressures

Relationship of liquid, vapour and inner wall pressures with height position for wicked and wickless heat pipes are shown in Figures 4-17 and 4-18 respectively. In the evaporation section, inner wall pressure is higher than vapour pressure, which results in liquid vaporization. In the condensation section, inner wall pressure is lower than vapour pressure, which results in vapour condensation. Liquid pressure is much lower than vapour and inner wall pressures as part of its static pressure is converted into velocity pressure, causing the fluid flow within the heat pipe.

Comparison between Figures 4-17 and 4-18 found that the wickless pipe has lower pressure than the wicked pipe, as the wickless pipe operated at a lower temperature.

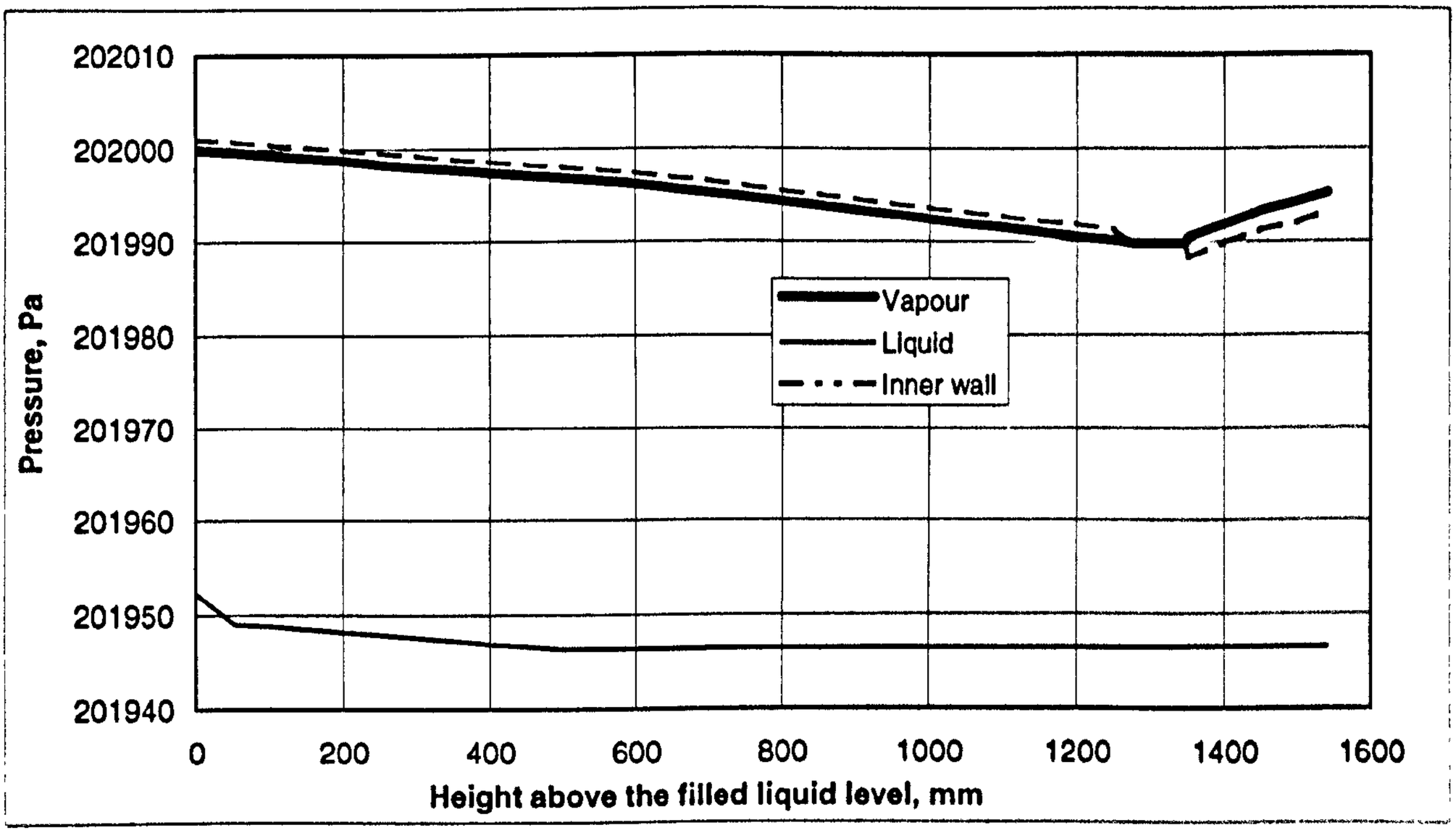

Figure 4-17. Variation of vapour, liquid and inner wall pressures along the position above the filled liquid level - the wicked heat pipe

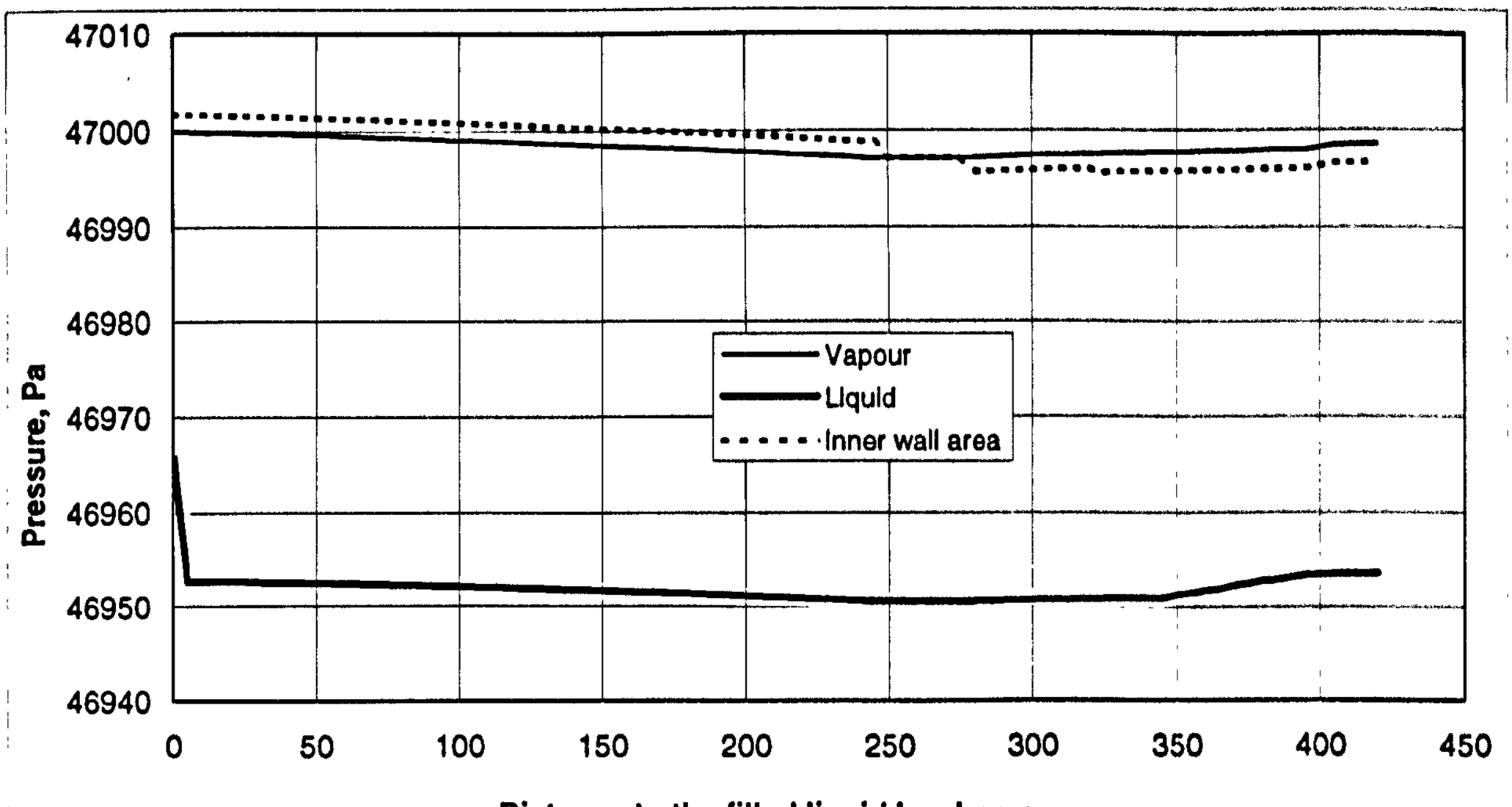

Figure 4-18. Variation of vapour, liquid and inner wall pressures along the position above the filled liquid level - the wickless heat pipe

Variation of temperatures

Variations of the temperatures of vapour, liquid, wall, heat/cool sources and heat conduction/convection mediums with height position for the wicked and wickless pipes are shown in Figures 4-19 and 4-20 respectively. There are very little differences among vapour, liquid and wall temperatures, compared to the differences of vapour (liquid or wall) and heat/cool sources and heat conduction/convection mediums. This demonstrates that both of the heat pipes are excellent heat transfer devices, and operate at an approximately constant temperature. The major heat resistances occur in the heat conduction/convection mediums, which result in significant variation of temperature within these areas. For the wicked case, the heat conduction/convection mediums are the still air filled in the heating element vessel in the evaporation section, and the cooling water circulated through water jacket in the condensation section. For the wickless case, the heat conduction/convection mediums are the same as the heating/cooling sources, i.e., hot water at 85°C within an insulated vessel and cold water at 45°C (average) within a water jacket.

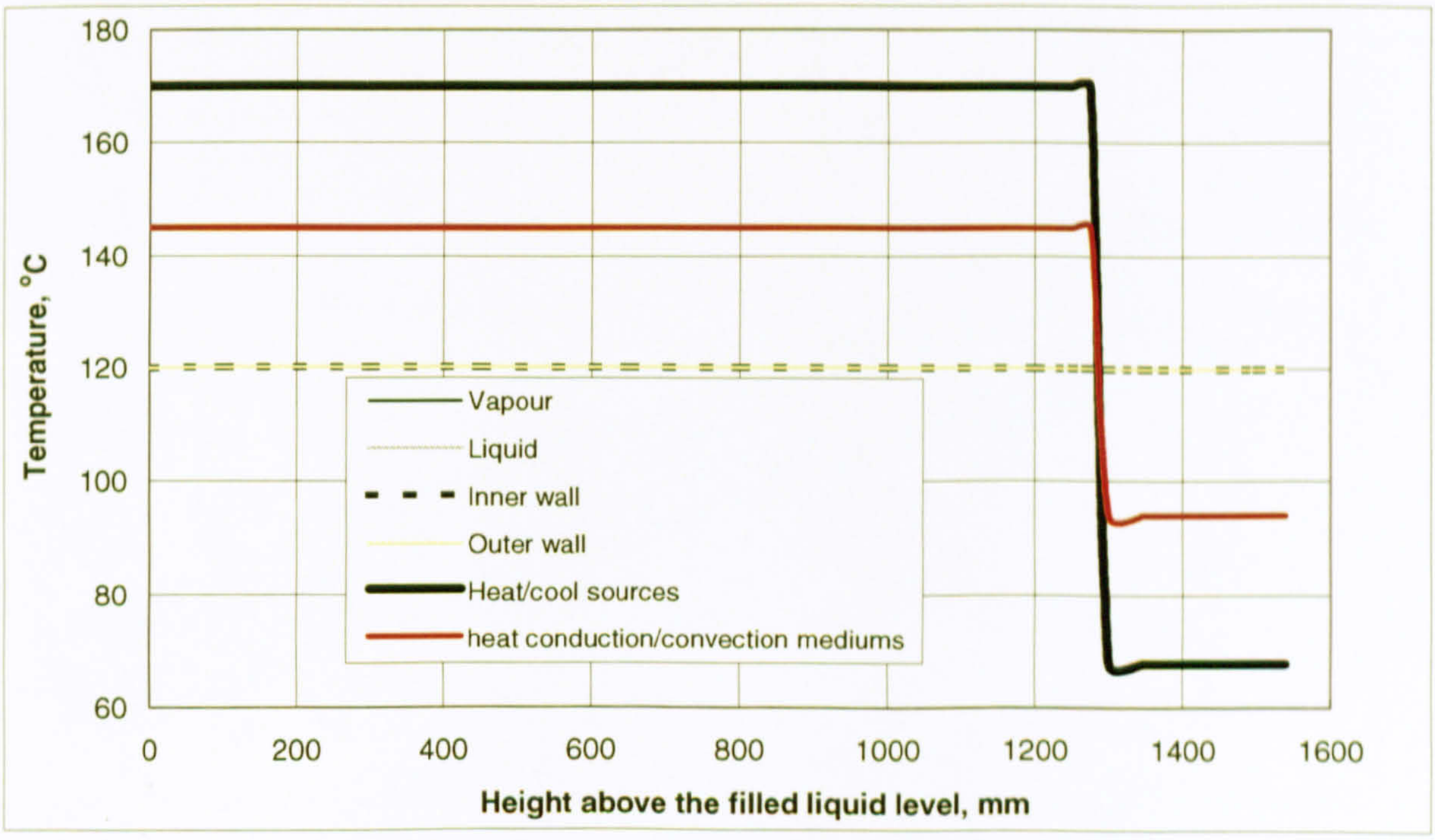

Figure 4-19. Variation of temperatures along the height position above the filled liquid level - the wicked heat pipe

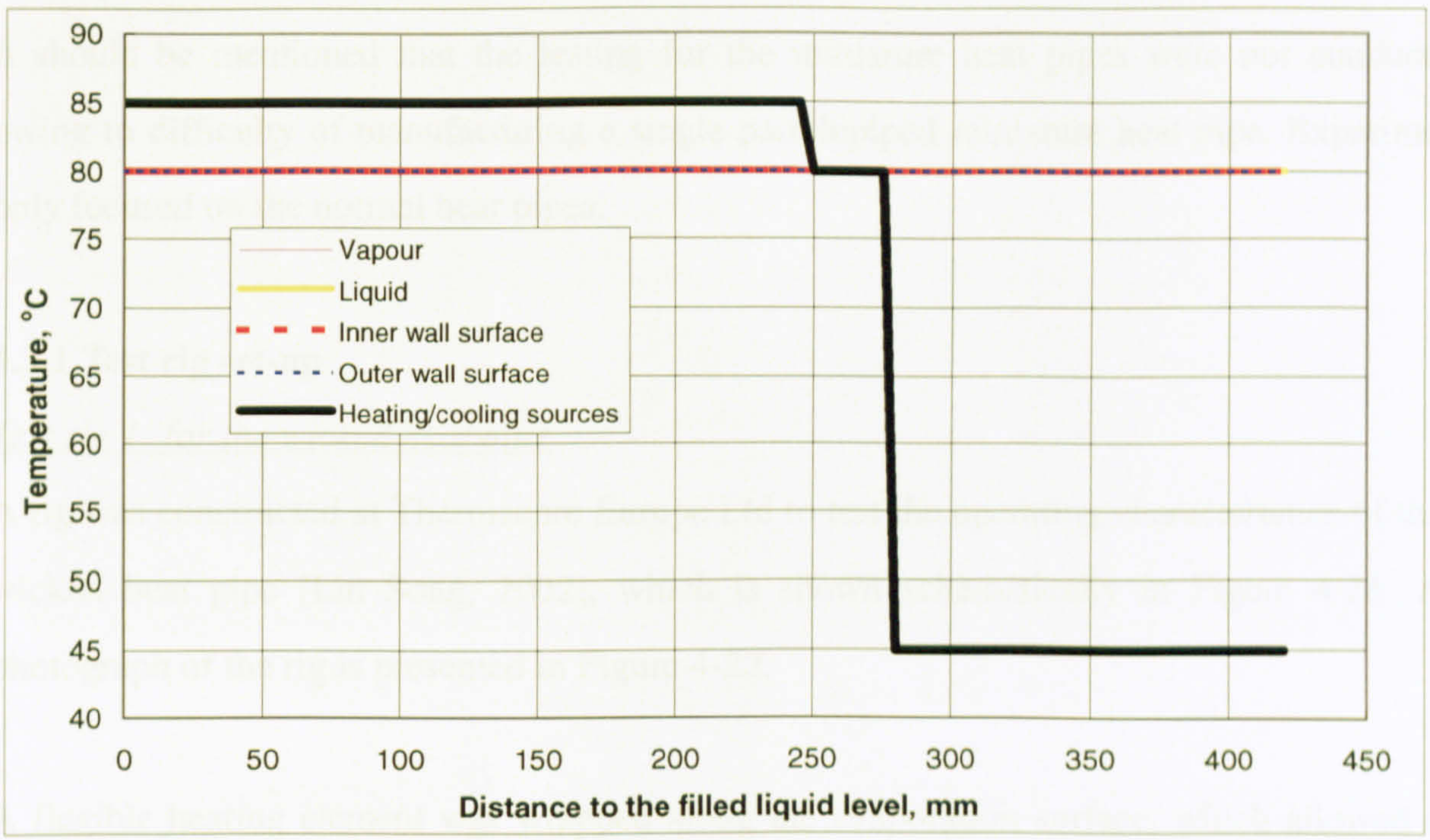

Figure 4-20. Variation of temperatures along the height position above the filled liquid level - the wickless heat pipe

4.3 Experimental testing of the selected heat pipes

It should be mentioned that the testing for the miniature heat pipes were not conducted owing to difficulty of manufacturing a single parrelepiped miniature heat pipe. Experiment only focused on the normal heat pipes.

4.3.1 Test rig set-up

Test rig 1- for the wicked heat pipe

A rig was constructed at Thermacore Europe Ltd to test the operating characteristics of the wicked heat pipe [Lin Song, 2002], which is shown schematically in Figure 4-21. A photograph of the rig is presented in Figure 4-22.

A flexible heating element was wrapped along the evaporation surface, which allowed a gap to exist between the heat pipe outer-surface and the heating element inner-surface in order to create an identical heat input over the evaporator area. Insulation was covered outside the heating element to reduce heat loss to the environment. The heating output of the element was controlled by a Variac.

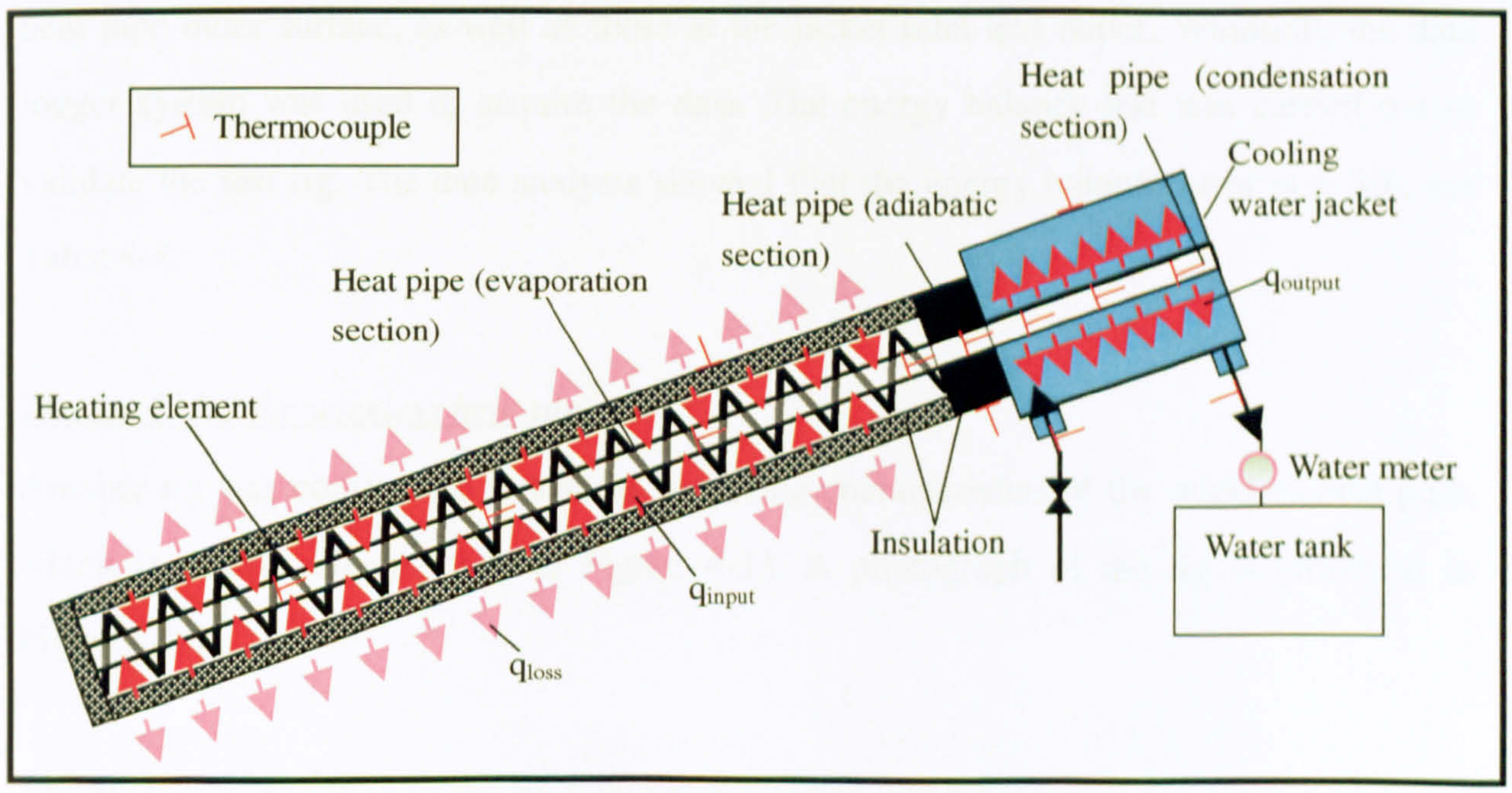

Figure 4-21. Schematic diagram showing the principle and layout of the test rig for the wicked pipe

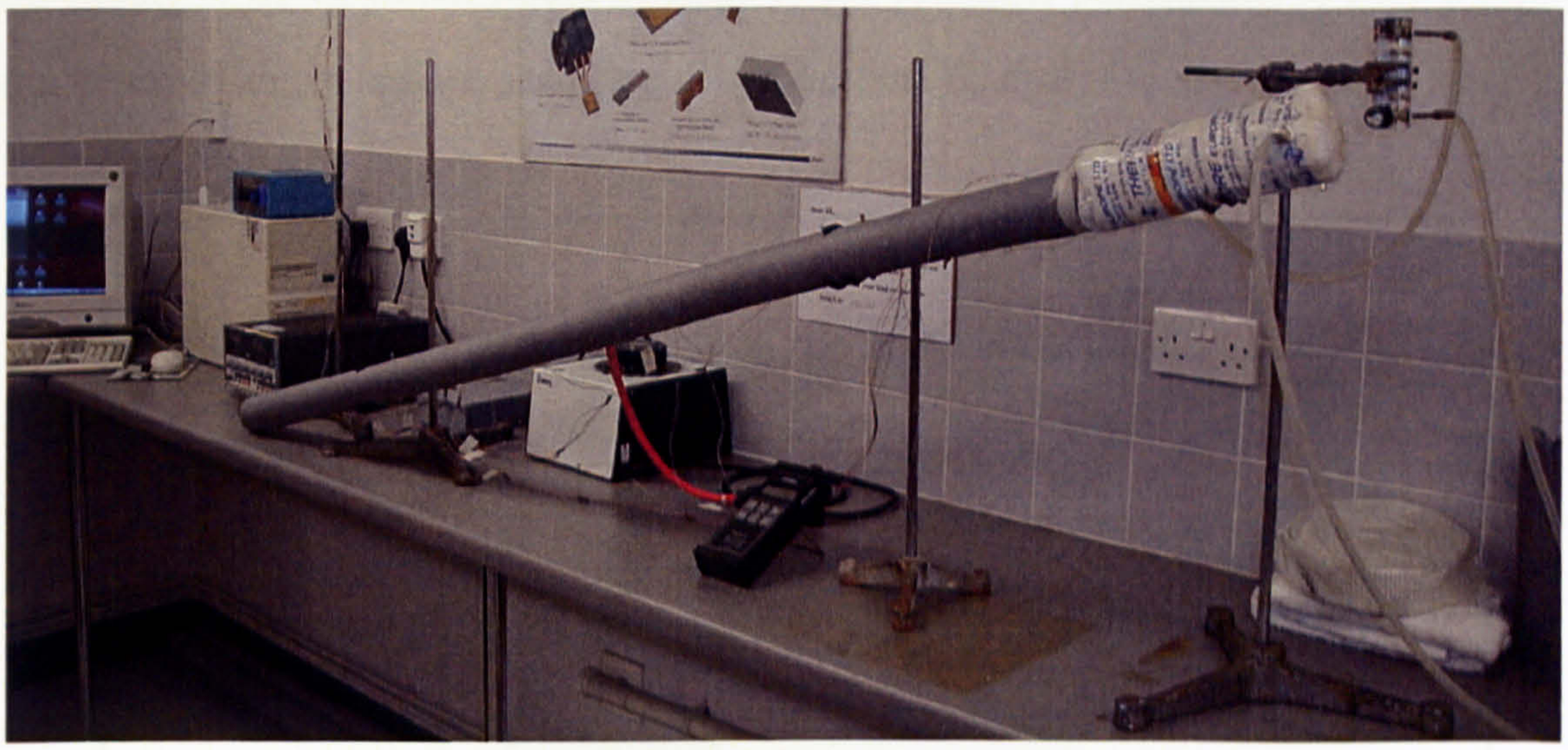

Figure 4-22. View of the test rig - for the wicked heat pipe

The condensation section of the heat pipe is inserted into a water-cooled jacket, which is connected to a cooling water tank on the outlet end and a water tap on the inlet end, as shown in Figure 4-21. A volume-additive water meter is mounted to measure the water flow rate, by giving the overall flow volume and time duration of the testing.

T-type thermocouples were mounted to measure the temperatures of a few points on the heat pipe outer surface, as well as those at the jacket inlet and outlet. Windmill, the data logger system was used to acquire the data. The energy balance test was carried out to validate the test rig. The data analysis showed that the energy balance error is ± 3%, see Table 4-4.

Test rig 2- for the wickless heat pipe

Another rig was constructed to test the operating characteristics of the wickless heat pipe, which is shown schematically in Figure 4-23. A photograph of the rig is presented in Figure 4-24.

The evaporation section of the heat pipe was inserted into a hot water container, which was insulated and connected to a water heater. The water heater produced hot water at

temperature of 85°C, which would be filled to the container periodically to keep a constant temperature in the container, resulting in a periodical discharge of the container water.

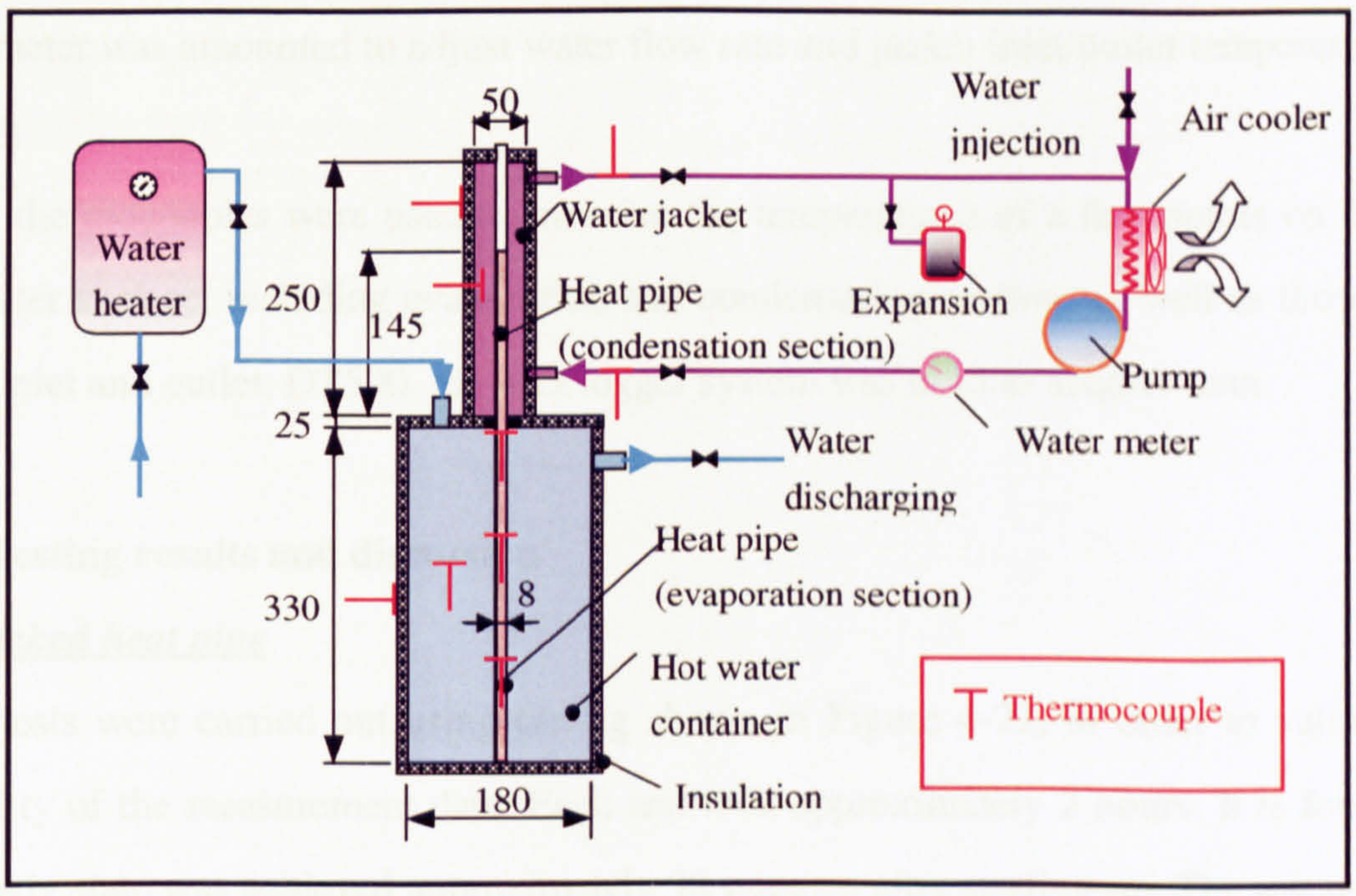

Figure 4-23. Schematic diagram showing the principle and layout of the test rig for the wickless pipe

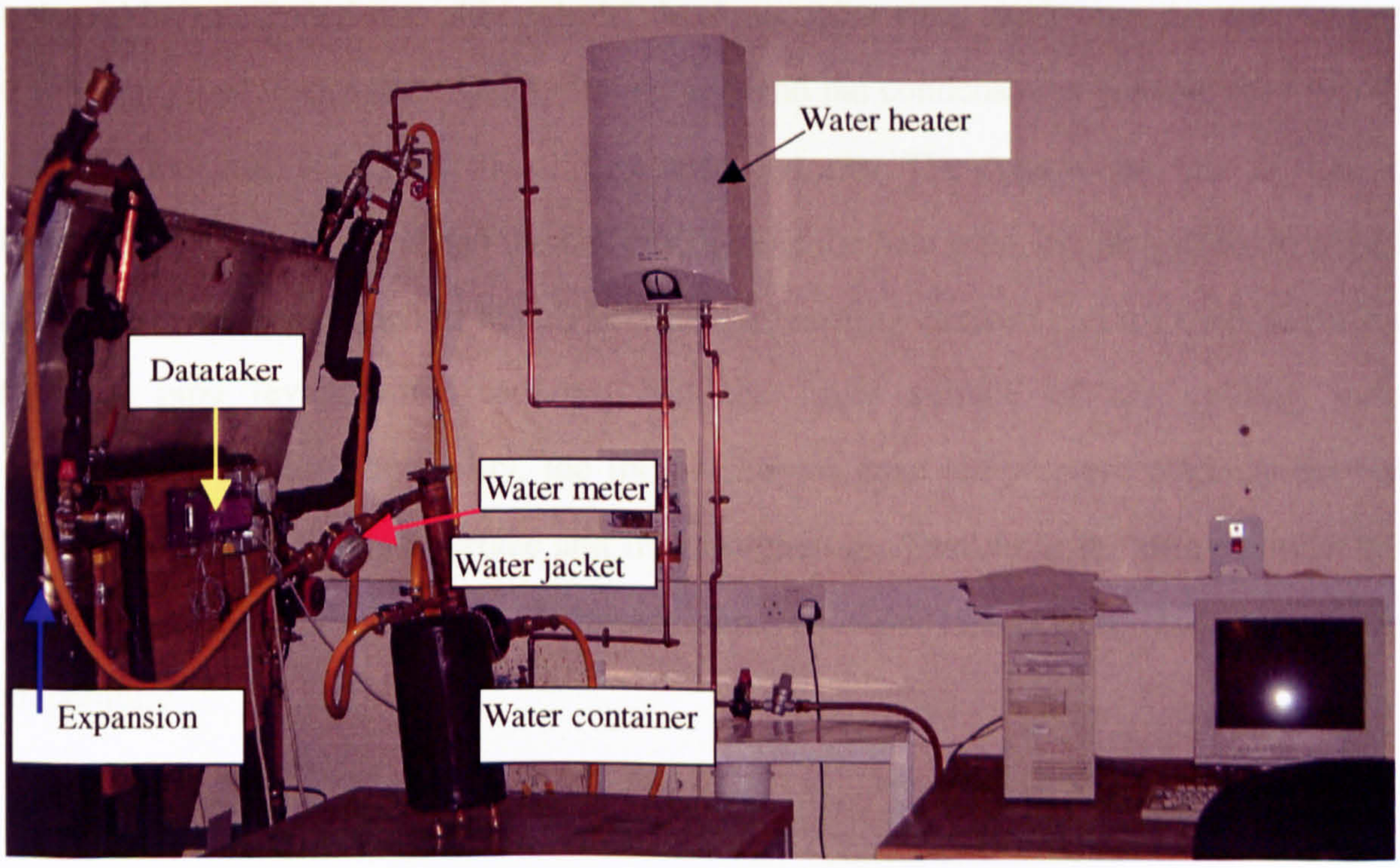

Figure 4-24. View of the test rig – for the wickless heat pipe

The condensation section of the heat pipe was inserted into a water-cooled jacket, which was connected to a cooling water loop, as shown in Figure 4-23. An air cooler was used to remove heat away from the heat pipe, and a pump used to run the circulation. A single-jet water meter was amounted to adjust water flow rate and jacket inlet/outlet temperatures.

T-type thermocouples were used to measure the temperatures of a few points on the heat pipe outer surface, including evaporation and condensation section, as well as those at the jacket inlet and outlet. DT500, the data logger system was used to acquire data.

4.3.2 Testing results and discussion

The wicked heat pipe

Three tests were carried out using the rig shown in Figure 4-22, in order to validate the reliability of the measurement data. Each test took approximately 2 hours. It is found that the steady state was achieved approximately 30 minutes after starting-up. The test results at the steady state were recorded, which are detailed in Table 4-4.

It should be mentioned that although the thermocouples were stuck onto the outer surface of the heat pipe either at the evaporation section and the condensation section, they still did not give the real values of the surface temperatures. The reason for this is that the thermocouples not only touched the outer surface of the heat pipe, but also were exposed to surrounding mediums, such as hot air between the heating element and the outer surface of the heat pipe (evaporation section), and the inner surface of the cooling jacket (condensation section). In reality, the thermocouples gave temperature readings between that for the heat pipe outer surface and its surroundings. Therefore, the measurement data should be the values that are between outer surface temperature and surrounding temperature.

Table 4-4 Energy balance and performance test data for the wicked heat pipe

Test No. Items	1	2	3
Ambient temperature,°C	23.60	23.46	23.50
HP evaporator temperature 1,°C	128.43	129.78	107.32
HP evaporator temperature 2, °C	137.03	138.22	114.56
HP evaporator temperature 3, °C	138.92	139.97	114.80
HP evaporator temperature 4, °C	138.64	139.99	116.90
Mean HP evaporator temperature, °C	135.76	136.99	113.39
Insulation layer temperature at HP evaporator, °C	64.11	64.36	55.81
HP adiabatic section temperature, °C	121.16	122.57	101.08
HP condenser temperature 1, °C	112.17	113.82	94.18
HP condenser temperature 2, °C	110.75	111.82	92.46
HP condenser temperature 3, °C	110.62	111.30	91.91
Mean HP condenser temperature, °C	111.18	112.31	92.85
Insulation layer temperature at HP condenser, °C	51.89	52.78	45.09
HP ΔT between evaporator and condenser, °C	24.57	24.68	20.54
Inlet temperature of cooling water, °C	39.80	41.39	36.55
Outlet temperature of cooling water, °C	95.34	95.53	78.38
Heater temperature, °C	175.8	173.2	150.4
Flow rate, CCM	35	35	35
Heat power, W	171.43	171.43	133.52
Estimated Heat loss, W	33.76	34.19	26.77
Power loss by water cooling, W	135.44	132.05	102.03
Energy balance error, %	1.31	3.03	2.54

<u>The wickless heat pipe</u>

Two tests were carried out using the rig shown in Figure 4-24. Each test took approximately 2 hours. It was found that the steady state was achieved approximately 20 minutes after starting-up. Similar to the case for the wicked heat pipe, the test results at the steady state were recorded, which are detailed in Table 4-5.

Similar to the situation of the wicked heat pipe, the thermocouple readings were at temperatures between that of the heat pipe outer surface and its surroundings.

Table 4-5. Energy balance and performance test data for the wickless heat pipe

Test No. Items	1	2
Ambient temperature,°C	22.48	21.98
HP evaporator temperature 1,°C	80.56	80.65
HP evaporator temperature 2, °C	80.64	80.68
HP evaporator temperature 3, °C	80.89	80.97
Mean HP evaporator temperature, °C	80.7	80.76
Insulation layer temperature at HP evaporator, °C	38.76	38.82
HP adiabatic section temperature, °C	79.1	79.24
HP condenser temperature 1, °C	76.17	76.21
HP condenser temperature 2, °C	76.06	76.1
HP condenser temperature 3, °C	76	76.04
Mean HP condenser temperature, °C	76.08	76.12
Insulation layer temperature at HP condenser, °C	25.36	25.38
HP ΔT between evaporator and condenser, °C	4.62	4.64
Inlet temperature of cooling water, °C	35.80	36
Outlet temperature of cooling water, °C	44.39	44.39
Heater temperature, °C	85	85
Flow rate, CCM	100	100
Heat power, W	60.75	59.502
Estimated Heat loss, W	0.81	0.952
Power loss by water cooling, W	59.94	58.55
Energy balance error, %	1.33	1.6

4.4 Comparison of Numerical Predictions and Testing Results

Comparisons between numerical predictions and testing results were made, as shown in Figures 4-25 (for the wicked pipe) and 4-26 (for the wickless pipe) respectively. For the wicked heat pipe, the results from tests 1 & 2 are in good agreement with numerical prediction as the test conditions are very close to the simulation assumptions. However, results from test 3 are away from the numerical predictions, as the test conditions are different from the simulation assumption. For the wickless heat pipe, the results from both tests 1 and 2 are in general agreement with the numerical prediction due to approximacy between the test conditions and the simulation assumptions.

Figures 4-25 and 4-26 display the data measured from the thermocouples on the outer surface of the heat pipes, as well as the numerical temperature values of outer surface, surrounding fluids (heat transfer fluids) and heat/cooling sources. It was found that the data given by the thermocouples are between heat pipe outer surface temperatures and surrounding temperatures, a little close to the surface temperatures.

This testing was constrained to temperature due to difficulty in testing any other parameters (pressure, velocity, flow distribution) for heat pipe operation using the rigs above. Therefore, further comparison of numerical predictions and experimental results is not possible. However, the comparison for temperature has already demonstrated that the numerical model is able to predict operating characteristics of both wicked and wickless heat pipes with a reasonable accuracy.

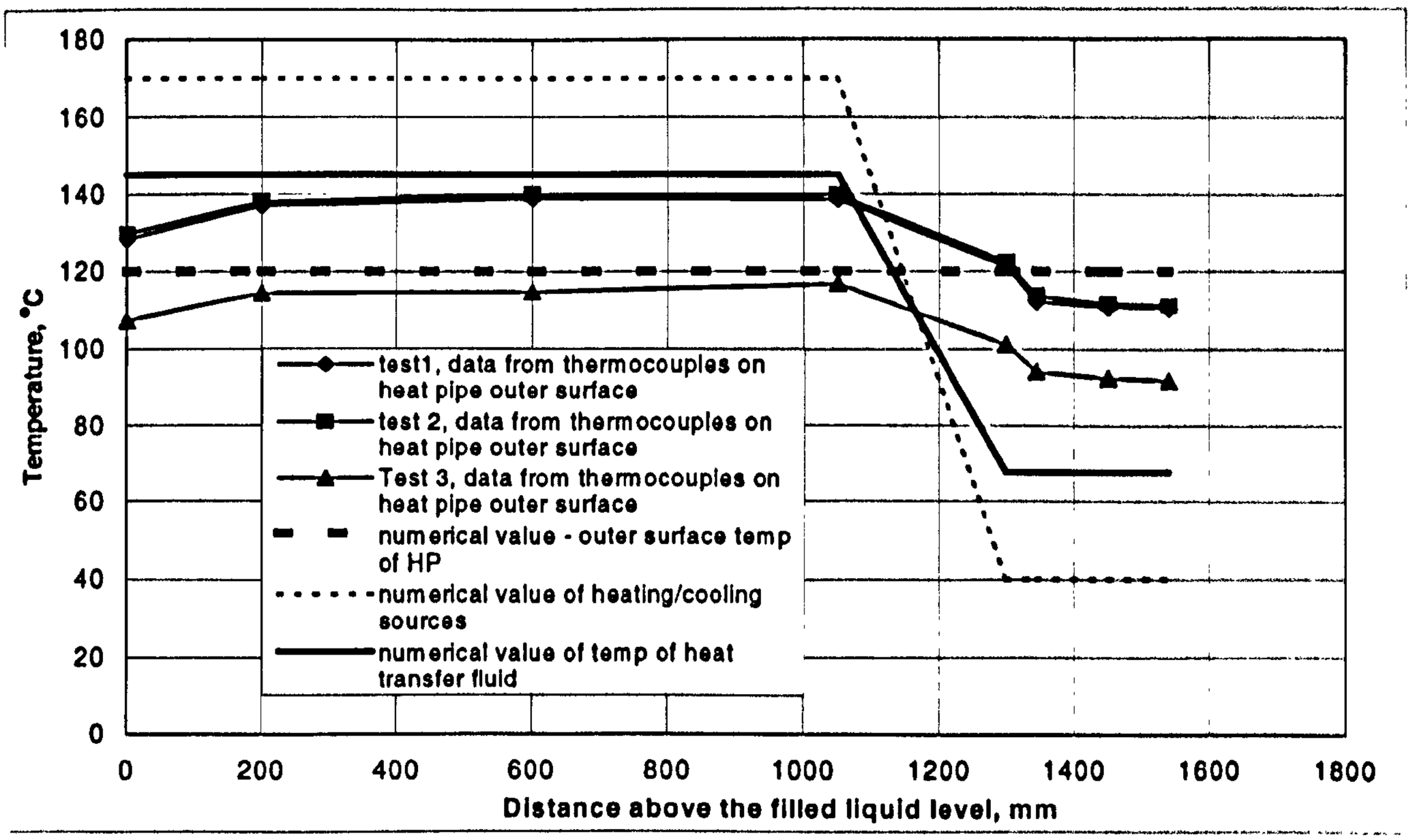

Figure 4-25. Comparison of numerical and experimental results for temperature profile – the wicked heat pipe

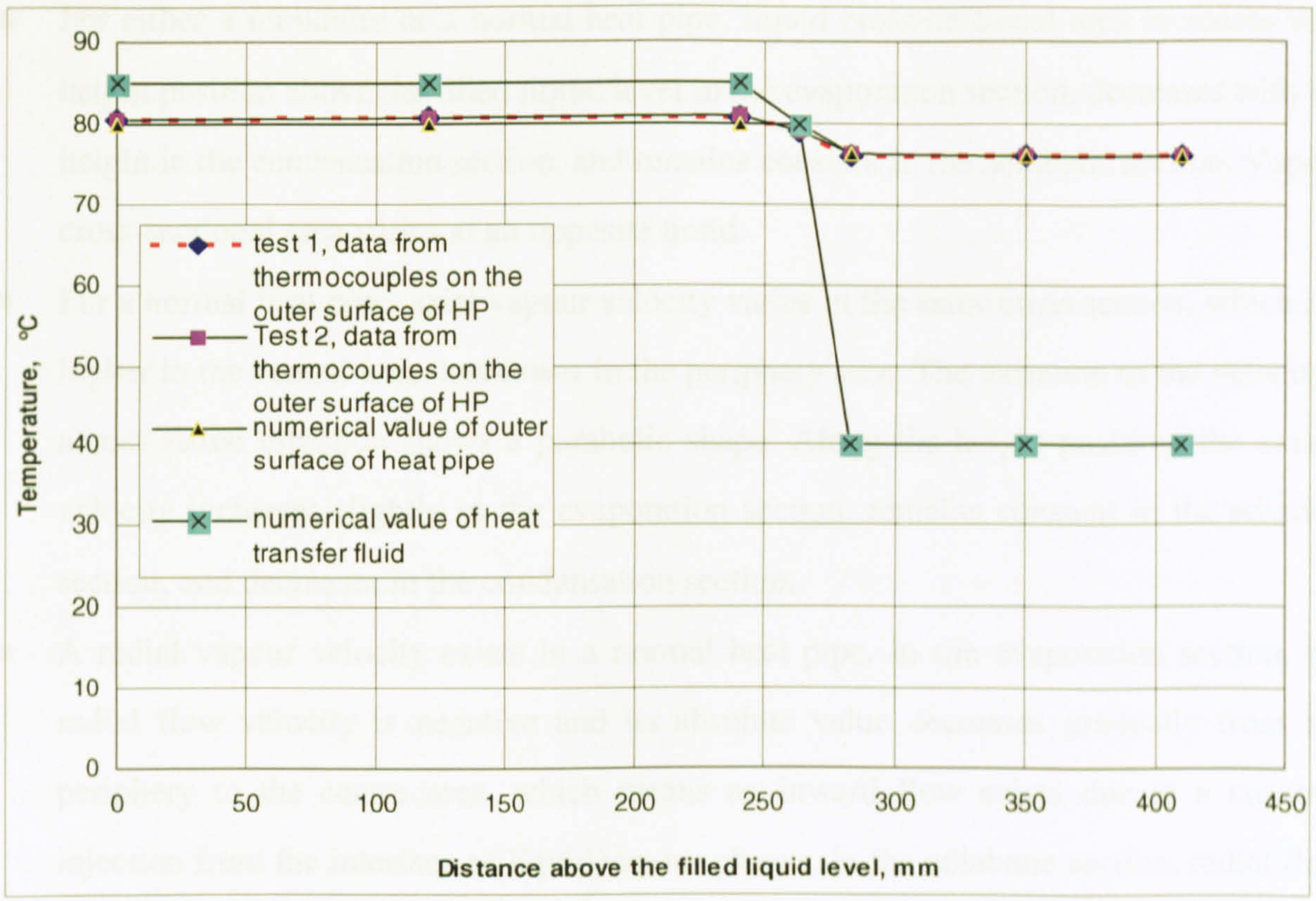

Figure 4-26. Comparison of numerical and experimental results for temperature profile – the wickless heat pipe

4.5 Summary

A simplified numerical model was developed based on the analysis of the published work. The numerical model has been proven to be able to give reasonable accuracy for predicting heat pipe operation characteristics. This model treated vapour flow in different ways for different heat pipes. Vapour flow in a miniature pipe was treated as a one-dimensional problem, and that in a normal heat pipe as a two-dimensional problem. Mathematical theory and numerical method used for miniature and normal heat pipes were detailed.

Numerical analysis was carried out to investigate the operating characteristics of the selected heat pipes, i.e., two miniature and one mini heat pipes, and two normal heat pipes, which were characterized in section 4-2. It was found that:

- For either a miniature or a normal heat pipe, liquid cross-sectional area increases with height position above the filled liquid level in the evaporation section, decreases with the height in the condensation section, and remains constant in the adiabatic section. Vapour cross-sectional area varies at an opposite trend.
- For a normal heat pipe, axial vapour velocity varies in the same cross section, which is higher in the central area, and lower in the periphery area. The variation of the velocity across radial direction shows a parabolic shape. Along the height position, the axial velocity increases slightly in the evaporation section, remains constant in the adiatic section, and decreases in the condensation section.
- A radial vapour velocity exists in a normal heat pipe. In the evaporation section, the radial flow velocity is negative and its absolute value decreases gradually from the periphery to the centre area, which means an inward flow exists due to a constant injection from the interface of liquid/vapour phases. In the adiabatic section, radial flow velocity is zero, which means no radial flow exists due to absence of injection/ejection on the interface of liquid/vapour phases. However, in the condensation section, radial velocity becomes postive and its absolute value increases gradually from the central area to the periphery, which means an outward flow exists due to a constant ejection on the interface of the liquid/vapour phases.
- For a miniature heat pipe, The total vapour-liquid pressure difference is an important factor which affects the operation of a heat pipe. The total pressure difference was shown to be significantly larger at the bottom of the evaporator section and decreases with height position above the reservoir fill level. Increasing the width 'b' of the miniature heat pipe, but with the cross-sectional area remaining constant, would reduce the flow resistance within the heat pipe, which results in reduced pressure differences.
- For a normal heat pipe, inner wall pressure is higher than vapour pressure in the evaporation section, resulting in liquid vaporization, but lower than vapour pressure in the condensation section, resulting in vapour condensation. Liquid pressure is much lower than vapour and inner wall pressures as part of its static pressure is converted into velocity pressure, causing the fluid flow within the heat pipe.

- For either a miniature or a normal heat pipe, there are very little differences among vapour, liquid and wall temperatures, compared to the differences of vapour (liquid or wall) and heat/cool sources and heat conduction/convection mediums. This demonstrates that the heat pipes are excellent heat transfer devices, which could be operated at an approximately constant temperature. The major heat resistances occur in the heat conduction/convection mediums, resulting in significant variation of temperature within these areas.

Lab testing was carried out to investigate the operating characteristics of the selected heat pipes experimentally. Two rigs were constructed for the testing of two types of normal heat pipes, i.e., the wicked and wickless ones. Quantities of heat transfer, as well as temperature distribution around the heat pipe outer surface were obtained through the testing, which are summarised in Tables 4-4 and 4-5.

Comparisons between numerical predictions and testing results were carried out. It was found that the results from tests are in general agreement with numerical prediction when the test conditions are close to the simulation assumption. Although tests have been constrained to temperature, the comparison carried out supports the validity of the numerical model.

Chapter 5. Heat Pipe Solar Collectors

5.1 Design of the Heat Pipe Solar Collectors

5.1.1 Thin Membrane Heat Pipe Solar Collector

A thin membrane heat pipe solar collector was designed to collect and distribute heat by means of vaporisation and condensation of a heat transfer fluid. It comprised mainly of an evacuated housing containing an absorber, a reservoir at the lower end of the collector and a condenser panel on the top end of the collector. Two additional absorbers (narrow strip panel) attached on the main absorber body were irradiated with solar irradiation concentrated by a lens on the outer cover, hence termed 'super heat pipes'. A micro-pore insulation material, attained with an aluminium/foam plastic tray, was fitted beneath the absorber panel to reduce downward heat loss. A clear acrylic cover was mounted on the top of the evacuated housing, creating an enclosed space where a vacuum could be maintained to eliminate convection/conduction heat loss. Two elliptical glass covers were attained on the top of the evacuated housing to increase flux of solar irradiation, and the Fresnel lens were fitted to the covers to provide concentrated radiation on the attained absorber (super heat pipe) area. One version of this solar collector is illustrated in Figure 1-2 (Chapter 1), and the other is shown schematically in Figure 5-1 [Riffat S. B. et al, 2002].

The main body of the collector comprised two plates separated by a thin evaporation gap. The plates were 'spot' welded together creating mini-channels (ribs) running parallel along the width of the absorber, as shown in Figure 5-2. Each mini-channel was considered to be a single 'miniature' heat pipe, as has previously been investigated in Chapters 3 and 4 using the analytical and numerical model developed. The miniature heat pipes connected the evaporation section to the condensation section of the collector to enable the flow of vapour refrigerant and condensed liquid refrigerant.

Two types of thin membrane heat pipe solar collectors were designed. These are classified as 'normal' and 'artery' types termed according to the method of returning of the condensed fluid. In the case of the 'normal' collector, condensed refrigerant is returned to the evaporation section along the sides of the miniature heat pipes by the combined effect of capillary and gravity forces. Part of the returned liquid is evaporated, as a result of absorbing solar irradiation striking the absorber surface, and the remainder is returned to the reservoir. This collector operates on the principle of miniature gravitational heat pipes

and hence is termed a 'normal' miniature heat pipe collectors, see Figures 1-2. In the case of the 'artery' collector, condensed refrigerant is returned to the reservoir via a tube. Liquid refrigerant from the reservoir flows to the evaporation section by capillary action. Here the refrigerant is vaporised, thus creating a continuous thermosyphon effect. This collector operates on the principle of miniature gravitational heat-pipes with additional artery, and hence termed 'artery' miniature heat pipe collectors, see Figures 5-1.

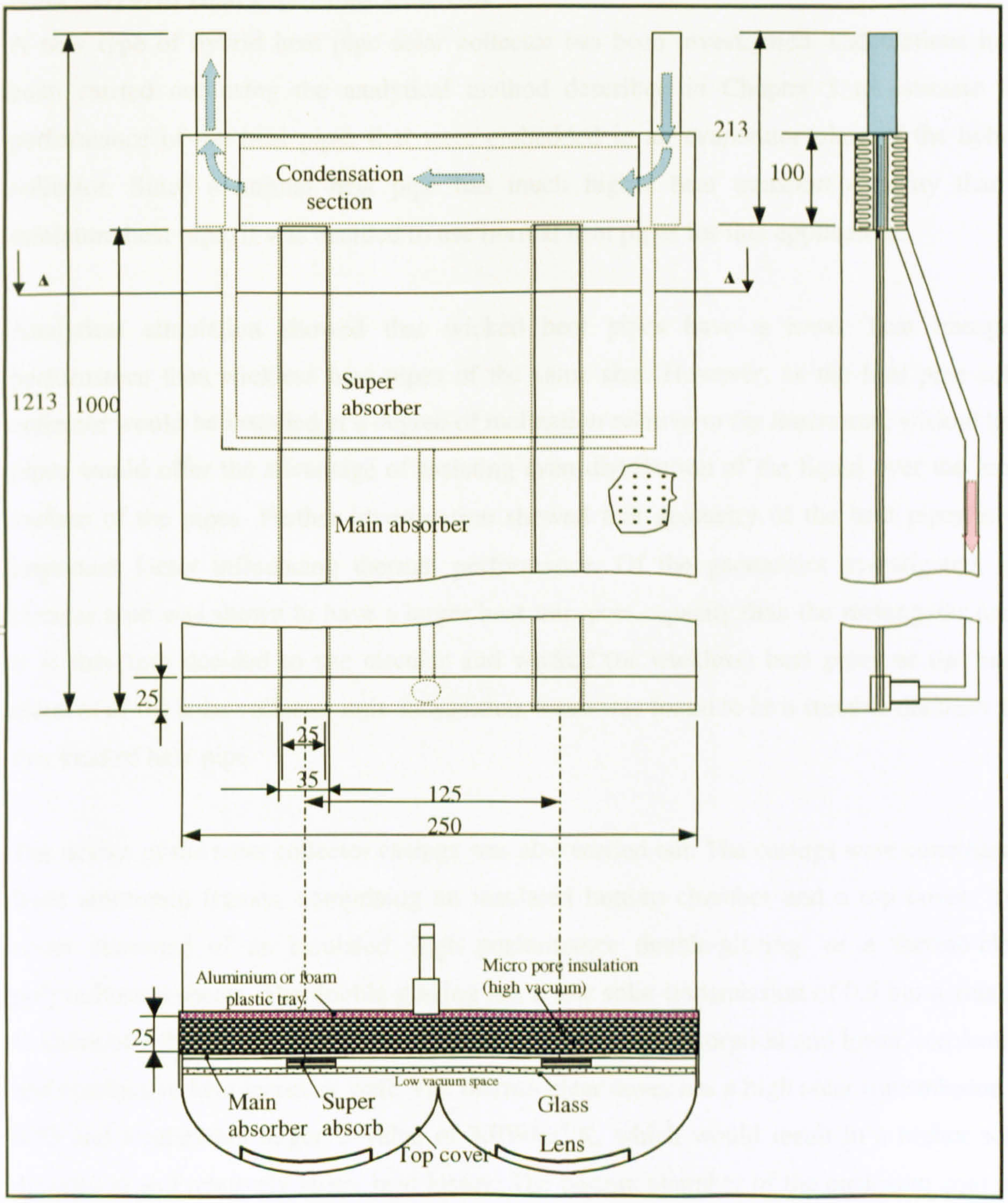

Figure 5-1. Schematic diagram of the 'artery' mniature heat pipe solar collector

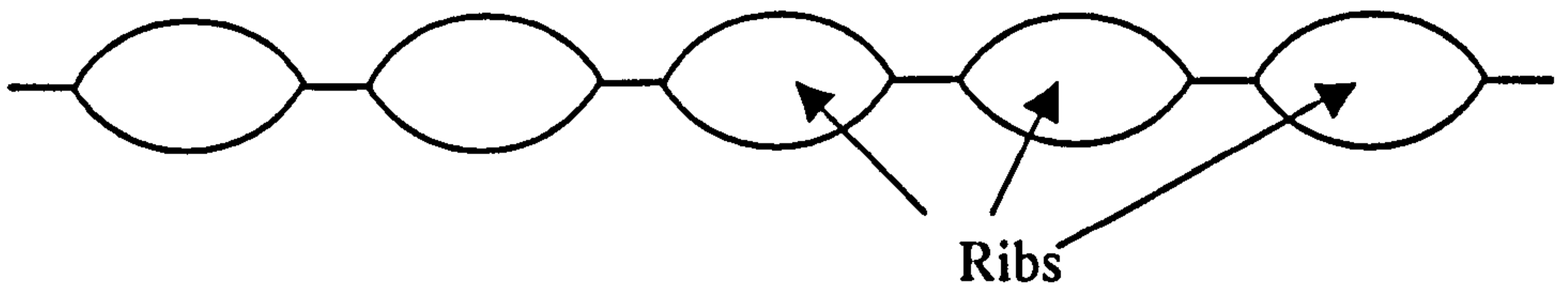

Figure 5-2. Schematic showing the cross section of the plate heat pipe (enlarged)

5.1.2 Hybrid Heat Pipe Solar Collector

A new type of hybrid heat pipe solar collector has been investigated. Calculations have been carried out using the analytical method described in Chapter 3 to estimate the performance of the heat pipes that were embedded in an evaporator plate of the hybrid collector. Since a normal heat pipe has much higher heat transport capacity than a miniature heat pipe, it was decided to use normal heat pipes for this application.

Analytical simulation showed that wicked heat pipes have a lower heat transport performance than wickless heat pipes of the same size. However, as the heat pipe solar collector would be installed at a degree of inclination relative to the horizontal, wicked heat pipes would offer the advantage of assisting even distribution of the liquid over the inner surface of the pipes. Further investigation showed that geometry of the heat pipes is an important factor influencing thermal performance. Of the geometries investigated, the circular type was shown to have a larger heat transport capacity than the rectangular ones. It is therefore decided to use circular and wicked (or wickless) heat pipes as the basic element of the solar collector unit. In addition, 8mm was found to be a suitable diameter for this kind of heat pipe.

The design of the solar collector casings was also carried out. The casings were constructed from aluminum frames, comprising an insulated bottom chamber and a top cover. Top cover consisted of an insulated, high performance double-glazing, or a thermo-clear polycarbonate sheets. The double-glazing has a low solar transmission of 0.5 but a smaller U value of 1.2W/m^2.K, which would result in lower solar absorption and lower convective and conductive heat losses as well. The thermo-clear cover has a high solar transmission of 0.85 and a relatively larger U value of 3.0W/m^2.K, which would result in a higher solar absorption and relatively larger heat losses. The bottom chamber of the enclosure contains a number of channels to allow exhaust gas discharged from a boiler to pass through to improve the efficiency of the collectors, as well as provide a back up (or compensation)

when solar irradiation is unavailable (or low). Fibre-glass insulation was fitted beneath and around the channels to reduce heat loss through the chamber. As heat from the sun and exhaust gas is collected, the unit is termed a 'Hybrid Heat Pipe Solar Collector'. Schematic diagrams describing the structure of the collector are given in Figures 1-3a, 1-3b and 1-3c (Chapter 1).

Two types of the collector were also designed [Riffat S. B. et al]. Each includes 20 heat pipes, and has the gross absorb area of $2.4m^2$. The first one used wickless heat pipes with separate condensers, which have a larger diameter (20mm) than the evaporators (8mm), and were connected to the evaporators by flexible hoses. The manifold was tightly fixed on the condensers using clamps to ensure good surface contact and efficient heat transfer. The structure is shown schematically in Figure 5-3. The second type used wicked heat pipes, which have integrated bodies and therefore no physical separations between the evaporators and condensers. The manifold was connected to the condensers of the heat pipes using copper rods, which were drilled with co-axial cylinder cavities. Heat transfer between the condensers and the manifold is largely dependent on the conductivity of the rods. The structure is shown schematically in Figure 5-4.

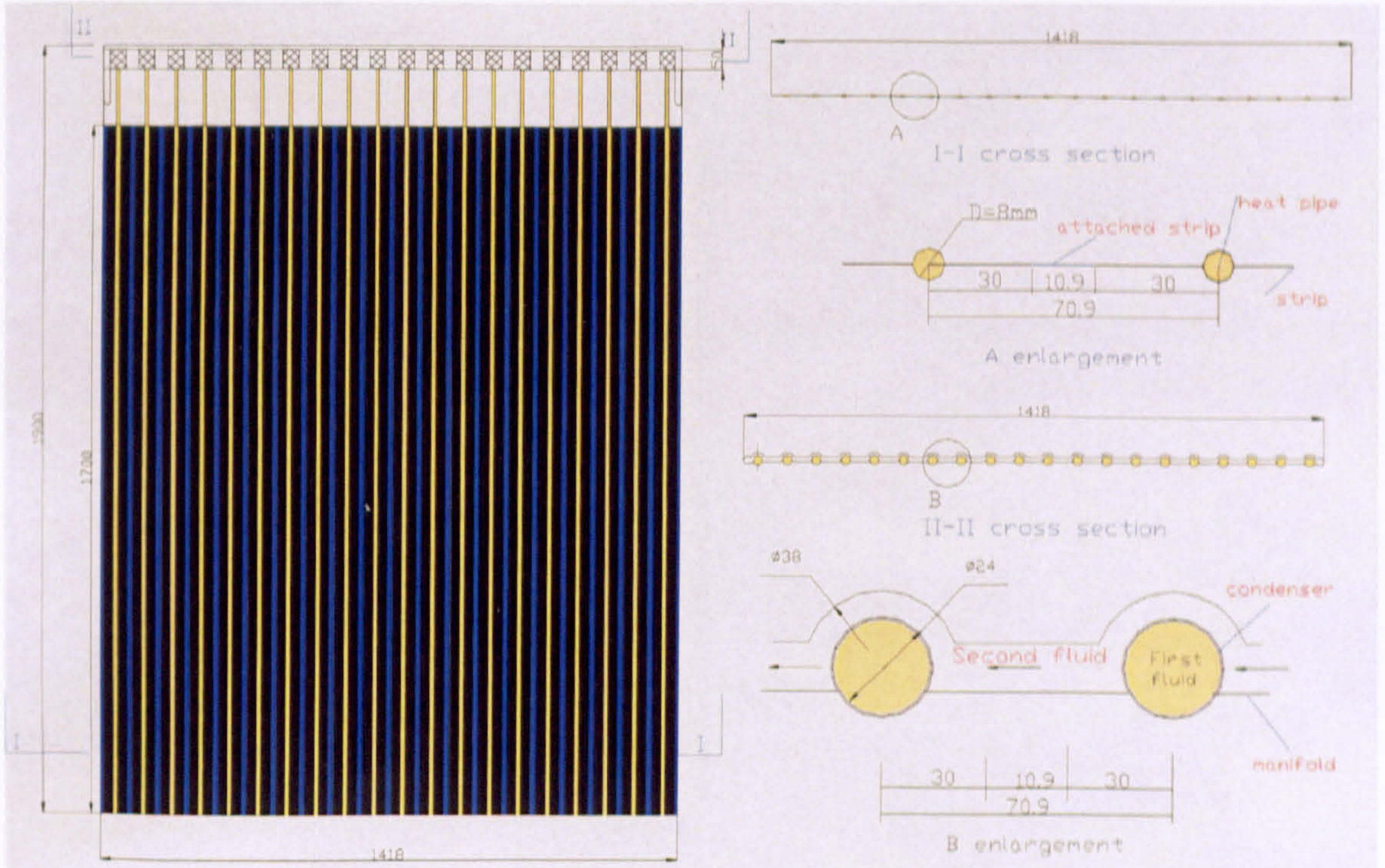

Figure 5-3. Structure design of the wickless heat pipe panel

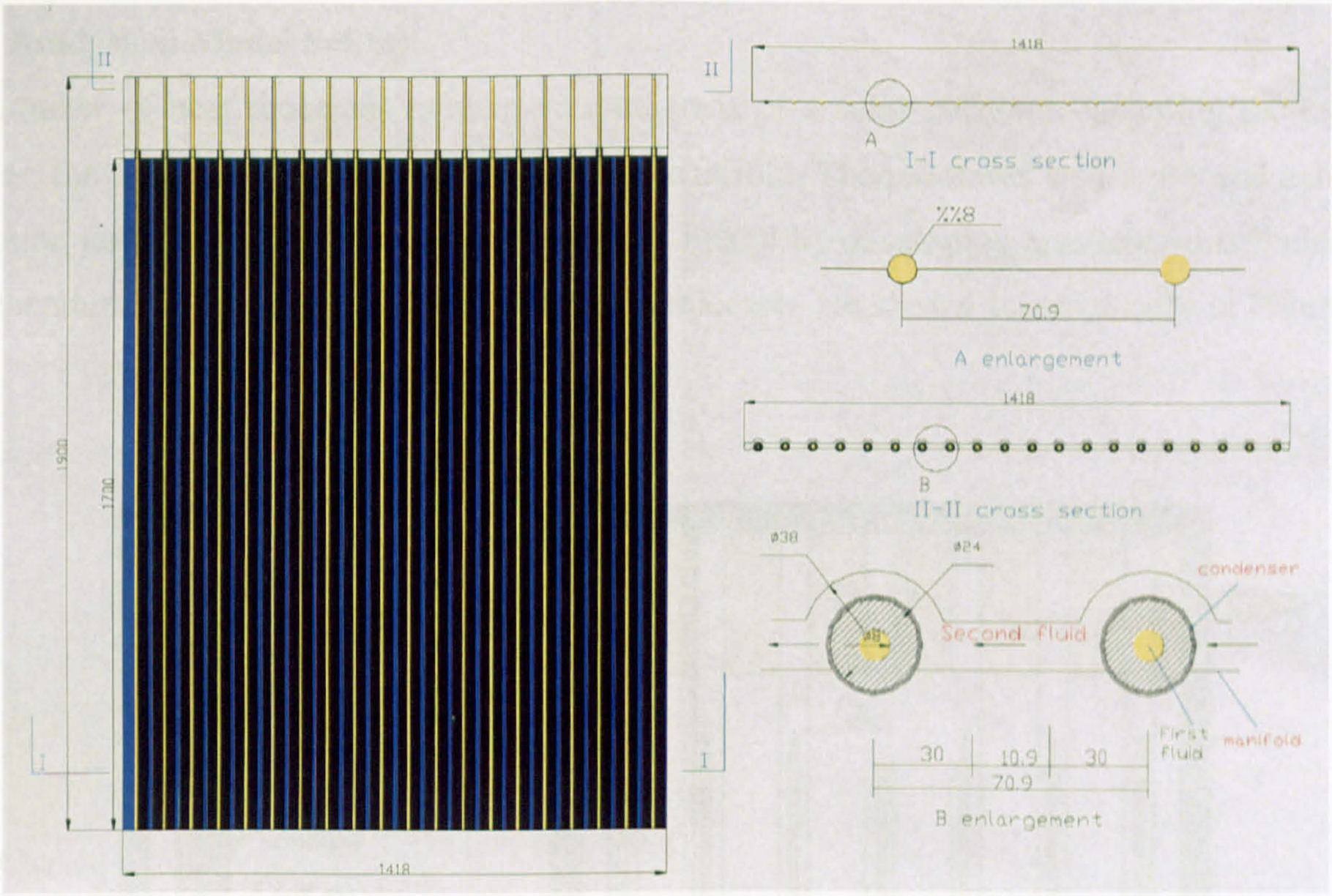

Figure 5-4. Structure design of the wicked heat pipe panel

5-2 Analytical Model Set-up

A number of heat processes exist in various areas of a solar collector, including the top cover, the evaporator plate and the condenser/manifold. The processes would proceed until balance states are achieved and would be inter-linked by developing a suitably-distributed temperature profile. The relations of the heat processes are shown schematically in Figure 5-5.

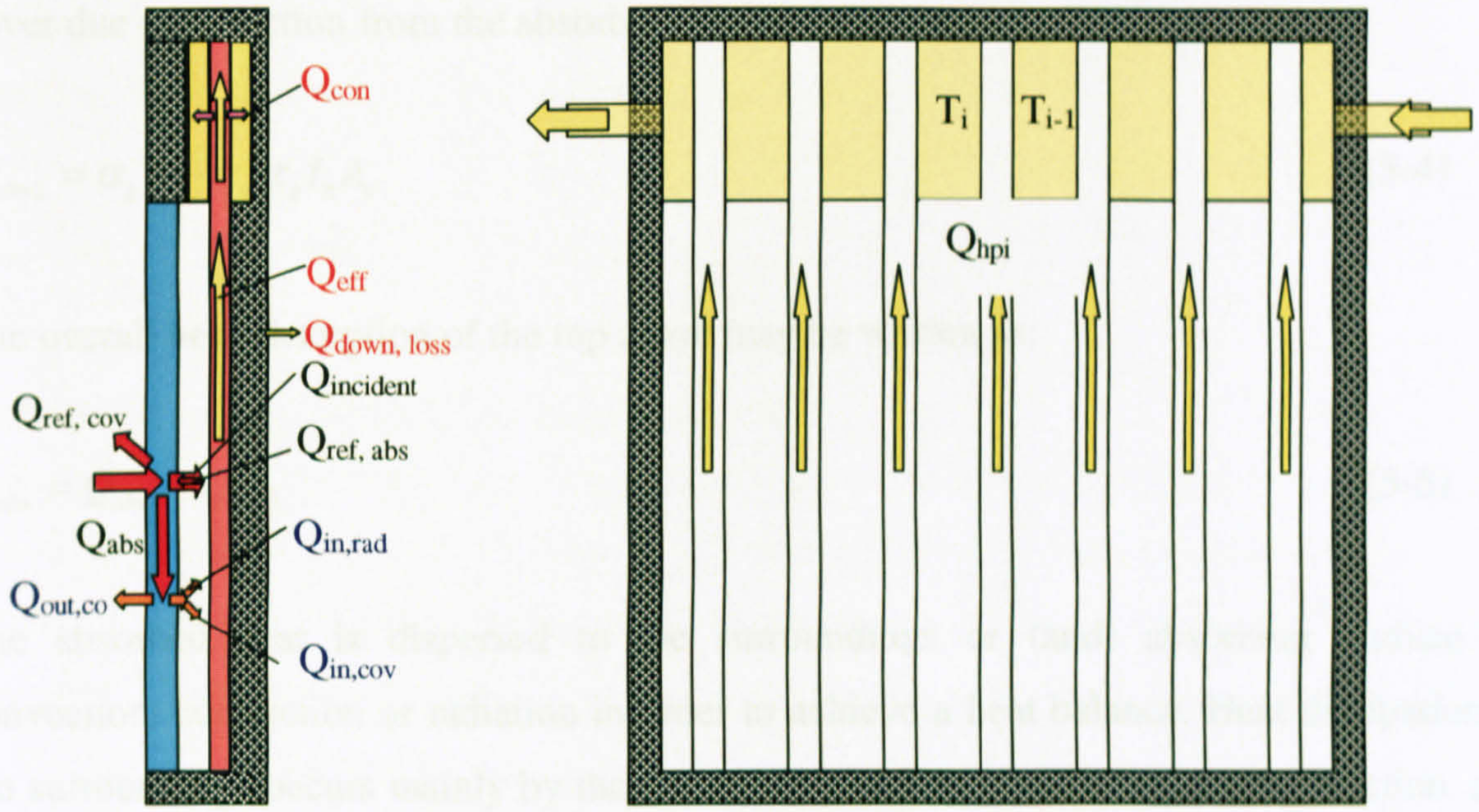

Figure 5-5. Schematic diagram showing relation of heat balances in different parts of a solar collector

<u>Heat process in the top cover</u>

For a given collector area and total solar irradiation, the heat striking the absorber surface may be expressed as:

$$Q_{incident} = \tau_g \alpha_s I_n A_s \tag{5-1}$$

The heat absorbed by the top cover may be expressed as:

$$Q_{abs1} = \alpha_g I_n A_g \tag{5-2}$$

and heat reflected to atmosphere is given by:

$$Q_{ref} = (1-\alpha_g - \tau_g) I_n A_g \qquad (5\text{-}3)$$

Since the absorptivity of the absorber is not 100%, a small part of the heat would return to the top cover area. Part of the reflected heat would be absorbed by the cover, and the remainder would re-enter the absorber chamber, which would establish long-wave radiation or heat convection between the cover and absorber. The additional heat absorbed by the top cover due to reflection from the absorber may be expressed as:

$$Q_{abs2} = \alpha_g (1-\alpha_s) \tau_g I_n A_s \qquad (5\text{-}4)$$

The overall heat absorption of the top cover may be written as:

$$Q_{abs} = Q_{abs1} + Q_{abs2} \qquad (5\text{-}5)$$

The absorbed heat is dispersed to the surroundings or (and) absorbing surface by convection, conduction or radiation in order to achieve a heat balance. Heat dissipation to the surroundings occurs mainly by the combined effect of conduction and convection, and may be expressed as:

$$Q_{up,loss} = A_g (t_{gc} - t_a) / (\delta_g / 2k_g + 1/h_2) \qquad (5\text{-}6)$$

Heat transfer between the top cover and absorber may be complex. If the absorber chamber were perfectly evacuated, heat transfer between the top cover and absorber would only be induced by radiation, which may be expressed as:

$$Q_{cover-absorber} = \sigma A_g ((273+t_{ci})^4 - (273+t_s)^4) / (1/\varepsilon_s + 1/\varepsilon_g - 1) = A_g (t_{gc} - t_{ci}) / (\delta / 2k_g) \qquad (5\text{-}7)$$

However, if the chamber were not evacuated, heat transfer between the top cover and the absorber will be a combined effect of conduction, convection and radiation, and may be expressed as:

$$Q_{cover-absorber} = h_1(A_s + A_g)(t_{ci} - t_s)/2 + \sigma A_g((273+t_{ci})^4 - (273+t_s)^4)/(1/\varepsilon_1 + 1/\varepsilon_2 - 1)$$
$$= A_g(t_{gc} - t_{ci})/(\delta/2k_g) \quad (5\text{-}8)$$

It should be noted that if the top cover inner surface temperature t_{ci} is higher than the absorber surface temperature t_s, heat flow will be directed toward the absorber surface, and $Q_{cover\text{-}absorber}$ is positive. Otherwise, heat flow will be directed to the top cover, and $Q_{cover\text{-}absorber}$ is negative.

The heat balance existing in the top cover may be expressed as:

$$Q_{abs} = Q_{cover-absorber} + Q_{up,loss} \quad (5\text{-}9)$$

Heat process in the absorber (evaporator) plate

Heat reaching the absorber plate comes mainly from one of the following two sources: the sun or the exhaust gas, or both. Part of the heat will be transferred to the working fluid through the flat plate and heat pipe wall, which causes the liquid to vaporise and this is therefore termed the effective heat input. The remainder will be dispersed to the environment through the top cover and bottom casings, resulting in heat losses due to conduction, convection and radiation.

There are temperature differences in the absorber area, which result in heat transmission from the flat plate to the pipes, or from one part to another part of the area. However, these differentials are small as both the plate and pipes are made of copper - an excellent heat conductor. In order to simplify the thermal analysis, the differentials are considered to be negligible and thus the absorber surface is assumed to be at the same temperature over the whole area.

If $Q_{cover\text{-}absorber}$ is negative, the absorber has an upward heat loss. If $Q_{cover\text{-}absorber}$ is positive, the absorber has a downward heat addition from the top cover. The heat flow has been described in Eqs. 5-7 and 5-8.

If the collector is not fitted with the channels allowing exhaust gas to pass through, such as the structures of Figures 1-2 and 5-1, insulation materials are directly placed below the absorber panel, and above the supporting frame. The downward heat loss will be:

$$Q_{down,loss} = A_d (t_s - t_a) / (\delta_i / k_i + \delta_f / k_f + 1/h_2) \qquad (5\text{-}10)$$

In addition, small part of side-wall loss exists with the configuration. However, the loss is negligible compared to the other losses, as the side-wall area is small and well insulated.

Actual heat obtained by the absorber (evaporator) plate is then expressed as:

$$Q_{obt} = Q_{incident} + Q_{cover-absorber} - Q_{down,loss} \qquad (5\text{-}11)$$

However, if the collector is fitted with channels allowing exhaust gas to pass through, such as the structure of Figure 1-3, there will be heat transfer between the flue gas, absorber panel and surroundings. The heat transfer process is shown in Figure 5-6.

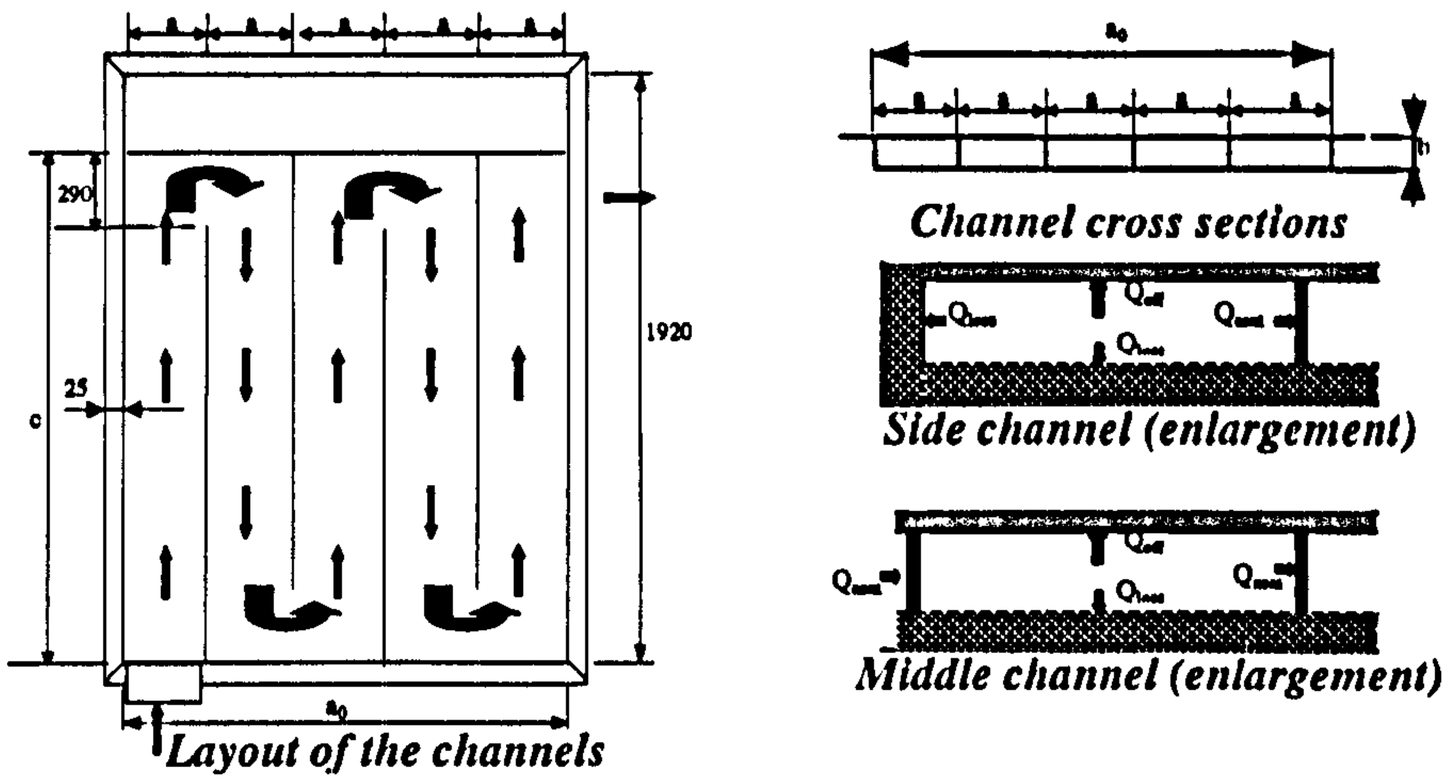

Figure 5-6. Schematic diagram showing fluid flow and heat transfer in exhaust gas flow channels beneath the heat pipe panel

The exhaust gas passes through a number of adjacent rectangular channels and heat transfer occurs through the enclosure walls. To simplify the analysis, the adjacent channels are treated as a continuous, straight channel. The heat transfer between channel flow, absorber and enclosure walls may then be expressed as follows [Yang S. et al, 1998]:

$$h_m A_s \Delta t_{m1} + h_m A_{dw} \Delta t_{m2} = m_s C_{ps}(t_f{}' - t_f{}'') = Q_{gas-heat-obtain} + Q_{down-loss} \quad (5\text{-}12)$$

Where m_s is the mass flow rate of the flue gas; t_f' and t_f'' are the temperatures of flue gas at inlet and outlet; A_s and A_{dw} are the areas of the absorber and the bottom casings respectively; and Δt_{m1} and Δt_{m2} are the average calculation temperature differences between flue gas and absorber, and that between flue gas and inner surface of the enclosure walls respectively, which could be expressed as follows:

$$\Delta t_{m1} = \frac{t_f{}' - t_f{}''}{\ln(\frac{t_f{}' - t_s}{t_f{}'' - t_s})} \quad (5\text{-}13)$$

$$\Delta t_{m2} = \frac{t_f{}' - t_f{}''}{\ln(\frac{t_f{}' - t_{w2}}{t_f{}'' - t_{w2}})} \quad (5\text{-}14)$$

The heat loss through the bottom chamber could also be written as:

$$Q_{down,loss} = A_{dw}(t_{w2} - t_a)/(\delta_i / k_i + 1/h_2) \quad (5\text{-}15)$$

h_m is the convective heat transfer coefficient and is largely dependant on the flow of the flue gas in channels. Since this flow is normally turbulent, h_m may be computed using Dittus-Boelter formula [Yang S. et al, 1998], which may be written as follows:

$$Nu_f = 0.023 \mathrm{Re}_f{}^{0.8} \mathrm{Pr}_f{}^{n} \quad (5\text{-}16)$$

If the gas flow is heated by the side-walls, then n = 0.4. Otherwise, n = 0.3. The formula is most suitable for the situation with medium temperature difference, i.e., 50°C or less. In this case the mean temperature of the gas flow is taken as the character temperature, and the inner diameter of the channel is taken as the character length. For the rectangular channel, an equivalent diameter is used and this may be written as follows:

$$d_e = \frac{4A_c}{p} \quad (5\text{-}17)$$

For the situation with a higher temperature difference, a correction factor, c_t, is defined as follows. The factor is added to the right side of the formulae 5-13 and 5-14.

If the gas flow is heated by the side walls of the flow channel, then

$$c_t = \left(\frac{T_f}{T_w}\right)^{0.5} \tag{5-18}$$

Otherwise, $c_t = 1$.

It is difficult to solve the coupled equations governing the heat transfer between the flue gas, absorber panel and ambient, as several parameters are undetermined. It is therefore necessary to assume values for some parameters, such as t_f'', and use a trial-and-error method for the solution-solving process. The algorithm used in the solving process is described as follows:

i) Given an assumed value for t_f'', calculating the overall heat output;

ii) Calculating h_m by using Eqs. 5-16 to 5-17;

iii) Calculating Δt_{m1} by using Eq. 5-13;

iv) Calculating Δt_{m2} by using Eq. 5-12;

v) Calculating t_{w2} by using Eq. 5-14;

vi) Calculating $Q_{down\text{-}loss}$ by using Eq. 5-15;

vii) Comparing the values of $h_m A_{dw} \Delta t_{m2}$ and $Q_{down\text{-}loss}$. If $(h_m A_{dw} \Delta t_{m2} - Q_{down\text{-}loss}) / h_m A_{dw} \Delta t_{m2} > 0.05$, then increase t_f'' by 1%, and return to step i) for re-calculation. If $(h_m A_{dw} \Delta t_{m2} - Q_{down\text{-}loss}) / h_m A_{dw} \Delta t_{m2} < 0.05$, then reduce t_f'' by 1%, and return to step i) for re-calculation. Otherwise, the accuracy of calculation is deemed to be satisfactory. A relatively larger error allowance, i.e., 5%, was used because a smaller error allowance was found unable to produce a converged solution.

The heat obtained by the absorber (evaporator) plate may then be expressed as follows:

$$Q_{obt} = Q_{incident} + Q_{cover-absorber} + Q_{gas-heat-obtain} \tag{5-19}$$

The obtained heat should be transferred to the heat pipes, causing evaporation of the operating fluid inside the pipes. However, if the heat transport capacity of the heat pipes is

not large enough to transport such an amount of heat, then part of the heat will be dispersed to the surroundings via the top cover and metal surface of the chamber, resulting in a change of temperature over the absorber area.

To investigate the heat transfer of a heat pipe solar collector, it is necessary to determine its heat transport limitation. The limit of heat transport capacity for a single heat pipe may be determined by using the analytical model illustrated in Chapter 3. The maximum heat transport capacity of the collector may then be obtained as:

$$Q_{max} = nQ_{lim} \tag{5-20}$$

Where n is the number of heat pipes included. If Q_{obt} is less than Q_{max}, then the heat obtained will be transported without any restriction. However, if Q_{max} is less than Q_{obt}, then part of the obtained heat will be dispersed to the surroundings, resulting in reduced heat removal, i.e., Q_{max}. In this case, the temperature of the absorber surface would be adjusted automatically until a new thermo-equilibrium is achieved. This new balance may be expressed as follows:

For the collector without flue gas channels:

$$\min(Q_{max}, Q_{obt}) = Q_{obt,real} = Q_{incident} + Q_{cover-absorber} - Q_{down,loss} \tag{5-21}$$

For the collector with flue gas channels:

$$\min(Q_{max}, Q_{obt}) = Q_{obt,real} = Q_{incident} + Q_{cover-absorber} + Q_{gas-heat-obtain} \tag{5-22}$$

Heat processes in the condensers and manifold

The heat obtained from the absorber, $Q_{obt,real}$, will be transported to the cooling fluid passing across manifold through evaporation and condensation of the working fluid in the heat pipes. There are several heat resistances in this process, namely, the evaporator wall resistance, the equivalent resistance of the working fluid and wick in the evaporator, the vapour flow resistance, the equivalent resistance of the working fluid and wick in the condenser, and the condenser wall resistance. These resistances may be expressed as follows [Dunn P. D. and Reay D. A., 1982]:

Evaporator wall resistance:
$$R_{p,e} = \frac{r_0^2 \ln(r_0 / r_i)}{2L_e k_p} \quad (5\text{-}23)$$

Evaporator saturated wick resistance:
$$R_{w,e} = \frac{r_0^2 \ln(r_i / r_v)}{2L_e k_e} \quad (5\text{-}24)$$

Vapour flow resistance:
$$R_v = \frac{\pi r_0^2 F_v T_v (L_e/6 + L_a + L_c/6)}{\rho_v \lambda J} \quad (5\text{-}25)$$

Condenser saturated wick resistance:
$$R_w = \frac{r_0^2 \ln(r_{i,c} / r_{v,c})}{2L_c k_e} \quad (5\text{-}26)$$

Condenser wall resistance:
$$R_{p,c} = \frac{r_0^2 \ln(r_{o,c} / r_{i,c})}{2L_c k_p} \quad (5\text{-}27)$$

Total resistance:
$$R = R_{p,e} + R_{w,e} + R_v + R_w + R_{p,c} \quad (5\text{-}28)$$

For a single heat pipe, heat transportation from the evaporator outer surface to the condenser outer surface may be written as:

$$Q_{hp,l} = \pi r_0^2 (t_{p,e} - t_{p,c}) / R \quad (5\text{-}29)$$

The heat will be transferred to the cooling liquid by heat conduction through the manifold wall, and heat convection between the manifold wall and the cooling liquid. The cooling liquid will be heated when flowing through the manifold channel, which is tightly fixed to the heat pipe condensers by means of clamps. For an inlet temperature given as t_0, a temperature increase Δt_1 (t_1-t_0) will be achieved after the fluid passes around the first heat pipe due to heat absorption from the pipe. The fluid temperature increases gradually along the flow direction due to continuous heat injection from the parallel-array of heat pipes. The heat transfer between a single heat pipe and the cooling liquid may be expressed as:

$$Q_{con,i} = \frac{A_{con}(t_{p,c} - (t_{i-1} + t_i)/2)}{\frac{\delta_{con}}{k_{con}} + \frac{1}{h_{con}}} = C_{p,l} m (t_i - t_{i-1}) = Q_{hp,i} \quad (5\text{-}30)$$

h_{con} is the convective heat transfer coefficient of the cooling fluid, which is largely dependent on the velocity of fluid passing over the surface and the cross-sectional area as well as the geometry of the flow channel. For the collectors indicated above, the flow of the cooling liquid flow and the manifold geometry are shown schematically in Figures 5-7, 5-8 and 5-9.

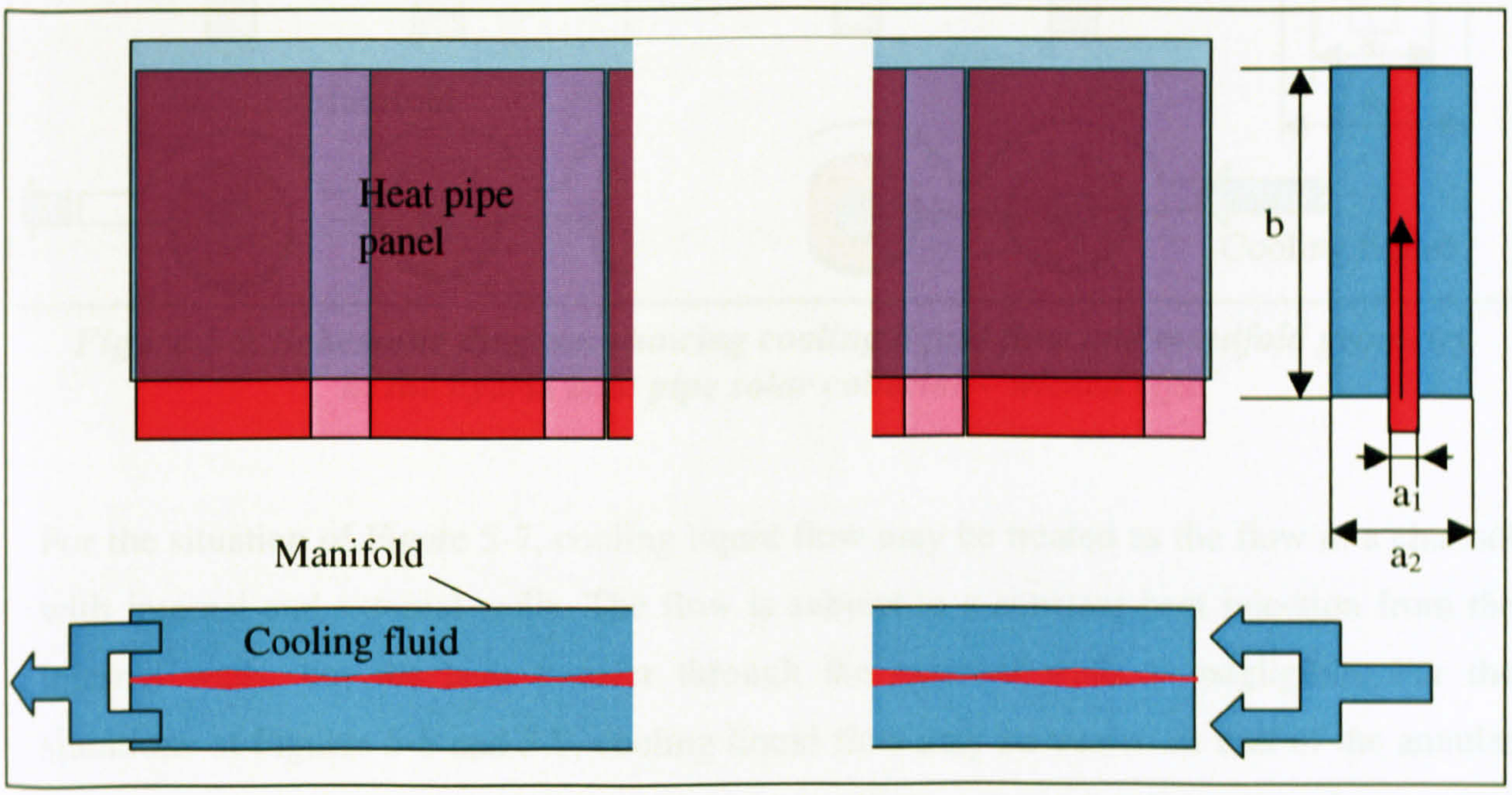

Figure 5-7. Schematic diagram showing cooling liquid flow and manifold geometry in the thin membrane heat pipe solar collector

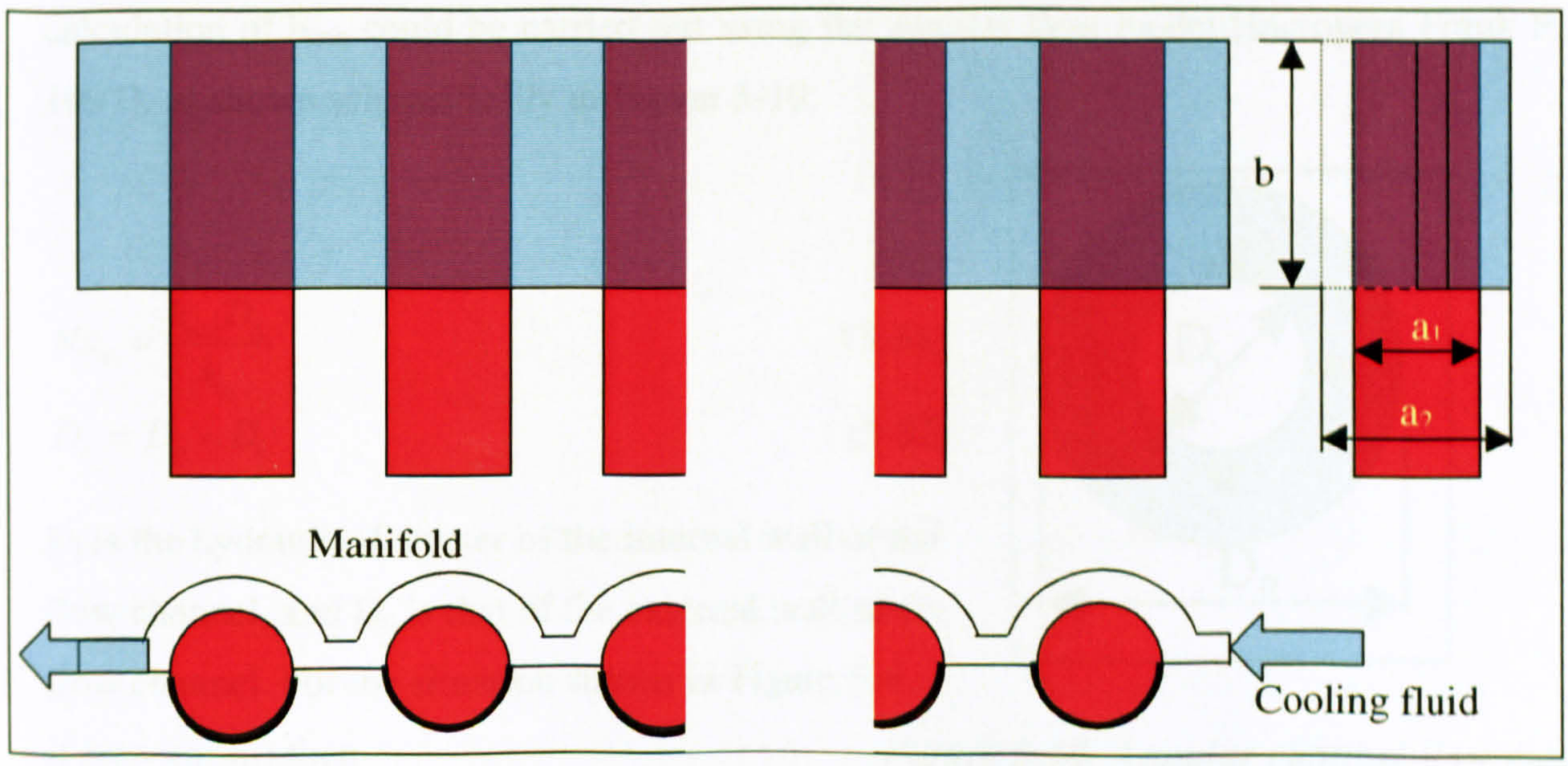

Figure 5-8. Schematic diagram showing cooling liquid flow and manifold geometry in the hybrid heat pipe solar collector – wickless type

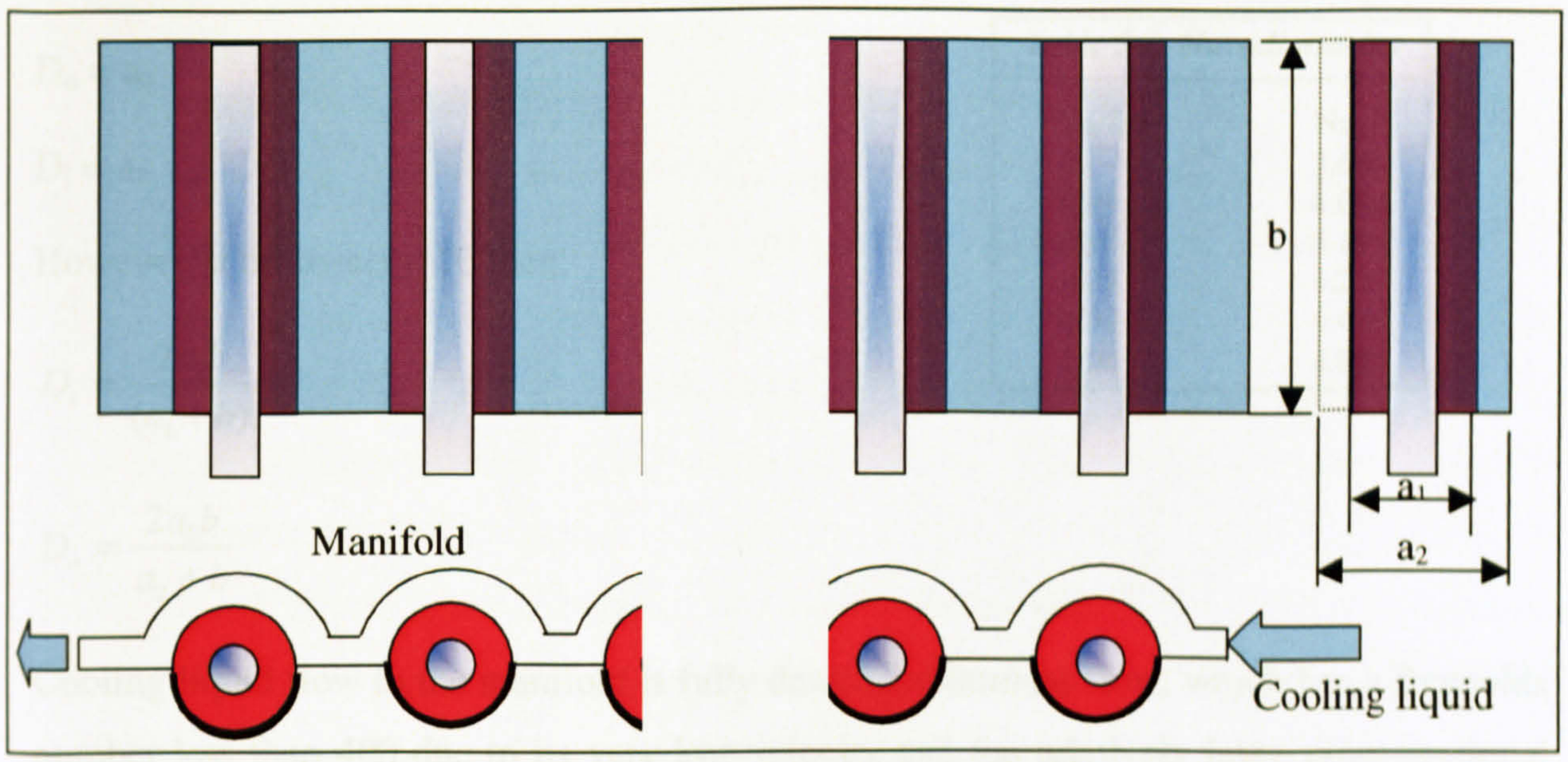

Figure 5-9. Schematic diagram showing cooling liquid flow and manifold geometry in the hybrid heat pipe solar collector – wicked type

For the situation of Figure 5-7, cooling liquid flow may be treated as the flow in a channel with internal and external walls. The flow is subject to a constant heat injection from the internal walls, but the heat transfer through the external walls is negligible. For the situations of Figures 5-8 and 5-9, cooling liquid flow may be treated as half of the annular flow. To solve for the convective heat transfer coefficient, h_{con}, the channel needs to treated as an annular geometry rather than a semi-annular one, and correspondingly, heat flow from the inner wall needs to be doubled to suit this treatment. Heat transfer through the outer walls was negligible as a satisfactory insulation was provided. For both situations, calculation of h_{con} could be carried out using the annular flow model [Incropera Frank P., 1997], as shown schematically in Figure 5-10.

$$Nu_o = \frac{h_{con} D_h}{k_h} \qquad (5\text{-}31)$$

$$D_h = D_o - D_i \qquad (5\text{-}32)$$

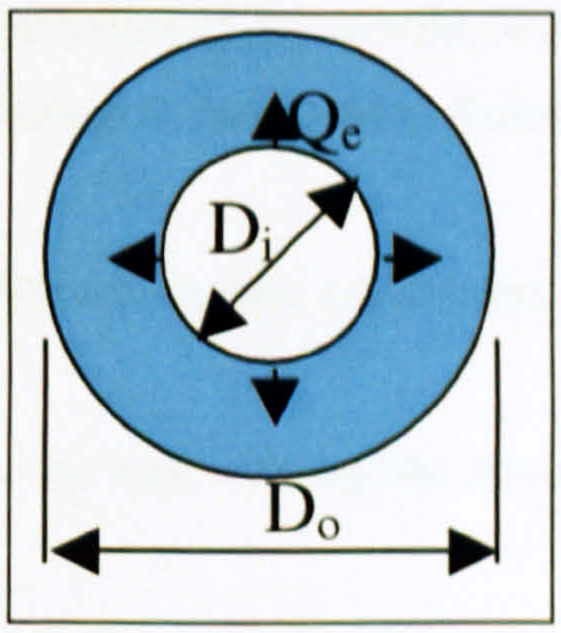

Figure 5-10. Annular channel flow model

D_i is the hydraulic diameter of the internal wall of the flow channel, and D_o is that of the external wall of the flow channel. For the situation shown in Figure 5-8, if $b >> (a_2-a_1)$ then:

$D_o = a_2$

$D_i = a_1$

However, if $b/(a_2-a_1) < 10$ then:

$$D_i = \frac{2a_1 b}{(a_1 + b)}$$

$$D_o = \frac{2a_2 b}{a_2 + b}$$

Cooling liquid flow in the manifold is fully developed laminar flow, which has a Reynolds number less than 400 due to its very low velocity and the relatively large cross-sectional area. For this case, Nu_o may be obtained from Table 5-1[Incropera Frank P., 1997].

Table 5-1. Nusselt number

Di/Do	Nu_o
0	3.66
0.05	4.06
0.10	4.11
0.25	4.23
0.50	4.43
1.00	4.86

For a single heat pipe, given the inlet temperature t_{i-1}, the outlet temperature t_i may be obtained by solving Eq. 5-30. For the whole condenser/manifold configuration, the overall heat transfer may be expressed as:

$$Q_{con} = Q_{con,1} + Q_{con,2} + \ldots + Q_{con,n} = C_{p,l} m (t_n - t_0) \qquad (5\text{-}33)$$

Q_{con} should be equal to $Q_{obt,real}$ according to the principle of heat balance. Eqs. 5-23 to 5-33 may be used to solve for the outlet temperature and the mean temperature of the cooling water, as well as the temperatures in different parts of the heat pipe panel.

Computer model set-up

The three heat processes described above are actually inter-linked by a well-developed temperature layout. The algorithm used for the model setting-up is indicated as follows:

1. Given the collector configuration, geometrical and thermodynamic parameters of the collector unit are determined;
2. Given the incident radiation and ambient temperature, the heat striking the absorber is determined.
3. Given the manifold configuration, as well as the cooling liquid flow condition, geometrical, thermodynamic and flow parameters of the cooling fluid are determined;
4. Assuming an absorber temperature t_s, heat analysis is carried out as follows:

- Heat balance of the top cover could be analysed by using Eqs. 5-1 to 5-9, which results in solution solving of the inner surface temperature of top cover t_{ci}.
- Heat balance of the absorber (evaporator) plate could be analysed using Eqs. 5-10 to 5-22, which results in solution solving of the absorber heat gain, Q_{obt}.
- Heat balance of the heat pipes, and condenser/manifold pair could be analysed using Eqs. 5-23 to 5-33, which results in solution solving of the heat gain of the cooling water passing through the manifold, as well as the temperature layout in different areas of collector.

5. If $(Q_{obt} - Q_{con})/Q_{obt} > 0.5\%$ (error allowance), then increase t_s by $0.1^{\circ}C$, and return to step 4 for re-calculation.
6. If $(Q_{obt} - Q_{con})/ Q_{obt} <- 0.5\%$ (error allowance), then decrease t_s by $0.1^{\circ}C$, and return to step 4 for re-calculation.
7. If $-0.5\% \leq (Q_{obt} - Q_{con})/ Q_{obt} \leq 0.5\%$, heat balances in the whole system, as well as different areas of the system, are achieved.
8. Calculating the cooling water temperature at the outlet and different points along the flow channel, as well as the temperatures at different areas of the collector.
9. Program stops.

5.3 Modelling Processing and Result Discussions

The data obtained by running the computer program could be used to evaluate the thermal performance of a solar collector. For a normal solar collector, its performance is usually evaluated using efficiency η, which is defined as the ratio of heat taken from the manifold by the cooling liquid, and the incident irradiation striking the collector absorber. However, in the case of the hybrid solar collector, another efficiency, η_1, will also be used for performance evaluation. This efficiency is defined as the ratio of heat taken from the manifold by the cooling liquid, and the sum of the incident irradiation striking the collector absorber and the heat from exhaust gas. In this case, exhaust gas heat means the potentially available energy contained in the gas, which is a value in relation to the energy of ambient air, and may be expressed as:

$$Q_{gas} = C_{ps}\rho_s Lt_f' - C_{pa}\rho_a Lt_a \qquad (5\text{-}34)$$

η and η_1 vary with a number of external parameters, including global solar irradiation I_n, ambient temperature t_a, as well as cooling fluid inlet temperature t_0 and mass flow rate m. These parameters may be grouped by a specially-defined parameter, termed, $(t_{mean}-t_a)/I_n$; whereby t_{mean} is the average temperature of the cooling fluid and may be written as:

$$t_{mean} = \frac{(t_0 + t_n)}{2} \qquad (5\text{-}35)$$

η and η_1 are usually expressed as the function of $(t_{mean}-t_a)/I_n$, as follows:

$$\eta = \eta_0 - \alpha_1(\frac{t_{mean} - t_a}{I_n}) \qquad (5\text{-}36)$$

$$\eta_1 = \eta_{01} - \alpha_{11}(\frac{t_{mean} - t_a}{I_n}) \qquad (5\text{-}37)$$

where η_0 (η_{01}) and α_1 (α_{11}) are the collector character parameters.

In addition to external conditions, collector structures, i.e., internal conditions, also have an essential impact on performance. The heat pipes and absorber plate are the major components influencing collector efficiency. For the thin membrane heat pipe solar collector, the absorber is made of two pieces of steel plates, which are 'spot' welded together creating 22 mini-channels (ribs), termed miniature heat pipes. The previous

analytical investigation showed such a single pipe had a heat transport capacity of 50W when it was operated at 80°C and installed with the inclination of 60deg relative to horizontal. Thus the whole panel would have an overall heat transport capacity of 1,100W, which is much higher than actual solar input (less than 250 W). For the hybrid heat pipe solar collector, the absorber is incorporated with a total of 20 wicked (or wickless) heat pipes of diameter of 8mm. Each of the pipes was found to have a heat transport capacity of 120W based on the investigation carried out in Chapter 3. Thus the whole panel would have an overall heat transport capacity of 2,400W, which is still higher than the actual solar input (less than 2,200W). These analyses demonstrate that the heat pipes selected allow the solar energy received to be transported without restriction under the given operation conditions.

These two collectors under consideration use the same coating material, called Maxorb-Nickel foil, on their absorber surfaces. The material has solar absorptivity of 0.95-0.99, and a long-wave emittance of 0.08-0.11[Yagoub WKA, 1999]. These are very favourable to solar absorption and act to enhance collector efficiency.

The top cover is another important component influencing collector performance. A top cover is usually a clear and transparent material, which has a high transmittance and a low U (heat transfer coefficient) value. Five top cover configurations are investigated in this section. These are:

- An acrylic cover fitted on an evacuated chamber;
- An acrylic cover fitted on an un-evacuated chamber;
- A double-glazing cover fitted on an un-evacuated chamber;
- A 10mm polycarbonate cover fitted on an un-evacuated chamber;
- A 16mm polycarbonate cover fitted on an un-evacuated chamber.

The condenser area, the manifold structure, and the cooling liquid flow velocity, also influence heat transfer. A number of condenser/manifold configurations are investigated in this section. These are:

- The configuration shown in Figure 5-7, whereby the length of the manifold varies but the length of the condenser remains constant.

- The configuration shown in Figure 5-8.
- The configuration shown in Figure 5-9.

For the hybrid solar collector, its efficiency is also influenced by the channel geometry and flue gas properties, such as mass flow rate, and inlet and outlet temperatures. Both η and η_1 are used to evaluate the performance of the collector. However, to enable performance comparison between normal collectors and the hybrid collector, η is normally used as the major index.

5.3.1 Thin membrane heat pipe solar collector

A prototype thin membrane heat pipe solar collector was constructed following the design scheme. However, a major simplification was made, i.e., avoiding the use of elliptical covers and Fresnel lens, in order to simplify manufacture. The top cover may be one of the five configurations illustrated in Table 5-2. The miniature heat pipes were used as the basic elements of the absorber panel. The specifications of the panel/pipes configuration are shown in Table 5-3. A number of condenser/manifold configurations were also considered, as shown in Table 5-4.

External parameters were given by duplicating the real testing conditions, shown in Table 5-5. This enables comparison among the theoretical and experimental results to be made.

Table 5-2. Specifications of the top covers and their solar optical & thermal parameters

Parameter / Cover condition	τ_g (transmit.)	α_g (absorpt.)	ref_g (reflectivity)	ε_g (emmitance)	U, W/m².°C Ra,m².°C/W
1. single acrylic cover with a vacuum chamber	0.8	0.08	0.12	0.88	5.9 ∞
2. single acrylic cover with a chamber un-vacuumed	0.8	0.08	0.12	0.88	5.9 0. 18
3 double-glazing cover with a chamber un-vacuumed	0.5	0.21	0.29	0.88	1.2 0.18
4 10mm polycarbonate cover with a un-vacuumed chamber	0.85	0.07	0.08	0.88	3 0.18
5 16mm polycarbonate cover with a chamber un-vacuumed	0.82	0.07	0.11	0.88	2.4 0.18

Table 5-3. Specifications of the heat pipes and absorber panel

Absorpvity of absorber surface, α_s	0.95	Thermal conductivity of bottom plate, k_f, W/ m.°C	0.0015
Reflectivity of absorber surface, ref_s	0.05	Thickness of bottom plate, δ_f, m	0.0015
Emmitance of absorber surface, e_g	0.1	Number of heat pipes	22
Absorber area, A_s	0.24	Equivalent diameter of heat pipe(inner) d_{hp}, m	0.002
Unshaded absorber area, A_{us}	0.233	Length of evaporator l_{pe}, m	1
Heat resistance of inner surface, R_{in}, m^2.°C/W	0.12	Length of condenser l_{con}, m	0.1
Heat resistance of outer surface, R_{out}, m^2.°C/W	0.06	Thermal conductivity of heat pipe wall, λ_{hp}, W/ m.°C	43
Thermal conductivity of insulation layer 1, k_{i1}, W/ m.°C	0.005	Thickness of heat pipe wall, δ_{hp}, m	0.001
Thickness of insulation layer 1, δ_{ins1}, m	0.025	Thermal conductivity of liquid film on heat pipe inner wall, λ_w, W/ m.°C	0.68
Thermal conductivity of insulation layer 2, k_{i2}, W/ m.°C	0.046	Equivalent diameter of vapour column in evaporator d_{ve}, m	0.00196
Thickness of insulation layer 2, δ_{ins2}, m	0.005	Equivalent diameter of vapour column in condenser d_{con}, m	0.0019

Table 5-4. Specifications of the condenser/manifold configurations

Condenser/manifold conditions	1. 100% of the orginal size	2. 75% of the original size	3. 50% of the original size
Heat transfer area in condenser/manifold A_{con}, m^2	1.884e-3	1.413e-3	0.992e-3
Thickness of the manifold wall, δ_{man}, m	0.001	0.001	0.001
Thermal conductivity of the manifold wall, λ_{man}, W/ m.°C	43	43	43
Mass flow rate of cooling liquid ms, kg/h	30	30	30
Cross sectional area of cooling liquid flow, A_{cross}, m^2	0.0014	0.00105	0.0007
Width of inner wall of the manifold a_1, m	0.006	0.006	0.006
Width of outer wall of the manifold a_2, m	0.03	0.03	0.03

Table 5-5. Summary of the external parameters

I_n, W/m^2	1033	1033	1027	998	1031	949	962	968
t_a, °C	19.1	19.9	20.3	21.3	22.5	17.7	18.3	18.9
m_s, kg/h	30.1	30	30	30.1	30.1	30.1	30.2	30
t_{inlet}, °C	17.1	17.2	17.4	54.9	55.0	79.4	79.5	79.7

Comparison of different cover conditions

η - $(t_{mean}-t_a)/I_n$ relations for different top cover conditions were investigated using the computer model developed, and the results are shown in Figure 5-11. Of the five cover configurations, the evacuated one has the highest efficiency, which results in the largest heat output, and the single acrylic with an un-evacuated chamber has the lowest efficiency, resulting in the smallest heat output. Although the polycarbonate has a higher U value than the double-glazing which may lead to more heat loss from the cover, it still performs better than the double-glazing. The major reason for this is that the polycarbonate sheet has higher solar transmittance than the double-glazing one, which would result in higher solar absorption. Due to difficulty in creating an evacuated condition for the chamber, a thermo-clear polycarbonate cover fitted for an un-evacuated chamber may be a better option. Theoretical investigation showed that the efficiency curve for this situation is close to that of the evacuated one.

For any cover condition, η decreased while $(t_{mean}-t_a)/I_n$ increased. The relation of η and $(t_{mean}-t_a)/I_n$ was approximately linear, which is shown in Figure 5-11. The character parameters for the five cover conditions are listed in Table 5-6.

Table 5-6. Characterstic parameters for the efficiency- $(t_{mean}-t_a)/I_n$ curves under different top covers

Cover condition / parameters	Cover condition 1	Cover condition 2	Cover condition 3	Cover condition 4	Cover condition 5
η_0	74.41	61.234	66.460	72.145	72.576
α_1	105.39	376.9	106.54	240.54	198.86

Comparison of different condenser/manifold configurations

η - $(t_{mean}-t_a)/I_n$ relations under different condenser/manifold conditions were investigated using the computer model developed, and the results are shown in Figures 5-12. Changing length of the condenser, resulting in changing of heat transfer area, was found to influence the collector efficiency. For any cover condition, the longer the condenser, the larger the heat transfer area, and hence the higher the efficiency. However, increasing length of the condenser may be limited by a few factors, such as the installation space etc, for most applications. In this case, length of the condenser was selected as 10% of the length of the evaporator, as the cooling liquid, i.e., water, has higher heat transfer rate than air for the evaporation section.

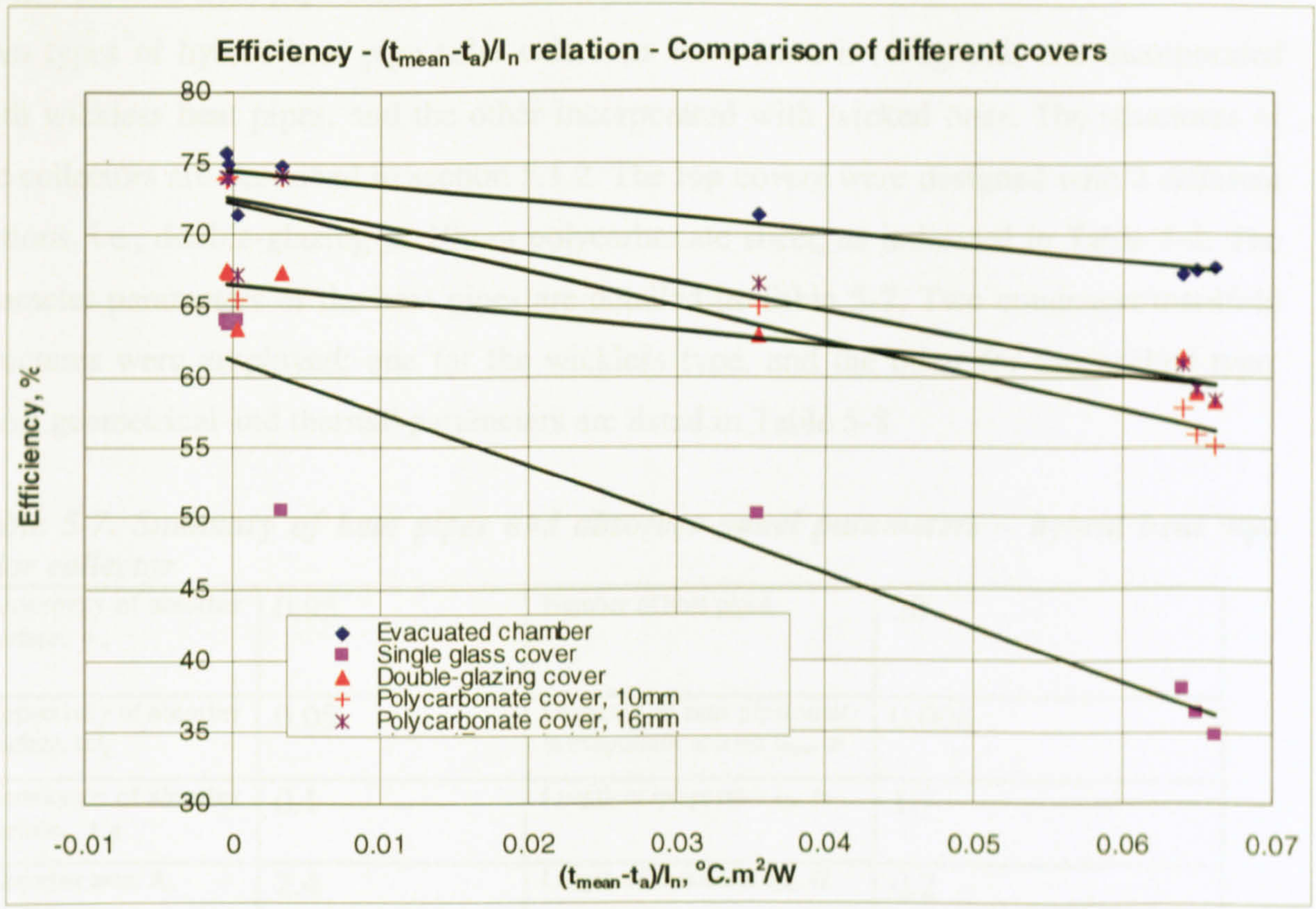

Figure 5-11. $\eta - (t_{mean} - t_a)/I_n$ relation – comparison of different top covers

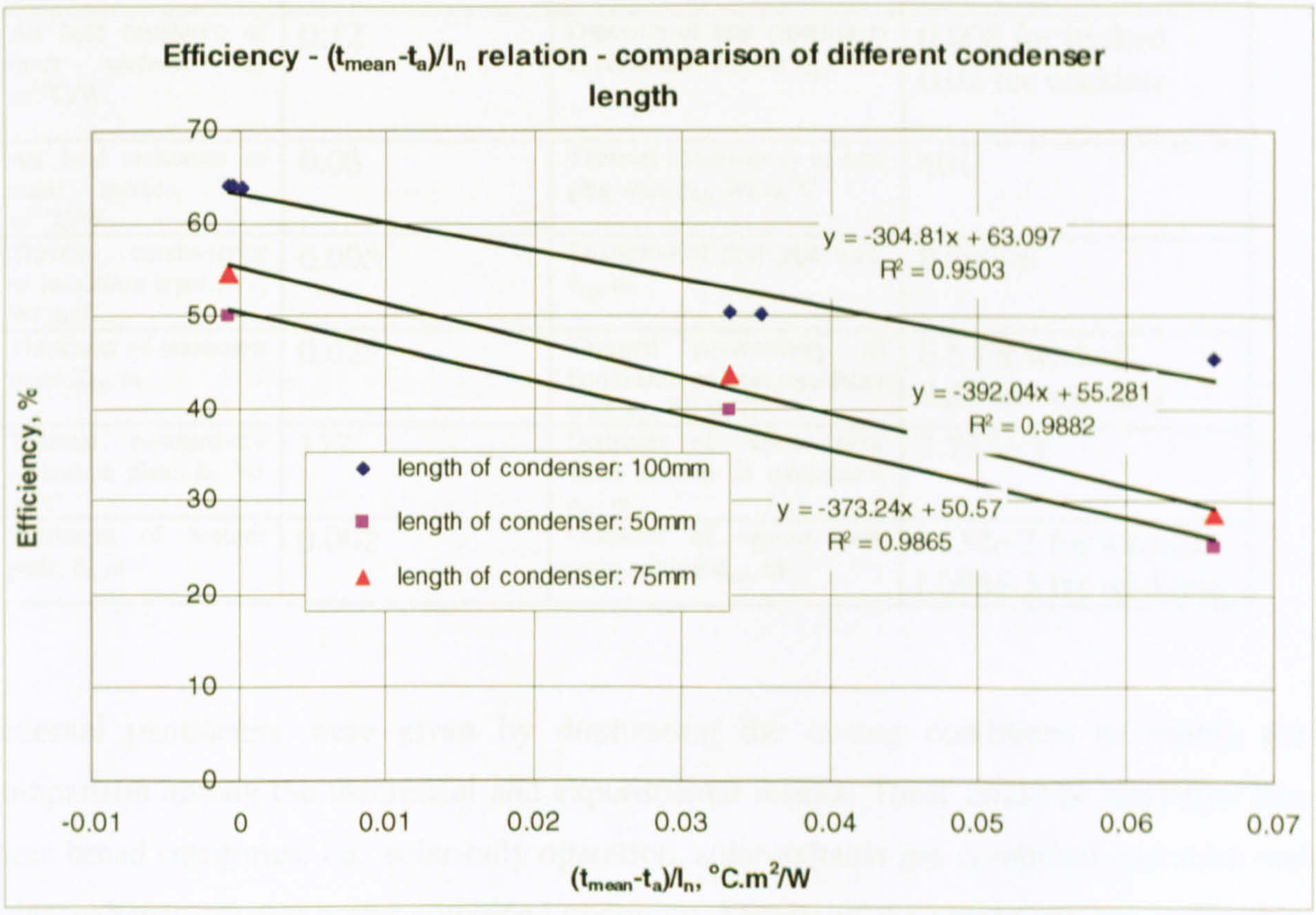

Figure 5-12. η - $(t_{mean}-t_a)/I_n$ relation – comparison of different lengths of condenser (un-evacuated single acrylic cover)

5.3.2 Hybrid heat pipe solar collector

Two types of hybrid heat pipe solar collectors have been investigated; one incorporated with wickless heat pipes, and the other incorporated with wicked ones. The structures of the collectors are described in section 5.1.2. The top covers were designed with 2 different options, i.e., double-glazing or 10mm polycarbonate sheet, as indicated in Table 5-2. The character parameters of the heat pipes are detailed in Table 5-7. Two condenser/manifold structures were employed; one for the wickless type, and the other for the wicked type. Their geometrical and thermal parameters are listed in Table 5-8.

Table 5-7. Summary of heat pipes and absorber panel parameters – hybrid heat pipe solar collector

Absorpvity of absorber surface, α_s	0.95	Number of heat pipes	20
Reflectivity of absorber surface, ref_g	0.05	Diameter of heat pipe(outer) in evaporator section d_{hpe}, m	0.008
Emmitance of absorber surface, ε_g	0.1	Length of evaporator l_{pe}, m	1.7
Absorber area, A_s	2.4	Length of condenser l_{con}, m	0.2
Unshaded absorber area, A_{us}	2.21	Length of adiabatic section l_{pa}, m	0.07
Air heat resistance of inner surface, R_{si}, $m^2.°C/W$	0.12	Diameter of heat pipe(outer) in condenser section d_{hpc}, m	0.008 for wicked 0.02 for wickless
Air heat resistance of outer surface, R_{out}, $m^2.°C/W$	0.06	Thermal conductivity of heat pipe wall, k_{hp}, W/ m.°C	401
Thermal conductivity of insulation layer , k_{i1}, W/ m.°C	0.005	Thickness of heat pipe wall, δ_{hp}, m	0.00376
Thickness of insulation layer , δ_{i1}, m	0.025	Thermal conductivity of liquid film on heat pipe inner wall, k_w, W/ m.°C	0.5 for wicked 0.68 for wickless
Thermal conductivity of bottom plate, k_f, W/ m.°C	177	Diameter of vapour flow cross section in evaporator d_{ve}, m	3.752e-3
Thickness of bottom plate, δ_f, m	0.002	Diameter of vapour flow cross section d_{con}, m	3.752e-3 for wicked 1.094e-3 for wickless

External parameters were given by duplicating the testing conditions to enable the comparison among the theoretical and experimental results. These could be classified into three broad categories, i.e., solar-only operation, solar-exhaust gas combined operation and solar, exhaust gas and boiler combined operation. Details of the conditions are outlined in Table 5-9.

Table 5-8. Summary of condenser/manifold structure conditions

Condenser/manifold conditions	Wicked 1	Wicked 2	Wickless 1	Wickless 2
Heat transfer area in condenser/manifold A_{con}, m^2	0.006	0.012	3.5325e-3	7.065e-3
Thickness of the manifold wall, δ_{man}, m	1.5e-3	1.5e-3	1.5e-3	1.5e-3
Thermal conductivity of the manifold wall, k_{man}, W/ m.°C	110	110	110	110
Mass flow rate of cooling liquid m, kg/h	168	168	168	168
Cross sectional area of cooling liquid flow, A_{cross}, m^2	3.998e-4	7.996e-4	3.999e-4	7.999e-4
Width of inner wall of the manifold a_1, m	0.012	0.012	0.012	0.012
Width of outer wall of the manifold a_2, m	0.020	0.020	0.020	0.020

Table 5-9. Summary of the external parameters

Parameter / Case	I_n, W/m^2	t_{air}, °C	m_s, kg/h	t_{inlet}, °C	L_{gas}, m^3/s	$t_{gas,in}$
Solar only	700	9	168	10-25	-	-
Solar-gas	720	11	168	9-24	0.035	92
Solar-gas-boiler	400	11	168	88-100	0.035	114

Case 1. Solar-only operation

Comparison of different types of solar collectors

η - $(t_{mean}-t_a)/I_n$ relations for two types of solar collectors (wickless and wicked) were investigated using the computer model developed previously, and the results are shown in Figures 5-13. Although the wicked collector was fitted with cavity-drilled copper rods between the condensers and the manifold which may introduce an extra heat resistance to heat transfer, the wicked version has a higher efficiency than the wickless collector. This is due to the wicked collector having a larger heat transfer area in the condensation section than the wickless collector. This indicates that the heat transfer area is an important parameter imposing a substantial effect on collector performance.

For any type of collector, η decreases while $(t_{mean}-t_a)/I_n$ increases. The relation of η and $(t_{mean}-t_a)/I_n$ is expressed by a second-order equation, which is shown in Figure 5-13.

Since the wicked collector is superior in performance to the wickless one, subsequent investigations focuse on the wicked type.

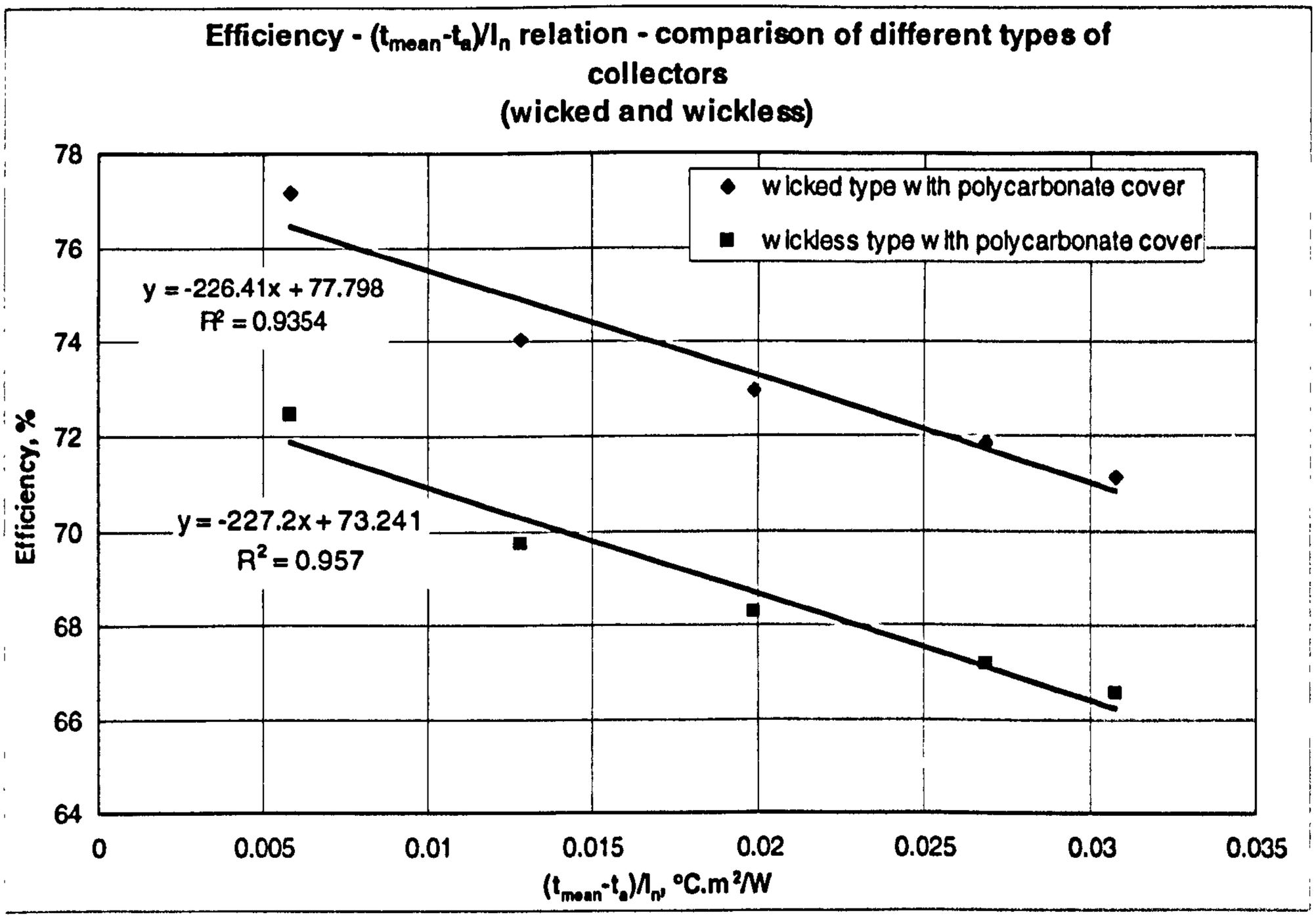

Figure 5-13. $\eta - (t_{mean}-t_a)/I_n$ relation – comparison of different types of collectors (wicked and wickless)

Comparison of different cover configurations

η - $(t_{mean}-t_a)/I_n$ relations for the two top cover configurations were investigated using the computer model developed, and the results are shown in Figure 5-14. Although the polycarbonate cover has a higher U value (3W/m^2.°C) than the double-glazing (1.1 W/m^2.°C) which may lead to a larger heat loss to the ambient, the collector with the polycarbonate cover still perform better than the one with double-glazing cover. This is due to the higher solar transmittance (0.85) of polycarbonate compared to double-glazing (0.49) leading to greater heat absorption. This demonstrates the greater impact of solar transmittance on heat efficiency compared to U value.

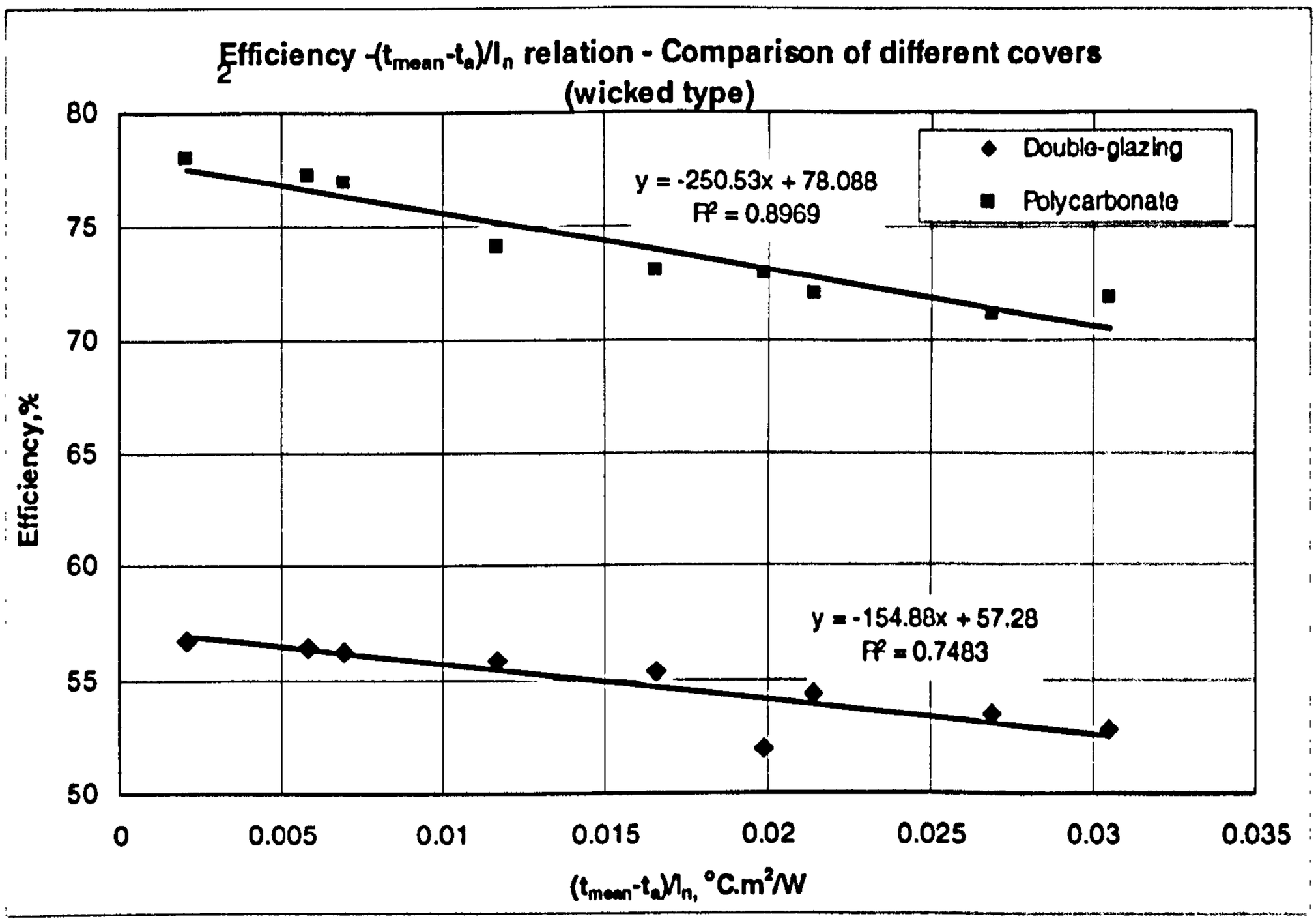

Figure 5-14. η - $(t_{mean}-t_a)/I_n$ relation – Comparison of different covers (wicked type)

<u>Comparison of different condenser/manifold configurations</u>

η - $(t_{mean}-t_a)/I_n$ relations for different condenser/manifold configurations were investigated using the computer model, and the results are shown in Figures 5-15. Effective length of the condenser is hereby used to evaluate the performance of the condenser/manifold configuration, and this is defined as the length of the part that the condenser and the manifold are in common. Increasing the effective length of the condenser results in an increase of the heat transfer area between the manifold and the condenser, and leads to an increase of collector efficiency.

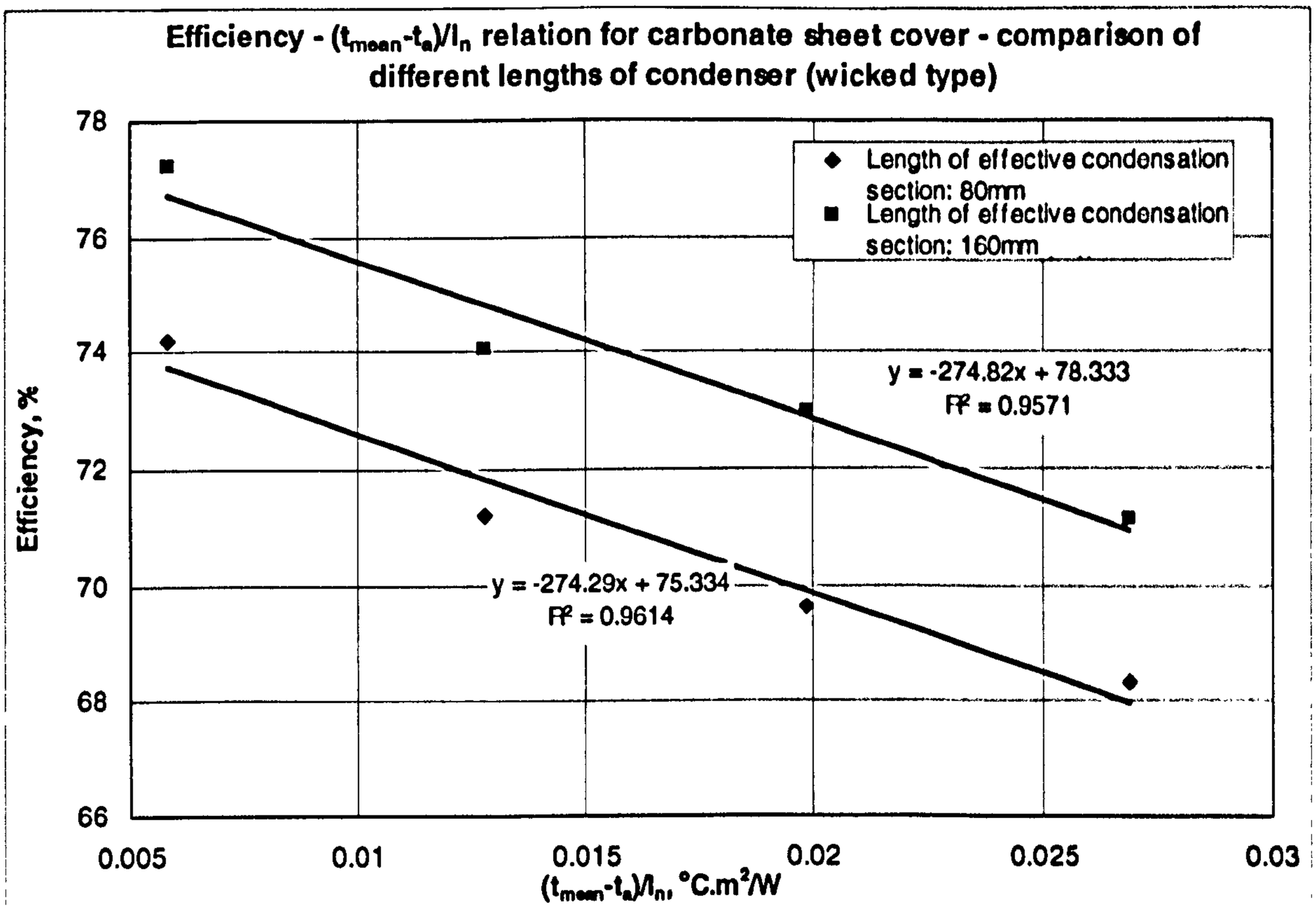

Figure 5-15. $\eta - (t_{mean}-t_a)/I_n$ relation for polycarbonate cover – comparison of different effective lengths of condenser (wicked type)

Case 2. Solar-exhaust gas combined operation

The collector incorporated by wicked heat pipes, fitted with a 10mm thick polycarbonate cover and having a 160mm long effective condenser section, was investigated. Two efficiencies, η and η_1, were calculated using the computer model and the results are shown in Figure 5-16. As in the previous cases, η and η_1 decrease while $(t_{mean}-t_a)/I_n$ increases. Compared to the case of solar-only operation, η increases by around 40% and achieves 100% to 120%. This demonstrates that utilising waste heat from exhaust gas could enhance collector efficiency significantly. The other efficiency parameter, η_1, is still low (around 35% to 45%), as the waste heat from exhaust gas was considered as a heat input.

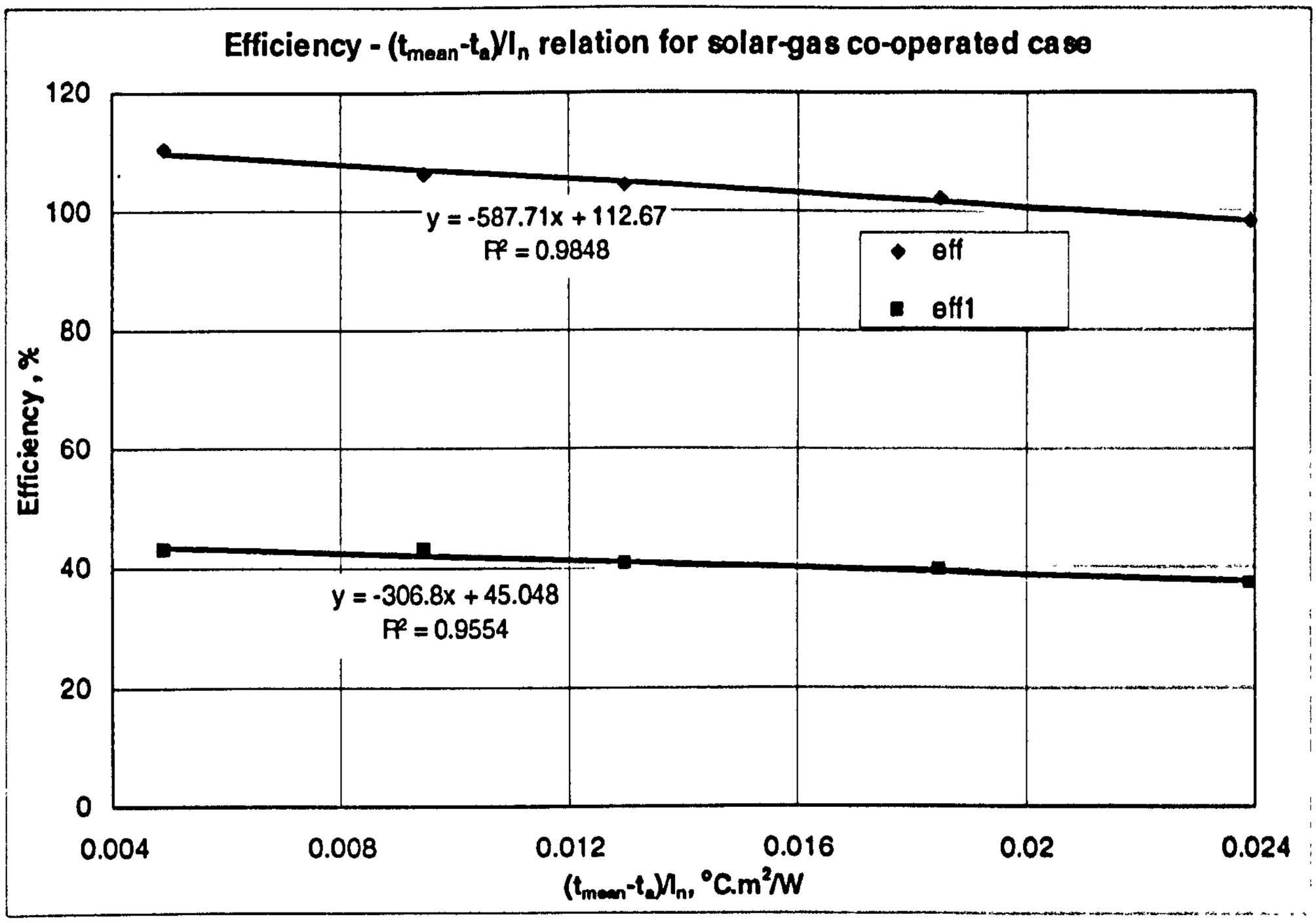

Figure 5-16. η (η_1) – $(t_{mean}-t_a)/I_n$ relations for solar-gas co-operated case

Case 3. Solar, exhaust gas and boiler combined operation

This collector could work in conjunction with a boiler in order to provide heat required for a CHP system operation. The boiler is able to produce a large amount of heat that could quickly raise the temperature of water to 90°C to 100°C. Part of the return water passed through the manifold to absorb heat from solar and exhaust gas inputs via the collector, and the remainder was compelled to by-pass the collector as the water flow rate in the system was so high that it was not possible to pass all of water through the collector manifold. The two diverted water flows were then merged before being delivered to the boiler for further heating. The collector was thus linked to a massive system, which has relatively large heat capacity than what the collector could provide.

As for the situation of case 2, two efficiencies, η and η_1, were calculated using the computer model, and the results are shown in Figure 5-17. It can be seen that as in the solar/gas case η and η_1 decrease while $(t_{mean}-t_a)/I_n$ increases. Compared to the case of solar-

gas combined operation, η decreases by around 60% and drops to 25% to 50%, and η_1 drops to even lower level (around 5% to 15%). This demonstrates that increasing the inlet water temperature would lead to a significant reduction of collector efficiency. If more heat is required for CHP operation it would therefore be necessary to increase the number of the solar collectors.

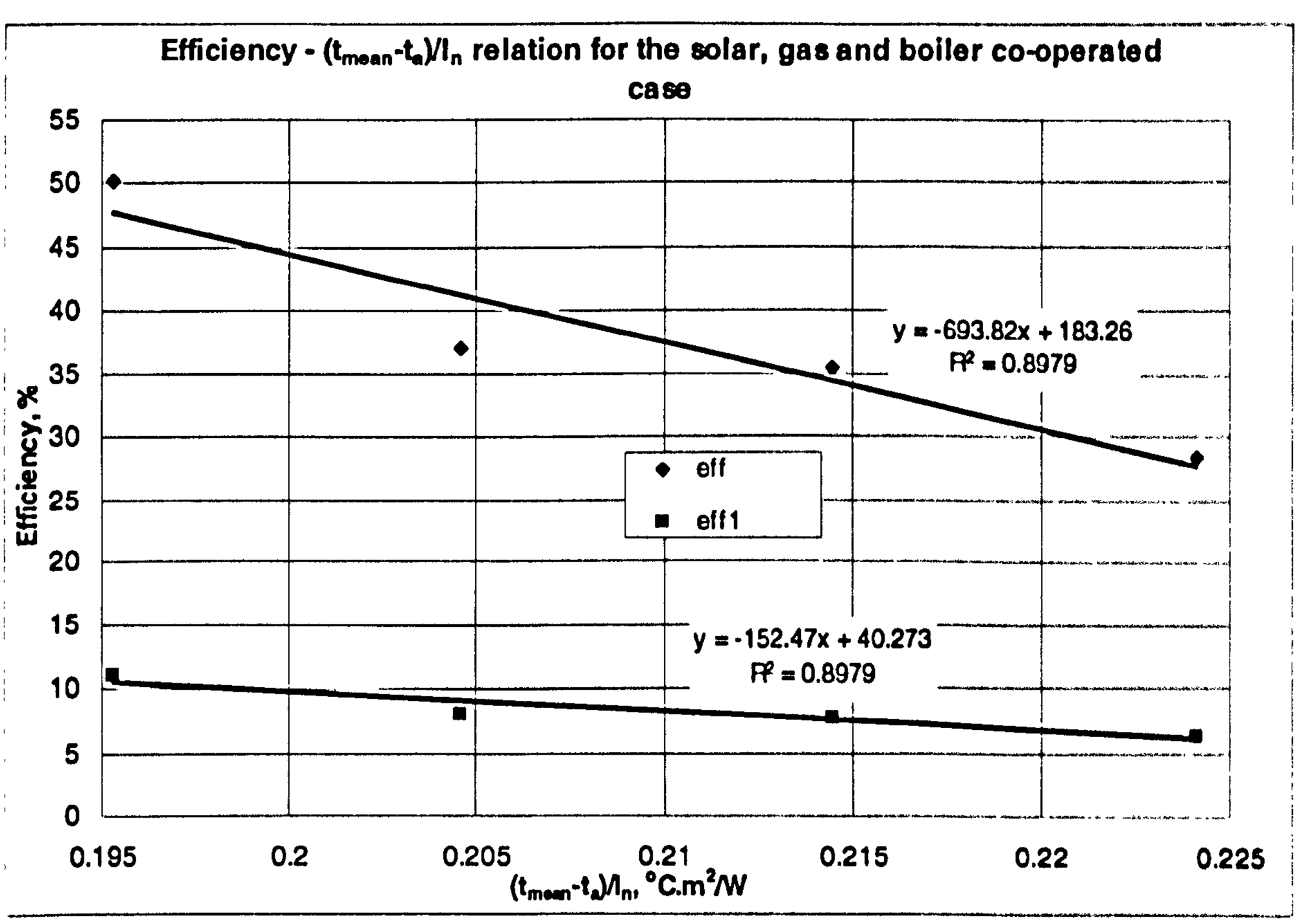

Figure 5-17. η (η_1) – $(t_{mean}-t_a)/I_n$ relations for solar, gas and boiler combined operation

5.4 Experimental Testing

5.4.1 Thin Membrane Heat Pipe Solar Collector

A prototype thin membrane heat pipe solar collector was tested at the laboratory of Fraunhofer Institute for Solar Energy System (ISE) in Germany, by complying with the European Standard of prEN 12975: 1999 [Rommel Matthias, 2000]. Photographs of the tested collector are shown in Figure 5-18(1) and 5-18(2). The collector has a gross area of 0.4m^2, of which 0.255 m^2 is the absorber area, and the rest the condensation area. The absorber area is also not completely utilised because of the edge effect, and the un-shadowed area is only 0.233m^2.

An outdoor climate was manually created in the Lab space. The wind speed was measured at the middle area of the collector module, 5cm above the transparent cover, and adjusted to 3m/s by using a ventilator. Special optical bulbs were scatter-distributed at the dome area to simulate the global solar irradiation. Photographs of the testing rig and laboratory layout are shown in Figures 5-19 (1) and 5-19(2), respectively.

Water was used as the cooling liquid, which passed through the collector manifold at the rate of 30kg/h during the period of testing.

Test conditions complied well with the European Standard prEN 12975: 1999, which are indicated in Table 5-10. Test results obtained were used to calculate collector efficiency, as shown in Table 5-10 as well as Figure 5-20. The character parameters indicating the collector performance are given as: $\eta_0 = 0.6969$; $\alpha_1 = 3.5333$; $\alpha_2 = 16.581$.

Table 5-10. Test results for the thin membrane heat pipe solar collector

I_n W/m^2	$I_{diffuse}$ W/m^2	t_a °C	m_s kg/h	t_{inlet} °C	t_{outlet} °C	$t_{outlet} - t_{inlet}$, °C	t_{mean} °C	$(t_{mean}-t_a)/I_n$ °C.m^2/W	η
1033	85	19.1	30.1	17.1	21.8	4.7	19.5	0.0003	0.6847
1033	87	19.9	30	17.2	22.1	4.9	19.7	-0.0002	0.7073
1027	90	20.3	30	17.4	22.2	4.8	19.8	-0.0005	0.7006
998	121	21.3	30.1	54.9	58.6	3.7	56.7	0.0335	0.5561
1031	135	22.5	30.1	55	58.8	3.8	56.9	0.0333	0.5578
949	110	17.7	30.1	79.4	81.8	2.4	80.6	0.0663	0.3869
962	109	18.3	30.2	79.5	82.1	2.5	80.8	0.0649	0.3944
968	110	18.9	30	79.7	82.3	2.6	81.0	0.0642	0.4040

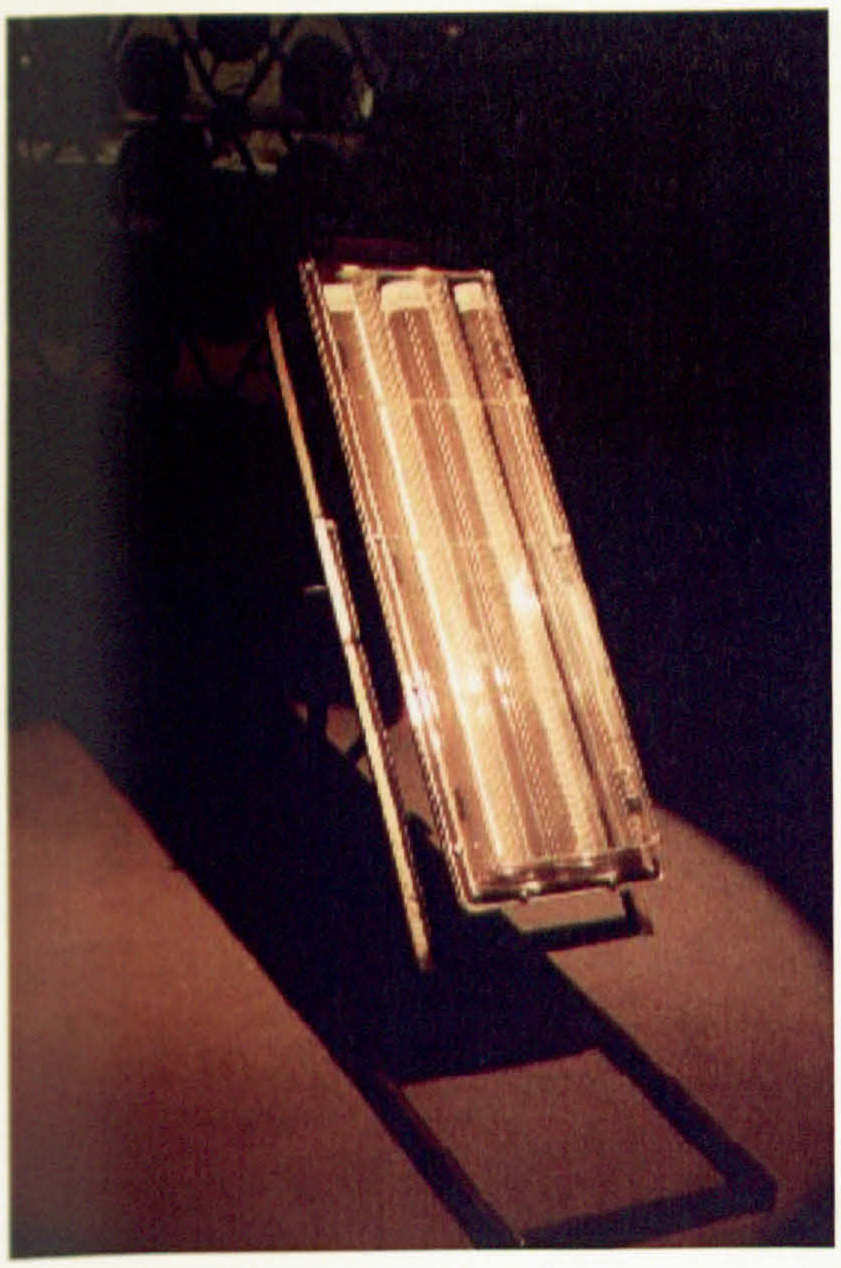

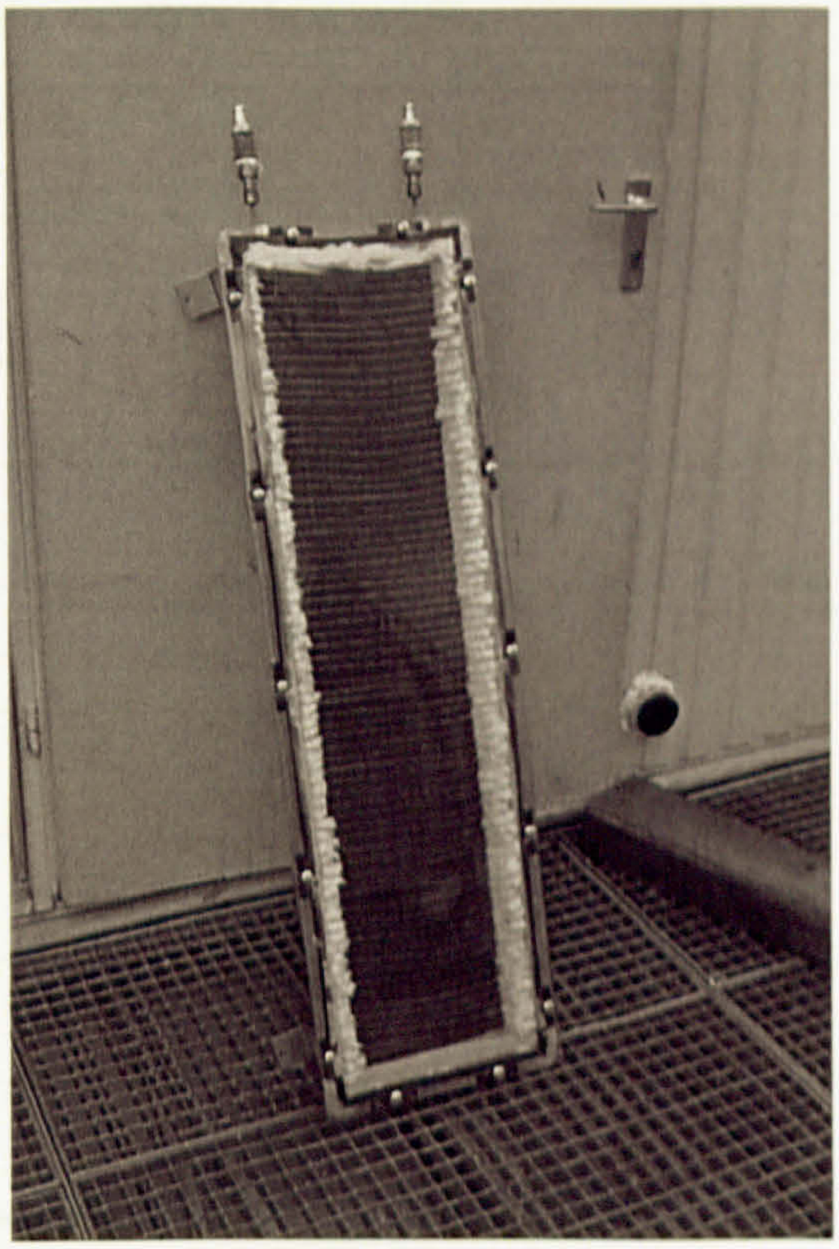

(1) *(2)*

Figure 5-18.The tested module collector

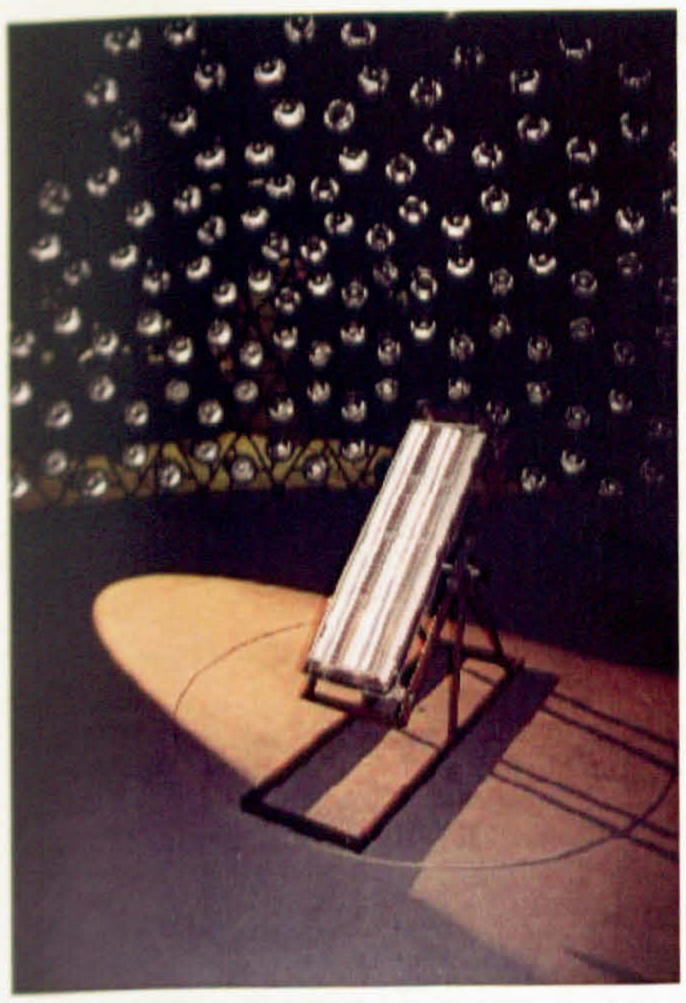

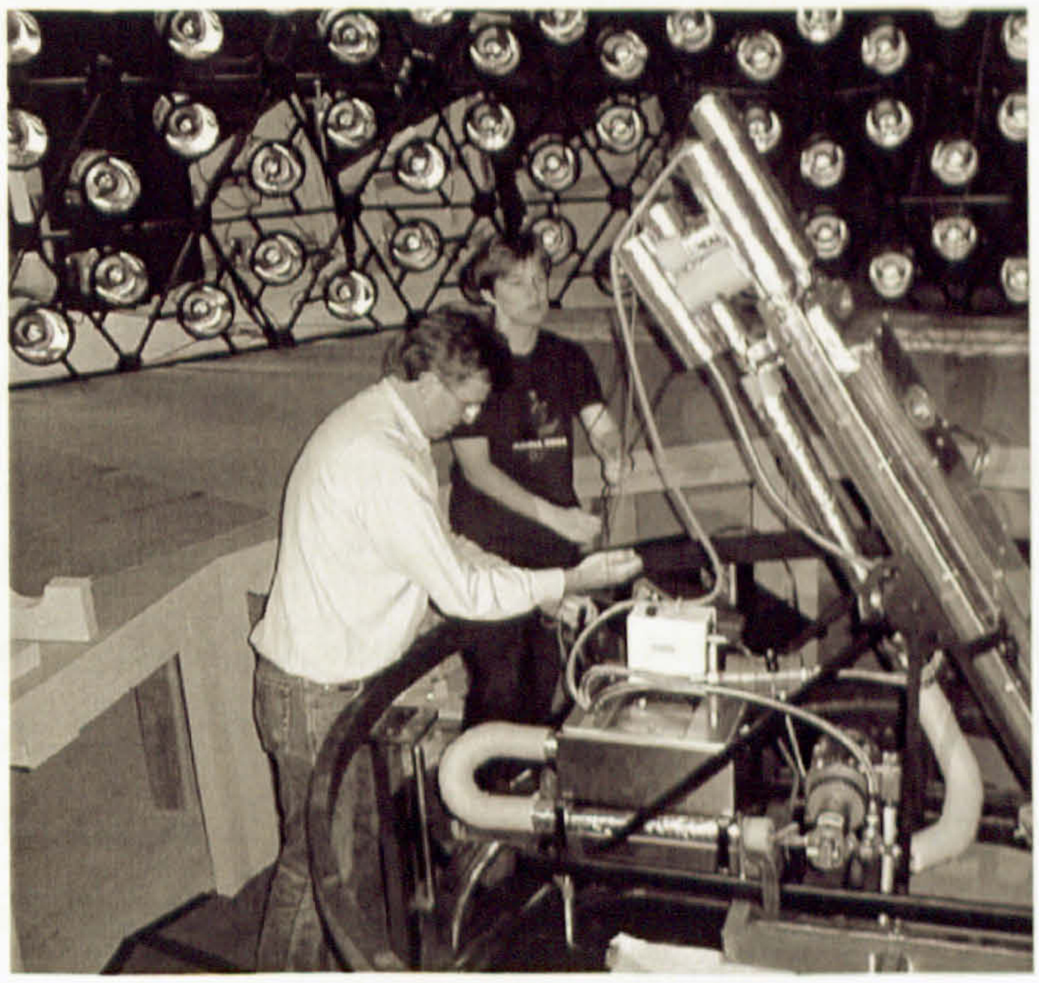

(1) *(2)*

Figure 5-19. The laboratory layout and test rig

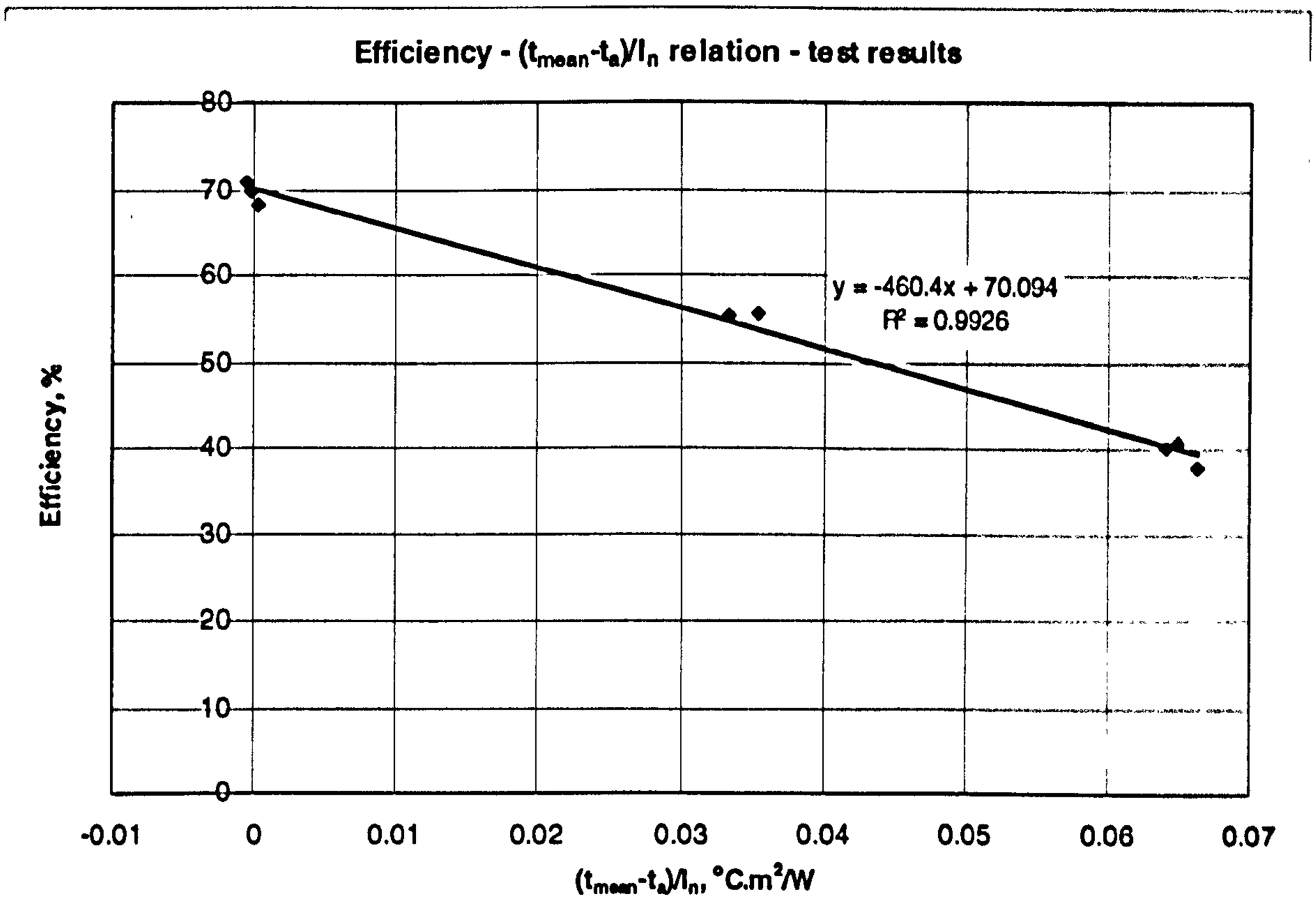

Figure 5-20. $\eta - (t_{mean} - t_a)/I_n$ relation – test results of the thin membrane heat pipe solar collector

5.4.2 Hybrid heat pipe solar collector

A prototype hybrid heat pipe solar collector (wicked type) was mounted outside a laboratory building at the University of Nottingham, adjacent to a shed housing the boiler that was to be used as part of the heat source of a CHP system. The collector was co-operated with the boiler to supply heat for the CHP system. It was intended to direct the exhaust flue gas from the boiler across the flow channels fitted to the backside of the solar collector to enhance its heat transfer, and provide compensation, or back up, when solar irradiation was low or unavailable. However, it was not possible to carry this out in practice for safety reasons. In order to simulate the intended situation, a flue gas simulator was used to generate hot air equivalent to gas flow. The specifications and outer view of the simulator are shown in Figure 5-21. T-type thermocouple probes (Figure 5-22) were mounted on the inlet and outlet of the collector to measure water temperature, and a single jet water meter (Figure 5-23) was mounted on the pipeline connected to the collector to measure water flow rate. A normal T-type thermocouple (Figure 5-24) was hung in the air to measure outdoor temperature, and a pyranometer (Figure 5-25) was fixed to the absorber surface of the collector to measure instant global solar radiation. Each of item measurement

instrumentation was connected to a Datataker (DT 500) which acquired data from the measured points and transferred these to a computer. The collector was connected to the main flow system that included the boiler and CHP test rig. When CHP operation stopped, the boiler also ceased operation. The layout of the integrated system, including the outdoor and indoor parts, is shown in Figures 5-26 and 5-27.

Heat output: 3kW;
Flow rate: 0.035m3/s;
Voltage: 120v – 240v;
Power: 2 phase, 50HZ

Figure 5-21. The flue gas simulator

Type: CM 6B;
Sensitivity: 9-15 mV/Wm-2;
Signal output: 0-25Mv;
Max irradiance: 2000Wm-2;
Accuracy: +/- 5%

Figure 5-25. The pyranometer

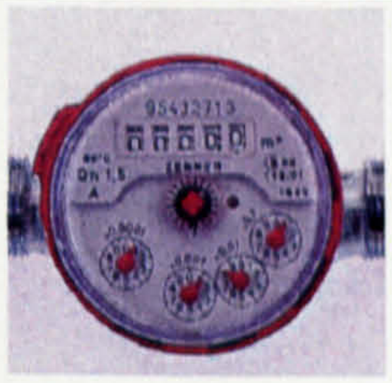

Pressure: <16bar;
Temperature: <100°C;
Flow rate: 100-5000 l/hr

Figure 5-23. The single jet water meter

Type: T
Temperature range: -418~700;
Probe length: ¼'';
Diameter: 0.25''
Time constant: 6 sec
Response time: 30 sec

Figure 5-22. The T-type thermocouple probe

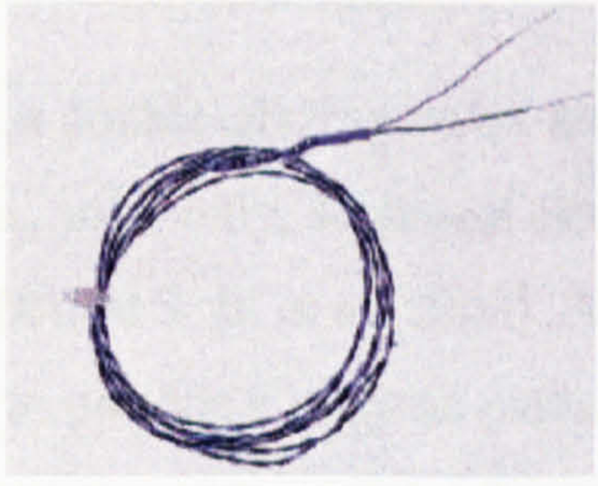

Type: T
Welded Tip PTFE Insulated;
Temperature range: -20~250°C;

Figure 5-24. The T-type thermocouple

Figure 5-26. Layout of the integrated hybrid solar collector/CHP system – outdoor part

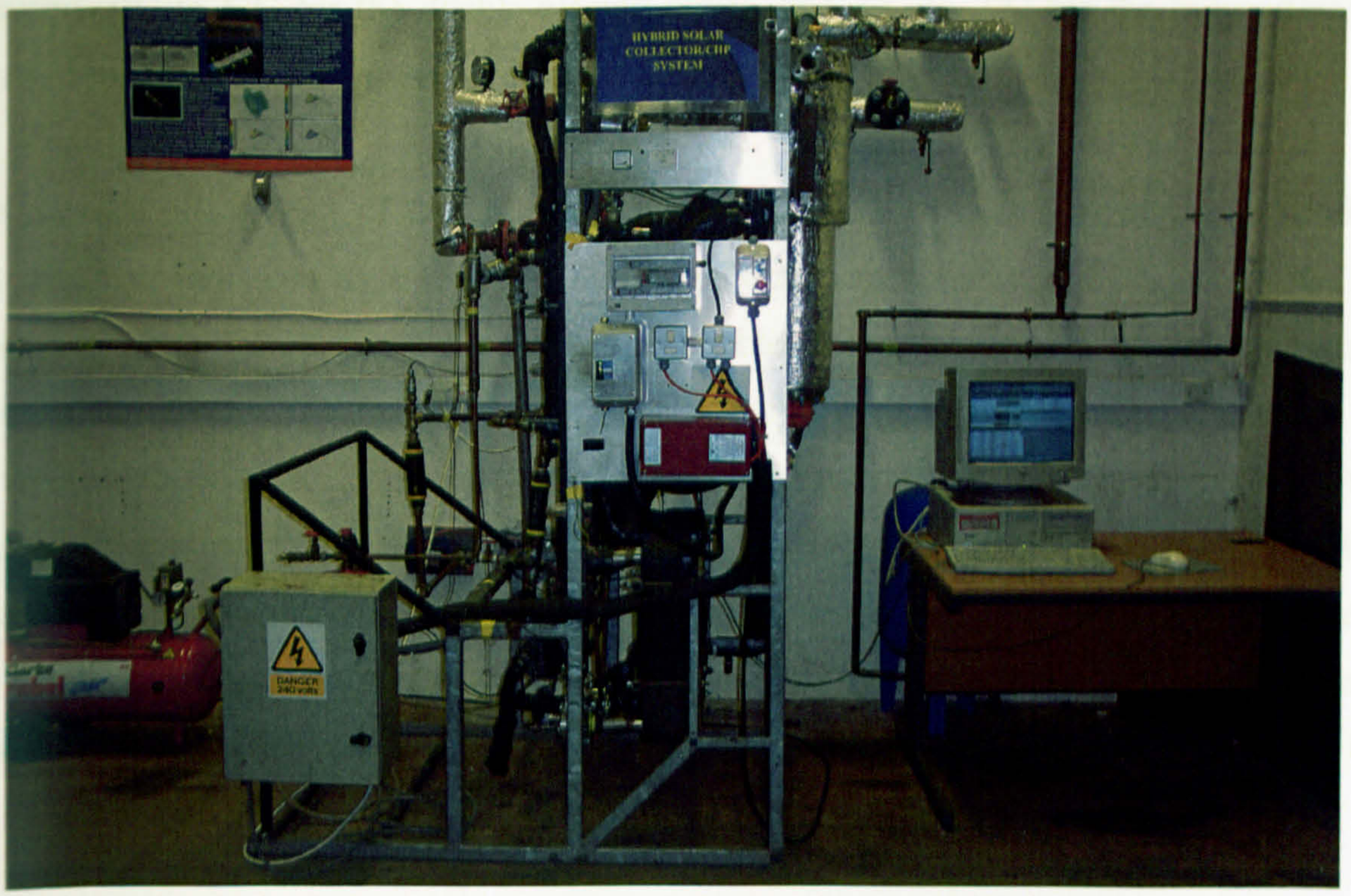

Figure 5-27. Layout of the integrated hybrid solar collector/CHP system – indoor part

Tests were carried out for collectors with a double-glazing cover and with a polycarbonate cover under three modes of operations, i.e., solar only, solar and exhaust gas combined and solar, gas and boiler combined operation [Riffat S. B. et al, 2003]. All the tests were carried out under real weather situations in order to provide a realistic evaluation of behaviour. For the collector with a polycarbonate cover, tests were carried out on three separate days for each mode of operation in order to examine the reliability and repeatability of its performance data. The collector with the polycarbonate cover was selected for this trial as it is the one most likely to be accepted for future application. The volume of the system is very large (about $8m^3$) compared to the measured flow rate (2.8l/m) through the collector, and this would ensure a steady solar-heating process during the testing period.

Tests for solar-only operation

For the situation of solar only operation, no flue gas flowed through the collectors. The heating processes for the collectors with the double glazing cover and with the polycarbonate cover are shown in Figures 5-28, 5-29, 5-30 and 5-31. The variation of solar irradiation, water inlet and outlet temperatures, and the outdoor temperature during the periods of testing are presented. It was found that the water temperature increased steadily for both types of collector, and the outlet/inlet temperature difference varied slightly

between 3°C to 5°C for the double-glazing cover, and 4°C to 7°C for the polycarbonate cover, depending on the intensity of solar irradiation.

The thermal efficiencies of the collectors were calculated using the experimental results, and are also indicated as a function of the general parameter $(t_{mean}-t_a)/I_n$, as shown in Figures 5-32 and 5-33, for the cases of the double-glazing cover and the polycarbonate cover, respectively. The moving average method was used in the calculation in order to provide average values for the measured parameters in every 10 minutes interval. Trend-lines were produced to describe this variation. For the two collectors investigated, the efficiency decreased when $(t_{mean}-t_a)/I_n$ increased. However, it may also be seen that there are several measurement points scattered away from the trend-lines, and hence square errors in the range 0.8 to 0.9 exist for the mathematical treatment. This may be caused by the slow response of the system due to its massive volume.

It was found that the double-glazed collector and the polycarbonate covered collectors had efficiencies in the range 30% to 45%, and 40% to 60%, respectively when $(t_{mean}-t_a)/I_n$ varied between 0 to 0.045. This indicates that the polycarbonate covered version performed better than the double-glazed collector owing to the higher solar transmittance of the former. It was therefore decided to use polycarbonate cover in the final version of the prototype.

It was also found that the efficiency curves of the polycarbonate covered version obtained from three separate tests show good similarity. This indicates that the collector had a relatively stable performance.

Figure 5-28. Heating process of the collector with double-glazing cover (solar only operation)

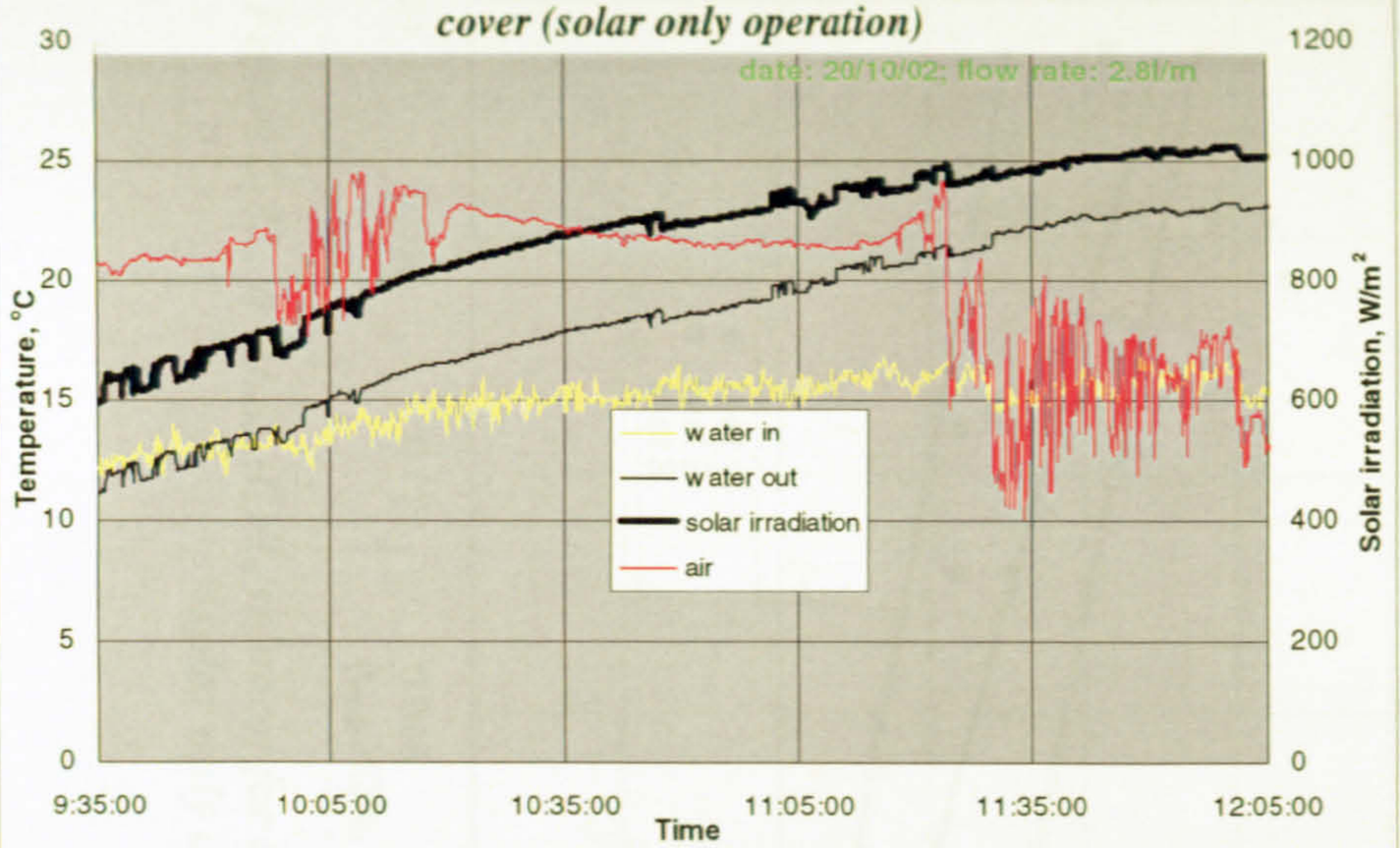

Figure 5-29. Heating process of the collector with polycarbonate cover (solar only operation) – test 1

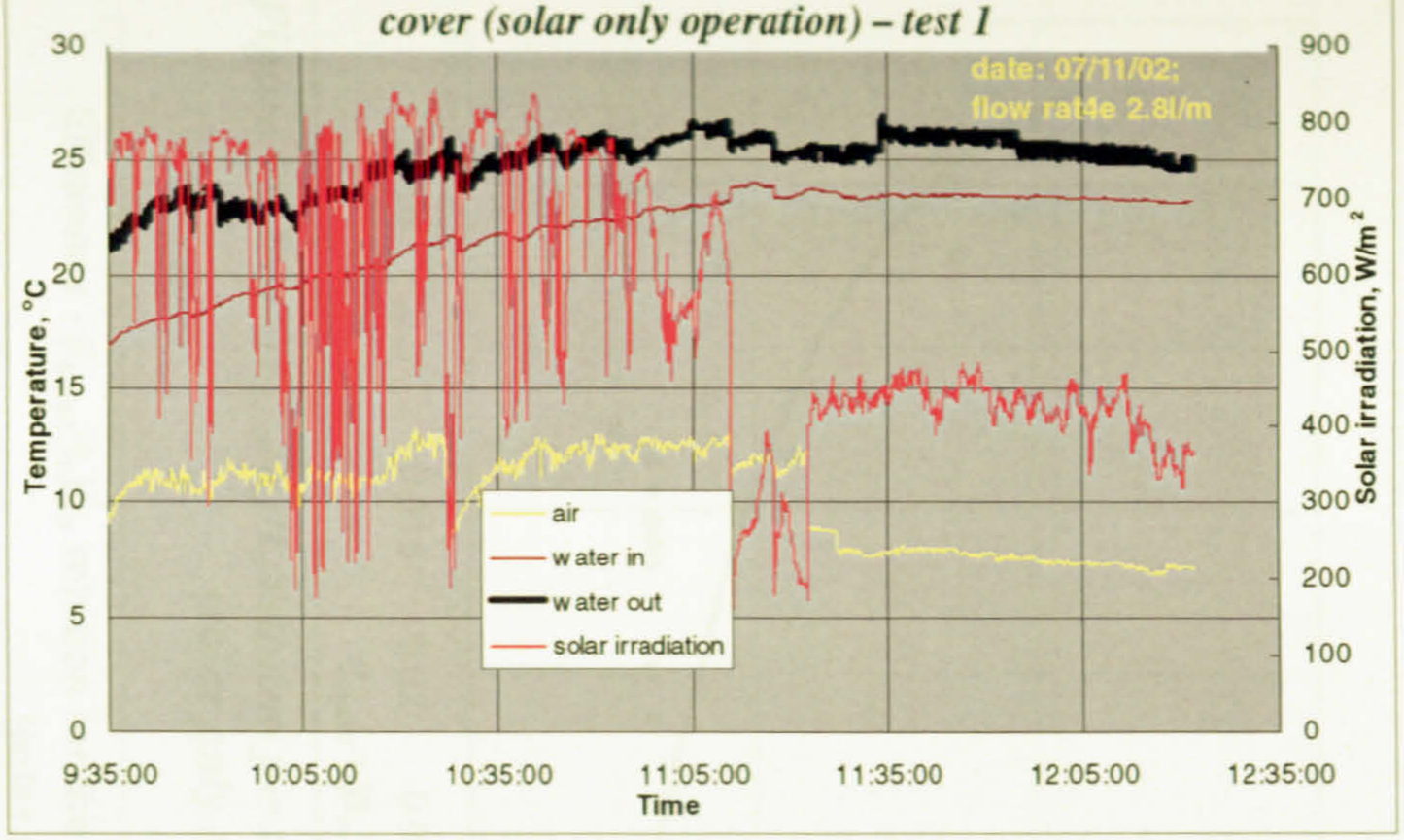

Figure 5-30. Heating process of the collector with polycarbonate cover (solar only operation) – test 2

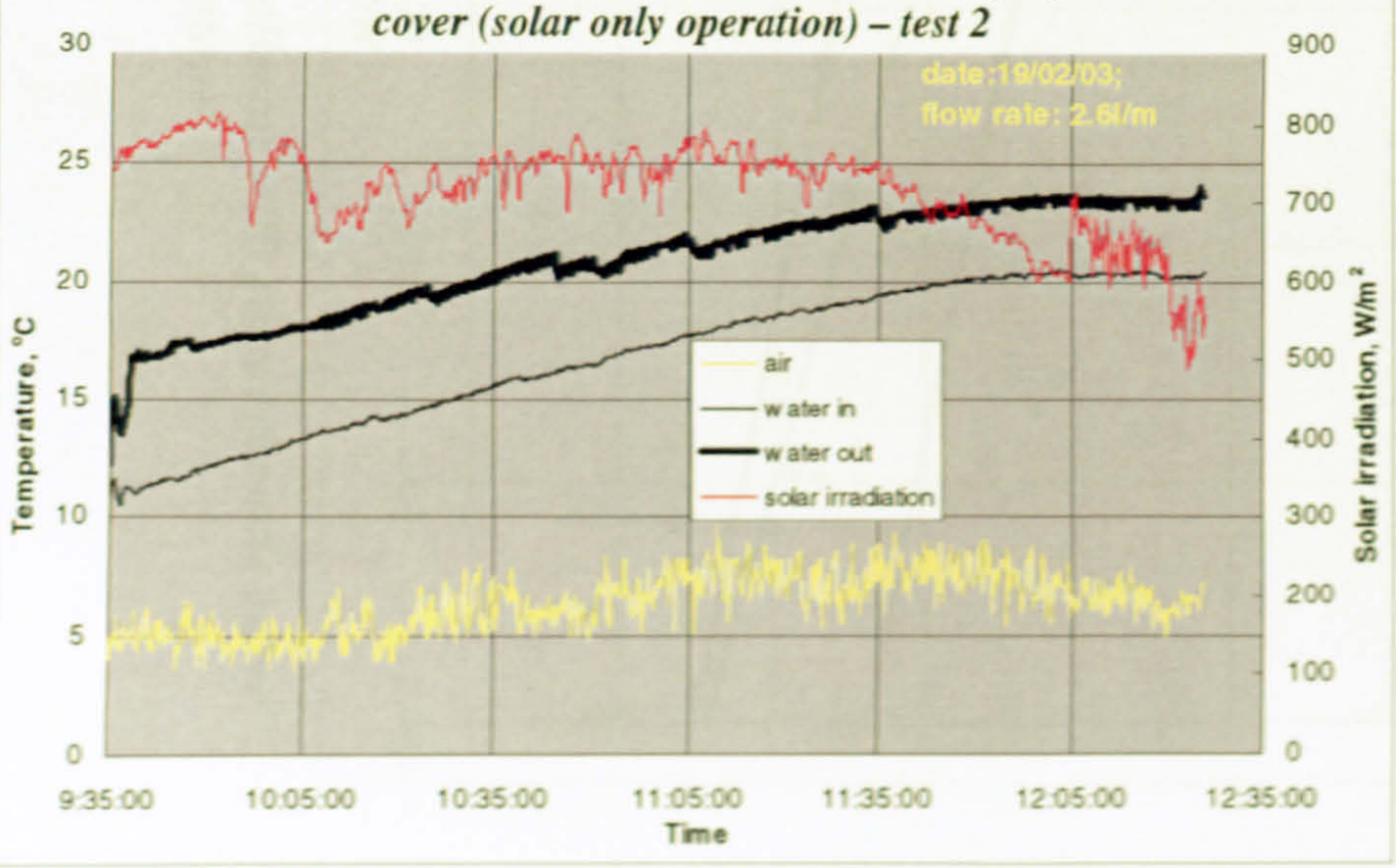

Figure 5-31. Heating process of the collector with polycarbonate cover (solar only operation) – test 3

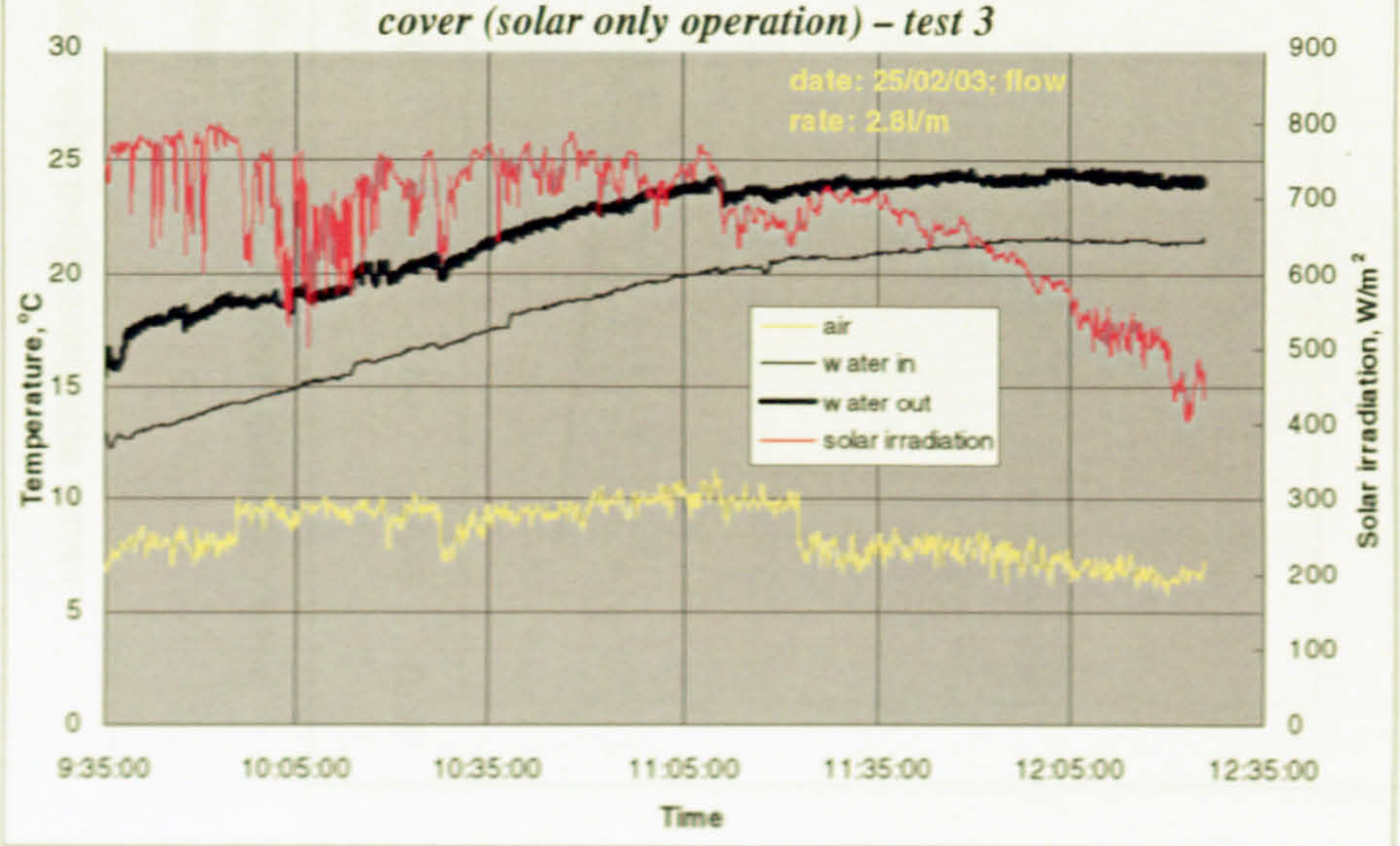

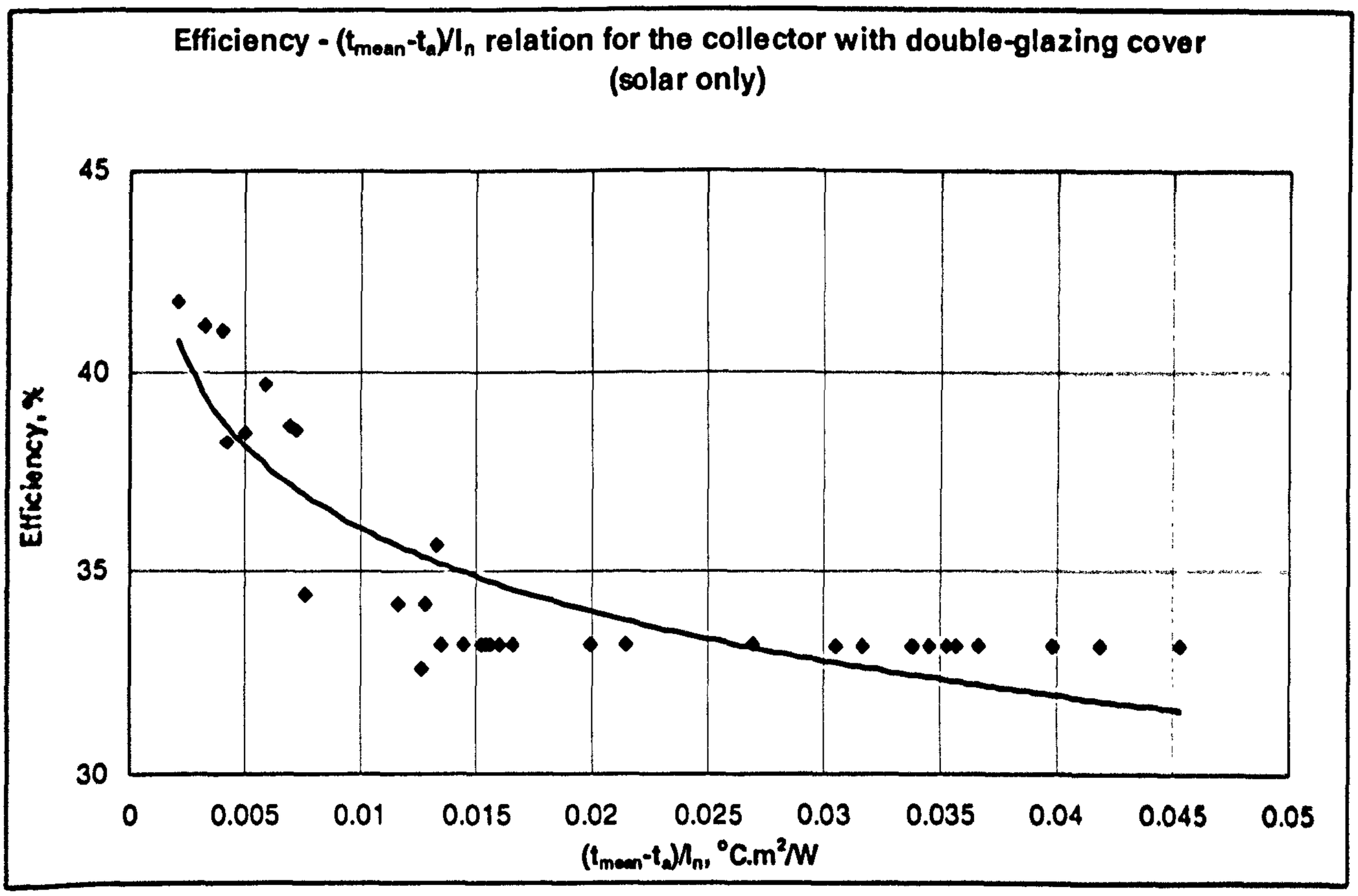

Figure 5-32. η - $(t_{mean}-t_a)/I_n$ relation for the collector with double-glazing cover (solar only operation)

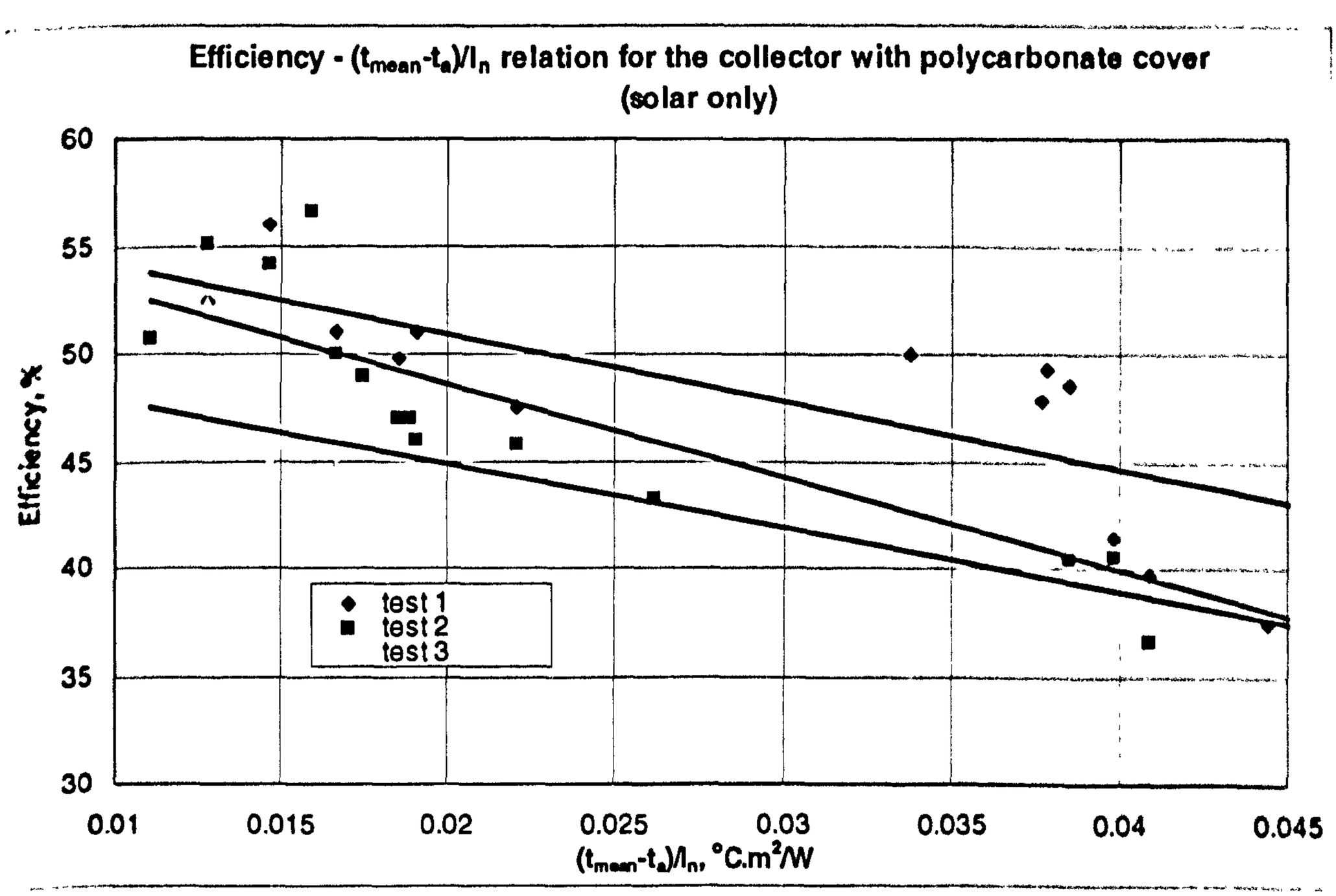

Figure 5-33. η - $(t_{mean}-t_a)/I_n$ relation for the collector with polycarbonate cover (solar only operation)

Tests for the combined solar and exhaust gas operation

Further tests were carried out for operation using both solar radiation and flue gas. The heating processes for the collector with a polycarbonate cover are shown in Figures 5-34 to 5-36. The variations of solar irradiation, inlet and outlet water temperatures, and the outdoor temperature are presented. Compared to solar-only operation, it was found that the water temperature increased more quickly. The outlet/inlet temperature difference varied between 5°C and 8°C, depending on the intensity of the solar irradiation, as well as the magnitude of flue gas input. This indicates that solar-gas co-operation is much more efficient than the solar-only operation.

Two efficiencies, η and η_1, were used to assess the collector performance for the combined operation. These were calculated using the test results, and are also indicated as a function of the general parameter $(t_{mean}-t_a)/I_n$, as shown in Figures 5-37 (for the polycarbonate cover). Trend-lines are shown to describe this variation. For three of the tests, efficiency decreased when $(t_{mean}-t_a)/I_n$ increased. However, it may also be seen that there are several measurement points scattered away from the trend-lines. This was caused by the slow response of the system due to its massive volume.

Compared to solar-only operation, η was approximately 20% higher, and achieved 60% to 85% for the polycarbonate cover. This again indicates that utilising waste heat from exhaust gas could enhance collector efficiency. The other efficiency parameter, η_1, was still rather low, i.e., 20% to 35%, while $(t_{mean}-t_a)/I_n$ varied from 0 to 0.028.

Figure 5-34. Heating process of the collector with polycarbonate cover (solar- gas combined operation) – test 1

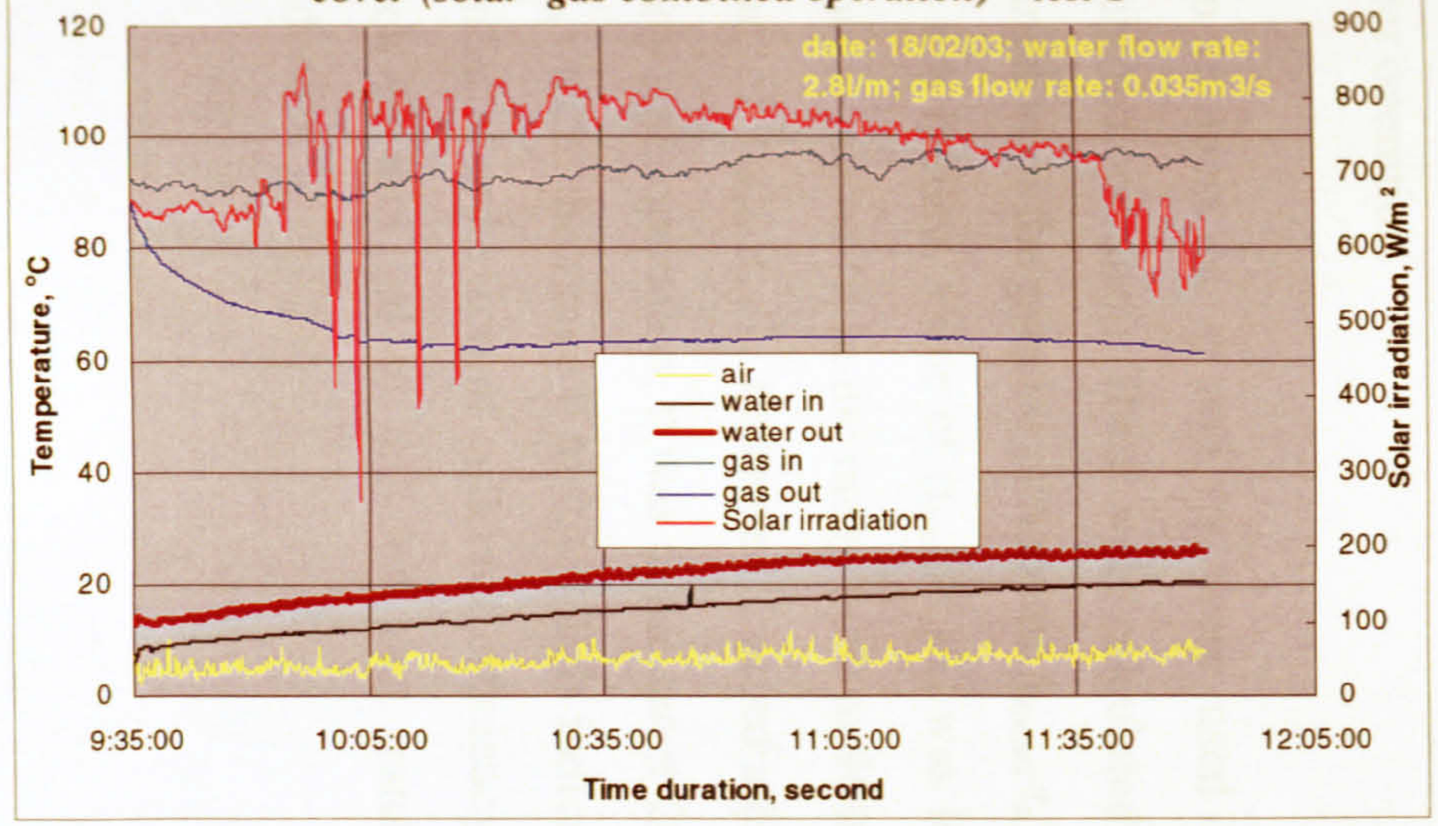

Figure 5-35. Heating process of the collector with polycarbonate cover (solar- gas combined operation) – test 2

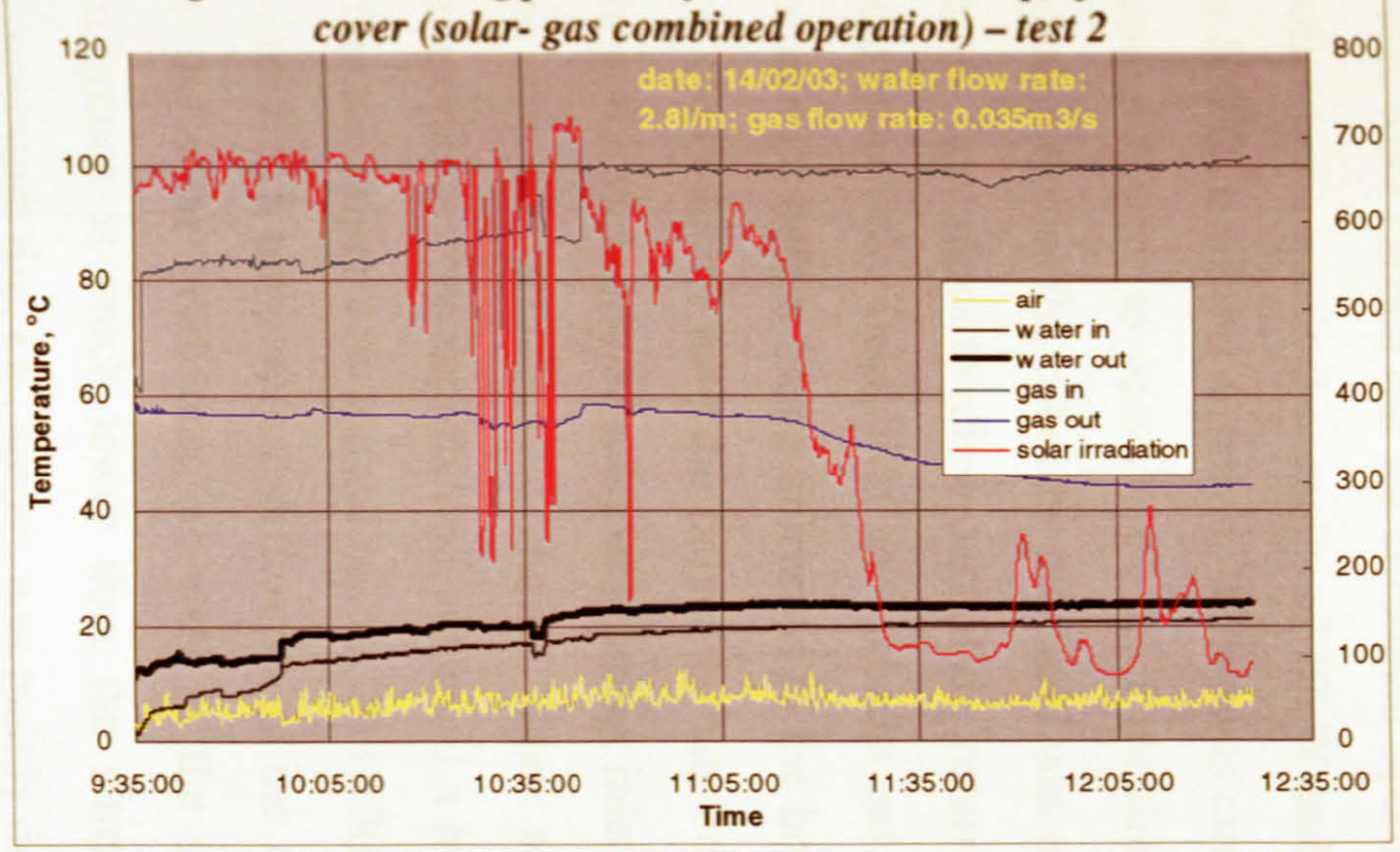

Figure 5-36. Heating process of the collector with polycarbonate cover (solar- gas combined operation) – test 3

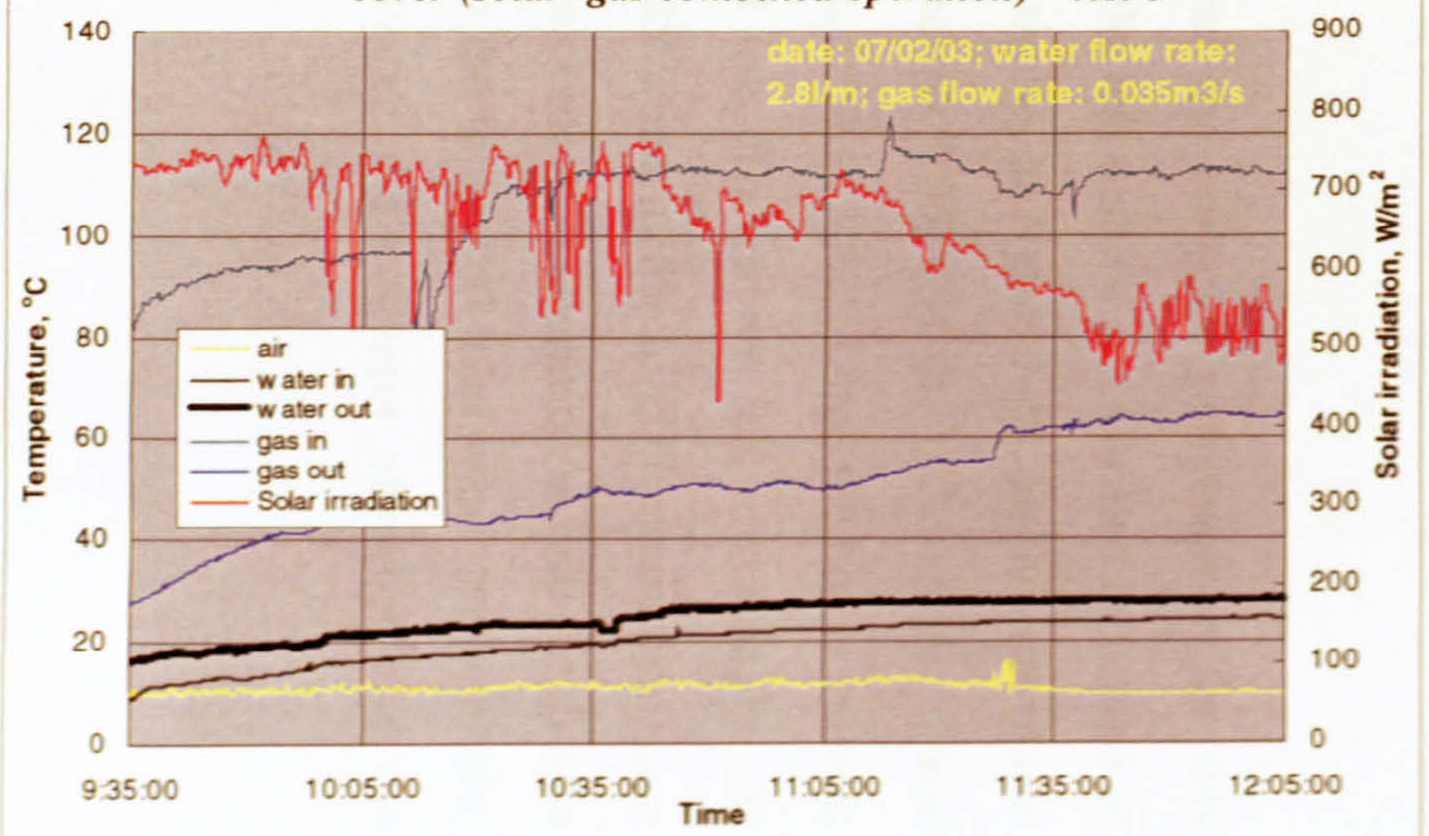

Figure 5-37. $\eta\,(\eta_1) - (t_{mean}-t_a)/I_n$ relation for the collector with polycarbonate cover (solar-gas combined operation)

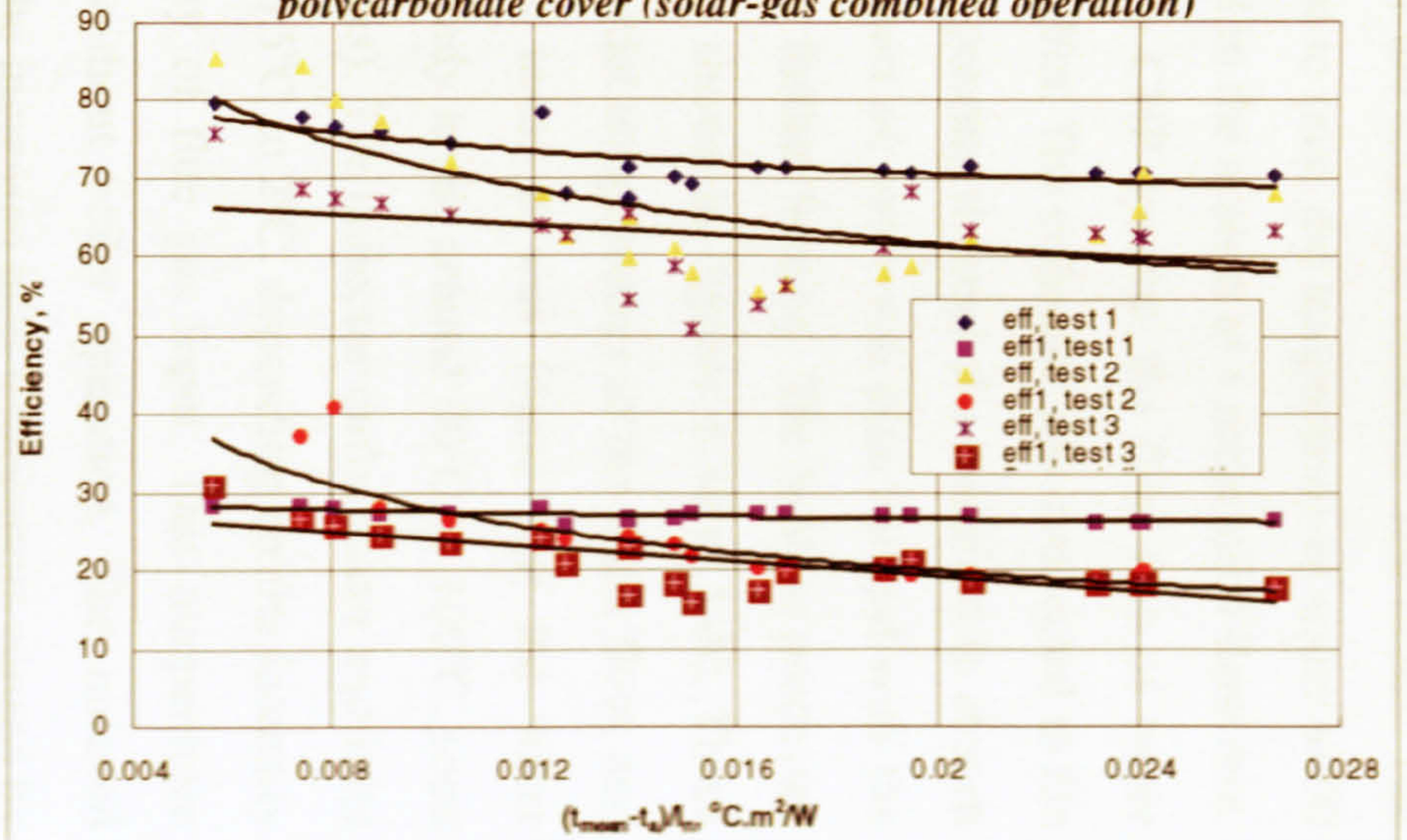

Tests for the combined solar, gas and boiler operation

Tests were carried out for combined operation of the solar/gas collector and boiler. The boiler has a nominal capacity of 70kW and is able to raise the temperature of water to 90 to 100°C in a short duration. Water was circulated in the system at a substantial flow rate, around 60l/m, to provide the heat required for a CHP system; the flow rate of water passing across the collector manifold was only 2.8l/m. The collector was connected to the return flow pipes to allow part of the return water passing through the manifold to absorb heat from solar insolation and exhaust gas. This part of water was then merged with the remainder before being delivered to the boiler for further heating. The heating processes for the collector with the polycarbonate cover are shown in Figures 5-38 to 5-40. These show the variation of solar irradiation, inlet and outlet temperatures of the water flow, and the outdoor temperature during three separate tests. It was found that the water temperature rose rapidly and achieved a high, steady level, around 90°C to 100°C, soon after the boiler was started (about 20 to 30 minutes). The collector outlet water and inlet water had a temperature difference in the range 0.5°C to 2°C, depending on the intensity of the solar irradiation, as well as the intensity of flue gas input. This temperature difference is much lower than the situation without boiler operation. The reduced temperature rise, i.e., output, was mainly due to the increased inlet temperature caused by boiler operation.

Two efficiencies, η and η_1, were used to assess the collector performance for this combined operation. These were calculated using the test results, and are also indicated as a function of the general parameter $(t_{mean}-t_a)/I_n$, as shown in Figure 5-41. Before the boiler was not ignited, value of $(t_{mean}-t_a)/I_n$ was lower (below 0.05) and the efficiencies, η and η_1, were higher (η in the range 60% to 90% and η_1 10% to 30%). Once the boiler started, value of $(t_{mean}-t_a)/I_n$ increased immediately, and the efficiencies fell accordingly. At steady state operation, η was in the range 20% to 25% and η_1 5% to 10% while the $(t_{mean}-t_a)/I_n$ was in the range 0 to 0.47. This indicates that combined operation would result in a significant reduction of collector efficiency due to the increased inlet water temperature, which in turn led to reduced heat transfer between the collector absorber and the condenser.

Figure 5-38. Heating process of the collector working with boiler – test 1

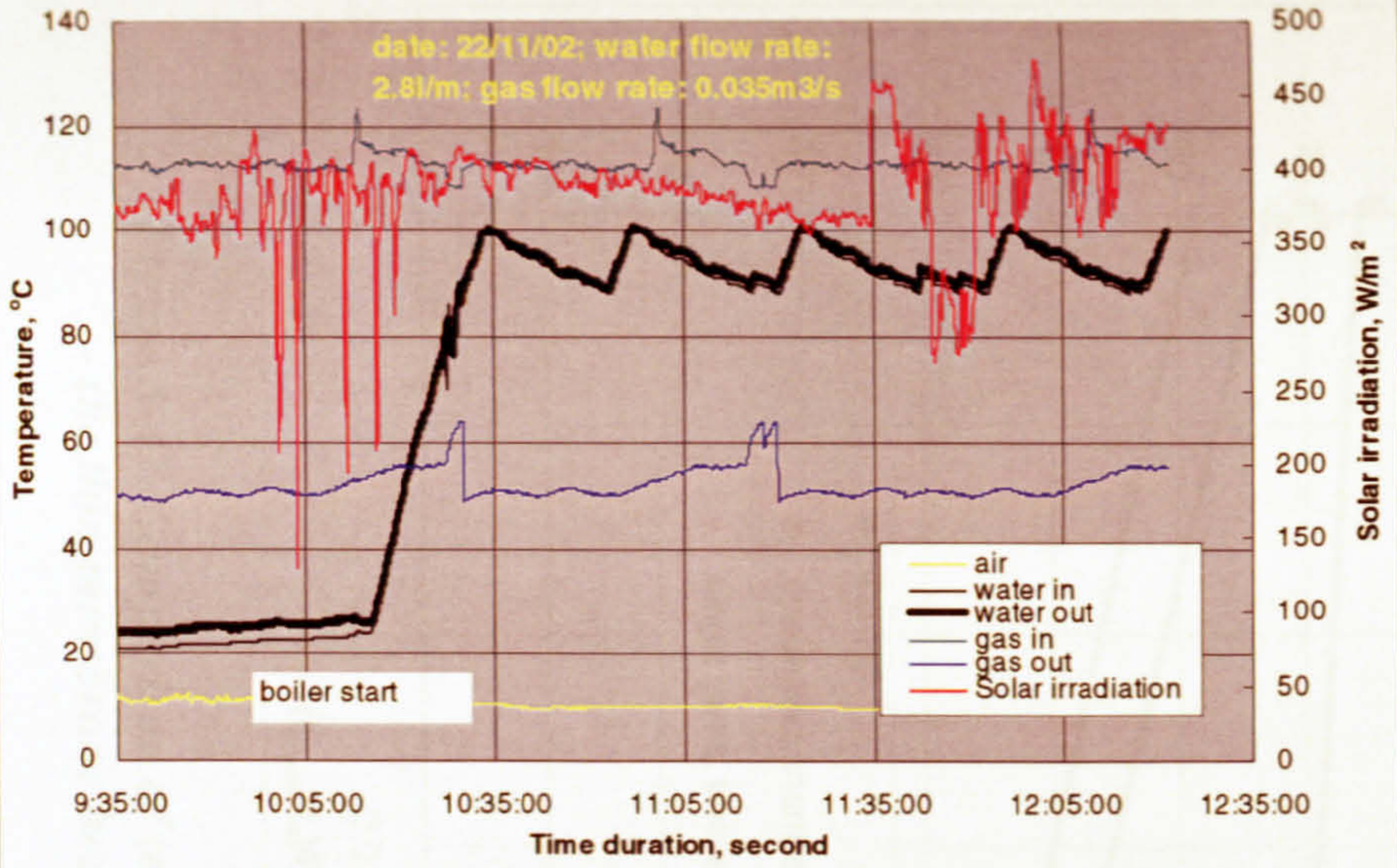

Figure 5-39. Heating process of the collector working with boiler – test 2

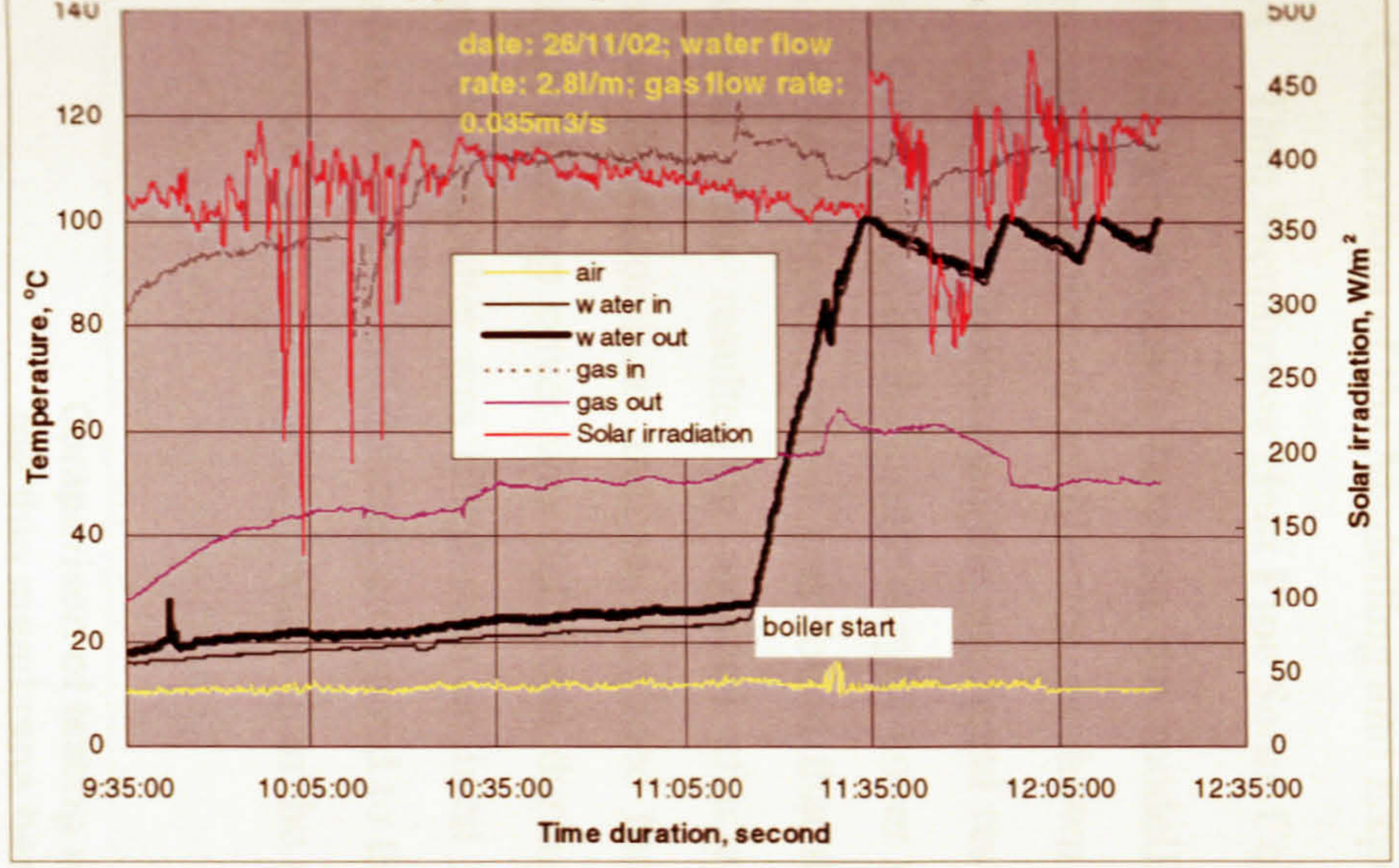

Figure 5-40. Heating process of the collector working with boiler – test 3

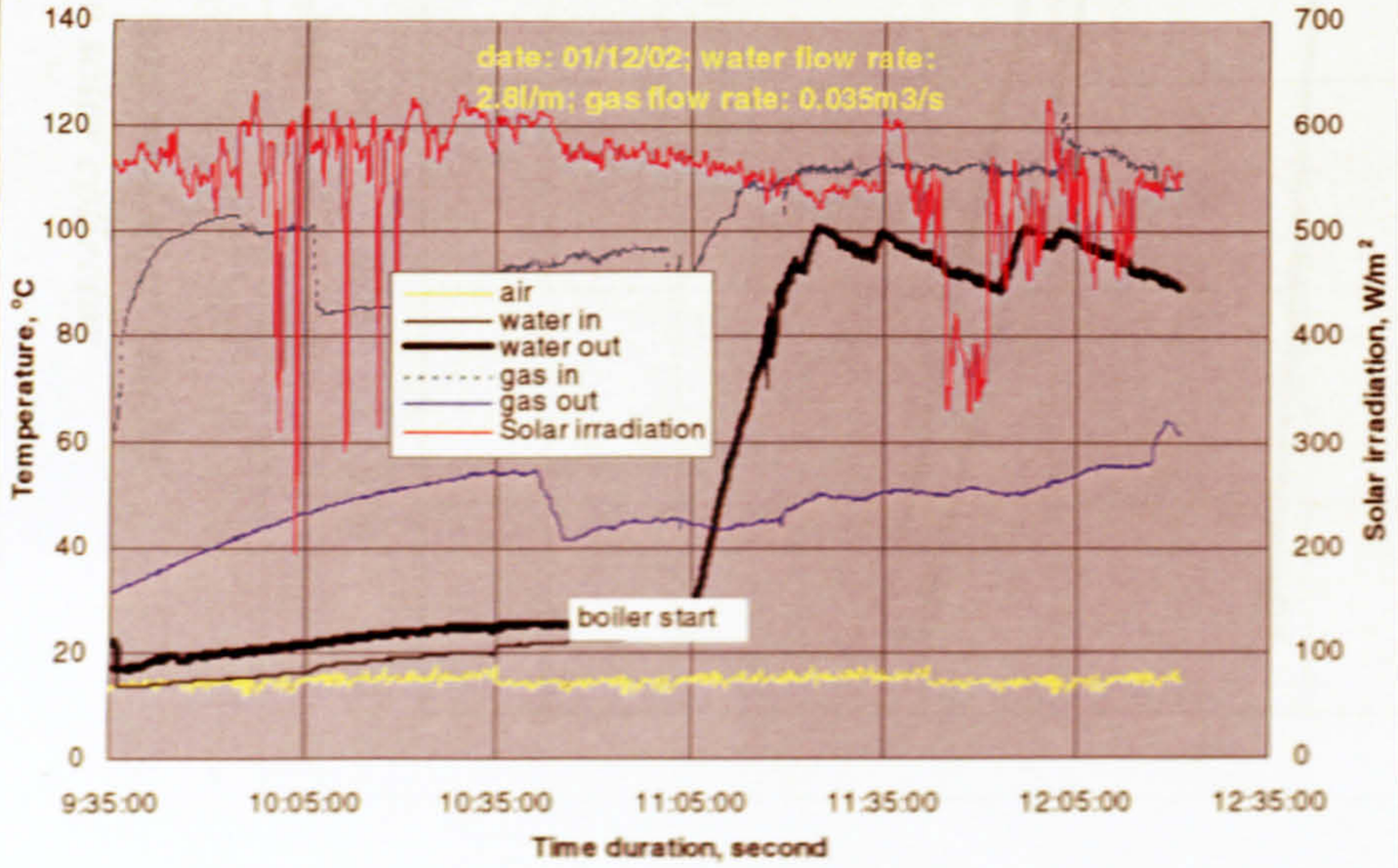

Figure 5-41. η (η_1) – $(t_{mean}-t_a)/I_n$ relation for the collector with polycarbonate cover (solar-gas combined operation)

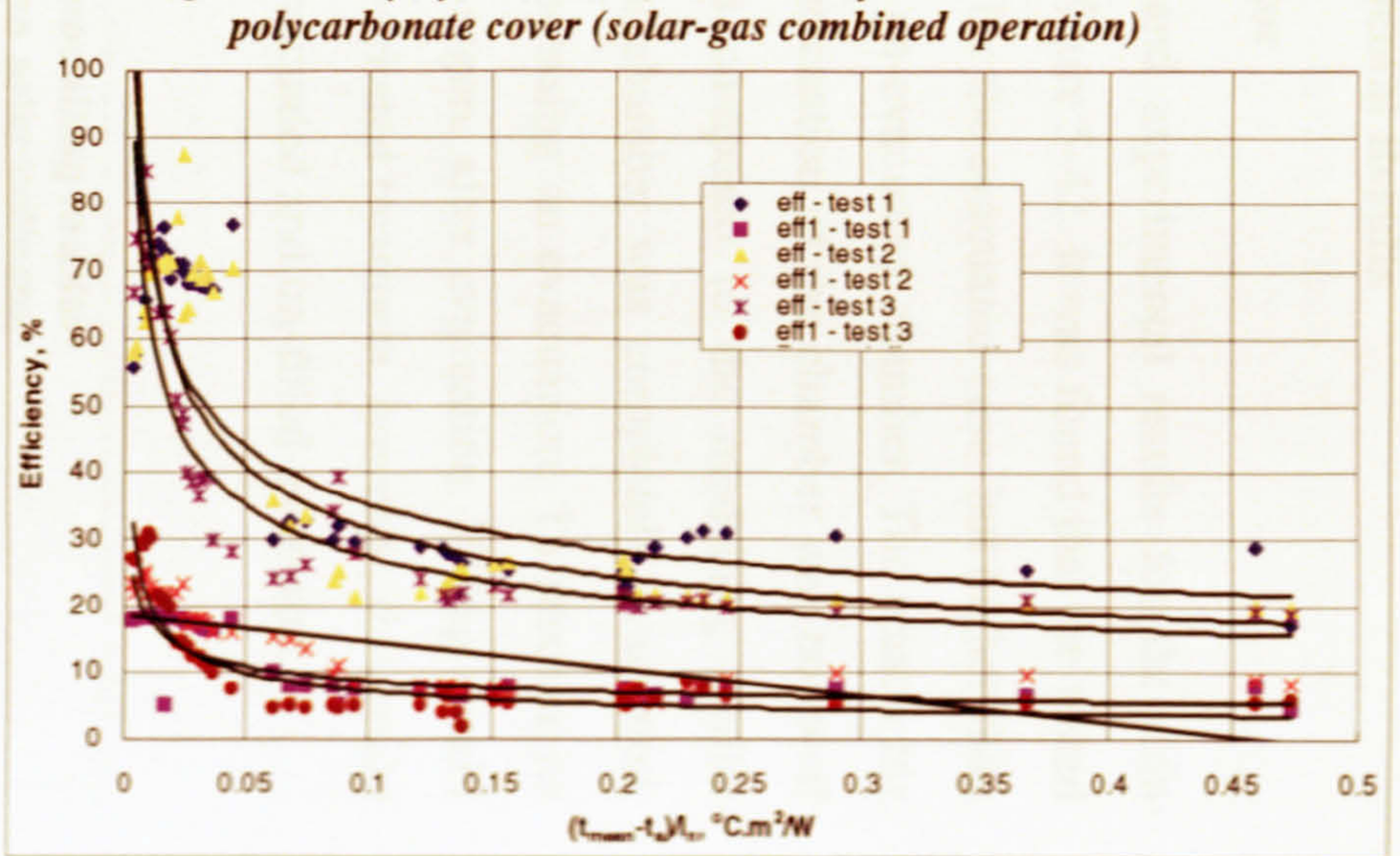

5.5 Comparison of the Modelling and Experimental Results

5.5.1 Thin Membrane Heat Pipe Solar Collector

Comparison was made between the modelling and experimental results for the thin membrane heat pipe solar collector, as shown in Figure 5-42. It was found that the tested efficiencies were lower than the predicted results for the evacuated case, but higher than those for the case of the single acrylic cover with un-evacuated chamber. The reason for this was investigated, and it was found that the evacuation of the chamber was not well processed. This resulted in reduced efficiencies compared to the modelling results because the theoretical analysis assumed that the chamber was completely evacuated. Actually, the top cover was deformed during processing an evacuation. To recover its shape, the chamber was filled with an inert gas, argon, after evacuation. Filling would result in a reduced efficiencies compared to the evacuated treatment, however, this could still provide higher efficiency values than the un-evacuated and un-filled treatment.

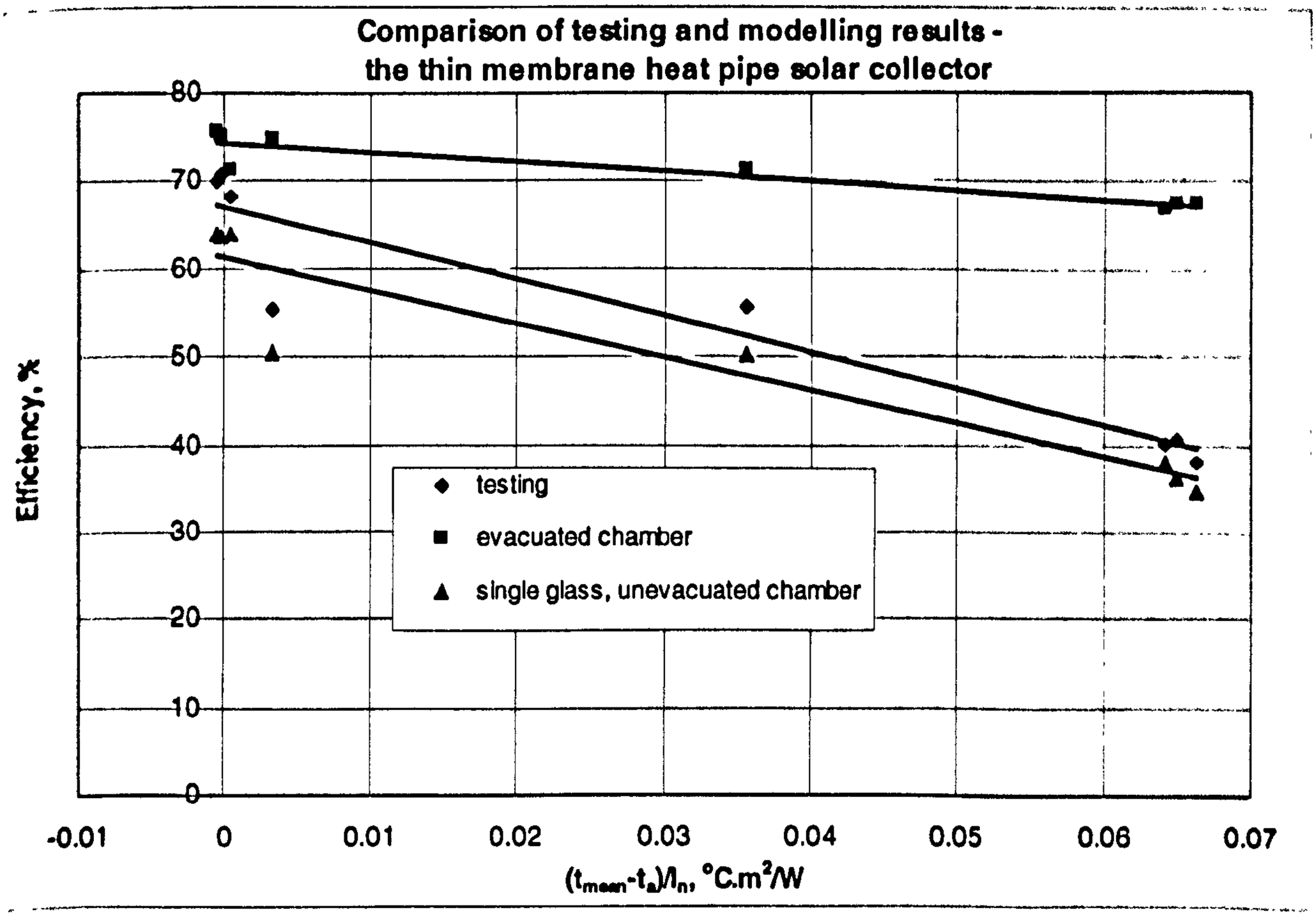

Figure 5-42. Comparison of testing and modeling results – the thin membrane heat pipe solar collector

5.5.2 Hybrid heat pipe solar collector

Comparison was also carried out between the modelling and experimental results for the hybrid heat pipe solar collector, for each of the three operation modes, i.e., solar-only operation, solar/waste gas combined operation, and solar/waste gas and boiler combined operation. The results of these comparisons are summarised in Figures 5-43, 5-44 and 5-45, respectively. For each mode of operation, the testing efficiencies are the average values of the efficiencies of three separate tests.

For solar-only operation, solar/gas combined operation, or solar, gas and boiler combined operation, the theoretical efficiencies are always higher than the corresponding testing efficiencies. The differences are in the range 20% to 30%. The reasons for this were investigated, and it was found that a number of factors contributed to the discrepancies. Firstly, the heat pipe panel was subject to a small edge heat loss as it was fixed onto a metal frame that would conduct part of the absorbed heat away from the panel. Secondly, the insulation of the chamber and manifold was not as good as expected, and contributed to an increased heat loss. Thirdly, the collector body absorbed part of the input heat to warm itself up at the beginning of operation. This resulted in a reduced heat output. Finally, several assumptions were made when developing the computer modelling, e.g., an identical temperature layout was assumed to exist on the absorber area, and a direct through channel was assumed to represent the actual multiple return channels for simplification of the analysis. These would also contribute to discrepancies.

Even so, the modelling results and experimental data showed a very similar trend for efficiency variation. Overall, efficiencies (either η or η_1) decreased with increasing of $(t_{mean}-t_a)/I_n$, but rates of variation differed for the three operation modes. Combined solar/gas and boiler operation showed the highest declination; the other two modes showed little difference for this trend.

Although differences exist between modelling and experimental results, the modelling program is still able to predict collector performance if a correction factor is provided. The factor was determined by dividing the experimental value by the modelling value under the same $(t_{mean}-t_a)/I_n$, and was still indicated as a function of $(t_{mean}-t_a)/I_n$, as shown in Figures 5-46 to 5-48 for the three modes of operations. These correlations would be

applied to any circumstance for this type of collector, and expected to improve the accuracy of the modelling predictions to a substantial extent.

Based on the theoretical investigation and experimental testing, the efficiencies of the hybrid heat pipe solar collector were determined and presented in Table 5-11.

Table 5-11. Summary of the solar collector efficiencies

Configuration	Flue gas setting	Operating temperature, °C	Efficiency η , %		Efficiency η_1, %	
			Testing	theoretical	Testing	theoretical
Double-glazing cover	Solar only operation	0-110	30 - 45	50-60	Not available	Not available
	Solar/exhaust gas operation	0-110	No data	No data	No data	No data
	Solar, gas and boiler operation	0-110	No data	No data	No data	No data
Polycarbonate cover	Solar only operation	0-110	45-70	65-78	Not available	Not available
	Solar/exhaust gas operation	0-110	60-90	95-110	20-35	35-42
	Solar, gas and boiler operation	0-110	25-70	30-110	5-25	5-40

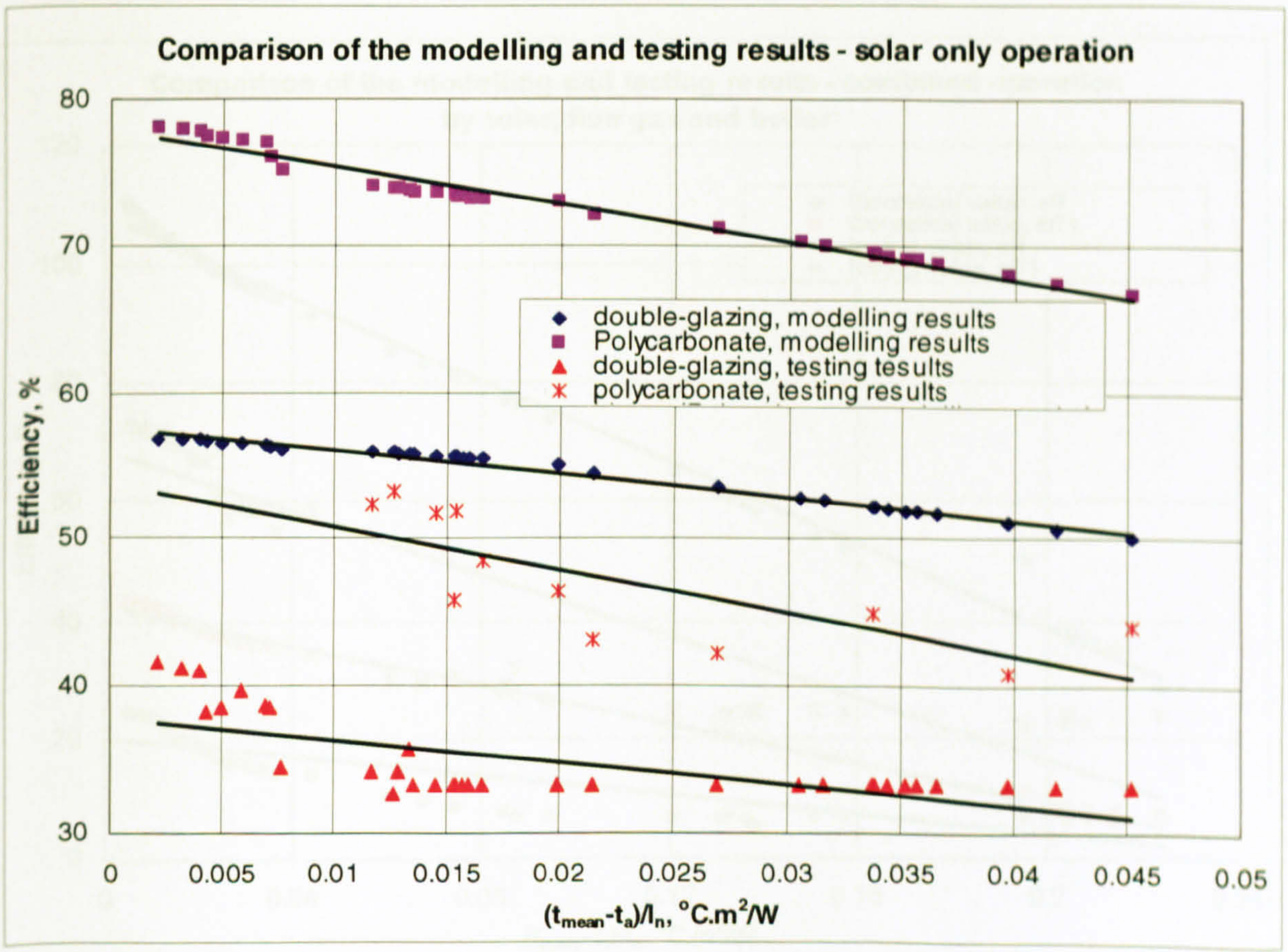

Figure 5-43. Comparison of the modeling and testing results – solar only operation

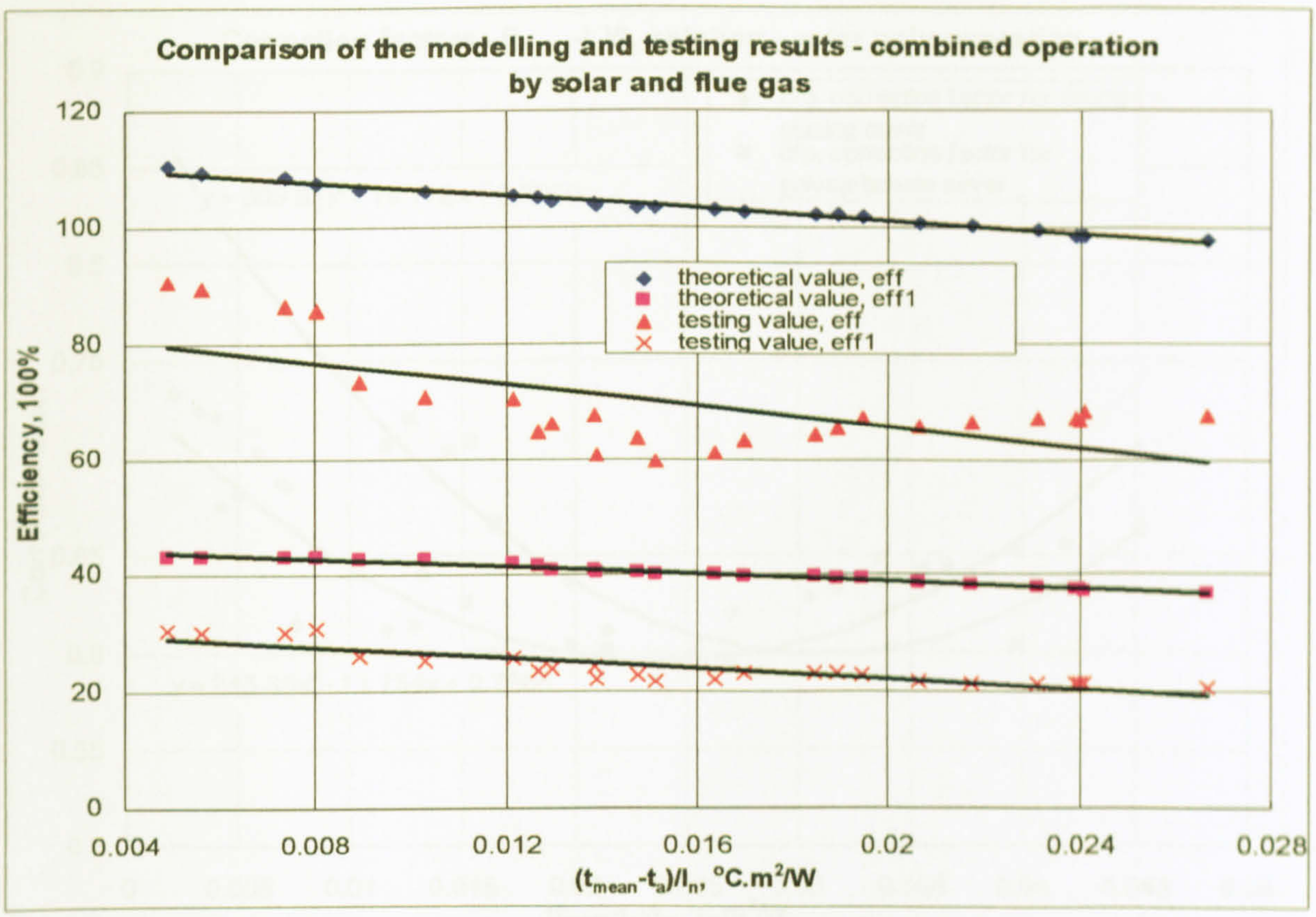

Figure 5-44. Comparison of the modeling and testing results – solar and flue gas combined operation

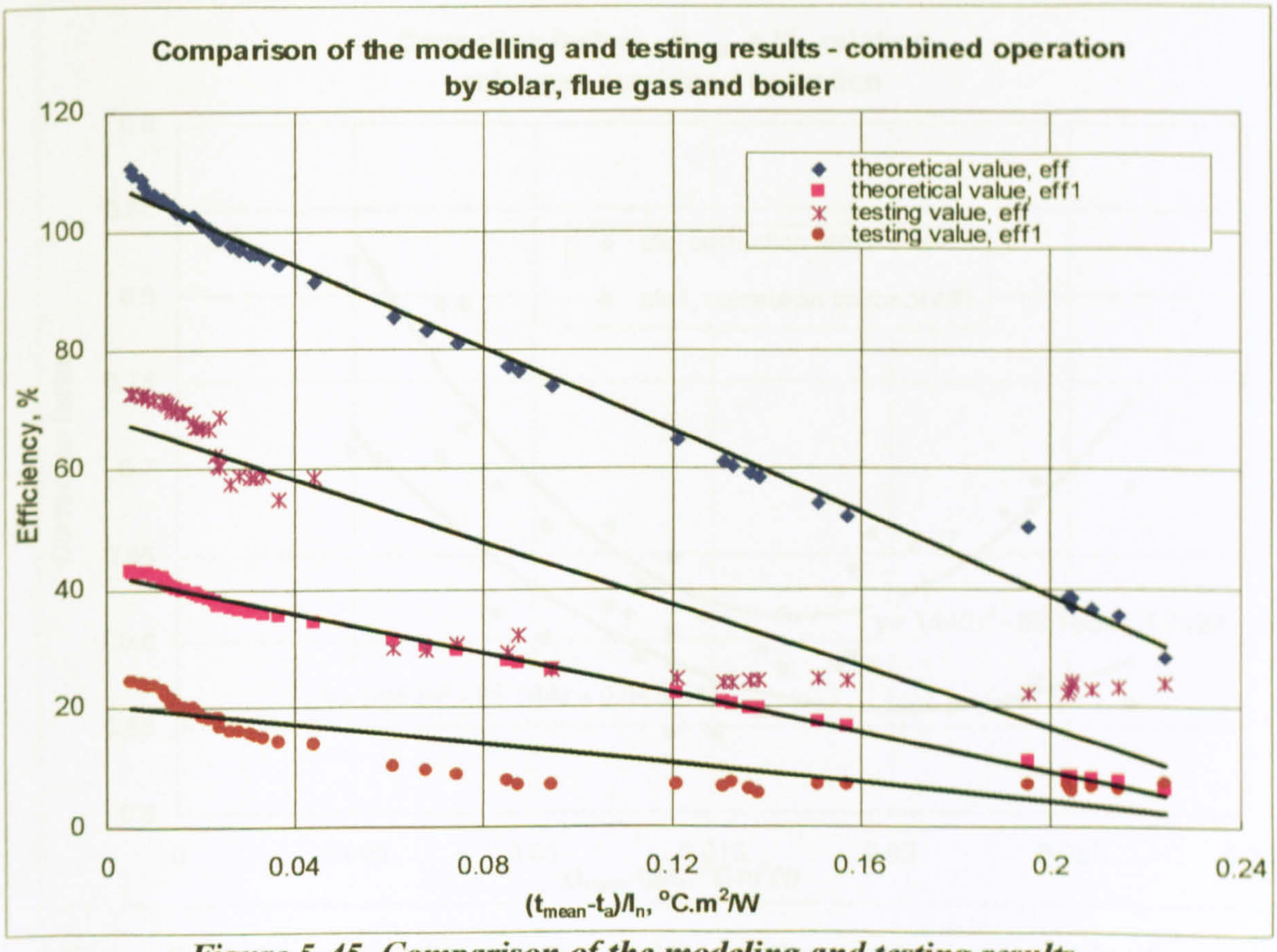

Figure 5-45. Comparison of the modeling and testing results – solar, flue gas and boiler combined operation

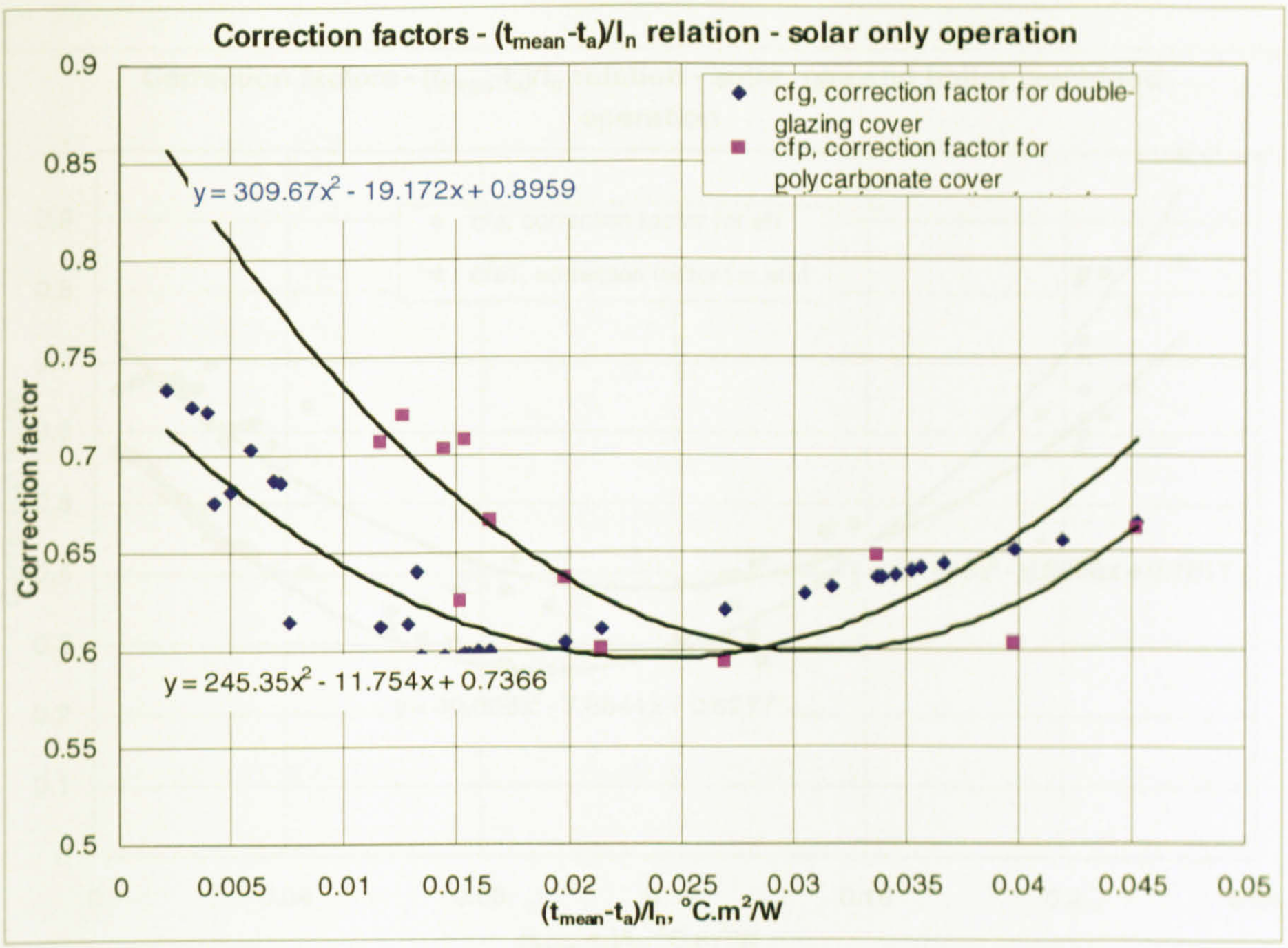

Figure 5-46. Correction factor – $(t_{mean}-t_a)/I_n$ relation – solar only operation

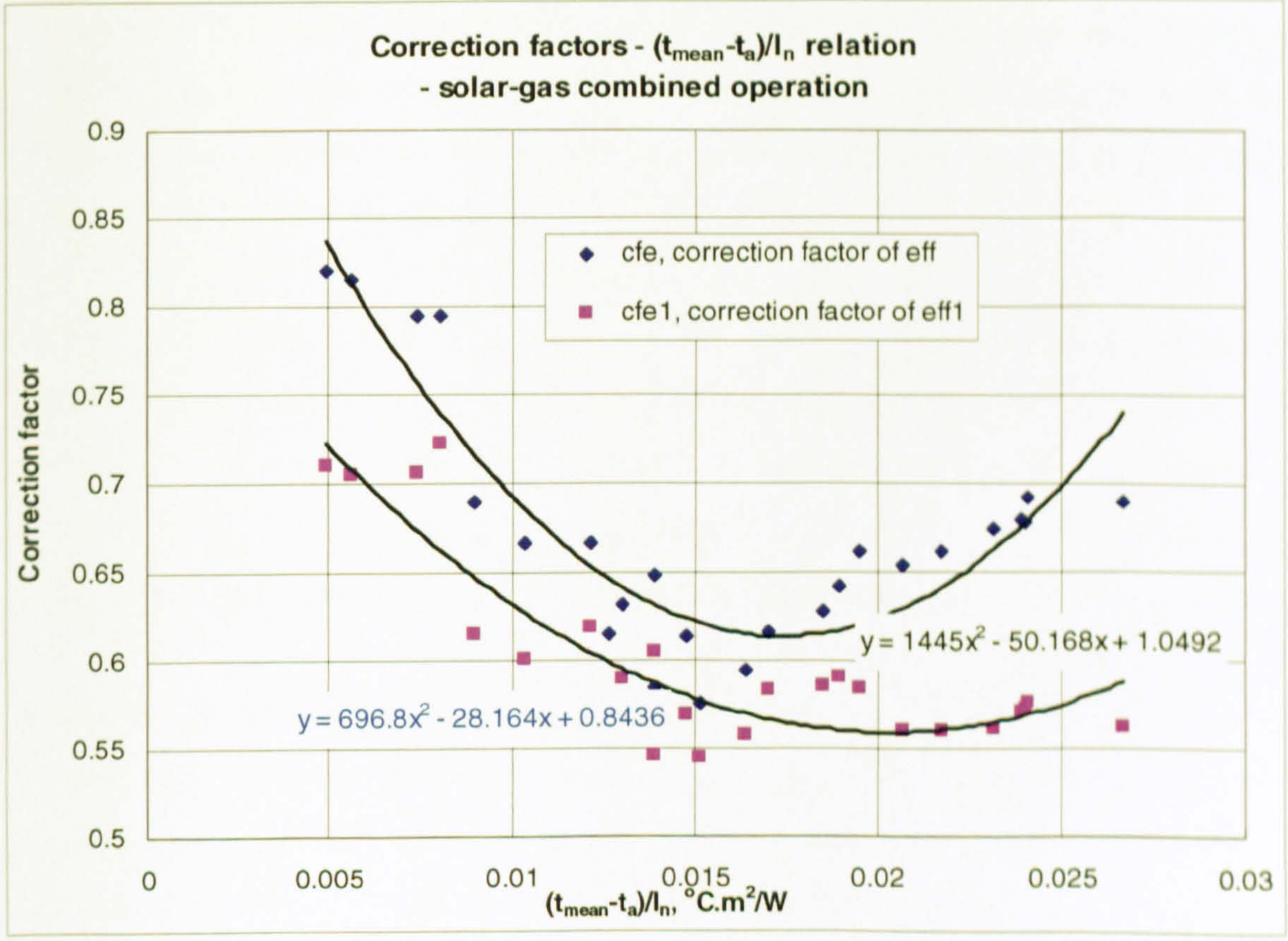

Figure 5-47. Correction factor – $(t_{mean}-t_a)/I_n$ relation – solar-gas combined operation

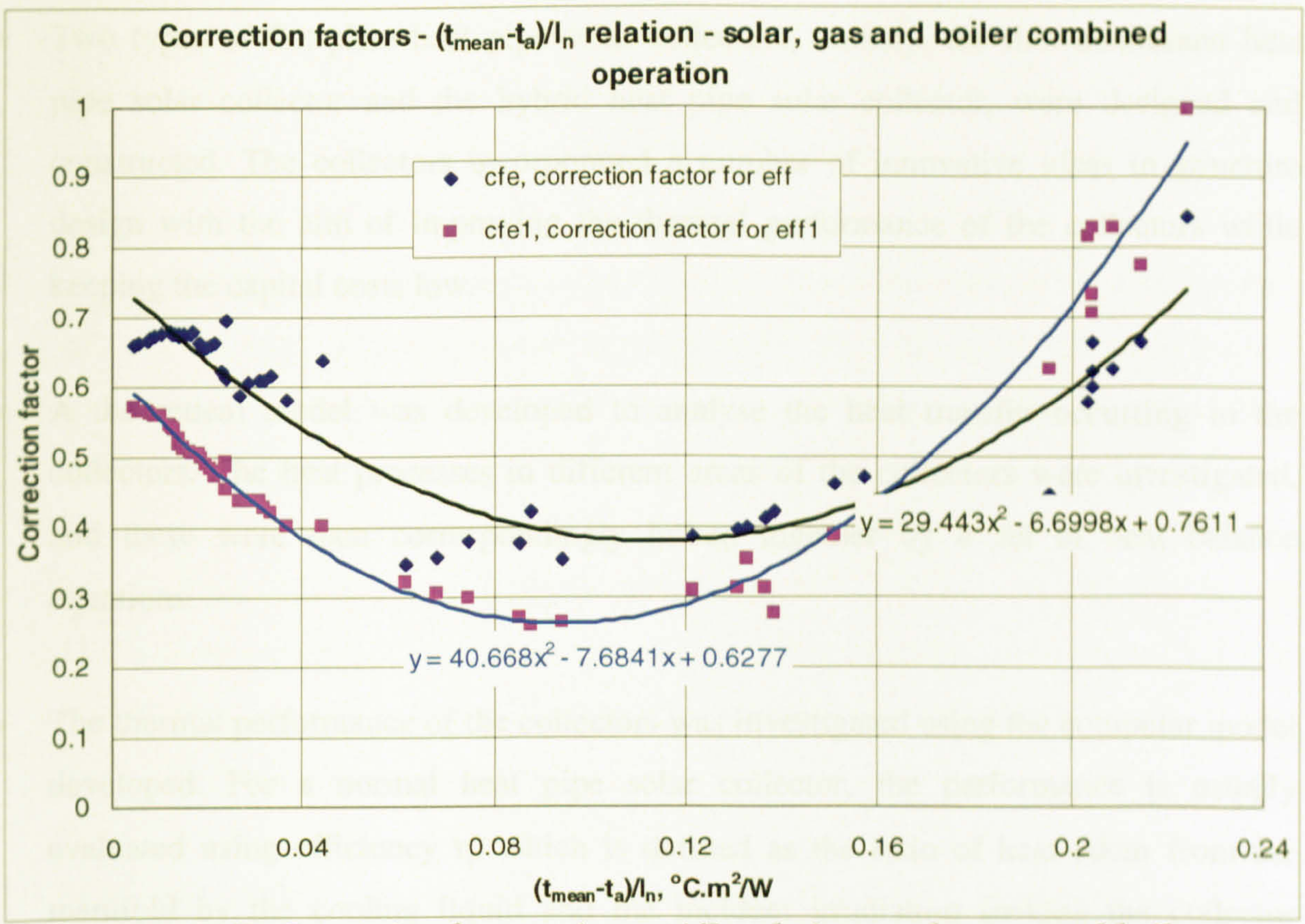

Figure 5-48. Correction factor – $(t_{mean}-t_a)/I_n$ relation – solar, gas and boiler combined operation

5.6 Summary

- Two types of flat-plate heat pipe solar collectors, namely, the thin membrane heat pipe solar collector and the hybrid heat pipe solar collector, were designed and constructed. The collectors incorporated a number of innovative ideas in structure design with the aim of improving the thermal performance of the collectors while keeping the capital costs low.

- A theoretical model was developed to analyse the heat transfer occurring in the collectors. The heat processes in different areas of the collectors were investigated, and these were then correspondingly linked together by a set of heat balance equations.

- The thermal performance of the collectors was investigated using the computer model developed. For a normal heat pipe solar collector, the performance is usually evaluated using efficiency η, which is defined as the ratio of heat taken from the manifold by the cooling liquid and the incident irradiation striking the collector absorber. However, for a hybrid heat pipe solar collector, another efficiency, η_1, is also used to evaluate its thermal performance and this includes the heat input from the exhaust gas. The efficiency is defined as the ratio of heat taken from the manifold by cooling liquid and the sum of the incident irradiation striking the collector absorber and the heat from the exhaust gas.

Given the structure of a solar collector, the efficiency varies with the external conditions, i.e., global solar irradiation I_n, ambient temperature t_a, as well as cooling fluid inlet temperature t_0 and mass flow rate m. The external conditions are usually grouped by an item given as $(t_{mean}-t_a)/I_n$. Overall, η and η_1 decrease with increasing $(t_{mean}-t_a)/I_n$. The relationship can be expressed by linear equations.

The top cover has an impact on collector performance. Of the five covers investigated, the single glass with an evacuated chamber is the best option, and the single acrylic glass with an un-evacuated chamber is the worst. Due to difficulty in creating an evacuated chamber for a flat-plate solar collector, choosing a 10mm thick polycarbonate sheet as a cover with an un-evacuated chamber may be an alternative

option. This is because polycarbonate sheet has a high solar transmittance (about 85%) and a relatively large heat resistance (about $3W/m^2.^oC$), which would result in an increased efficiency that approximately approaches the value for the evacuated case.

The heat transfer area in the condenser, the flow rate of the cooling fluid within the manifold, as well as the manifold structure also have an influence on collector performance. Variation of the length of the condenser (or the length of the manifold), resulting in a variation of the heat transfer area between the manifold and the condenser, was found to influence the efficiency. The longer the condenser and the larger the heat transfer area, the higher the efficiency. However, increasing the length of the condenser may be limited by installation space in many applications. For the two collectors investigated here, the condenser length (also the manifold length) was taken as 10% of the evaporator length.

For the hybrid heat pipe solar collector, the mode of operation was found to be the major factor influencing collector performance. For solar-only operation, the theoretical efficiency is in the range 30%-45% for the double-glazed cover and 45%-70% for the polycarbonate cover. Solar-exhaust gas combined operation enhances collector efficiency, η, by 15%-20%, while the efficiency, η_l, remains at 35%-42%. When solar-exhaust gas operation is combined with boiler input, there is a significant reduction in collector efficiency, down to 30% for η and 5% for η_l. This is because the boiler increases the inlet cooling water temperature, which leads to a reduced temperature difference between the absorber and condenser, and therefore, reduced heat transfer in the collector.

- Laboratory tests were carried out to validate modelling predictions and provide experimental results on the thermal performance of the collectors. For the thin membrane heat pipe solar collector, tests were carried out in a standard solar energy laboratory in Germany, and the experimental efficiency was in the range 40%-70%, and decreased with increasing $(t_{mean}-t_a)/I_n$. For the hybrid heat pipe solar collector, a set of tests were carried out under real climatic conditions by connecting it to a CHP/boiler system. Three modes of operation, i.e., solar-only, combined solar-

exhaust gas, and combined solar, exhaust gas and boiler operation, were examined, and each type of operation was studied on three separate days to examine the repeatability and reliability of the performance data. The efficiency values obtained from each of the three tests for a given mode of operation were similar and are presented in Table 5-11.

- Modelling and experimental results were compared for the thin membrane and the hybrid solar collectors. For the thin membrane heat pipe solar collector, experimental efficiencies were in the range 40%-70%, which are lower than the values predicted by modelling for the evacuated case, but higher than those for the case of the single glass cover with un-evacuated chamber. The reason for this is that the chamber was filled with an inert gas, argon, after being evacuated, which has a larger heat resistance than air, but still gave rise to an extra conductive or/and convective heat loss compared to the evacuated situation. These treatments were not taken into account in modelling development and processing.

For the hybrid heat pipe solar collector under each of the three operation modes, the theoretical efficiencies are always higher than the corresponding experimental efficiencies. The differences are in the range 10% to 20%, and the reasons for this are mainly due to the several factors, including edge heat loss, unsatisfactory insulation, heat storage of the collector body itself and the simplified assumptions made in modelling setting-up. Even so, the modelling program is still able to predict collector performance if an appropriate correction factor is provided. The factor was determined by dividing the experimental value by the modelling value under the same $(t_{mean}-t_a)/I_n$, and was still indicated as a function of $(t_{mean}-t_a)/I_n$,. These correlations could be applied to any circumstance for this type of collector.

Chapter 6. Micro Steam Turbines

6.1 The Steam Turbine Configurations

A steam turbine is defined as a form of heat engine in which the energy of the steam is transformed into kinetic energy by means of expansion through nozzles, and the kinetic energy of the resulting jet is in turn converted into force doing work on rings of blades mounted on a rotating part. The steam is caused to fall in pressure in a passage or nozzle, which causes the conversion of a certain amount of heat energy into mechanical kinetic energy. As a result, the steam is set moving with a greater velocity. The rapidly moving particles of steam enter the moving part of the turbine and here suffer a change in direction of motion which gives rise to a change of momentum and therefore a force. This constitutes the driving force of the machine. The process of expansion and direction-changing may occur once, or a number of times in succession, and may be carried out with differences of detail [Kearton William J., 1972].

The passage of the steam through the moving part of the turbine, commonly called the blade, may take place in such a manner that the pressure at the outlet side of the blade is equal to that at the inlet side. Such a turbine is broadly termed an 'impulse turbine'. On the other hand, the pressure of the steam at outlet from the moving blades of the turbine may be less than that at the inlet side of the blades; the drop in pressure suffered by the steam during its flow through the moving blade causes a further generation of kinetic energy within the blade and adds to the propelling force which is applied to the turbine rotor. Such a turbine is broadly termed an 'impulse-reaction turbine'.

The majority of steam turbines have, therefore, two important elements, or sets of such elements. These are:

- The Nozzle, in which the steam expands from a high pressure and a state of comparative rest to a lower pressure and a state of comparatively rapid motion.
- The Blade or deflector, in which the stream of steam particles has its direction and hence its momentum changed. The blades are attached to the rotating element of the machine, or rotor; whereas, in general, the nozzles are attached to the stationary part of the turbine, which is usually termed the stator, casing or cyclinder.

The steam turbines usually have very large sizes and hence substantial electricity output. There is no report for commercial application for a micro steam turbine less than 50kWe. However, this research has employed a specially designed impulse-reaction steam turbine that could provide 1.5-3kWe outputs and hence is suitable for use in a domestic micro CHP system. Furthermore, this research has also tried a novel application of a micro turbo-alternator that is driven by compressed air and able to provide 0.25kWe output. The second application was actually to investigate the possibility of using an alternative refrigerant, such as HFE or n-pentane, to drive the mini turbine, rather than the compressed air, and to investigate the approaches of modification to the construction to allow it to be applied in the large-scale development.

Figure 6-1 is the Auto CAD drawings showing the outer view of turbine, including inlet, outlet and the cylinder casing. Figure 6-2 is a photograph showing the connection between the turbine and generator, and Figure 6-3 is the geometry contour showing internal structure of the turbine unit, including nozzle on the stationary part, the blades attached onto the rotor, as well as flow passages formed by the blades, rotor and the inner surface of cylinder, which was created by pre-BFC, a part of FLUENT CFD simulation software.

Figure 6-4 is a photograph of a modified turbo-alternator, which was used as the second application of the CHP system and had an output of 0.25kWe under working pressure of 5bar.

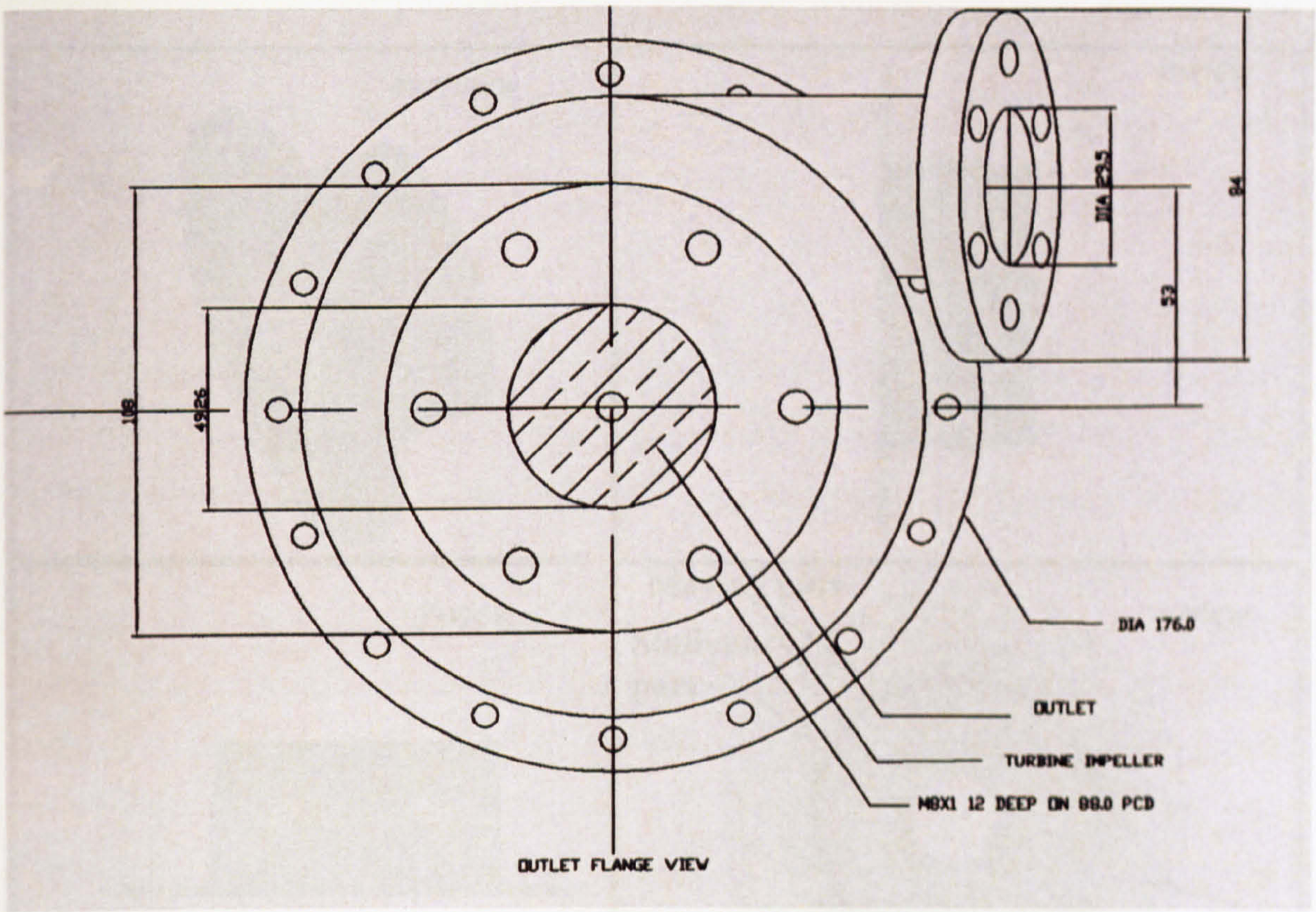

Figure 6-1. Auto-CAD drawing of the turbine configuration

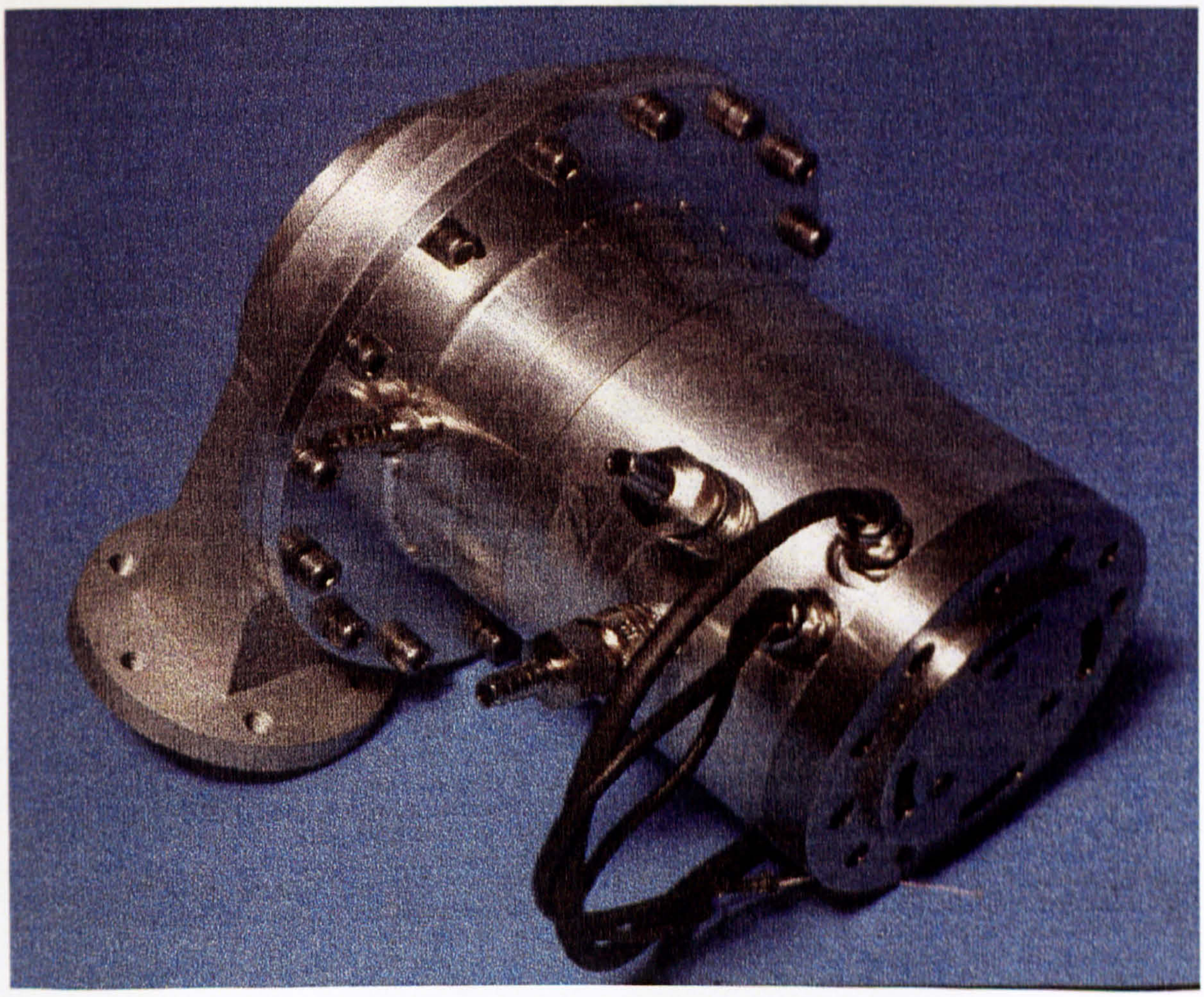

Figure 6-2. A photograph showing the connection of the turbine and generator

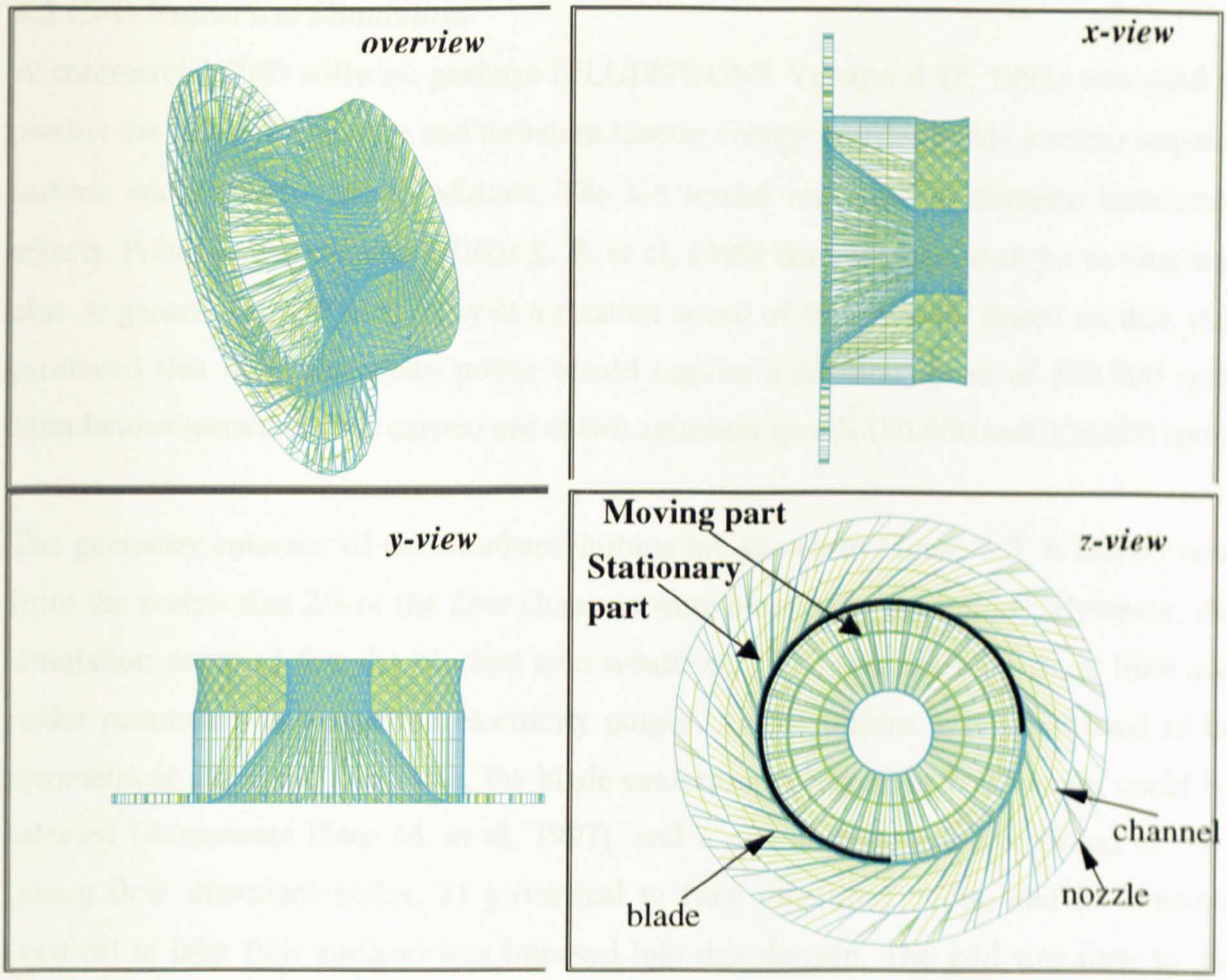

Figure 6-3. Geometry contour of the internal structures of the turbine unit

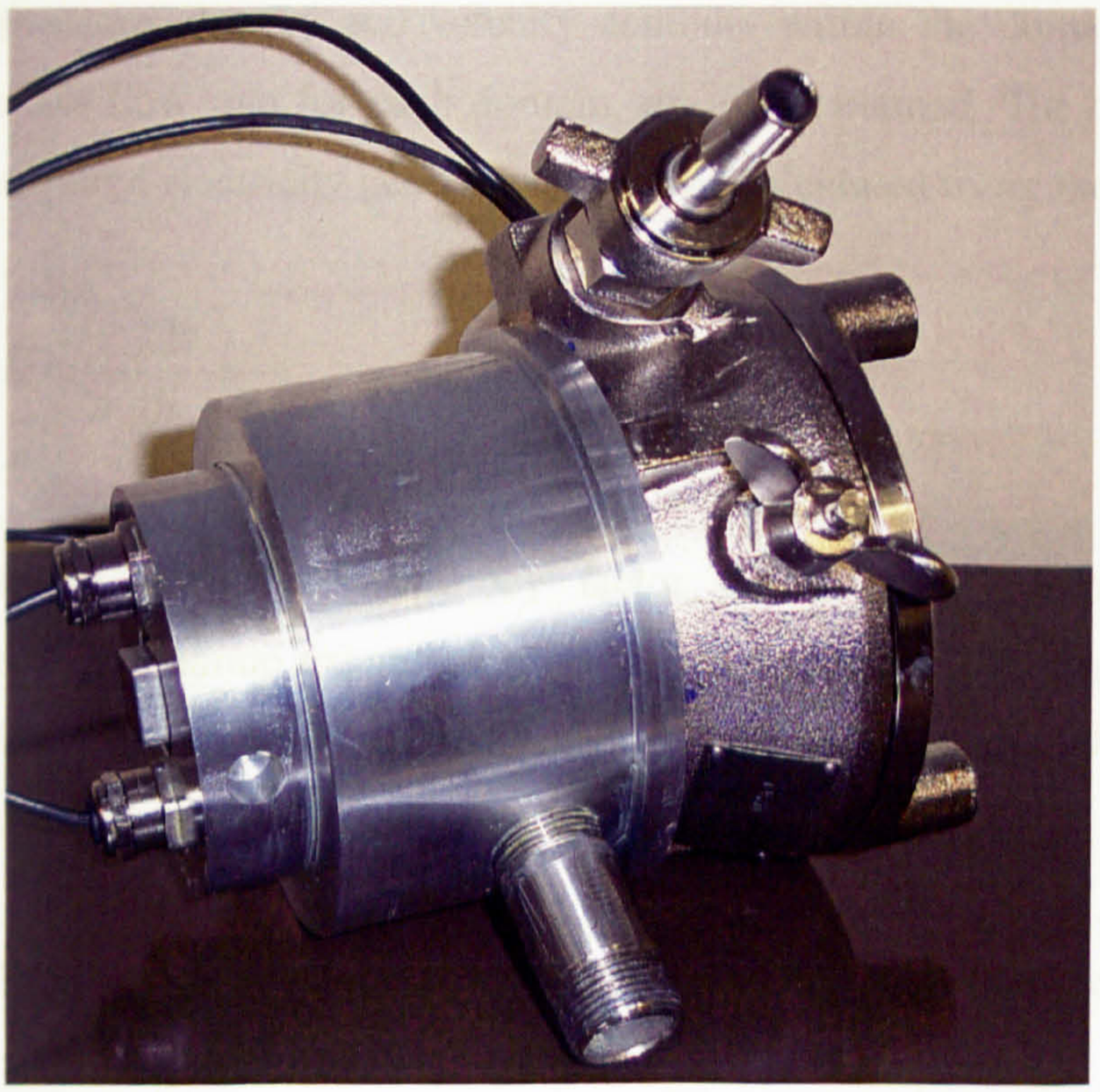

Figure 6-4. A photograph of the modified turbo-alternator

6.2 CFD Numerical Simulation

A commercial CFD software package (FLUENT/UNS Version 4.32, 1995) was used to predict the velocity, pressure and turbulent kinetic energy profiles inside a micro impulse turbine under steady-state conditions. The k-ε model was used to describe turbulence effects. Previous experiments [Riffat S. B. et al, 1999] demonstrated that the turbine was able to generate 1.5kW electricity at a rotation speed of 80,000 rpm. Based on this, it is estimated that 6kW electricity power would require a rotation speed of 320,000 rpm. Simulations were therefore carried out at two agitation speeds (80,000 and 320,000 rpm).

The geometry contours of the simulated turbine are shown in Figure 6-3. It can be seen from the z-view that 2/3 of the flow channels were blocked in the turbine. However, the simulation assumed that the blocked area would vary with the working fluid, inlet and outlet parameters and required electricity output. As the turbine was considered to be symmetrical along the z axis, i.e, the blade centerline, a repeating 10^{o} domain could be selected [Armenante Piero M. et al, 1997], and a non-uniform grid composed of 33 i (along flow direction) nodes, 11 j (vertical to flow direction) nodes, and 28 z nodes (vertical to inlet flow surface) was imposed into this domain. The grid was finer in the region near the blades.

Pressure, density and velocity contours within the domain were investigated, and the mass flow rate for each domain, m_e, was obtained. The overall mass flow rate for the required electricity generation could be calculated using the following formula:

$$m = \frac{W}{\eta_m (h_1 - h_2)} \qquad (6\text{-}1)$$

where η_m is an efficiency factor that is used to indicate irreversibility of the thermodynamic expansion process and the energy loss caused by mechanical and fluid flow friction. Previous investigation [Riffat S. B. et al, 1999] gave an estimated value of the factor of 0.2.

The number of domains required for a specified electricity output was:

$$n = \frac{m}{m_e} \tag{6-2}$$

Several working fluids, namely, water, n-pentane, methanol and R141b, were investigated, and different boundary conditions (inlet/outlet) were assumed, as shown in Table 6-1. In the simulation, fluid was treated as a supersonic, compressible medium as its flow speed was above sonic speed. The compressible flow model was applied using the gas law option. The fixed pressure boundary condition was given and the relative pressure values in relation to inlet conditions were used. Supersonic outflow boundary terms were used since the flow at the exit was a supersonic flow. Two different zones, i.e., inner and outer ones, were considered. The inner zone was set at a rotation speed of 80,000 rpm for 1.5kW electricity generation, and 320,000 rpm for 6kW electricity generation, using the fan/blower model.

Table 6-1. Summary of the simulation conditions

Working fluid	Inlet pressure, bar	Inlet temperature, °C	Outlet pressure, bar	Outlet temperature, °C	Rotation velocity, rpm (1.5kW)	Rotation velocity, rpm(6kW)
Water	7.55, 7, 6, 5, 4, 3	240, 231, 214, 193, 169, 140	0.199	60	80,000	320,000
n-pentene	7.5, 7, 6, 5.14, 5, 4	111, 108, 101, 95, 96, 90	2.14 (1.15)	60 (38)	80,000	320,000
mathanol	7, 6, 5	131, 118, 103	2.863	60	80,000	320,000
R141b	7, 6, 5, 4	102, 95, 88, 82	2.18, 2.24, 2.24, 2.24	60	80,000	320,000

The predicted velocity, pressure and density distributions for one case, i.e., using water as the working fluid, which was in the state of 7.55bar/240°C at the inlet, and 0.1992bar/60°C at the outlet, are shown in Figures 6-5 to 6-7, respectively. It was found that the velocity varied significantly along the flow channel, from initially 6m/s to 710m/s at the exit, and the maximum velocity occurred at the area immediately after the throat section. It was also found that the flow was always turned to one side of the channel boundary due to limitations of the channel geometry, causing a high-speed rotation. Consequently, fluid pressure and density reduced significantly along the flow path. The flow was found to be a typical compressible, supersonic, vortex flow.

Based on the simulation conditions described previously, the mass flow rate of a single flow domain was determined and the percentage of un-blocked area required was calculated for different situations, as shown in Figures 6-8 to 6-11. Vapour at the inlet was considered as a saturated vapour. The inlet pressures were assumed and the temperatures were calculated correspondingly. The outlet temperatures were assumed to be 60°C to allow a hot water of 40 to 50°C to be produced, and the outlet pressures were calculated based on the assumption of the isotropic process occurring in the turbine. The simulation conditions are summarised in Table 6-1. Results indicate that water is the best of the four fluids investigated, as it could produce the required electricity output using a lower mass flow rate and smaller flow area. It was also found that water is the only fluid that allowed 6kW electricity output using this turbine. For all the working fluids, the higher the inlet pressure, the less the mass flow rate and the smaller the required flow area if the electricity output remained constant. For a 6kW electricity output using the turbine, only water could be considered as the working fluid and the inlet pressure would be at least 4bar. However, if only 1.5kW electricity output is required, n-pentane, methanol, R141b and water would be all suitable working fluids. If the outlet temperature reduced from 60°C to 38°C, the outlet pressure reduced, and the inlet pressure would reduce correspondingly.

Provided that the inlet pressure remained unchanged, reducing the outlet temperature (pressure) would result in a significant increase in power. However, if the power output remains constant, reduction of the outlet pressure would lead to reduced mass flow rate and flow area.

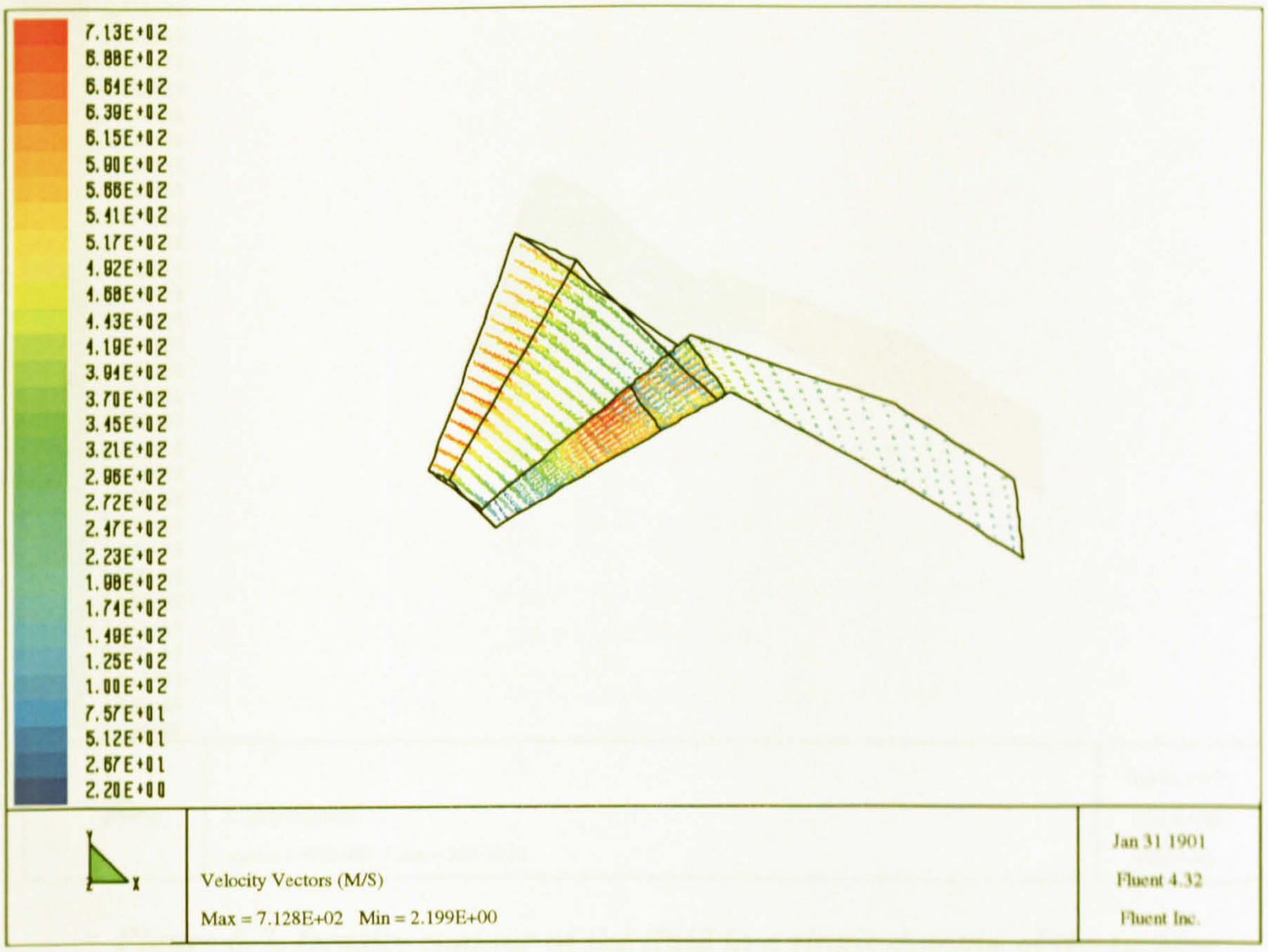

Figure 6-5. Velocity vectors in a single domain of the turbine

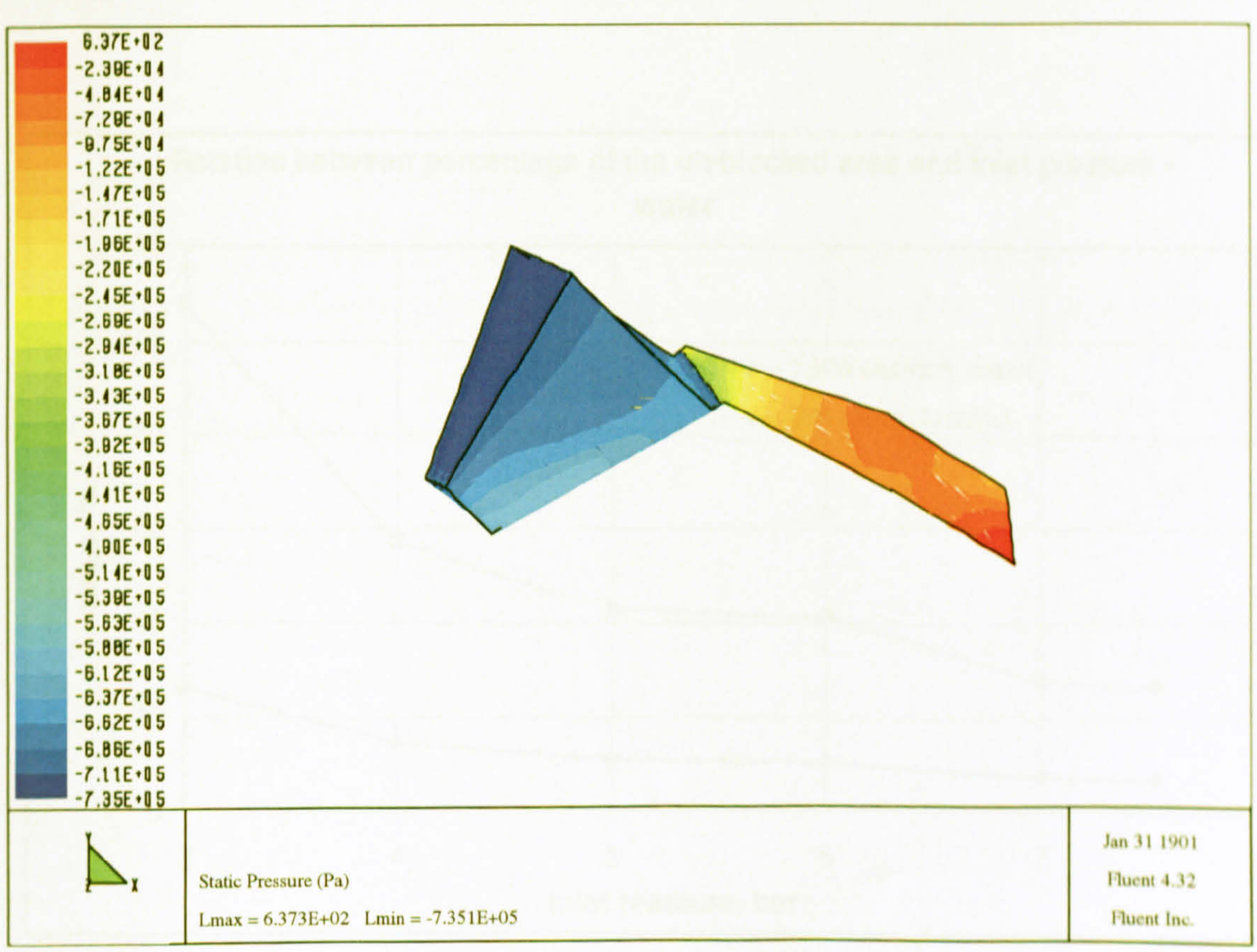

Figure 6-6. Static pressure contour of the fluid in a single domain of the turbine

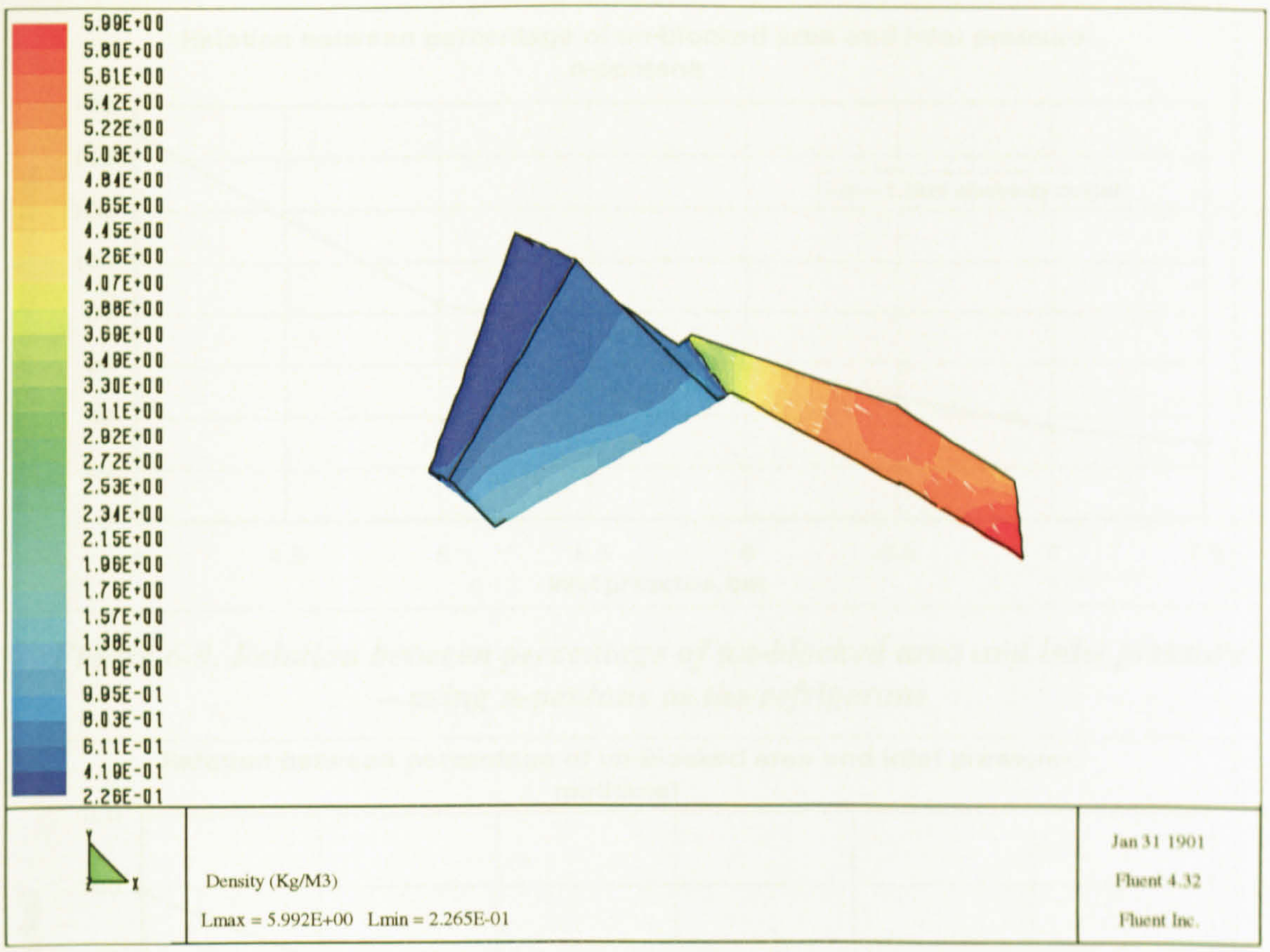

Figure 6-7. Density contour of the fluid in a single domain of the turbine

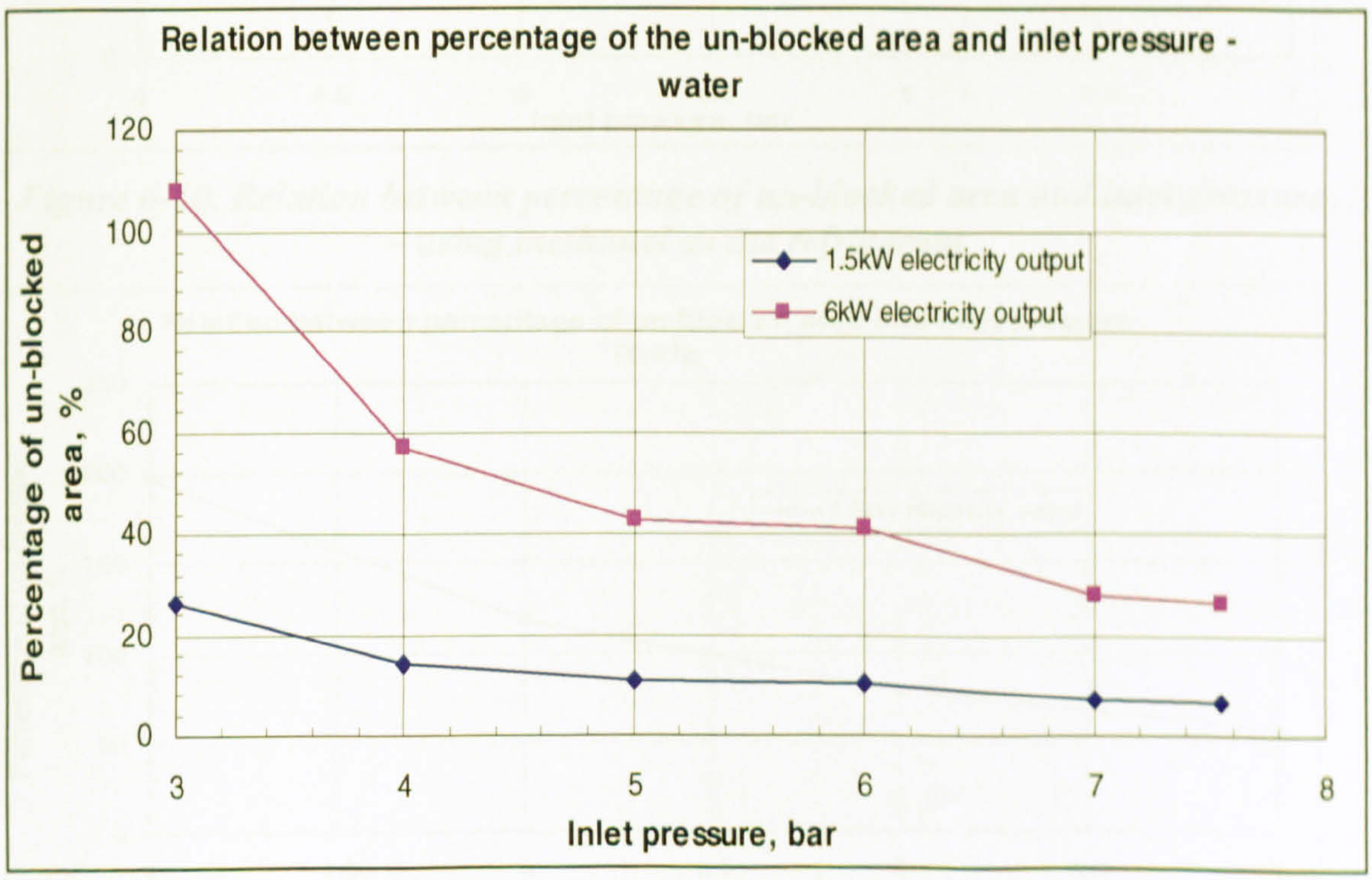

Figure 6-8. Relation between percentage of the un-blocked area and inlet pressure – using water as the refrigerant

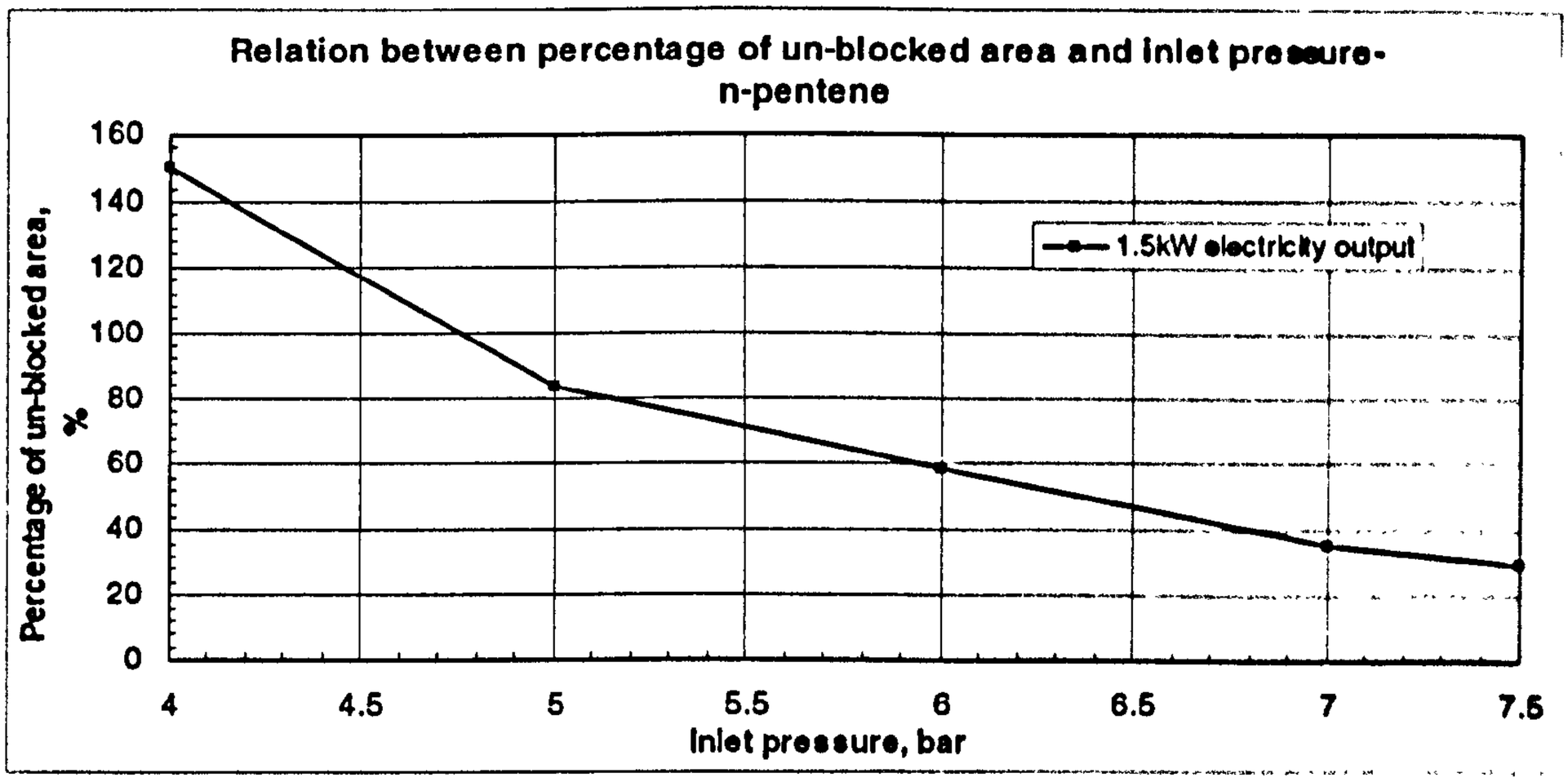

Figure 6-9. Relation between percentage of un-blocked area and inlet pressure – using n-pentane as the refrigerant

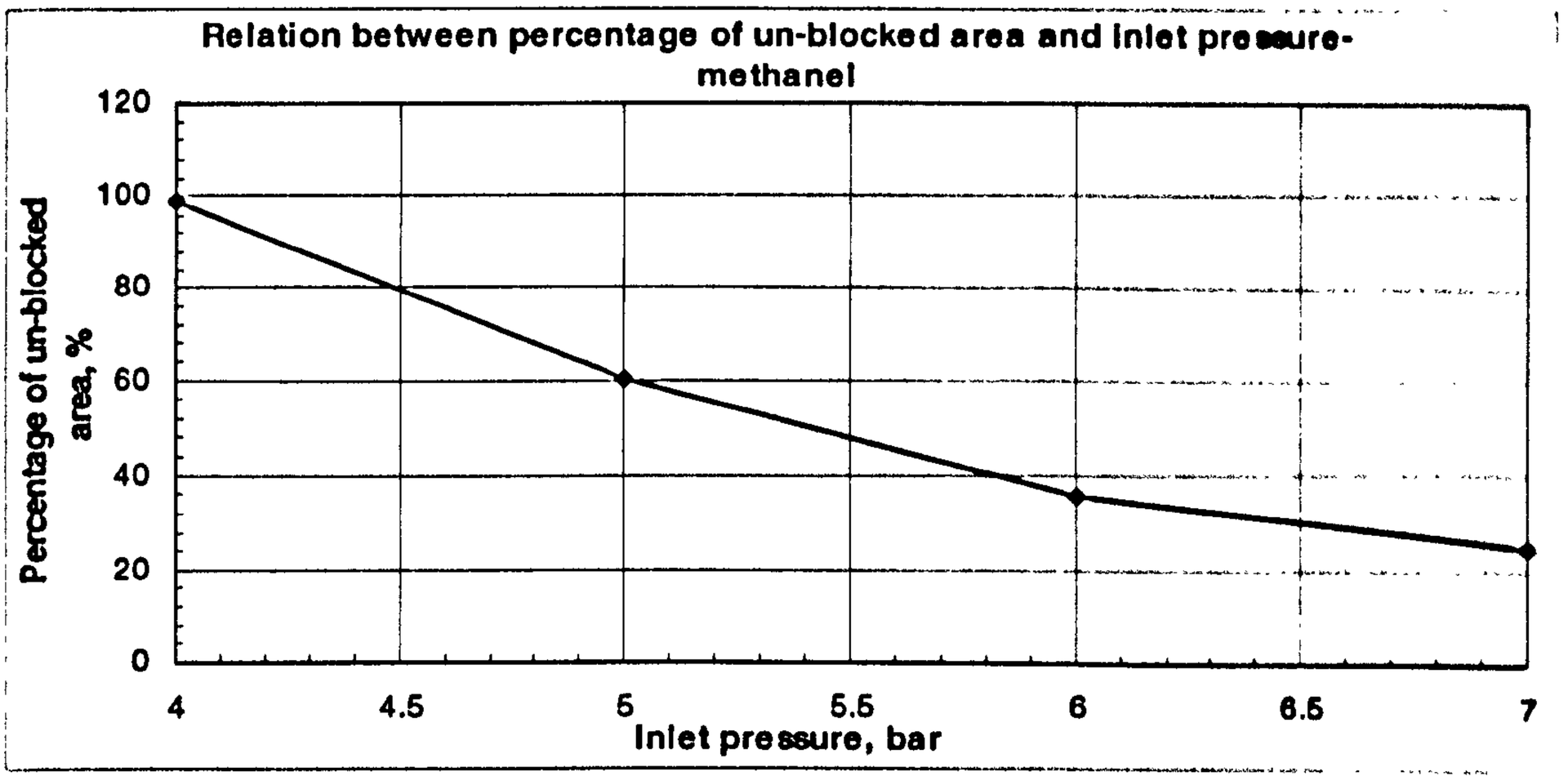

Figure 6-10. Relation between percentage of un-blocked area and inlet pressure – using methanol as the refrigerant

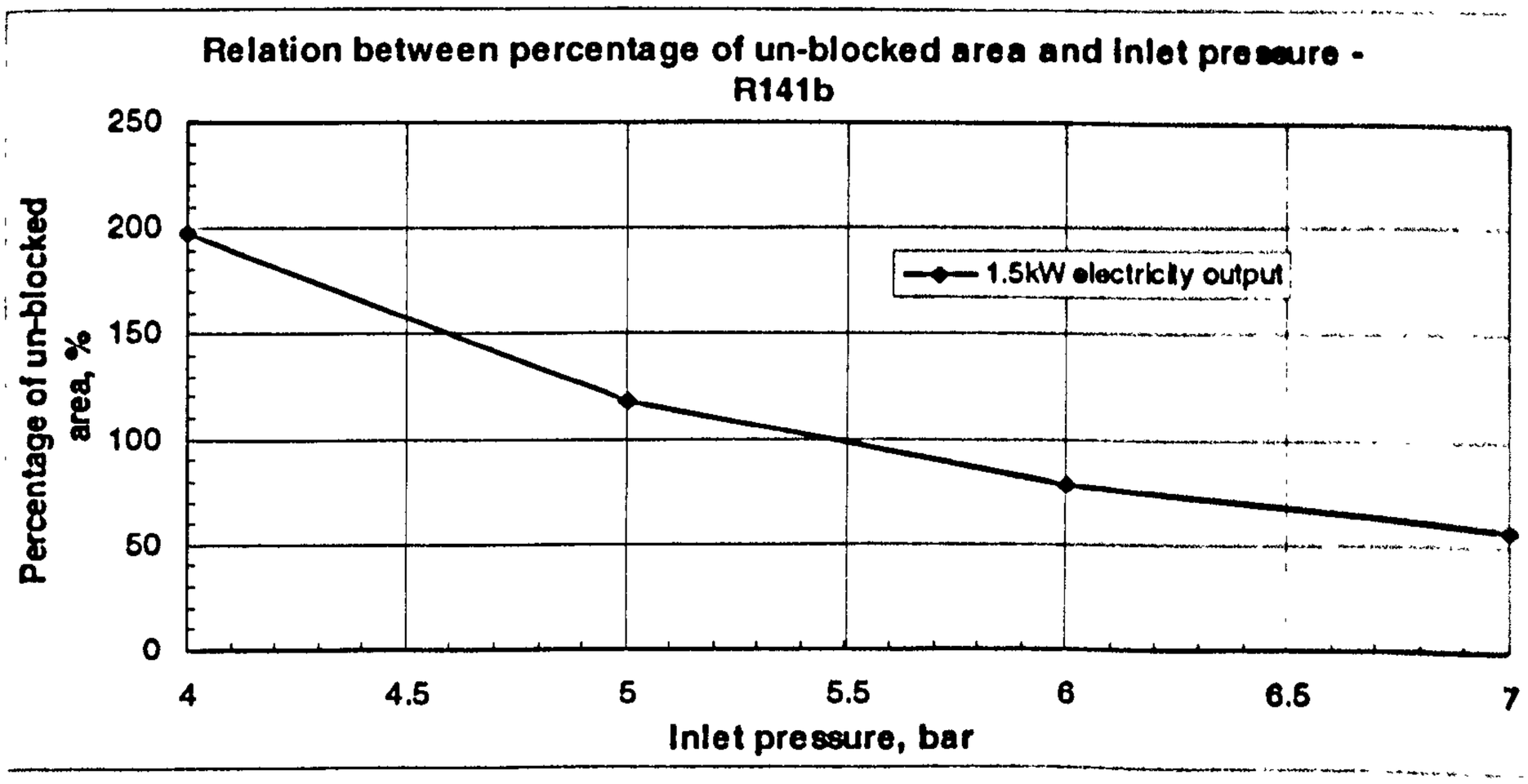

Figure 6-11. Relation between percentage of un-blocked area and inlet pressure – using R141b as the refrigerant

6.3 Experimental Testing

A prototype system was constructed to carry out laboratory testing. The system used a normal pressure boiler and a normal pressure solar collector as heat sources. These produced high temperature hot water of 110°C. The hot water was used to heat a secondary fluid, n-pentane or HFE7100, using a generator, a super-heater as well as a separator, as shown in Figure 1-1. Both n-pentane and HFE7100 are refrigerants that have low boiling points, i.e., 35°C and 60°C respectively, and can be converted to a pressured, superheated vapour if heated in the generator and superheater. The vapour was used to drive the turbine to generate electricity, causing its temperature to fall significantly. It became a mixture of vapour and liquid, which was used to produce domestic hot water via the condenser. The schematic diagram showing the configuration of the system is presented in Figure 1-1.

A 70kW nominal capacity boiler was used in the system, and a hybrid heat pipe solar collector was also incorporated, which was indicated in Chapter 5. However, the first set of tests excluded the collector operation by simply shutting off the valves on the pipelines connected to the collector. A photograph of the boiler is shown in Figure 6-12.

A 100kW nominal capacity fan condenser was installed to cool the chill water, and the water was then used to condense refrigerants (HFE7100 or n-pentane) from the turbine by using a pair of flat-plate heat exchangers each with 25kW nominal capacity. The fan condenser is shown in Figure 6-13, and the flat-plate heat exchanger is shown in Figure 6-14.

Preliminary test was carried out using the hybrid CHP system. The impulse-reaction turbine was installed in the system, and n-pentane was used as the working fluid. The n-pentane liquid would be vaporized into superheated vapour with a pressure up to 5-6 bar if heated to 100°C. The heat required for the CHP operation was supplied solely by the boiler, generating hot water at temperature of 110°C.

Figure 6-12. A 70kW nominal capacity boiler

Figure 6-14. A 25kW nominal capacity heat exchanger

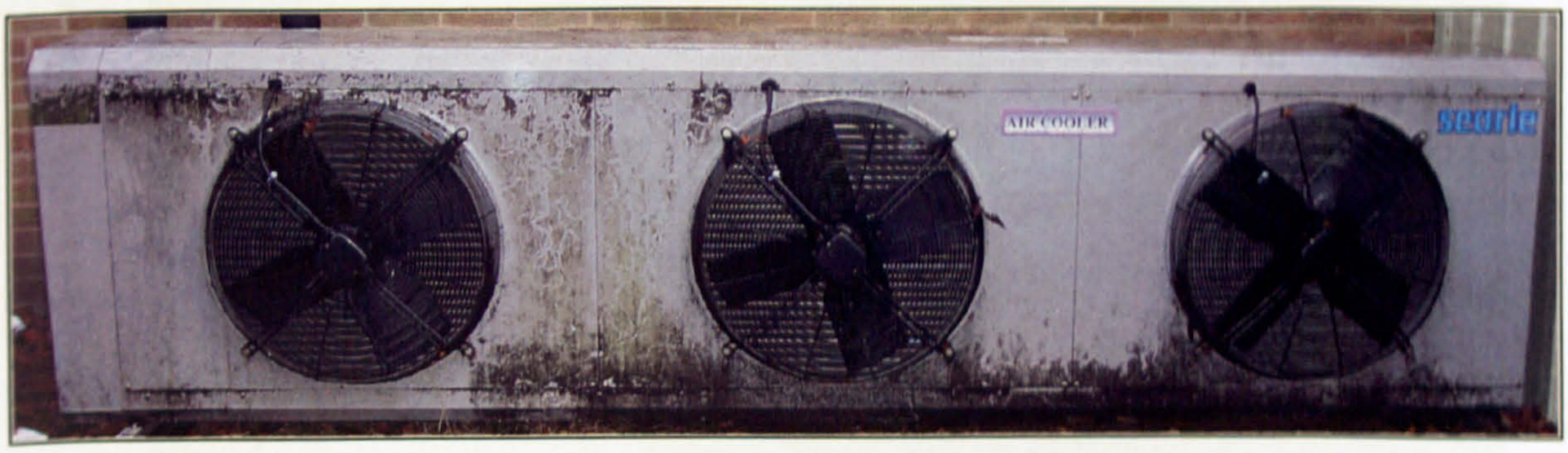

Figure 6-13. A 100kW nominal capacity fan condenser

The variation of refrigerant pressure at different points is shown in Figure 6-15. It is seen that n-pentane was heated rapidly and entered a steady state situation soon after the system was started up. The pressure at the inlet of the turbine was as high as 5.14 bar (average), and this fell to 1.14bar (average) after the refrigerant flowed across the turbine machine due to a conversion of fluid kinetic energy to mechanical energy, which was used to drive the generator for electricity generation.

The variation of refrigerant temperatures is shown in Figure 6-16. It is seen that temperature of the refrigerant at the outlet of the super-heater was as high as 95°C, and this dropped to about 38°C after the vapour fluid passed through the turbine machine, due

to the significant reduction in pressure. The fluid then experienced a 5-6°C reduction in temperature in flowing through the flat-plat heat exchangers for condensation. However, the temperature gained about 0.8°C after the condensate was pumped to a higher pressure. The flow rate measured at the outlet of the condensers was 12 l/m, equivalent to 435kg/h.

The voltage and current readings were 131 volts and 10.3 amps respectively, giving a power output of approximately 1.35kW.

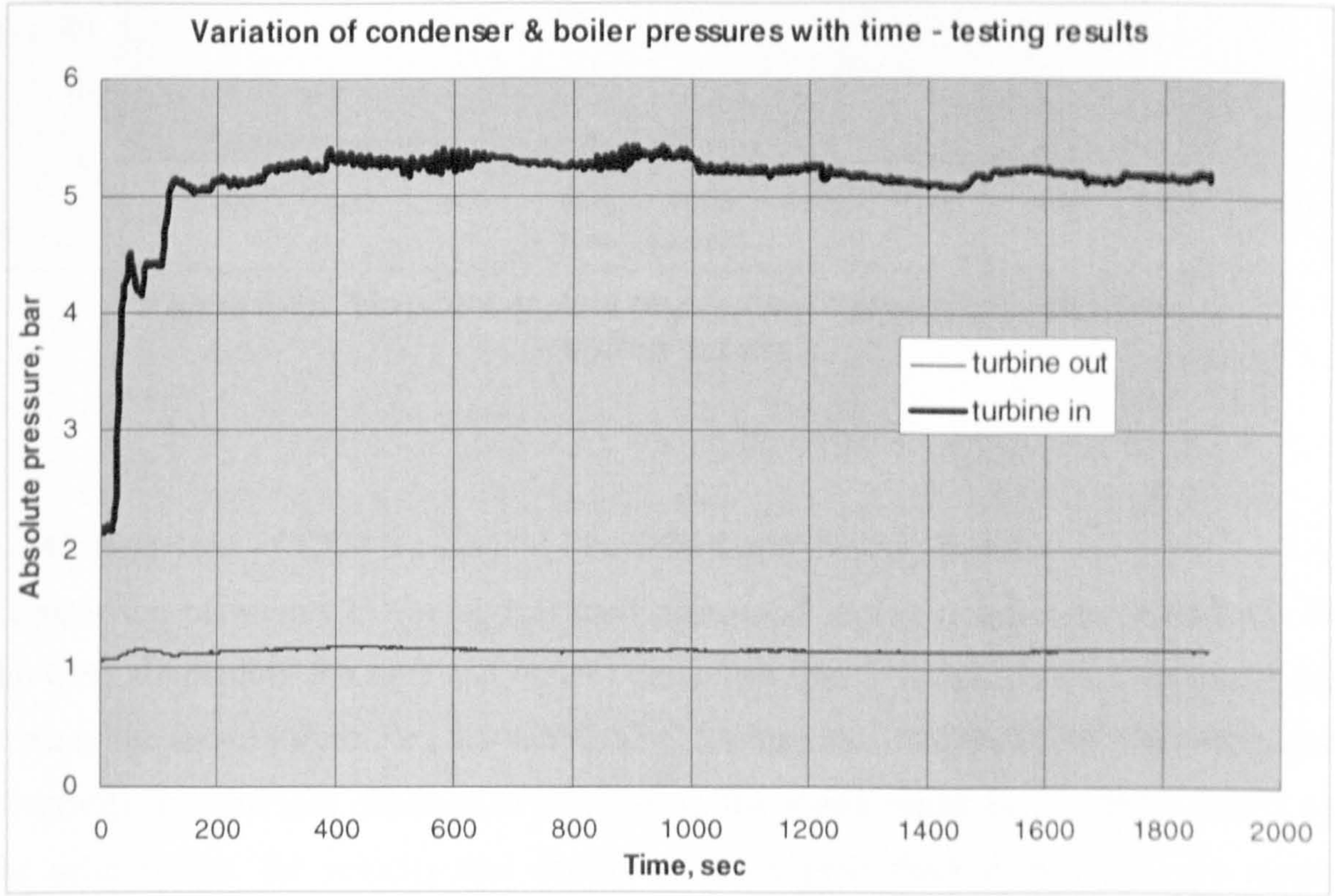

Figure 6-15. Variation of fluid (n-pentane) pressures with time – testing results

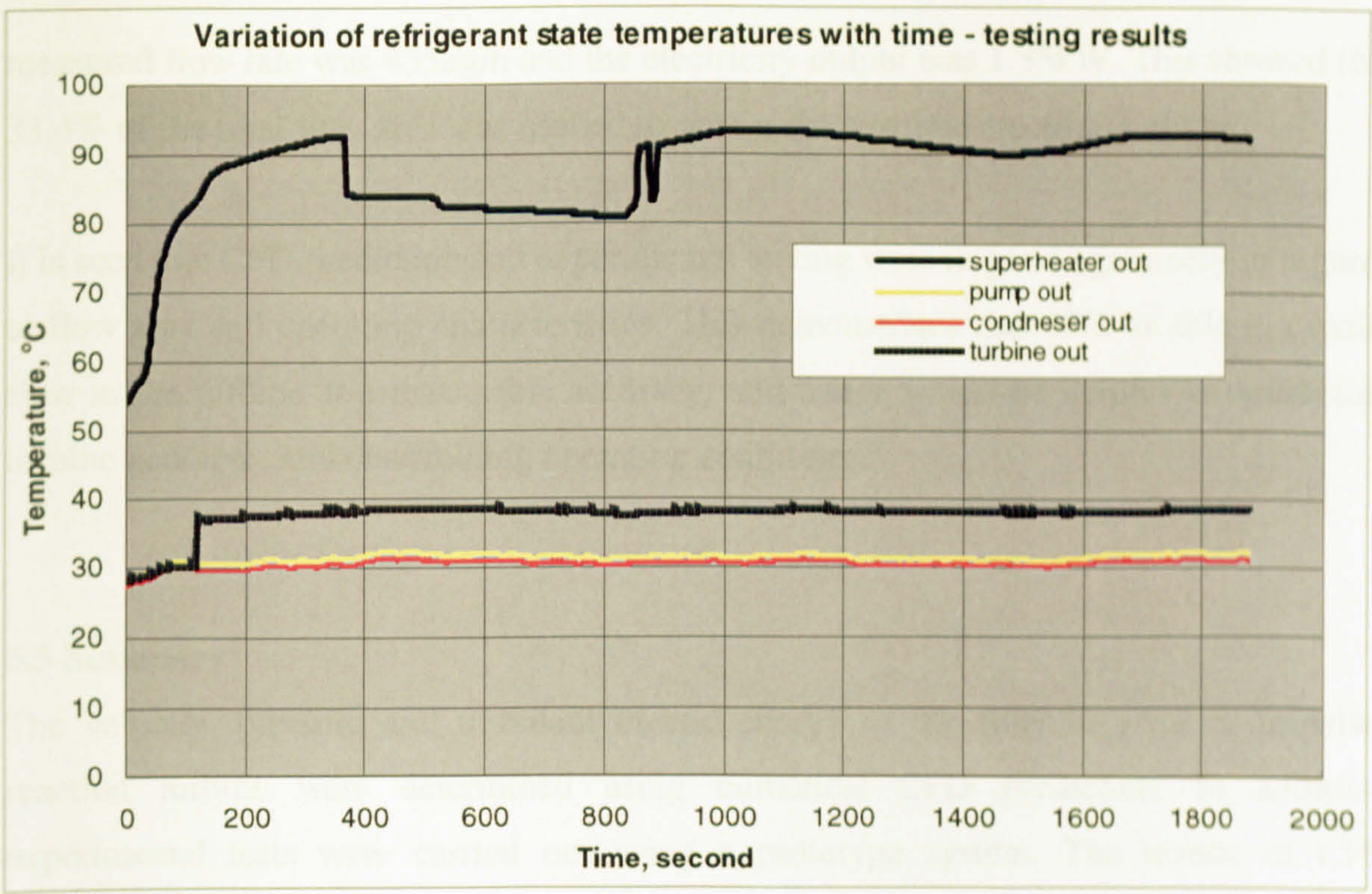

Figure 6-16. Variation of fluid (n-pentane) temperatures with time – testing results

6.4 Comparison of CFD Numerical Prediction and Testing Results

Comparison between CFD numerical predictions and testing results was carried out. In the CFD simulation, the inlet and outlet parameters (pressure and temperature) were the same as the tested values, i.e., 5.1 bar/93.57°C for inlet and 1.15bar/56.8°C for outlet, and electricity demand was assumed to be equal to the tested value, i.e., 1.35kW. Based on the assumptions, the velocity and density of the vapour fluid at the inlet of a single domain were determined using the CFD numerical technique, given as 63.8m/s (average) and 13.95kg/m^3 respectively. The mass flow rate of the fluid passing through a single channel was then calculated by timing the inlet area (10^{-5}m^2), given as 0.0089kg/s. By using Eqs. 6-1 and 6-2, the number of domains involved in the operation was determined as 13.6. This means that 38% of the total flow area needs to be utilized and the rest could be blocked in order to achieve the required electricity output.

In the experimental testing, 2/3 of the flow channels of the turbine were blocked by using a curved baffle. The average pressure and temperature of the n-pentane vapour flow at the inlet and outlet were same as the values assumed in the CFD simulation. The

measured flow rate was 435kg/h and the electricity output was 1.35kW. This showed that 33.4% of the total flow area was needed to obtain the required electricity output.

It is seen that CFD prediction and experimental testing were in good agreement in regards to flow area and operating characteristics. This demonstrates that CFD is able to predict flow in the turbine at a reasonable accuracy, and hence would be helpful in optimizing turbine geometry and determining operating conditions.

6.5 Summary

The velocity, pressure and turbulent kinetic energy of the flow in a micro impulse-reaction turbine were determined using numerical CFD prediction. In addition, experimental tests were carried out using a prototype system. The results of CFD simulation and testing show good agreement. This indicates that CFD could be used as an effective tool for optimizing turbine geometry and determining operating conditions.

Water is the best of the four working fluids investigated, as it could produce the required electricity output using a lower mass flow rate and smaller flow area. Water is the only working fluid which would allow the turbine to produce a 6kW electricity output.

The higher the inlet pressure, the lower the mass flow rate and the smaller the required flow area if the electricity output and outlet pressure remained unchanged. To produce 6kW electricity output using the turbine, the inlet pressure of water vapour would be at least 4bar. However, If only 1.5kW electricity output were required, n-pentane, methanol, R141b and water would all be suitable working fluids. If the outlet temperature were reduced from 60°C to 38°C, the required inlet pressure would also be reduced correspondingly.

.

Chapter 7. Hybrid Heat Pipe Solar Collector/CHP System

7.1 Description of the System

CFD modelling indicated that water is be an efficient working fluid for the system as it could produce a given power at a low mass flow rate and smal flow area [Riffat S. B. et al, 2002]. However, the vapour would need to be at high pressure and temperature, e.g., 6bar and 200°C, respectively, which could only be obtained using a pressurized steam generator and a pressurized solar collector manifold. These requirements would make the system unsuitable for residential use due to safety reasons.

An alternative arrangement using a boiler and solar collector at normal pressure was therefore investigated. This system would produce high temperature hot water, at around 110°C, which would be used to heat a secondary fluid, either n-pentane or HFE7100, using a generator, and a super-heater as well as a separator, as shown in Figure 1-1. Since both n-pentane and HFE7100 are refrigerants having low boiling points, i.e., 35°C and 60°C respectively, they could easily be converted to pressured, saturated or superheated vapour when heated in the generator and super-heater. The vapour would be used to drive the turbine to generate electricity, causing its pressure and temperature fall, and would exit the turbine as a superheated vapour, or mixture of vapour and liquid. The low pressure vapour (or mixture) would be used to produce domestic hot water by passing it through the heat exchangers to allow heat exchange between the refrigerant and chill water. A schematic diagram showing the configuration of the system is presented in Figure 1-1.

Two types of solar collectors were designed and constructed; one was the thin membrane heat pipe solar collector, and the other was the hybrid heat pipe solar collector. Previous investigation (Chapter 5) showed that hybrid one was more suitable to this application, as it could recover part of the waste heat from boiler exhaust gas and so would have a higher thermal efficiency than the thin membrane type. Decision was therefore made to choose the hybrid type as the final option.

For the hybrid type, two structures were considered; one uses the wicked heat pipes made by Thermacore (UK) and the other uses the wickless heat pipes made by Thermomax (UK). The analytical investigation (Chapter 3) showed that the wicked heat pipes are better at distributing liquid film over the inner surface of the heat pipes and are therefore expected to

achieve a higher level on heat transfer than the wickless ones. Decision was therefore made to choose the wicked pipes in the construction. Each heat pipe is a tube structure that has no physical separation between the evaporation section and condensation section. The manifold was in touch with the condensation areas of the heat pipes by using copper rods, which were drilled with co-axial cylinder cavities. Heat transfer between the condensers and the manifold is largely dependent on the conductivity of the rods. Totally 20 heat pipes were incorporated in the collector panel which has a gross absorption area of 2.4m^2 and an effective absorption area of 2.2m^2. CAD drawings showing the structure of the heat pipe absorber panel are presented in Figure 5-4.

The casings of the collector were constructed with aluminium frames, comprising an insulated bottom chamber and a top cover. The bottom chamber of the enclosure contained 5 conjugated channels, which allow exhaust flue gas from the boiler to pass through to improve the efficiency of the collectors, as well as provide a back up (or compensation) when solar irradiation is unavailable (or low). Fibre-glass insulation was fitted beneath and around the channels to reduce heat loss through the chamber. The top cover is a thermo-clear polycarbonate sheet, which has a solar transmission of 0.85 and U value of 3.0W/m^2.K.

Schematic diagrams showing the structure of the solar collectors are given in Figures 1-3a, 1-3b and 1-3c. A photograph of the solar collector is shown in Figure 7-1.

Previous tests (Chapter 5) showed that the efficiency of the collector was only 20% to 30% if it was operated at a temperature in the range 100 to 110°C. For solar irradiation of 800W/m^2 (or equivalent), the heat output of such a collector unit would be 350W to 500W. It was estimated that producing 1.5kW electricity would need a heat input of 12kW[Facão Jorge et al]. If 50% of the heat input, e.g., 6kW, was supplied by the collectors, then 15 or more collectors would be required. Manufacturing and installing so many units would be unrealistic for this application due to limited budget and space, and so an alternative system was considered. The alternative system was based on one collector unit, but incorporated a 70kW nominal heat capacity boiler (Figure 6-12), as the replacement of the other collectors. During operation, the boiler produced exhaust flue gas at the rate of 185m^3/h [Hamworthy, 1997]. The flue gas had a temperature of 205°C at the immediate outlet of the boiler and it was intended to utilise its waste heat by mixing the flue gas with an metered

amount of cold air before delivering the mixture to the solar collectors for heat recovery. Mixing the flue gas with cold air would result in an increased air/flue gas flow volume in order to serve more than four collector units for heat recovery.

Unfortunately it was found that in this application, it was not possible to mount the solar collector on the roof adjacent to the chimney owing to its unsuitable north-west orientation. The collector was therefore mounted on the ground near the shed housing the boiler. As it was not possible to transport the chimney flue gas to the collector, a flue gas simulator, which provided hot air of 110°C-120°C at the rate of 0.035m^3/s, was employed. A photograph of the simulator is shown in Figure 5-21.

A 100kW nominal capacity fan condenser was installed to cool the chill water, and the chill water was then used to condense refrigerants (HFE7100 or n-pentane) discharged from the turbine by using a pair of flat-plate heat exchangers, each with 25kW nominal capacity. The fan condenser is shown in Figure 6-13, and the flat-plate heat exchanger is shown in Figure 6-14.

Two types of turbine units were investigated; one is a micro impulse-reaction turbine which operated at very high rotation speed, up to 80,000rpm, and provided an electrical output of 1.5kW to 3kW, shown in Figure 6-2. The other is a compressed-gas driven, turbo-alternator which operated at a low rotation speed, up to 1,000rpm, and gave an electricity output of 250W, shown in Figure 6-4.

The impulse-reaction turbine used n-pentane as the working fluid. This would be vaporized into saturated vapour with a pressure of 5-6bar, when heated to 90-100°C. This is realistic as a solar collector/boiler can provide hot water at a temperature up to 120°C, and this could be used to heat n-pentane to the desired temperature. The turbo-alternator used HFE-7100 as the working fluid. This would be vaporized into superheated vapour with a pressure of 3-4bar, when heated to 100°C. This is also realistic in view of the solar collector/boiler's capacity to provide hot water at a temperature up to 120°C. The hot water could be used to heat HFE-7100 to 100°C and then vaporize it using a generator and a super-heater. Although initial trials indicated that the output of the turbo-alternator was lower than the requirement, further work is being carried out to establish if its output can be increased.

As n-pentane is a flammable liquid, a diaphragm pump driven by compressed air was used in the CHP cycle for safety reasons. A photograph of the diaphragm pump is shown in Figure 7-2.

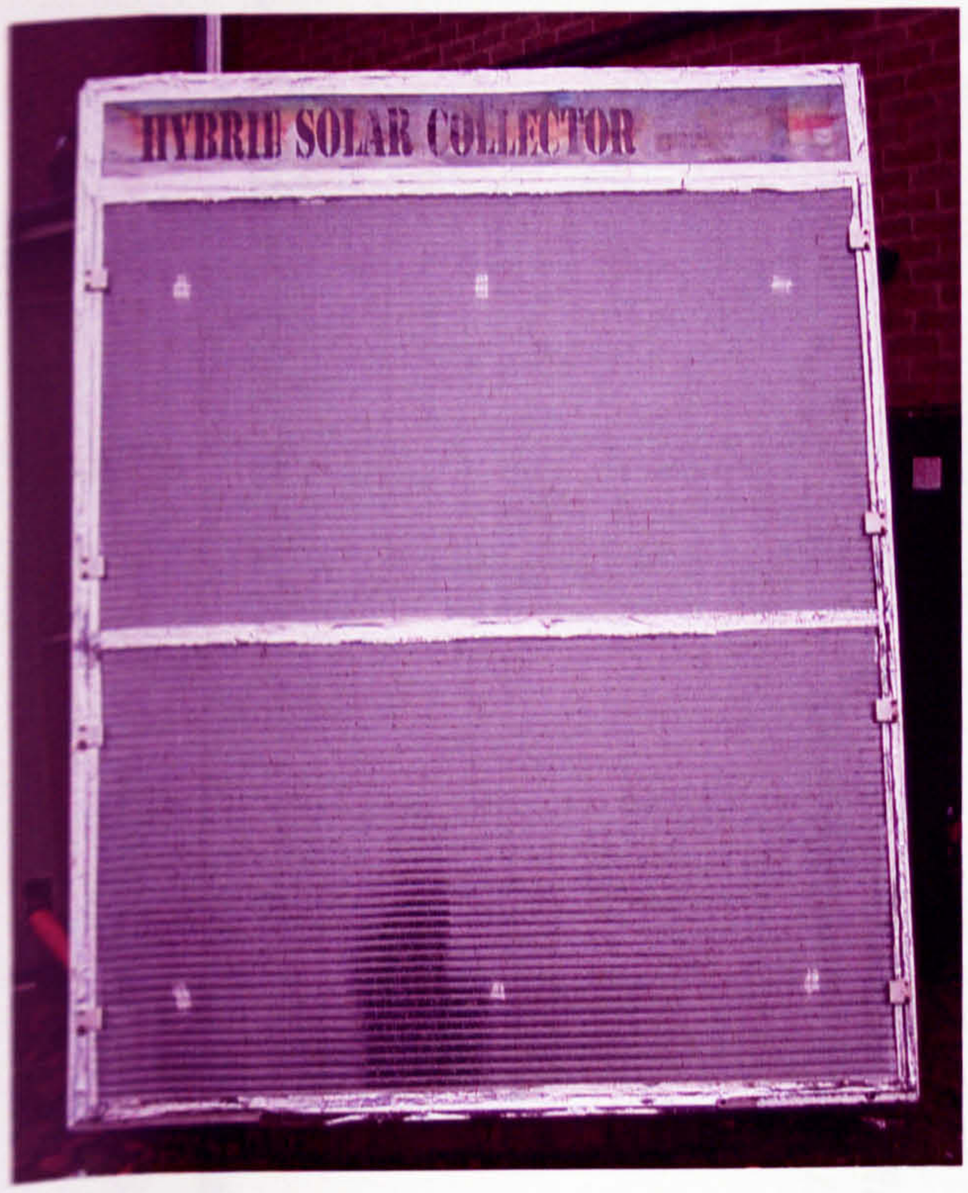

Figure 7-1. Heat pipe solar collector – prototype 1 (wicked panel)

Figure 7-2. A diaphragm pump used for the hybrid solar collector/CHP system

A prototype system was constructed based on the integration of the components described above, see Figures 7-3. Performance of the prototype unit would be investigated theoretically using classical thermodynamic principles, and also tested in a building of Nottingham University. Comparison between theoretical and testing results would be carried out to give a general mapping of the system's performance, availability as well as energy and environmental benefits.

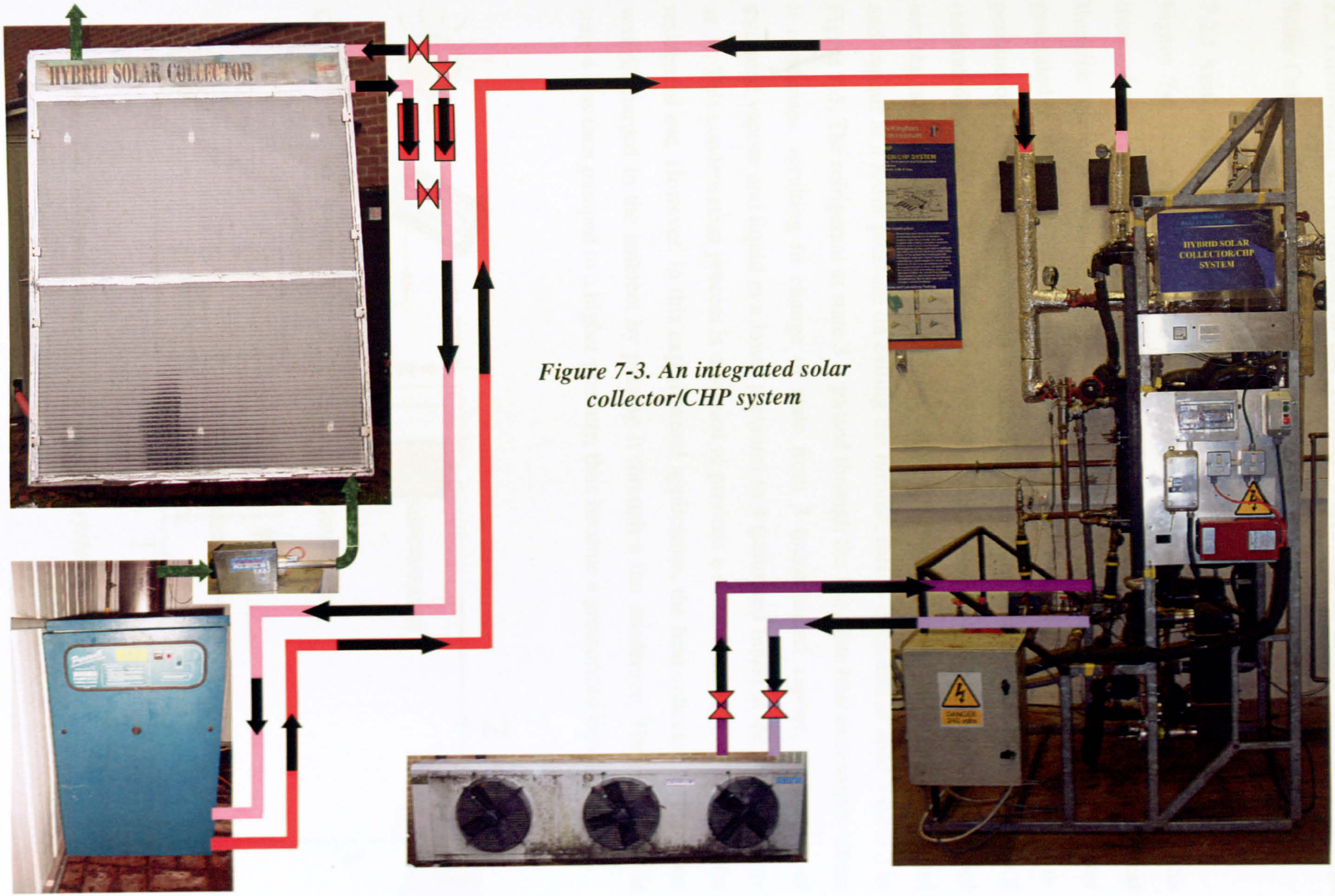

Figure 7-3. An integrated solar collector/CHP system

7.2 Theoretical Investigation of the Thermal Performance of the Hybrid Heat Pipe Solar Collector/CHP System

7.2.1 Analysis of the Thermodynamic Cycle and Heat Transfers

Figure 7-4 presents a schematic of the system layout, and Figure 7-5 indicates the thermodynamic cycle using T(temperature)-s(entropy) chart. The system uses a typical Rankine cycle powered by both solar and gas energy. High temperature hot water generated by the boiler/collector unit is used to heat and vaporize the refrigerant (either n-pentane or HFE-7100), resulting in a change of state from 1 (under-saturated liquid) to 2 (saturated vapour) or 2' (super-heated vapour). The vapour at a high pressure is then fed into the turbine to generate electricity, becoming superheated vapour or a mixture of liquid and vapour at a lower pressure on exiting the turbine; this is indicated as state 3 (or 3') in Figure 7-5. The refrigerant at state 3 is passed through the flat-plate heat exchangers where it condenses, resulting in change of state from 3 (superheated vapour, or mixture of saturated vapour and liquid at a lower pressure) to 4 (saturated liquid at the same pressure as 3). This condensation process is designed to produce a suitable amount of hot water for residential use. However, in this experimental application, the heat collected by the water was discharged to the ambient by passing it through a fan condenser. The refrigerant at state 4 was then pumped to a higher pressure, thus become a pressurized liquid state at 1.

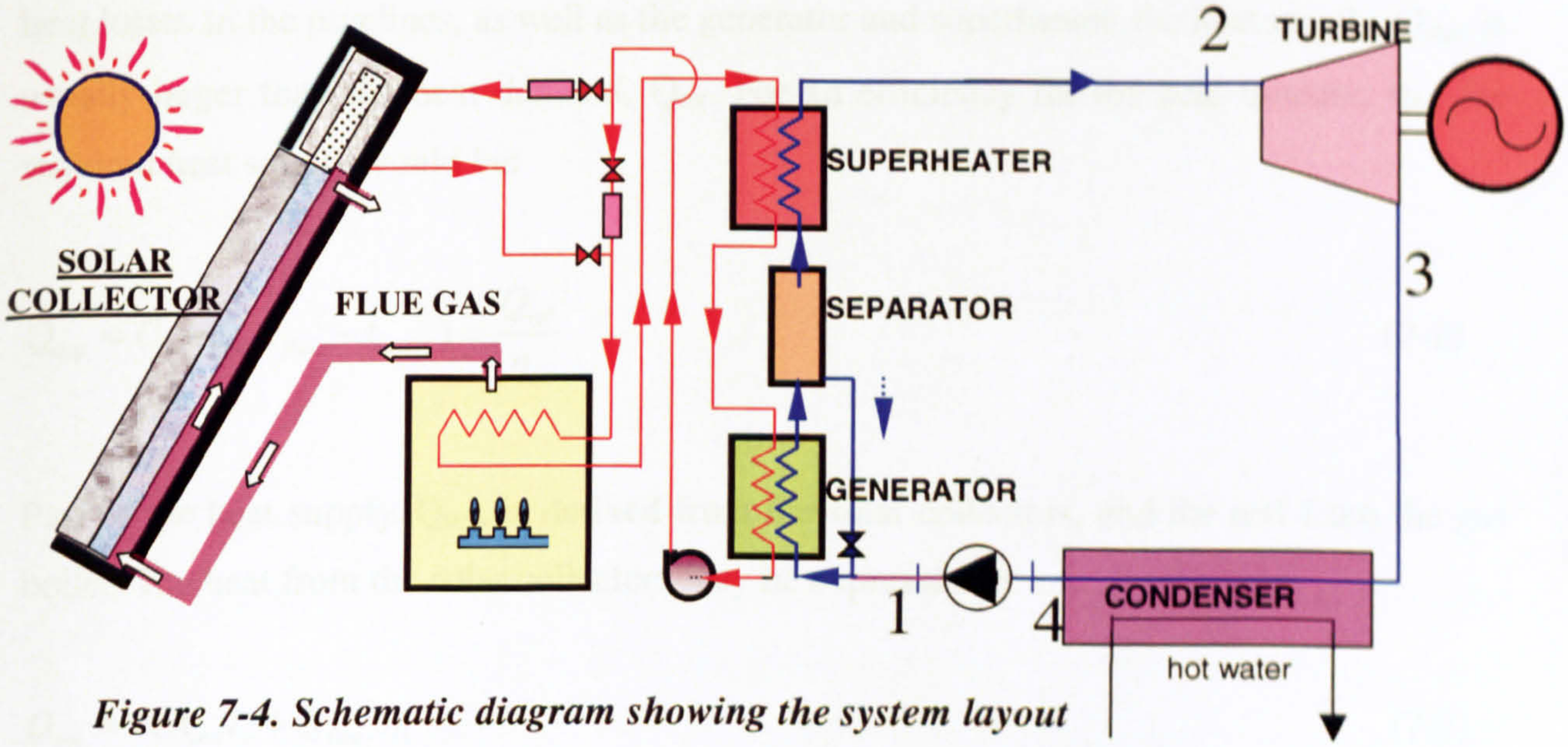

Figure 7-4. Schematic diagram showing the system layout

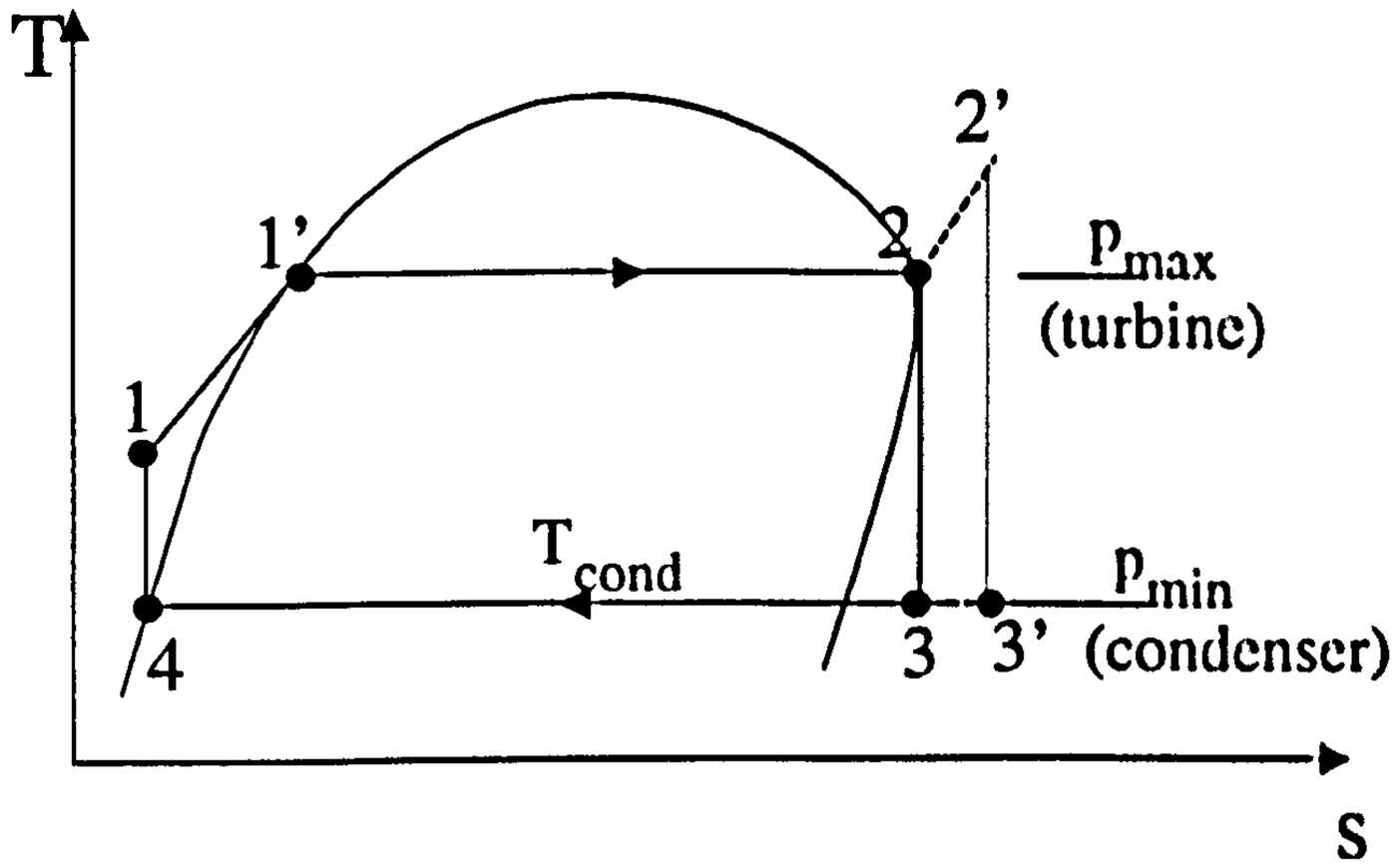

Figure 7-5. Schematic diagram showing the thermodynamic cycle of the system (T-s chart) (ideal process)

For an evaporation pressure, p_e, as well as condensation pressure, p_c, the heat obtained from the generator and superheater by the refrigerant may be expressed as:

$$Q_{ref} = m_r(h_2 - h_1) \tag{7-1}$$

This heat is provided by a combination of the solar collectors and gas boiler. Owing to the heat losses in the pipelines, as well as the generator and superheater, the heat supply, Q_{sup}, is usually larger than the heat demand, Q_{ref}. For an efficiency for the heat transfer, η_{hr}, the required heat supply would be:

$$Q_{sup} = C_p m_{flow}(t_{flow} - t_{return}) = \frac{Q_{ref}}{\eta_{hr}} \tag{7-2}$$

Part of the heat supply, Q_{sup}, is derived from the solar collectors, and the rest from the gas boiler. The heat from the solar collectors may be expressed as:

$$Q_{sol} = n(A_{abs} I_n + Q_{flue})\eta_1 \tag{7-3}$$

where n is the number of the collector units to be used; A_{abs} is the absorber area of each

collector (m^2); I_n is the global solar irradiation (W/m^2); Q_{flue} is the available energy included in the flue (W), which could be calculated using Eq. 5-34; and η_1 is the overall efficiency of the hybrid collector, which could be obtained by using the correlations given in Figures 5-45 and 5-48.

The efficiency of the gas boiler, η_{boiler}, was assumed to be 0.9, thus the gas energy required for the heat supply may be expressed as:

$$Q_{gas} = (Q_{sup} - Q_{sol})/\eta_{boiler} \qquad (7\text{-}4)$$

It was found that for either n-pentane or HFE-7100, state 3 is always located within the superheated area. It is therefore not necessary to create a superheated state at the inlet of the turbine (2), which was aimed to increase the dryness of the refrigerant at the outlet.

Due to the irreversibility of the expansion process for turbine operation, there will be an entropy increase when the state change from 2 to 3. However, this theoretical analysis neglects this increase for reasons of simplification. The error this may cause may be corrected by using a factor, η_m, which considers both the irreversibility of the expansion process and the loss due to mechanical and fluid flow frictions

Given s_3(equal to s_2) and p_3 (equal to p_c), the enthalpy of state 3, h_3, may be obtained by using a program specially designed for property calculation [University of Idaho, 1996] of several refrigerants.

The energy available for electricity generation in this process may be expressed as:

$$Q_e = m_r(h_2 - h_3) \qquad (7\text{-}5)$$

Due to the irreversibility of the expansion process, as well as mechanical friction and fluid flow resistance that usually exist in the turbine-generator unit, the whole of the energy could not be completely converted into electricity power. The efficiency factor, η_m, mentioned above was considered, and this was initially given a value of 0.6 [Facão Jorge et al]. Thus the power output could be expressed as:

$$W = \eta_m Q_e \tag{7-6}$$

Theoretically, the condensation process from 3 to 4 is a constant pressure process, and the enthalpy of state 4 may be considered as that of the saturated liquid at the same pressure as state 3. The energy available for residential hot water production in the condensation process may therefore be expressed as:

$$Q_{con} = m_r(h_3 - h_4) \tag{7-7}$$

Since heat losses usually exist in condensers due to the temperature difference between the condensed refrigerant and room air, the condensed energy cannot also be completely converted into residential hot water output. An efficiency for condensation heat transfer, η_{ce}, was therefore considered, and this was initially assumed to be 0.7 for the flat-plate heat exchangers used in this application [Fullarton D., 2002]. Thus the heat output of the cycle could be expressed as:

$$Q_h = \eta_{con} Q_{con} \tag{7-8}$$

Since the power consumption of the pumps in the refrigerant cycle, hot water system and chill water system were negligible compared to the energy input, and heat and electricity outputs, the electricity efficiency, η_e, heat efficiency, η_h, as well as the overall efficiency, η_{total}, could be therefore be expressed approximately as follows:

$$\eta_e = \frac{W}{Q_{gas}} \tag{7-9}$$

$$\eta_h = \frac{Q_h}{Q_{gas}} \tag{7-10}$$

$$\eta_{total} = \frac{W + Q_h}{Q_{gas}} \tag{7-11}$$

7.2.2 Case Calculation – Impulse-reaction Turbine Using n-pentane as the Working Fluid

The impulse-reaction turbine system was investigated using the theoretical analysis described above. In this investigation, the evaporation pressure, p_e, was assumed to take the value of 6, 5.1 and 4 bar, and the condensation pressure, p_c, was constant at 1.15bar. The vapour at the inlet of the turbine was at a saturated state, and the expansion process in the turbine-generator was treated as a reversible process. Condensation occurring in the condensers was a constant pressure process, and the refrigerant at the outlet of the condenser was considered to be a saturated liquid. The thermodynamic properties of the refrigerant at various states were obtained using the computer program designed for property calculation [University of Idaho, 1996], and are shown in Tables 7-1, 7-2 and 7-3. The mass flow rate in the cycle was assumed to be 435kg/h.

The boiler flow temperature was assumed to be 100°C and the mass flow rate was taken as 62.8l/m. These values are similar to those for the experimental tests so that comparison between theoretical and experimental results may be made more easily. The temperature of the return flow from the generator was calculated using Eq. 7-2. The heat obtained from the collector was calculated using Eq. 7-3, using the assumptions solar irradiation is 550W/m^2, ambient temperature is 14°C, flue gas temperature is 110°C and flue gas flow rate is 0.035m^3/s. The heat demand and corresponding gas energy required for boiler operation were obtained using Eq. 7-4. Finally, the electricity, heat and overall efficiencies for system operation were obtained using Eqs. 7-10, 7-11 and 7-12. It should be emphasised that all the calculations were based on the assumption that the system operated on a typical Rankine cycle. The results derived from the calculation are listed in Table 7-4.

Theoretical investigation was made for three sets of operating conditions, e.g., 6, 5.1 and 4 bar evaporation pressures, and the quantity of the collectors used was assumed to vary from 1 to 4 for each data set. The results for each set of data were compared and the influence of evaporation pressure and quantity of collectors on system performance was evaluated.

Another system, e.g., turbo-alternator using HFE-7100 as the working fluid, was not investigated, as the turbo-alternator was already known to be too small in output to be unsuitable for this system.

Table 7-1. Properties of n-pentane at different states in the cycle process (p_e=6bar)

Properties / State point	P, bar	t, °C	ρ, kg/m³	s, kJ/kg.K	h, kJ/kg
1	6	39.83	603.45	3.757	-1585.4
2	6	100.7	16.4	4.99518	-1136.4
3	1.15	59.49	3.12	4.99518	-1198
4	1.15	39.67	603.01	3.757	-1586.2

Table 7-2. Properties of n-pentane at different states in the cycle process(p_e =5.1bar)

Properties / State point	P, bar	t, °C	ρ, kg/m³	s, kJ/kg.K	h, kJ/kg
1	5.1	39.7	603.436	3.757	-1585.7
2	5.1	93.57	13.95	4.98	-1147.8
3	1.15	56.8	3.15	4.98	-1202.8
4	1.15	39.67	603.01	3.757	-1586.2

Table 7-3. Properties of n-pentane at different states in the cycle process(p_e =4bar)

Properties / State point	P, bar	t, °C	ρ, kg/m³	s, kJ/kg.K	h, kJ/kg
1	4	39.69	603.337	3.757	-1585.9
2	4	83.42	10.99	4.96	-1164.1
3	1.15	53.2	3.19	4.96	-1209.5
4	1.15	39.67	603.01	3.757	-1586.2

Table 7-4. Theoretical calculations of the energy efficiency of the hybrid solar collector system

Operating condition	P_e = 6bar				P_e=5.1bar				P_e=4bar			
Power output, kW	4.47				3.99				3.30			
Hot water generation, kW	32.8				32.4				31.8			
Overall heat input required, kW	60.2				58.7				56.6			
Number of collector unit	1	2	3	4	1	2	3	4	1	2	3	4
Boiler HW flow temperature, °C	100	100	100	100	100	100	100	100	100	100	100	100
HW return temperature at the outlet of the generator(inlet temperature of the collector), °C	86.3	86.3	86.3	86.3	86.6	86.6	86.6	86.6	87.1	87.1	87.1	87.1
HW outlet temperature of the collector, °C	88.16	88.16	88.16	88.16	88.46	88.46	88.46	88.46	88.96	88.96	88.96	88.96
Boiler HW return temperature	86.38	86.46	86.55	86.64	86.68	86.76	86.85	86.93	87.18	87.26	87.35	87.43
Heat from solar and exhaust flue gas, kW	0.364	0.728	1.091	1.455	0.364	0.728	1.091	1.455	0.364	0.728	1.091	1.455
Boiler gas consumption, kW	66.48	66.08	65.67	65.27	64.81	64.41	64	63.6	62.48	62.08	61.67	61.27
Elec. efficiency η_e, %	6.72	6.76	6.80	6.85	6.15	6.19	6.23	6.27	5.28	5.31	5.35	5.38
Heat efficiency η_h, %	49.34	49.64	49.95	50.25	49.99	50.30	50.63	50.94	50.89	51.22	51.60	51.90
Overall efficiency η_h, %	56.06	56.40	56.75	57.10	56.14	56.49	56.86	57.21	56.17	56.53	56.91	57.28

7.2.3 Energy and Efficiency Analysis

Figure 7-6 indicates the energy profiles of the system for one operating condition and one collector configuration, i.e., the evaporation pressure is 5.1bar and one collector unit is used in the system. It is seen that the power generation was 3.99kW and hot water output was 32.4kW. The required heat input was 58.7kW; of which 0.364kW was produced by the collector and the remainder was supplied by the boiler. This would require a gas consumption of 64.8kW for the system operation.

Figure 7-7 shows the relation between efficiency and working pressure (evaporation). This is based on using one collector unit in the system. It was found that the electricity efficiency increased and the heat efficiency decreased when the evaporation pressure increased. However, the overall efficiency remained nearly same during this variation. It was also found that increasing the quantity of collector units did not affect on the trend of this variation.

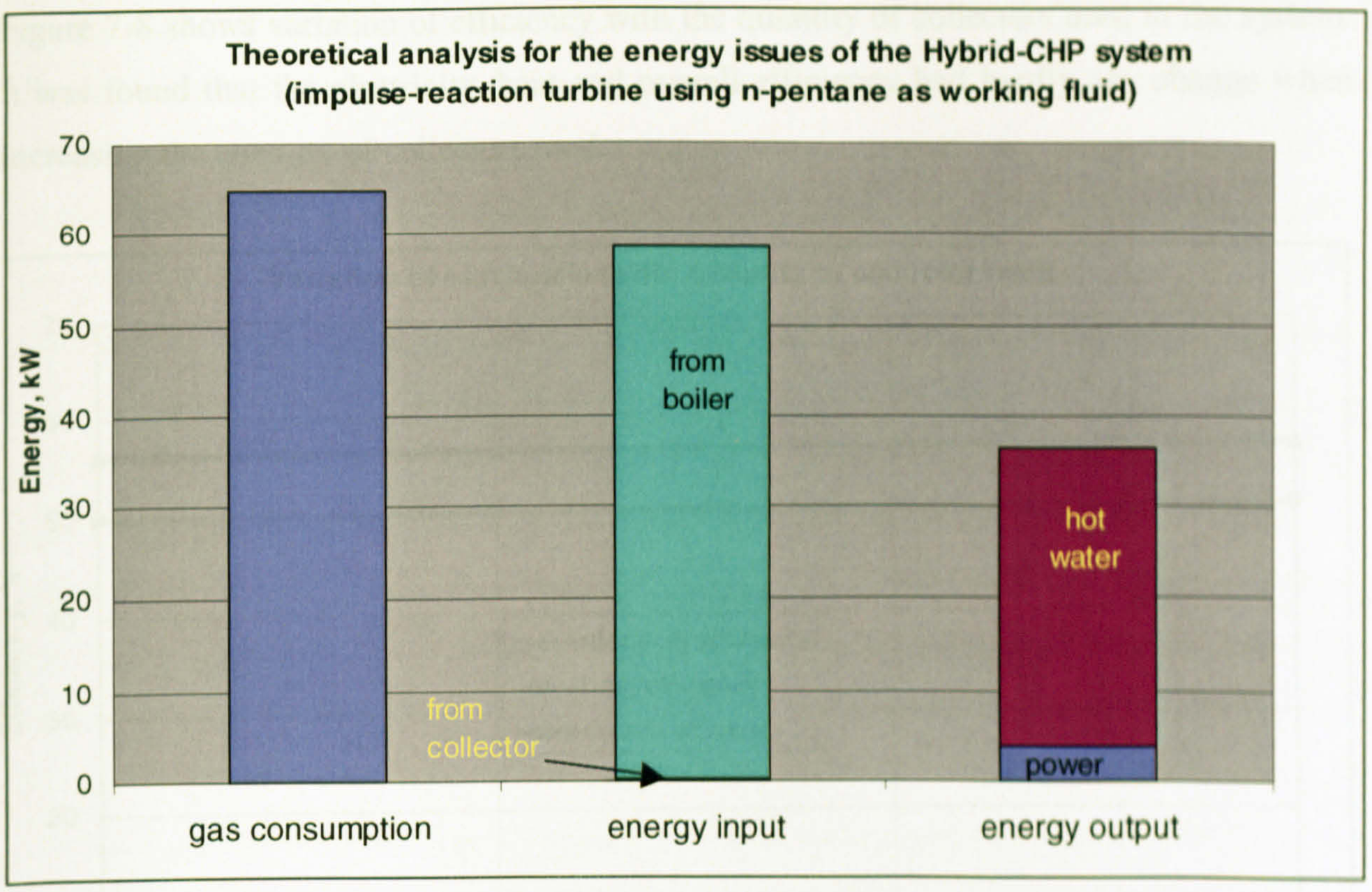

Figure 7-6. Energy profiles of the hybrid solar collector/CHP system – (p_e = 5.1bar, one collector employed)

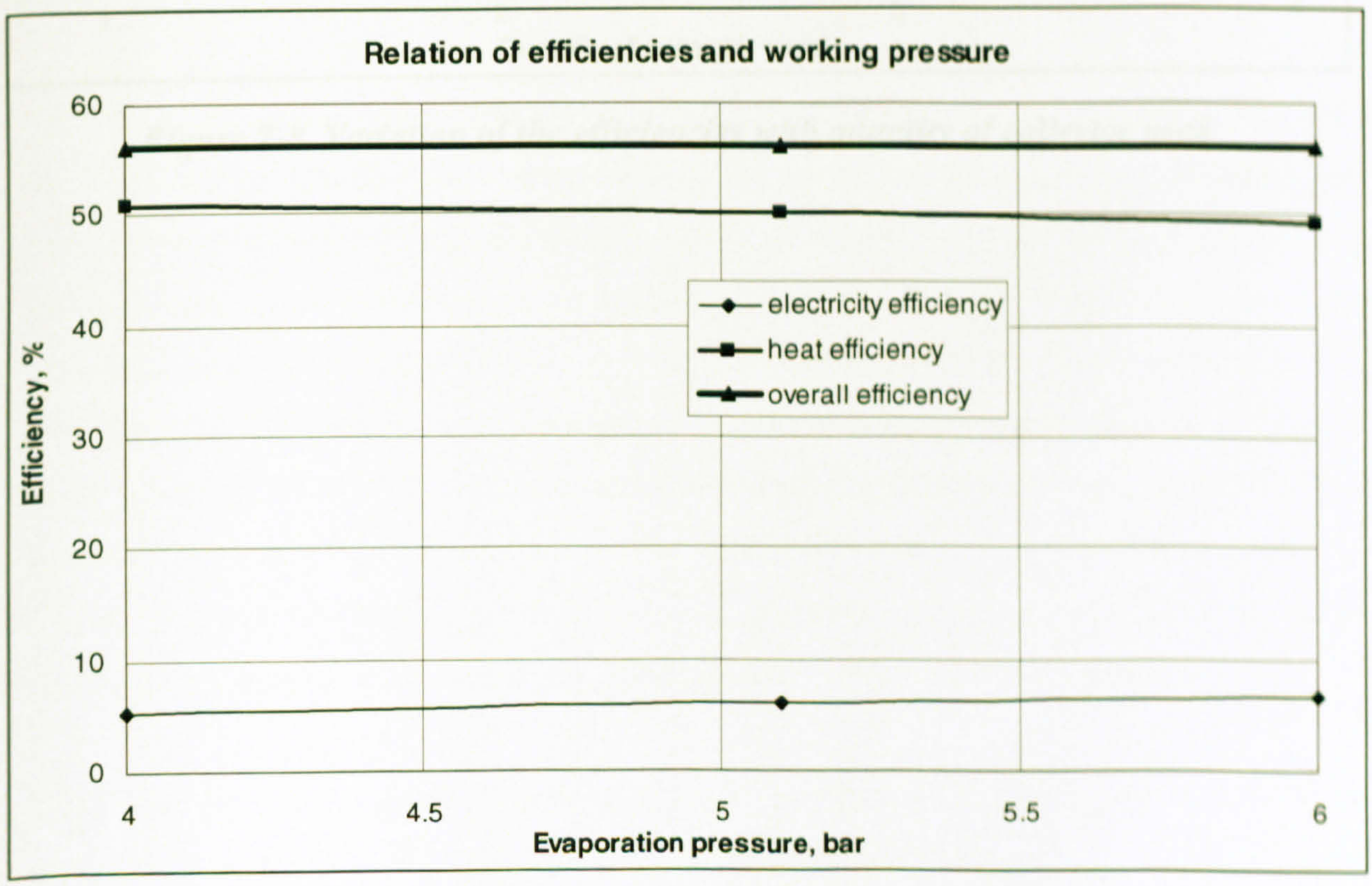

Figure 7-7. Relation of efficiencies and working pressures (evaporation)

Figure 7-8 shows variation of efficiency with the quantity of collectors used in the system. It was found that the electricity, heat and overall efficiency had hardly any change when increasing the quantity of collectors used.

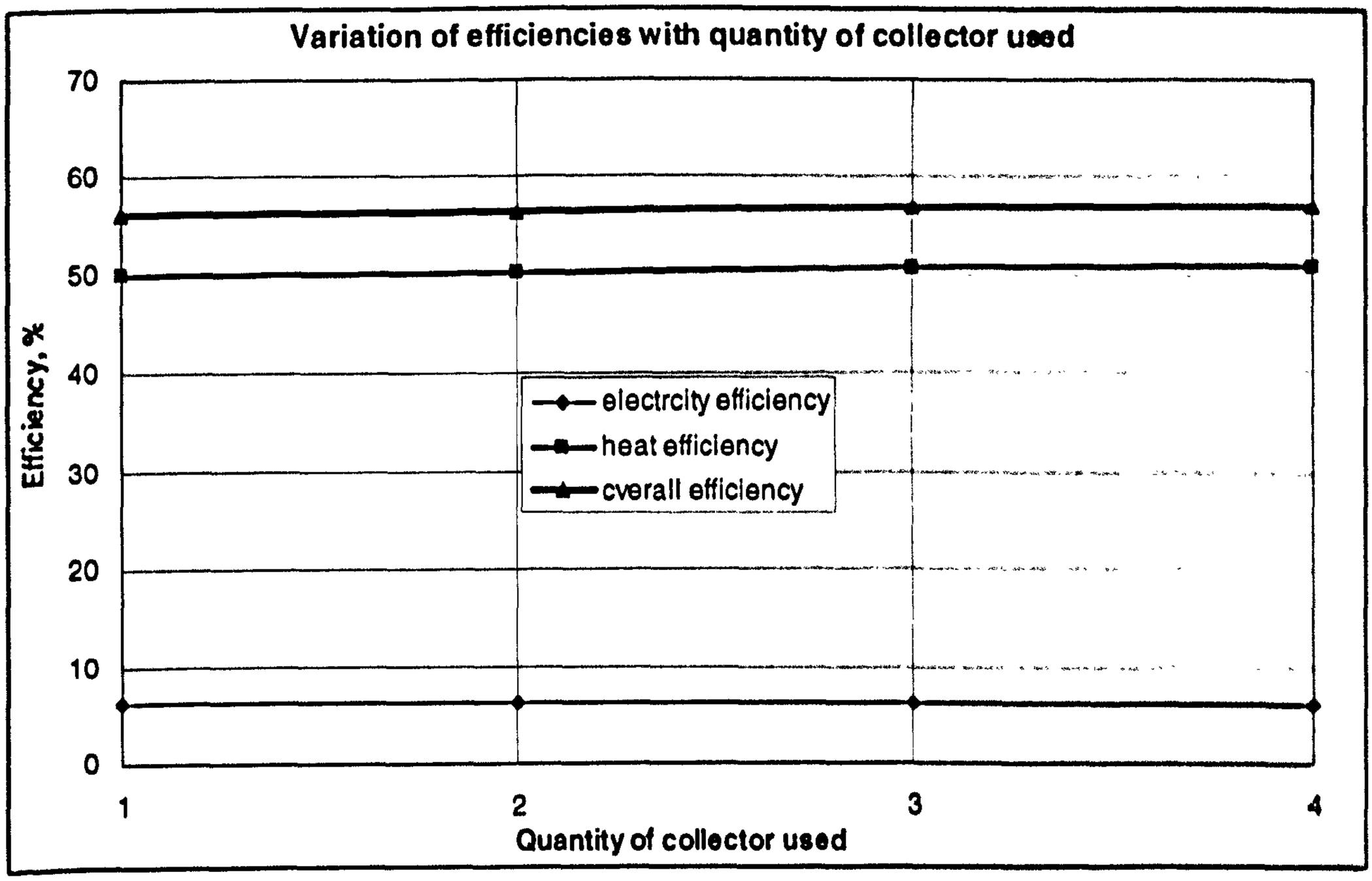

Figure 7-8. Variation of the efficiencies with quantity of collector used

7.3 Experimental Testing of the Hybrid Solar Collector/CHP System

Experimental testing was also carried out for the prototype system. The heat pipe solar collector was mounted outside the test building, the Squash Court on the campus of the University of Nottingham, adjacent to a shed housing the boiler. The collector, in conjunction with the boiler, was operated to supply heat for the domestic micro CHP system. The exhaust flue gas from the boiler was intended to direct across the flow channels fitted to the backside of the solar collector to enhance its heat transfer, and provide compensation, or back up, when solar irradiation was low or unavailable. However, this intention was unrealistic for this application due to safety reasons. To simulate this situation, a gas flue simulator was employed to generate hot air (equivalent to gas flow). T-type thermocouple probes (Figure 5-22) were mounted on the inlet and outlet of the collector to measure the water temperature, and a single jet water meter (Figure 5-23) was mounted on the pipeline connected to the collector to measure water flow rate. A normal T-type thermocouple (Figure 5-24) was used to measure outdoor temperature, and a pyranometer (Figure 5-25) was fixed to the absorber surface of the collector to measure instant solar irradiation. The collector was connected to the main flow system that covered the boiler and CHP rig. The layout of the integrated system is shown in Figures 7-3.

Two types of turbine units were tested using the prototype system; one is an impulse-reaction turbine, designed to operate at very high rotation speed up to 80,000rpm and provide an electricity output of 1.5kW to 3kW. The other is a compressed gas-driven, turbo-alternator which was designed to operate at a low rotation speed, up to 1,000rpm, and give an electricity output of 250W. The impulse-reaction turbine used n-pentane as the working fluid; This would be vaporized into superheated vapour with a pressure of 5-6bar, when heated to 90-100°C. The turbo-alternator used HFE-7100 as the working fluid; this would be vaporized into superheated vapour with a pressure up to 3-4bar, when heated to 100°C. The heat required for the system was supplied by a combination of the solar collector and boiler, which were designed to generate hot water at temperature of 120°C.

T-type thermocouple probes (Figure 5-22) and pressure transducers (Figure 7-9) were mounted at a number of points of the CHP circuit, chill water circuit and boiler and collector flow circuits to measure temperatures and pressures. Flow indicators (Figure 7-10) were mounted in these circuits to measure flow rates of hot water, chill water and refrigerant. A moving iron voltmeter meter (Figure 7-11) and an A.C. ammeter (Figure 7-

12) were mounted to measure the voltage and the electrical current output of the turbines. All of the measurement apparatus were connected to a Datataker (DT 500) which acquired data from the measured points and transferred these to a computer.

0-100mV output;
-40 to 125°C temp. range;
1% accuracy

specifications of the pressure transducer

Working pressure: 10 bar;
Temperature.: 5-110°C;
Accuracy: 5%;
Weight: 0-4kg

Specifications of the flow indicatoir

Figure 7-9. The pressure transducer mounted in the system

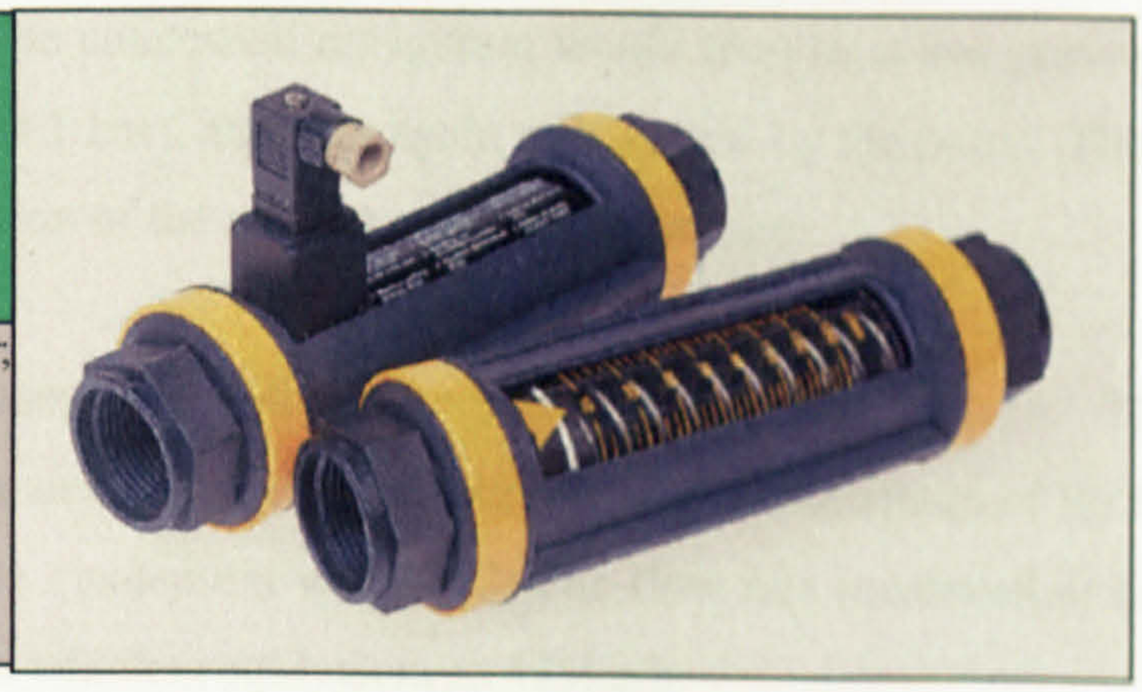

Figure 7-10. The flow indicator installed in the system

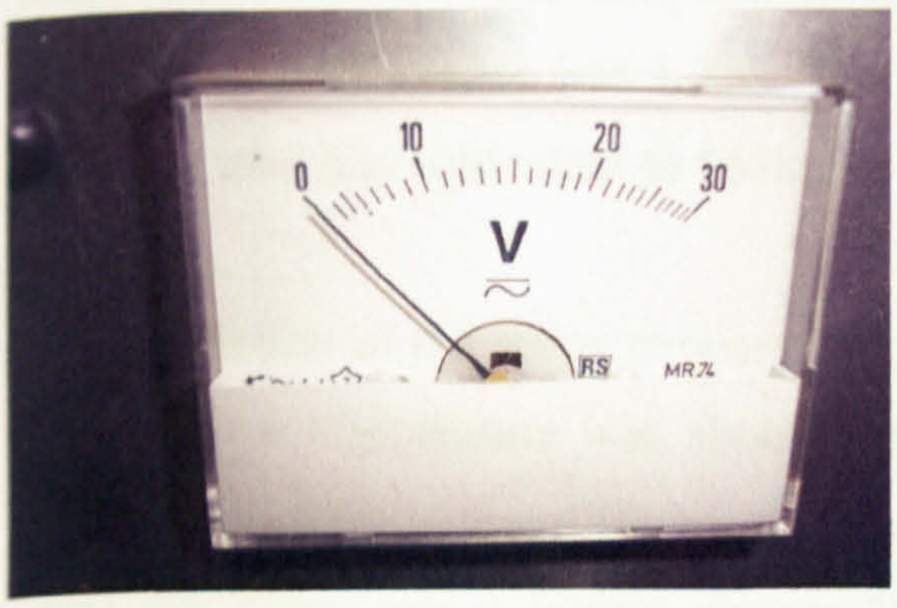

Figure 7-11. The voltmeter used in the system

Figure 7-12. The A.C. ammeter used in the system

7.3.1 Testing of the Impulse Turbine System

The variation of refrigerant pressure with time is shown in Figure 7-13. It can been seen that the pressure of n-pentane fluid increased rapidly and achieved a stable level soon after the system started operation. The pressure rose to its maximum at the outlet of the pump (about 5.3 bar) due to pressurization, and fell slightly (about 0.1bar) after passing through the generator, separator and super-heater. The refrigerant at the outlet of the superheater was a saturated, high pressure vapour as a result of absorbing heat from the boiler/collector. The vapour was fed into the turbine, causing high-speed rotation, owing to the conversion of kinetic energy to mechanical energy. The mechanical energy was used to drive the

generator to provide electrical power. The refrigerant at the outlet of the turbine therefore became a low pressure, superheated vapour (about 1.1bar) as a result of the essential pressure loss that occurred within the turbine. The vapour was further cooled by passing it across the flat-plate heat exchangers for condensation to produce domestic hot water by the recovery of the condensing heat. The condensed refrigerant would then be a low pressure mixture of vapour and liquid (about 1 bar), and was again pressurized by the pump. Thus, the thermodynamic cycle for operation of the steam turbine was complete.

The variation of refrigerant temperature with time is shown in Figure 7-14. The temperature of the refrigerant at the outlet of the superheater reached a maximum of 95°C. The temperature at the outlet of the condensers was 31°C. The flow rate measured at the outlet of the condensers was 12 l/m, which is equivalent to 435kg/h.

The variation of the water temperature in the solar collector system is shown in Figure 7-15. The average water temperature in the collector was 102.5°C, and the outlet/inlet temperature difference was 1.2°C. The flow rate measured at the connecting pipeline was 2.8l/m, which is equivalent to 168kg/h.

The variation of the water temperatures in the boiler main flow system is shown in Figure 7-16. Flow temperature was about 104°C and return temperature was about 102°C; the outlet/inlet temperature difference was about 2°C. The flow rate measured on the main flow line was 60l/m, which is equivalent to 3600kg/h.

The variation of the water temperatures in the chill water system is shown in Figure 7-17. The inlet temperature was about 14.5°C and outlet temperature was 16.25°C; the outlet/inlet temperature difference was 1.75°C. The flow rate measured was 30l/m, which is equivalent to 1800kg/h.

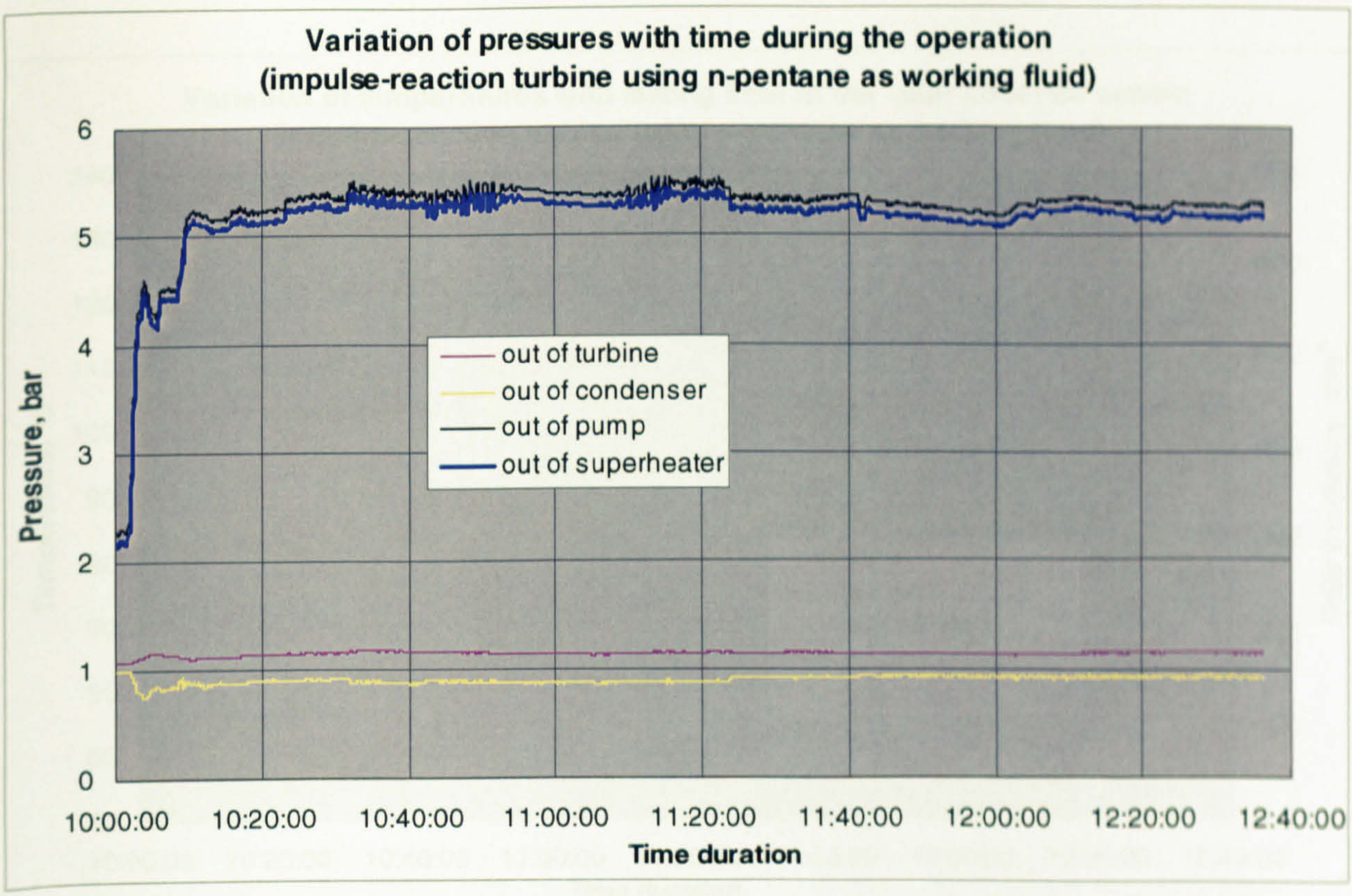

Figure 7-13. Variation of refrigerant pressures with testing time in the CHP cycle

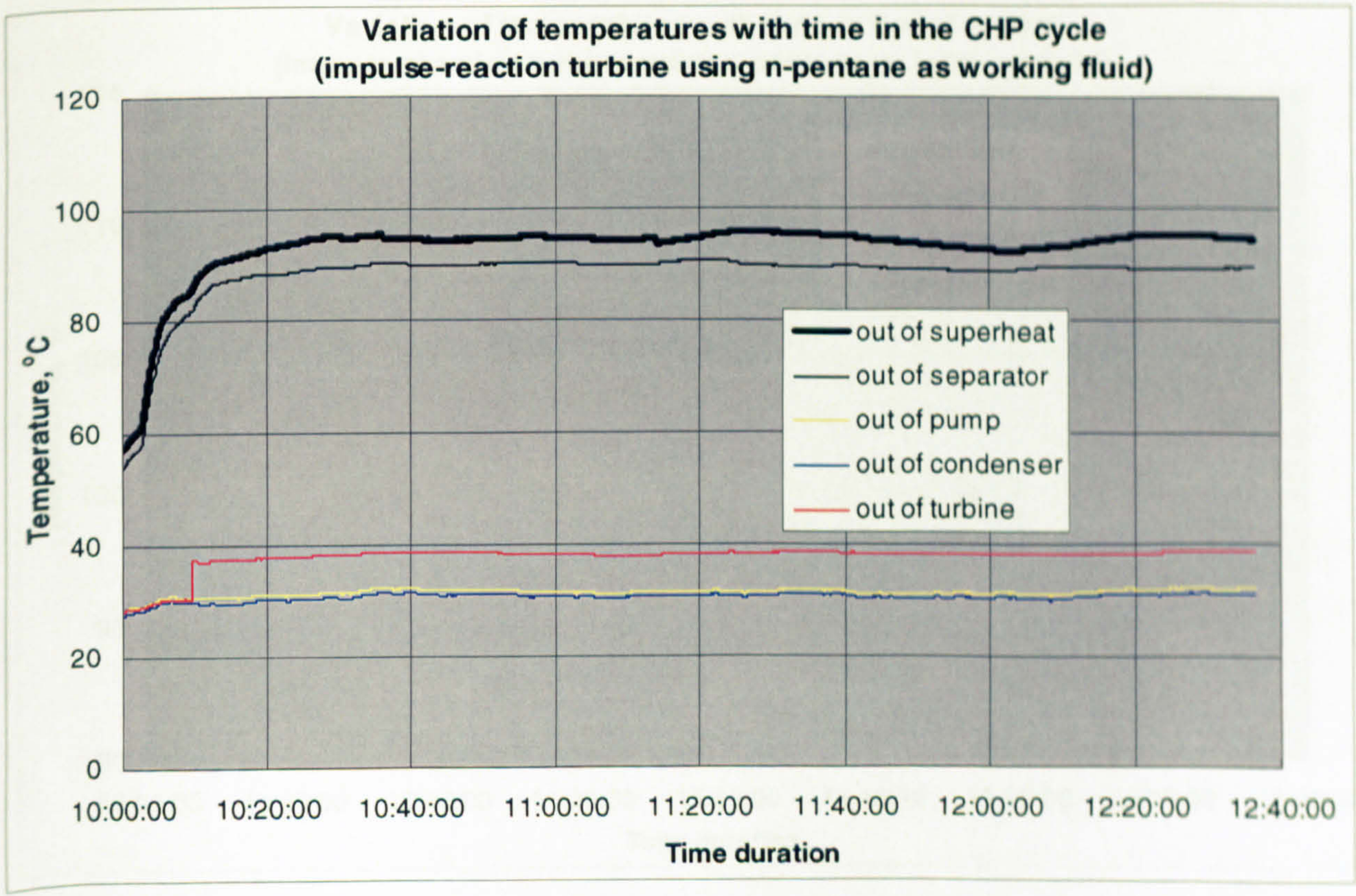

Figure 7-14. Variation of refrigerant temperatures with testing time in the CHP cycle

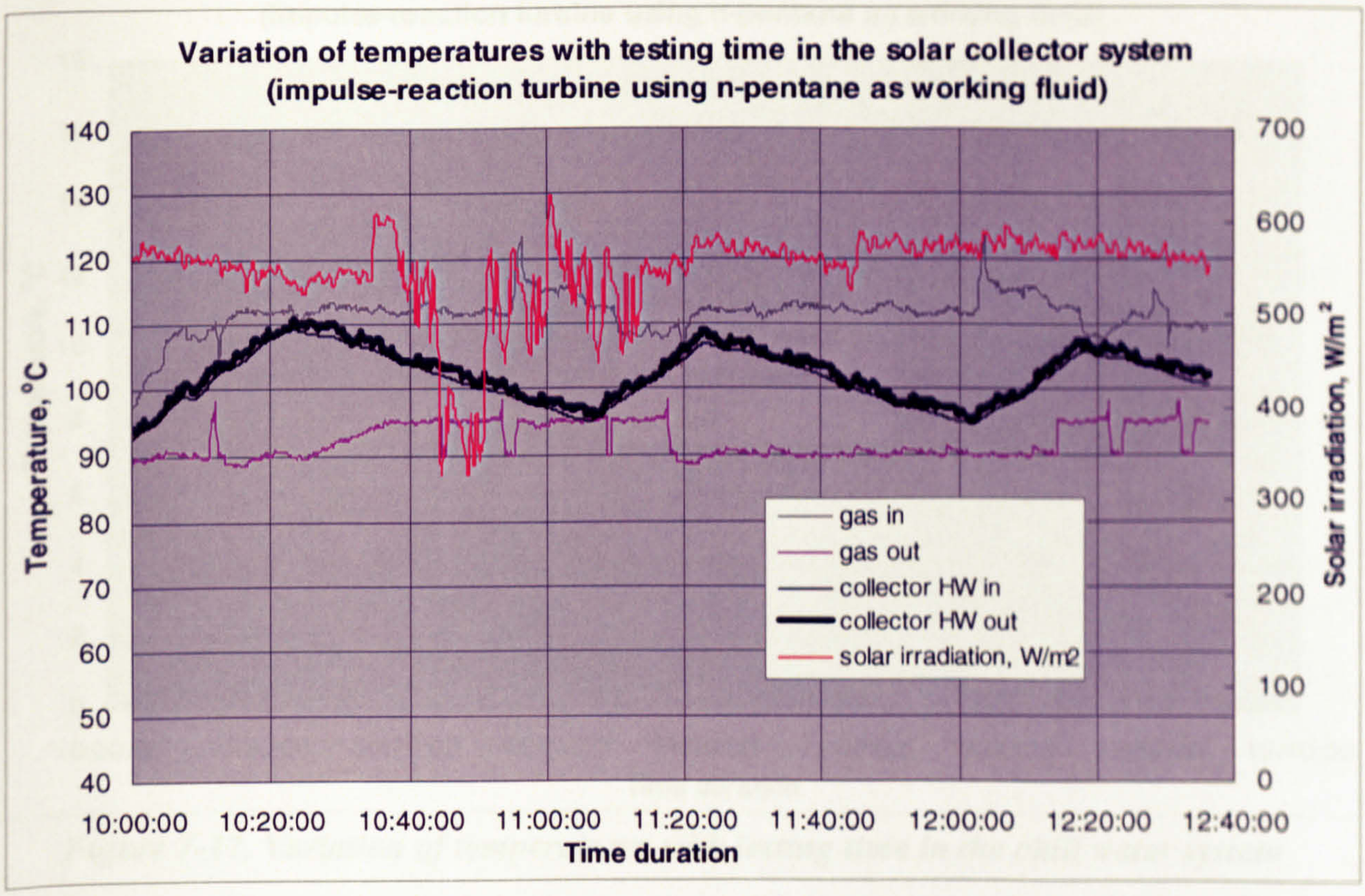

Figure 7-15. Variation of water temperatures with testing time in the collector system

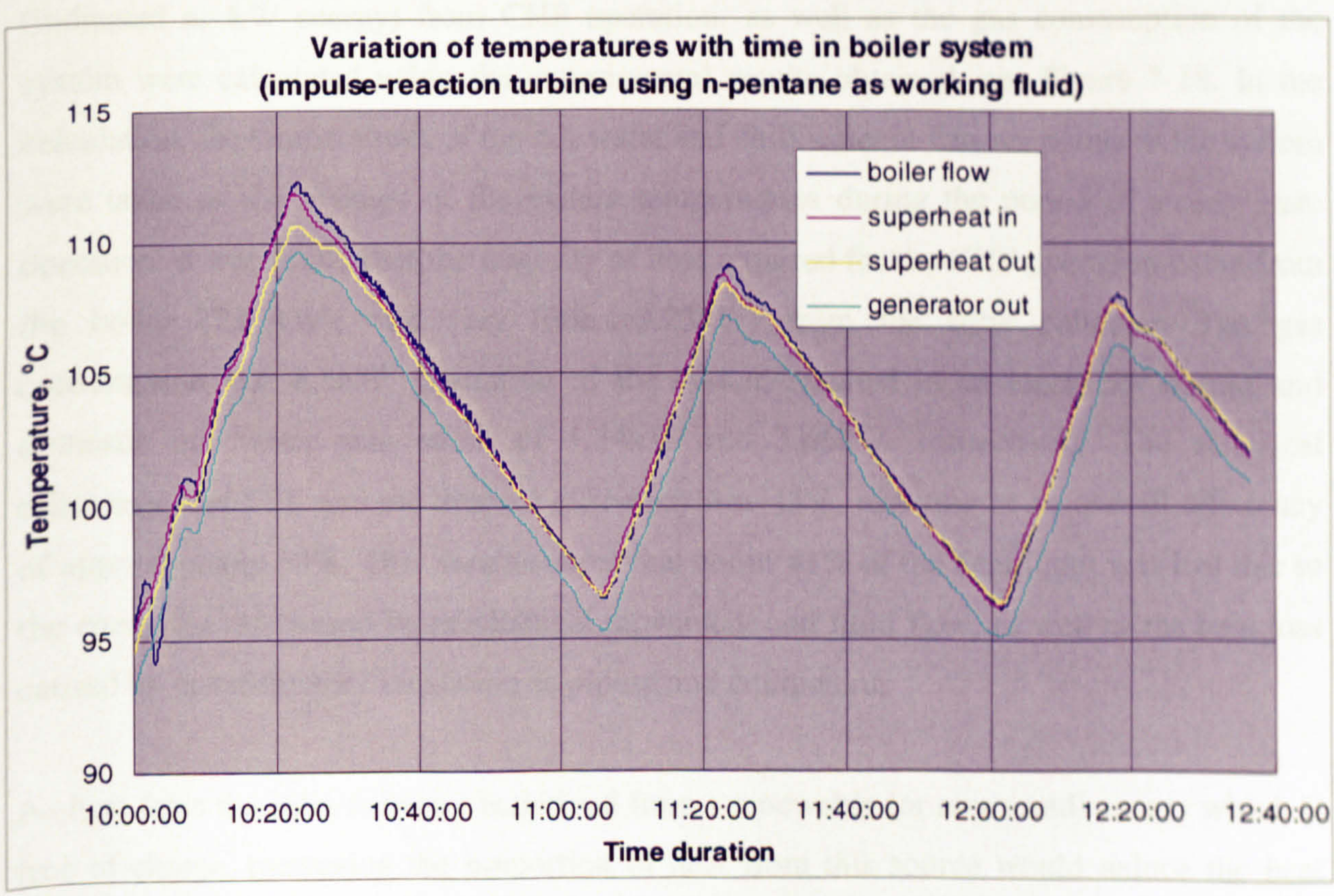

Figure 7-16. Variation of water temperatures with time in the boiler main flow system

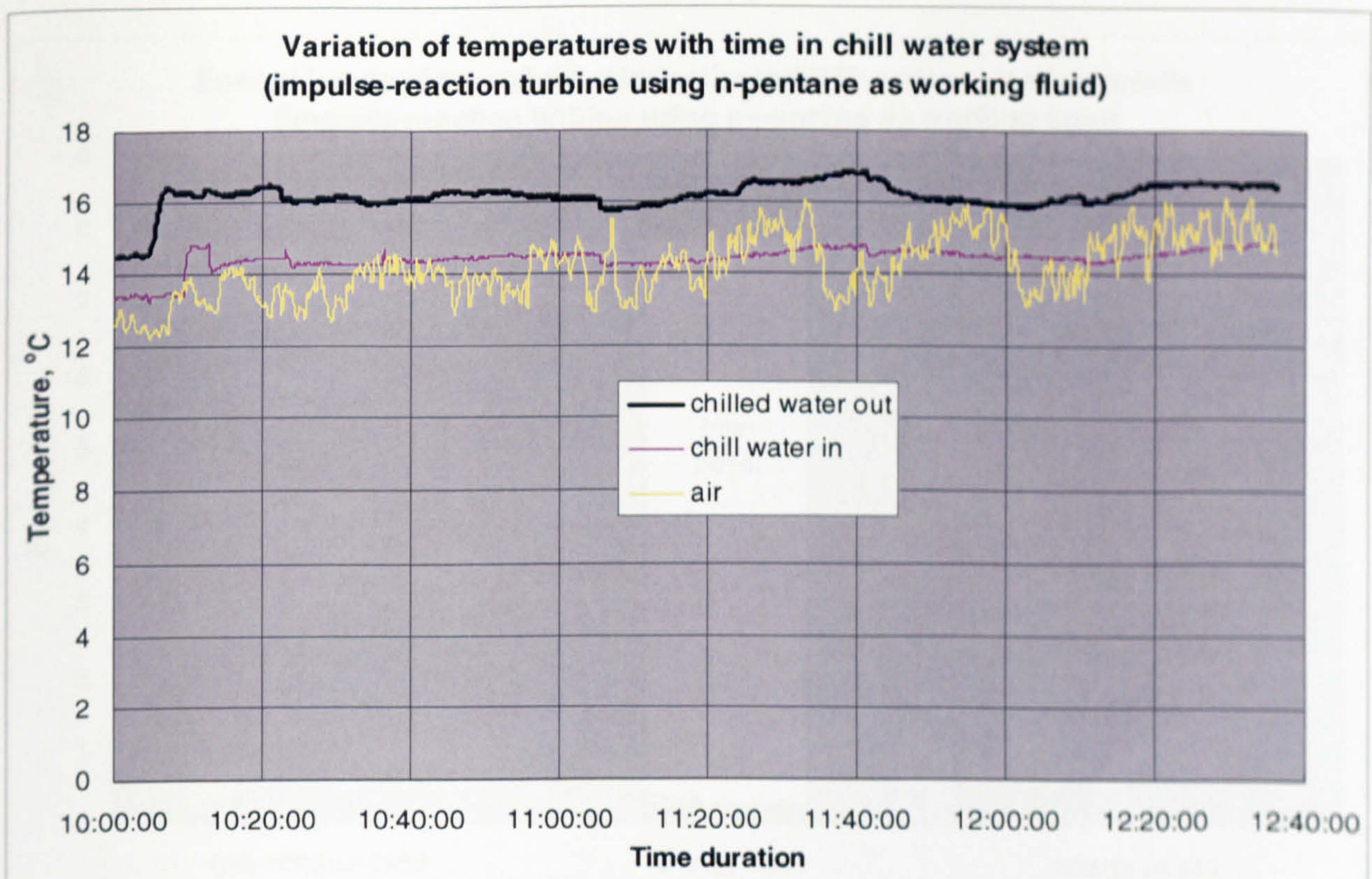

Figure 7-17. Variation of temperatures with testing time in the chill water system

The heat inputs from the boiler and collector, the electricity and hot water generation (indicated as kW energy) from CHP operation, as well as the gas consumption of the system were calculated using the experimental results obtained, see Figure 7-18. In the calculation, the temperatures of the hot water and chill water at various points in the system were taken as the average of the instant temperatures during the period of steady state operation. It was found that the majority of heat required for the CHP operation came from the boiler (7.65kW), and very little (0.23kW) from the solar collector. The gas consumption was 8.5kW. Operation of the system resulted in an electricity output and domestic hot water generation, of 1.34kW and 3.66kW, respectively. The electrical efficiency was 16% and the thermal efficiency was 43%, resulting in an overall efficiency of approximately 59%. This demonstrates that about 41% of the heat input was lost due to the energy losses caused by mechanical movement and fluid flow, as well as the heat loss caused by unsatisfactory insulation to piping and equipment.

As heat from the solar collector is derived from a renewable (or recovered) energy which is free of charge, increasing the proportion of heat from this source would reduce the heat required from the boiler, and consequently reduce primary energy consumption and running cost. This would contribute to a reduction in CO_2 emission to environment.

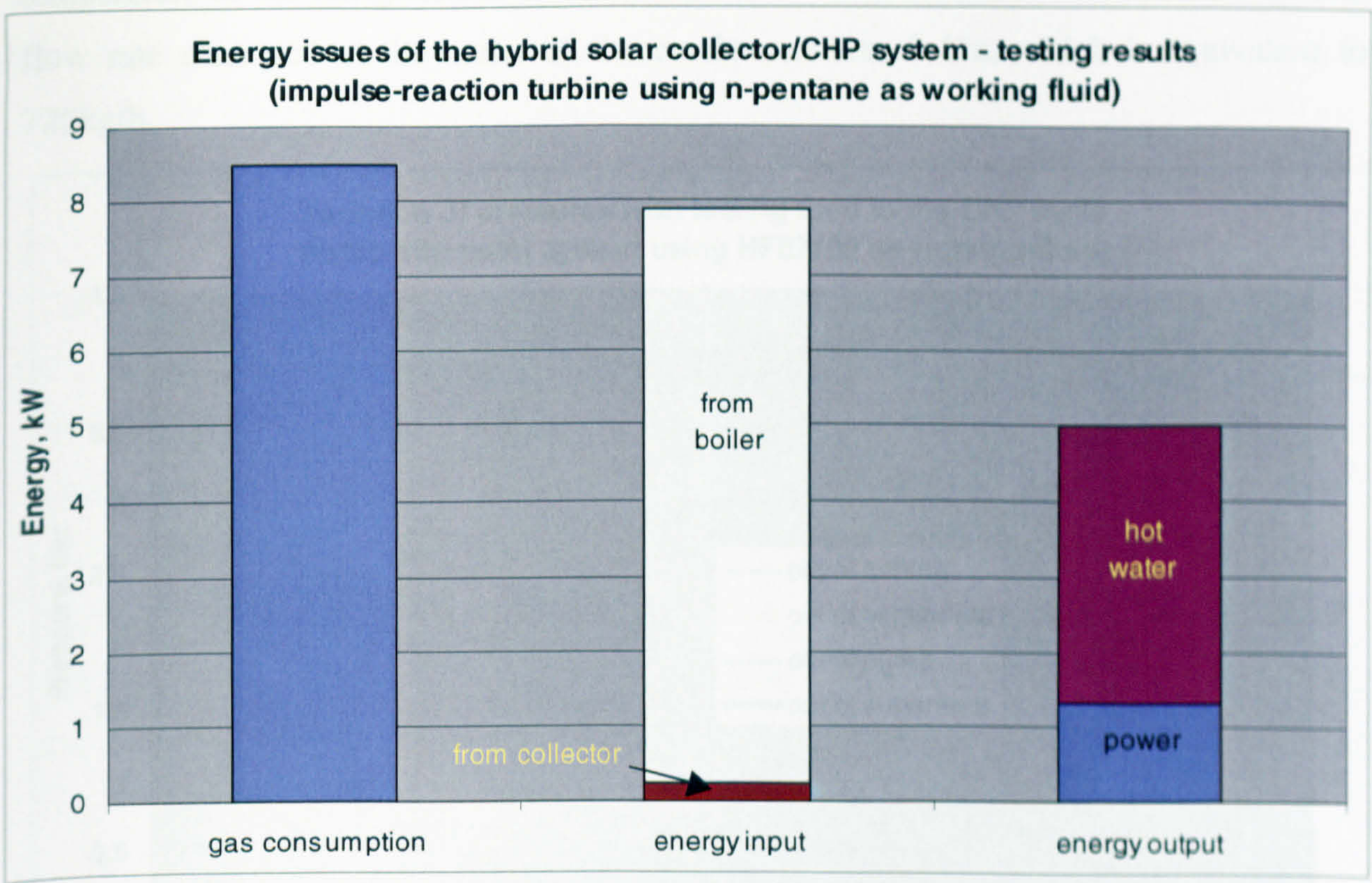

Figure 7-18. Energy analysis of the hybrid solar collector/CHP system – (impulse-reaction turbine using n-pentane as the working fluid)

7.3.2 Turbo-alternator System

The variation of refrigerant pressures with time is shown in Figure 7-19. The refrigerant pump was started about 5 minutes later than the boiler system. The pressure of HFE-7100 fluid increased rapidly and achieved a stable level after about 2 minutes. The pressure rose to its maximum at the outlet of the pump (about 4 bar) due to pressurization, and this fell slightly (about 0.2bar) after passing through the generator, separator and superheater. The HFE-7100 refrigerant at the outlet of superheater was a saturated, high pressure vapour as it had absorbed heat from the boiler/collector due to heat transfer, and the refrigerant at the outlet of turbine was a superheated vapour at low pressure (about 0.4bar) due to the substantial pressure loss that occurred within the turbo-alternator. The superheated refrigerant vapour was further cooled after passing across the flat-plate heat exchangers and became a low pressure mixture of vapour and liquid (about 0.2bar). The cycle was very similar to that of the impulse-reaction turbine system.

The variation of refrigerant temperatures with time is shown in Figure 7-20. The temperature of the refrigerant at the outlet of the superheater achieved about 105°C, and the

temperature of the refrigerant at the outlet of the condensers was reduced to 12.5°C. The flow rate measured at the outlet of the condensers was 8 l/m, which is equivalent to 720kg/h.

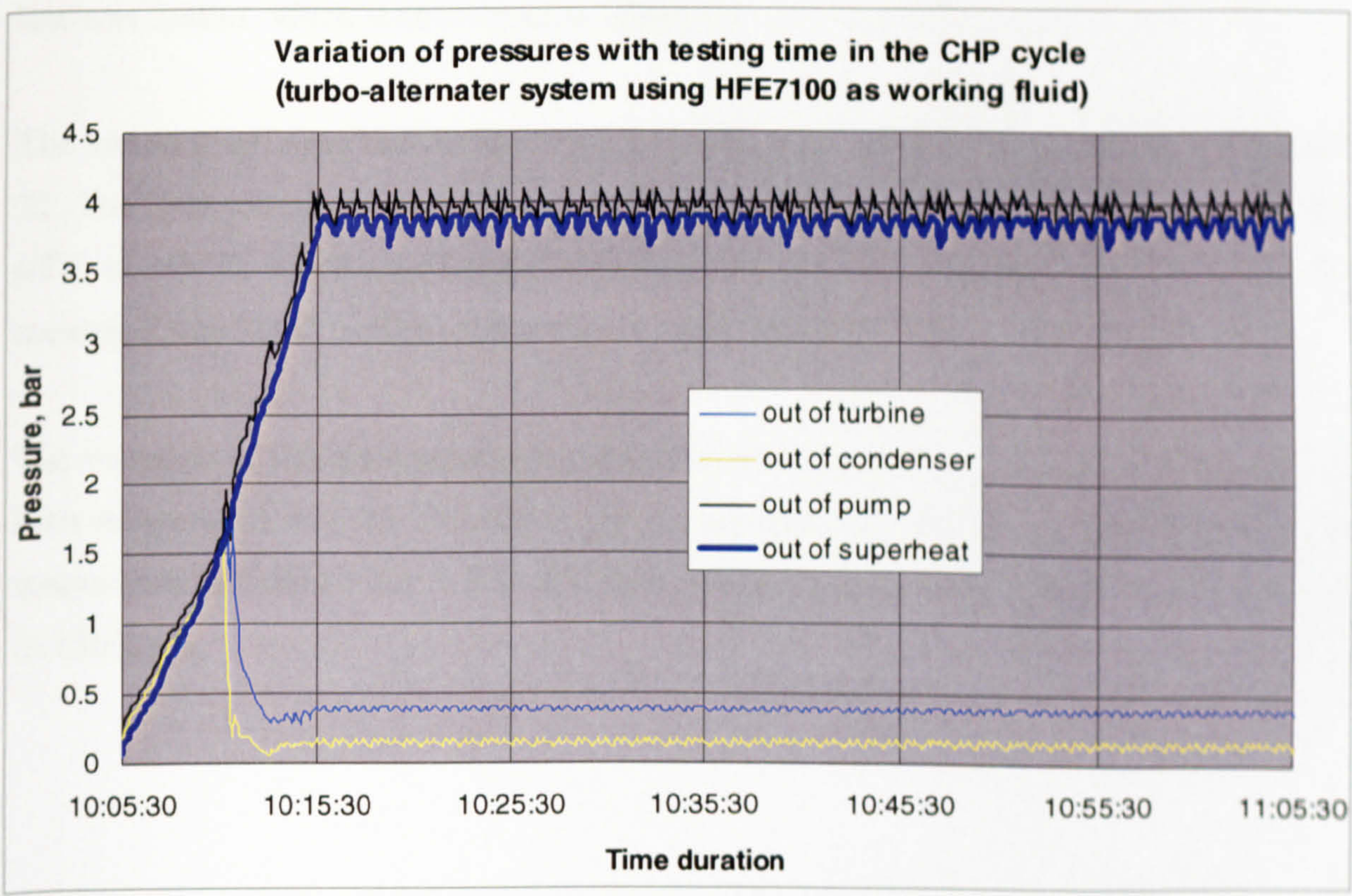

Figure 7-19. Variation of refrigerant pressures with time in the CHP cycle

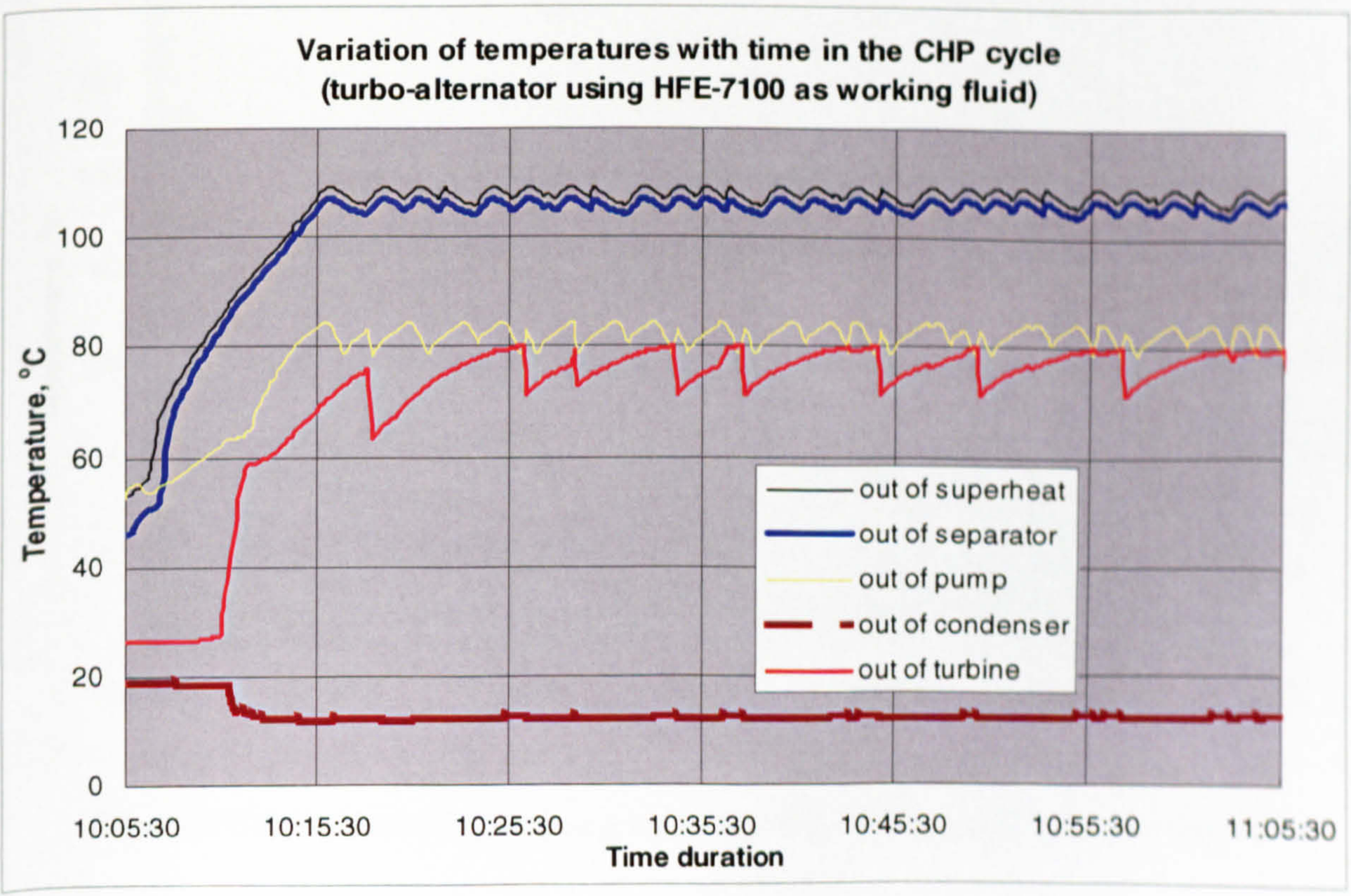

Figure 7-20. Variation of refrigerant temperatures with time in the CHP cycle

The variation of water temperatures in the solar collector system with time is shown in Figure 7-21. The average temperature in the collector varied from 90°C to 100°C, and the outlet/inlet temperature difference was about 0.8°C. The flow rate measured on the flow line was 2.8l/m, which is equivalent to 168kg/h.

The variation of water temperatures in the boiler main flow system is shown in Figure 7-22. The flow temperature varied from 65°C to 105°C, the return temperature varied from 65°C to 100°C, and the outlet/inlet temperature difference was about 3°C. The flow rate measured was 50l/m, which is equivalent to 3000kg/h.

The variation of water temperatures in the chill water system is shown in Figure 7-23. The inlet temperature was 26.7°C, the outlet temperature was 28.5°C, and so the outlet/inlet temperature difference was 1.8°C. The flow rate measured was 26l/m, which is equivalent to 1560kg/h.

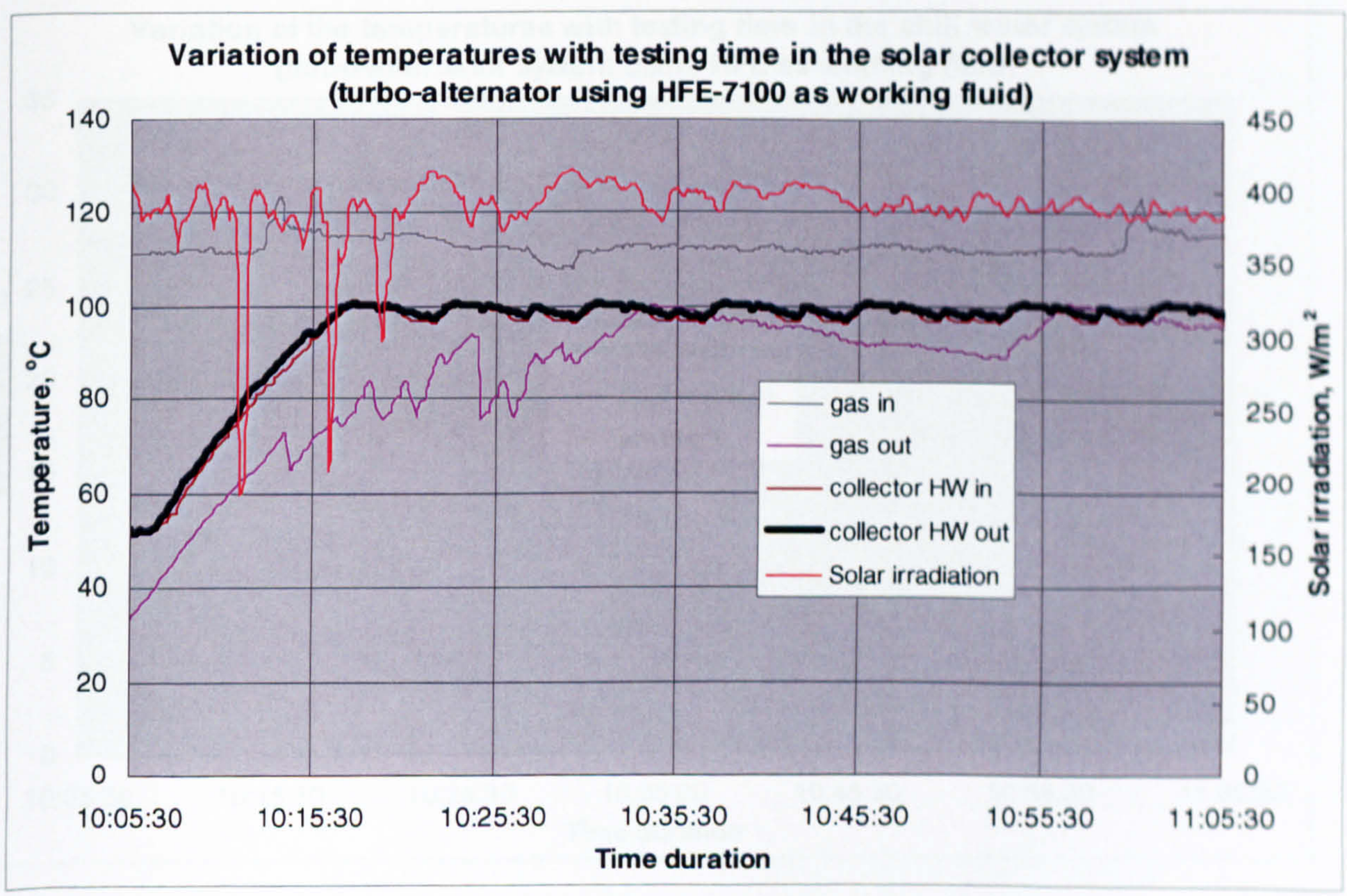

Figure 7-21. Variation of temperatures with time in the solar collector system

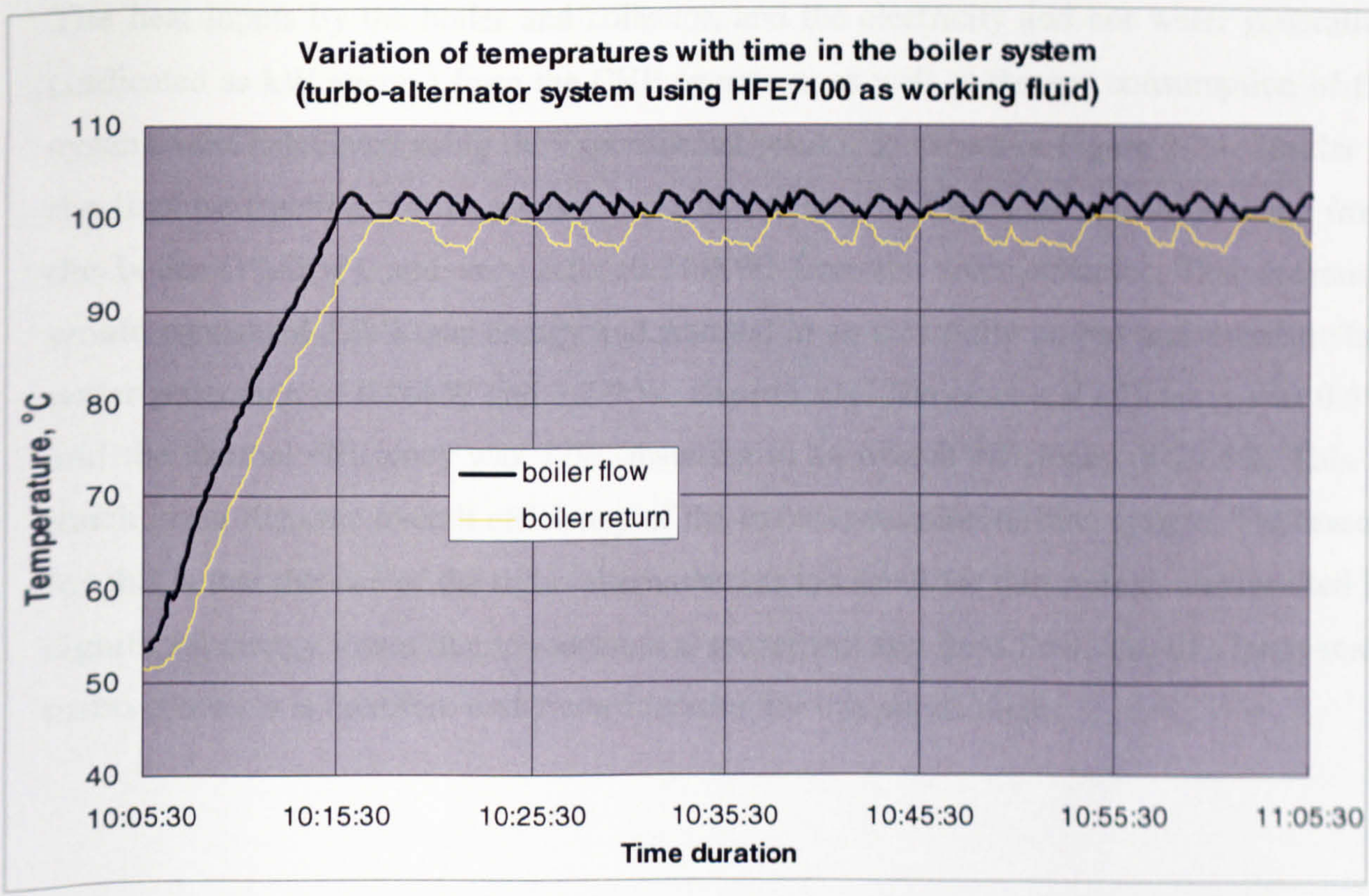

Figure 7-22. Variation of temperatures with time in the boiler system

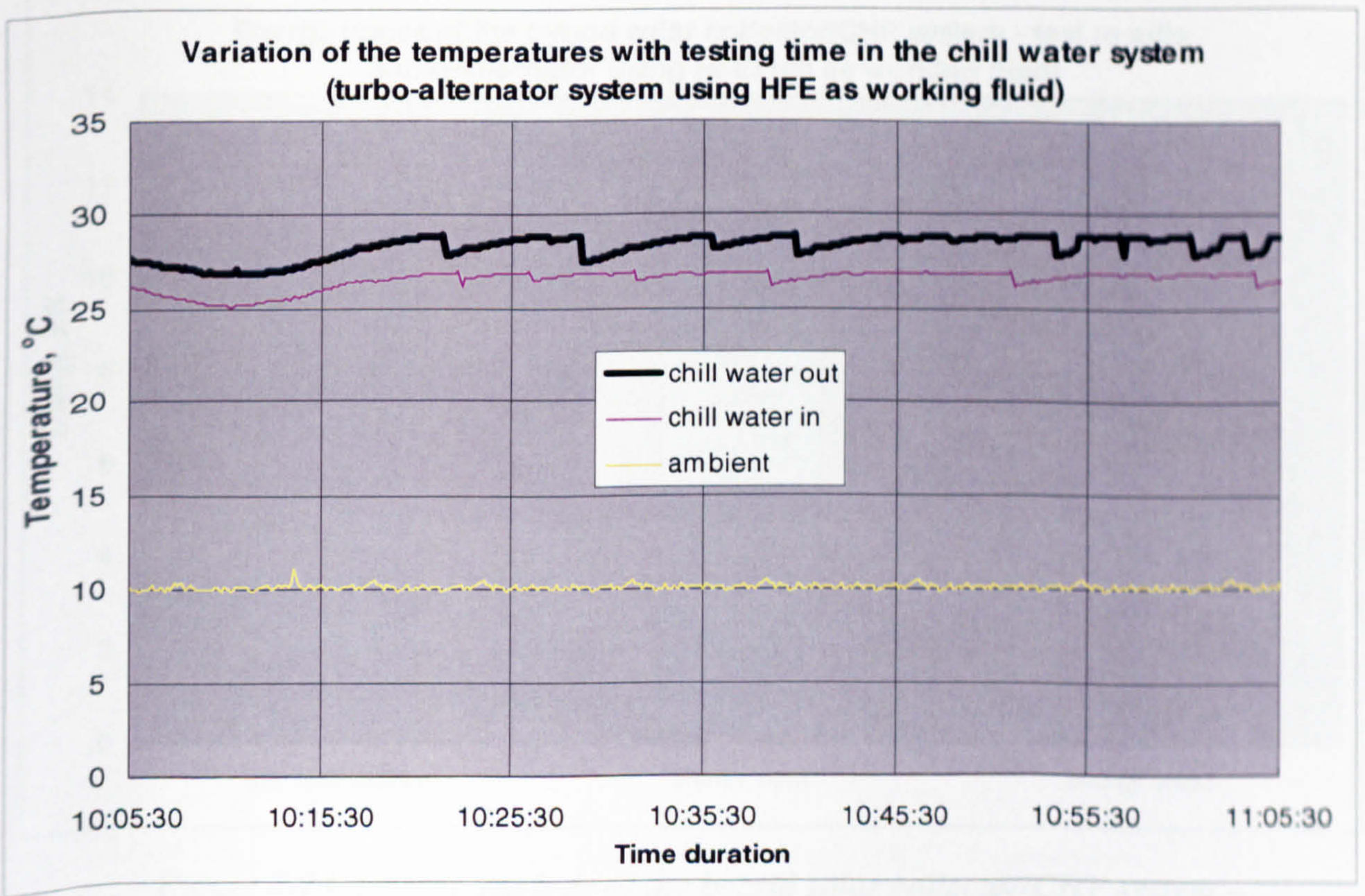

Figure 7-23. Variation of temperatures with time in the chill water system

The heat inputs by the boiler and collector, and the electricity and hot water generation (indicated as kW energy) from the CHP operation, as well as the gas consumption of the system were calculated using the experimental results, as shown in Figure 7-24. Similar to the impulse-reaction turbine system, most of heat required for CHP operation came from the boiler (10.8kW), and very little (0.214kW) from the solar collector. This operation would consumed 12kW gas energy and resulted in an electricity output and domestic hot water generation of 0.06kW and 3.22kW, respectively. The electrical efficiency was 0.5% and the thermal efficiency was 27%, resulting in an overall efficiency of 27.5%. This is much lower than the overall efficiency of the impulse-reaction turbine system. The reason for this is that the size of the turbo-alternator was too small for this system, and resulted in significant energy losses due to mechanical movement and fluid flow. Use of a large-scale turbo-generator is therefore under consideration for this application.

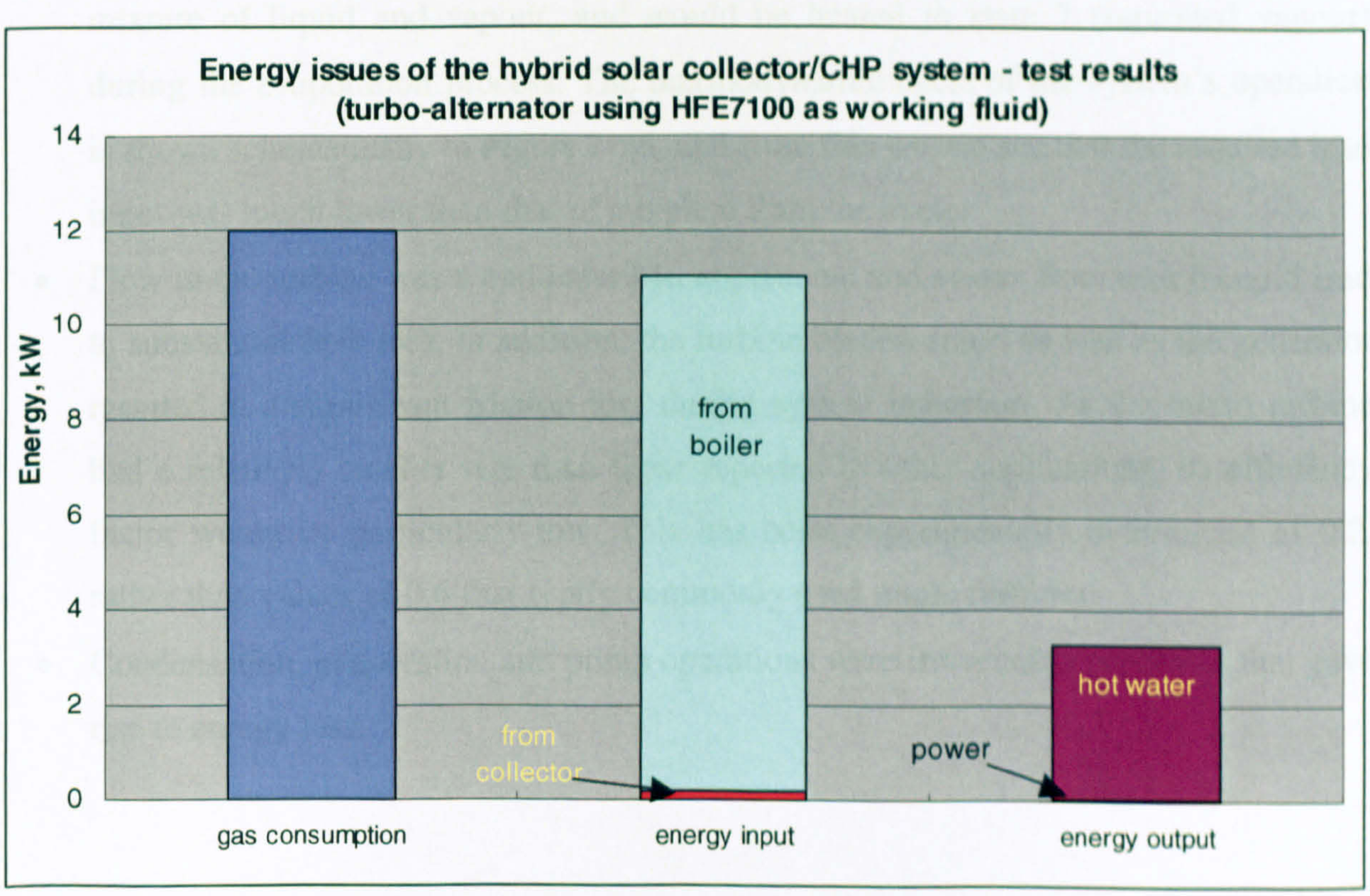

Figure 7-24. Energy analysis of the hybrid solar collector/CHP system – (turbo-alternator usingHFE-7100 as the working fluid)

7.4 Comparison of Theoretical and Experimental Results

A comparison was made between the theoretical and experimental results for the impulse-reaction turbine system, and the results are shown in Figure 7-25. Both the theoretical analysis and testing were carried out at approximately the same evaporation and condensation pressures for the purpose of comparison. It was found that there were significant differences between the experimental results and the theoretical values. The major reasons for these are as follows:

- The real thermodynamic process occurring in the system is not a typical Rankine cycle. State point 3 (outlet of the turbine), located in the superheated area, represents superheated n-pentane vapour that is unlikely to be condensed completely due to its large volume and large velocity as it passes through the condensers. This would produce a mixture of vapour and liquid at the outlet of the condensers (state 4), and as a result, the heat transfer in the condensation process would be reduced significantly. The mixture was then pumped to a higher pressure causing condensation of part of the vapour before finally achieving state 1. The fluid at state 1 was probably still a mixture of liquid and vapour, and would be heated to state 2 (saturated vapour) during the evaporation process. The thermodynamic cycle of the system's operation is shown schematically in Figure 7-26, and from this we can see that the required heat input was much lower than that of a typical Rankine cycle.
- Flow in the turbine was a compressible, supersonic and vortex flow which could lead to substantial flow loss. In addition, the turbine blades, rotor, as well as the generator resulted in a significant friction loss during system operation. As the micro turbine had a relatively smaller size than those reported in other applications, its efficiency factor would be particularly low. This has been experimentally determined as 0.2, rather than values of 0.6 that typify commonly used micro turbines.
- Condensation, evaporation and pump operations were irreversible processes that gave rise to energy loss.

It should be emphased that although incomplete condensation led to reduced heat output, it allowed heat input to be reduced as well. This may be desirable in situations where a low heat output is required. The reduced heat input may lead to another consideration regarding

system configuration, e.g., using only solar/exhaust gas collector, instead of using both the collector and boiler, to provide heat. This variation will be discussed in the following section.

Increasing the number of collectors used resulted in increased electricity, heat and overall efficiency. The variation of efficiencies with the quantity of collectors was calculated using the experimental results obtained, as shown in Figure 7-27.

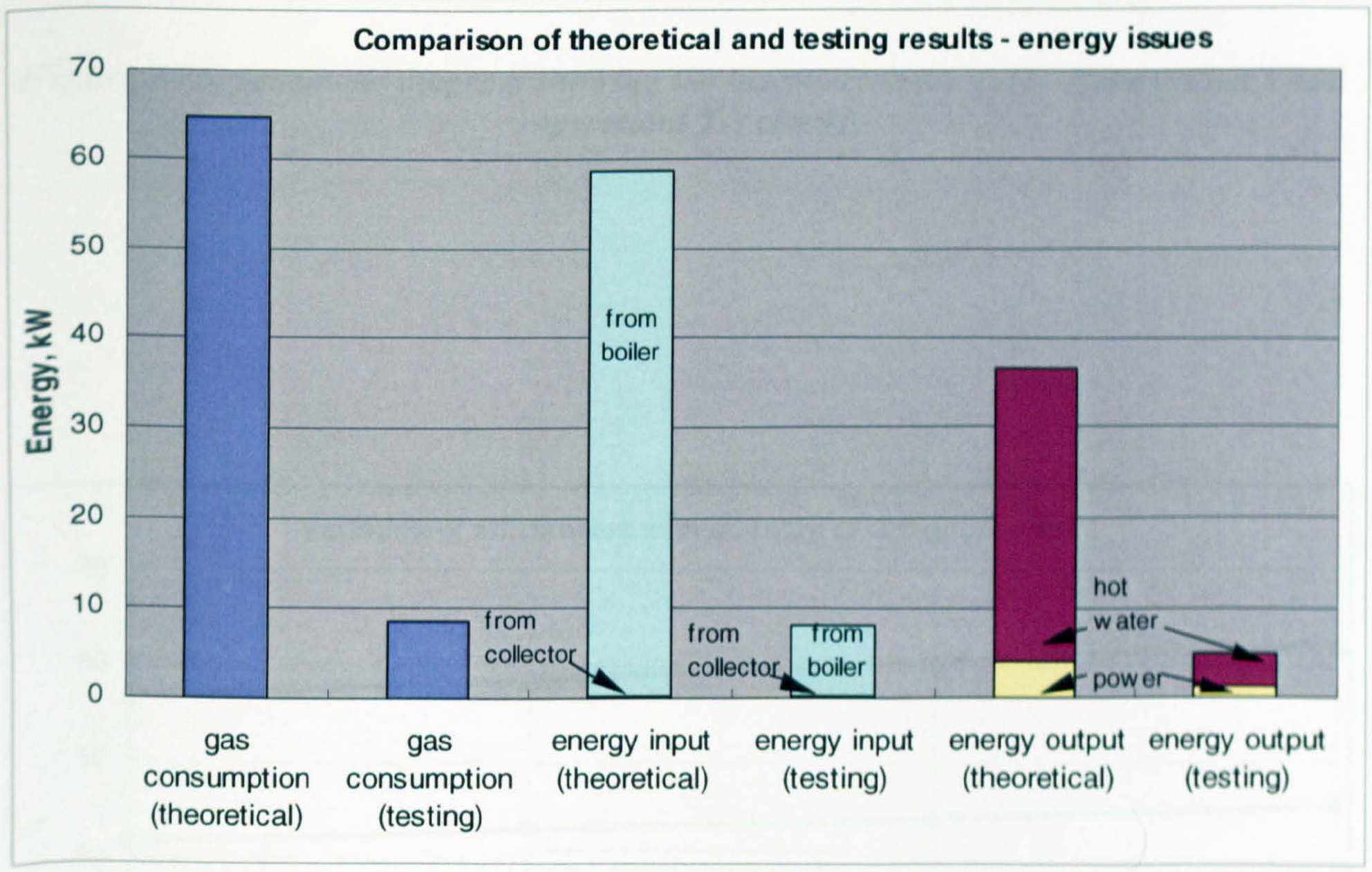

Figure 7-25. Comparison of the theoretical and testing results – the impulse-reaction turbine system using n-pentane as working fluid

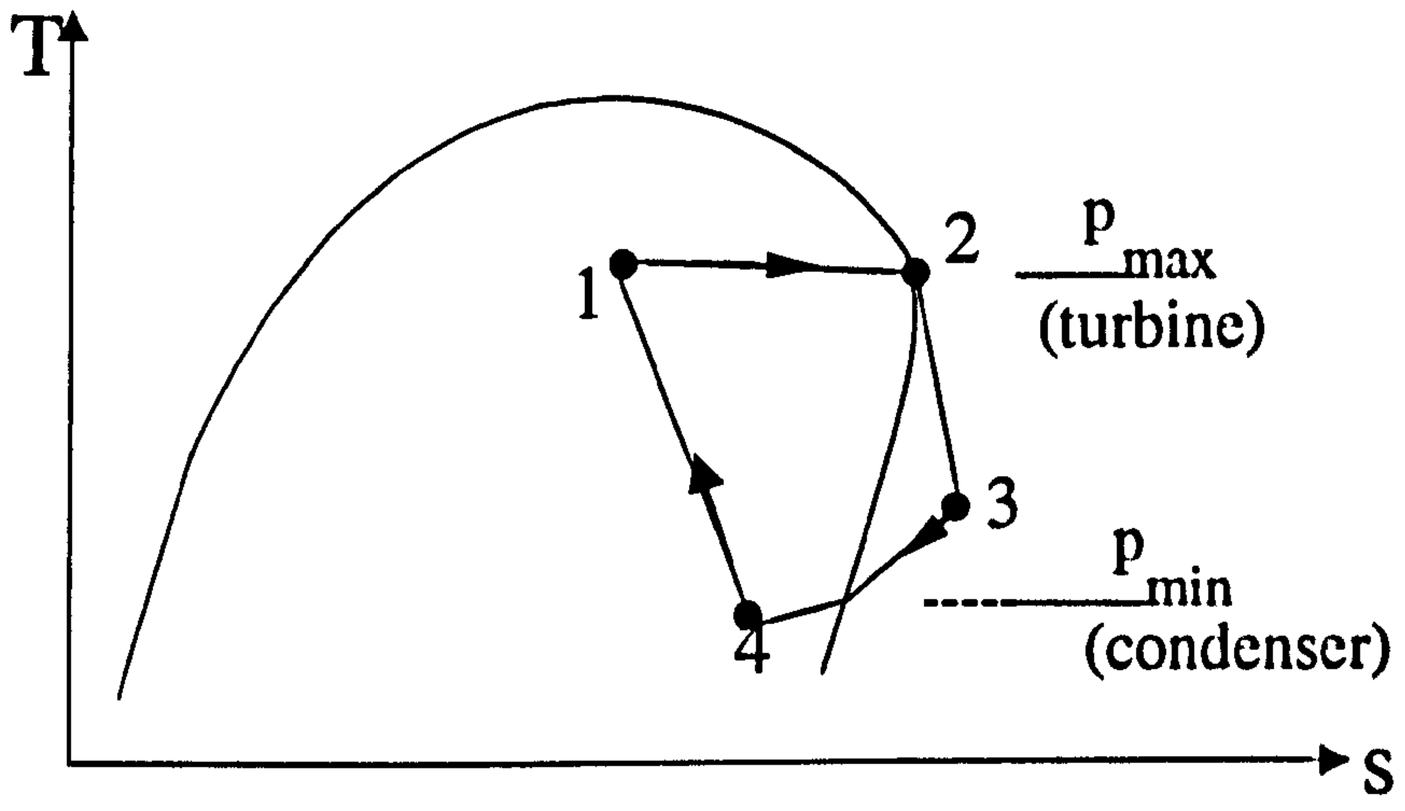

Figure 7-26. Schematic diagram showing the thermodynamic cycle of the system's real operation(T-s chart)

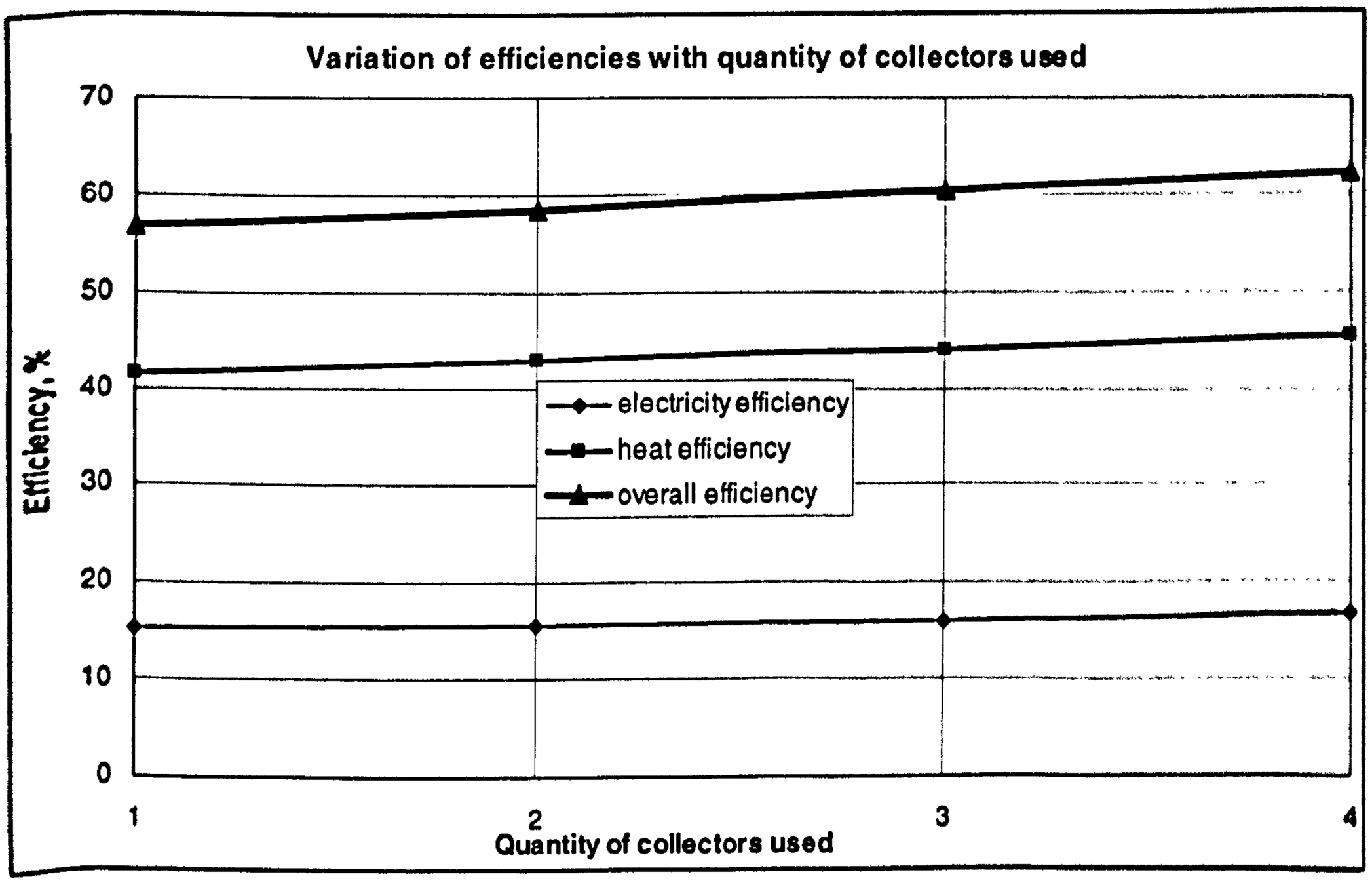

Figure 7-27. Variation of efficiencies with quantity of the collectors used – testing results

7.5 Energy and Environmental Effects – Simple Analysis

A simple analysis to determine the energy and environmental benefits of the proposed system has been carried out by comparing the primary energy consumption of the proposed system with that of conventional heat and electricity supply systems. The results are outlined in Table 7-5. The investigation assumed that the system was incorporated with four collector units and operated at 40% of the hours in the whole year on an average load basis. The conventional systems were assumed to operate on the same basis to enable comparison. During operation, each of the solar collectors would provide an average heat output of 230W, assuming heat was taken from the sun and exhaust flue gas, based upon the previous analysis of the solar collectors [5]. For the conventional systems, electricity was supplied from the national grid, i.e., produced by a central power station at an efficiency of approximately 33%, and the heat was provided by a domestic boiler, at an efficiency of 80 to 90%. The cost of electricity from national grid was assumed to be £0.05/kWh [London Electricity, 1998], and the charging rate of gas was £0.009/kWh [Butlin, 1998].

Table 7-5. Analysis of energy and environment effects of the hybrid solar collector/CHP system

System / Items calculated	The conventional systems			The proposed system	
	Electricity	Heat	Total	Electricity	Heat
Demand, kW	1.34	3.66		1.34	3.66
Duration of operation, hours per annum	3500	3500		3500	3500
Gas power required, kW	4.06	4.57	8.63	7.73	
Primary energy consumption, kWh per annum	14,210	15,995	30,205	27,055	
CO_2 emission, tonnes per annum	6.68	7.52	14.2	12.7	
Running cost, £ per annum	235	145	380	240	

The analysis indicated that the combined system would save primary energy of approximately 3,150kWh per annum compared to conventional electricity and heating supply systems, and this would result in reduction of CO_2 emission of up to 1.5 tonnes (about 15% of that of the conventional systems). The running cost of the system would also be lower. These estimates, based on experimental results, understate the performance of the system as the turbine used was too small to allow the system to be operated at its maximum efficiency. System performance would be improved by employing a more suitable turbine

and developing an improved collector configuration to allow more efficient utilization of both solar energy and waste heat.

7.6 Summary

- A novel hybrid solar collector/CHP system was proposed. The system used a hybrid solar/gas collector, in conjunction with a boiler, to produce high temperature hot water, which was used to heat a secondary fluid, either n-pentane or HFE7100, using a generator, a superheat as well as a separator. Since both n-pentane and HFE7100 are refrigerants that have low boiling points, i.e., 35°C and 60°C respectively, they could be converted to a pressured, saturated vapour when being heated. The vapour was used to drive the turbine to generate electricity, causing its pressure and temperature fall to a lower level, and becoming a superheated vapour or mixture of vapour and liquid after flowing through the turbine. The lower pressure mixture was used to produce domestic hot water by passing it through the heat exchangers where heat exchange occurred between the refrigerant and chill water.

- A theoretical analysis was carried out to investigate the thermodynamic and heat transfer characteristics of the proposed system. The system was assumed to operate on a typical Rankine cycle which was powered by both solar and gas energy through utilization of a solar collector and gas boiler. Energy profiles of the system for a given operation condition and collector configuration were presented. It was found that the electricity efficiency increased and the heat efficiency decreased when the evaporation pressure increased and the condensation pressure remained the same. However, the electricity, heat and overall efficiencies all increased when the quantity of collectors used increased. This demonstrates that using more collector units would help to improve the system's energy efficiency.

- The prototype system was tested in a building at University of Nottingham. Two types of turbine unit were examined; one is an impulse-reaction turbine which was designed to operate at very high rotation speed up to 80,000rpm and give an electricity output of 1.5kW to 3kW. The other is a compress gas-driven, turbo-alternator which was designed to operate at a low rotation speed up to 1,000rpm and

give an electricity output of 250W. The impulse-reaction turbine used n-pentane as the working fluid; and the turbo-alternator used HFE-7100 as the working fluid.

In both cases, the variation of refrigerant pressure and temperature, hot water temperature in the collector and boiler systems, as well as chill water temperature with testing time were monitored. The heat inputs from the boiler and collectors, and the electricity and hot water generation (indicated as kW energy) from CHP operation, as well as the gas consumption of the system were calculated using the experimental results. It was found that the turbo-alternator was too small for this system and affected its power output significantly. Work was therefore focused on the system using the micro impulse-reaction turbine. Testing showed that the majority of the heat required for impulse-reaction turbine operation came from the boiler (7.65kW), and very little (0.23kW) from the solar collector. The gas consumption was 8.5kW. Operation resulted in an electricity output and domestic hot water generation of 1.34kW and 3.66kW, respectively. The electrical efficiency was 16% and the thermal efficiency was 43%, resulting in an overall efficiency of approximately 59%. This indicates that about 41% of the energy input was lost due to the resistances of mechanical movement and fluid flow, as well as heat loss due to unsatisfactory insulation of piping and equipment.

- A comparison was made between the modelling and experimental results for the impulse-reaction turbine system. Experimental results were found to be significantly lower than the theoretical predictions. The major reasons for this are that the real thermodynamic process was not a typical Rankine cycle, and incomplete condensation occurred in the condensers. As a result, the required heat input and energy input were much lower than an ideal Rankine cycle system. In addition, irreversibility in turbine, evaporation and condensation operations also contributed to substantial energy losses.

- A simple analysis of the energy and environmental benefits of the combined system was carried out. The analysis indicated that the proposed system would save primary energy of approximately 3,150kWh per annum compared to conventional electricity and heating supply systems, and this would result in reduction of CO_2 emission of up to 1.5 tonnes. The running cost of the proposed system would also be lower. These

results are an underestimate of the system's practical performance than the theoretical predictions as the turbine used was too small to achieve the desired efficiency. The system's performance would be improved by employing a more suitable turbine and developing an improved collector configuration to allow more efficient utilization of both solar energy and waste heat.

Chaper 8. Conclusions and Further Work

8.1 Summary of the Work

This research investigated a novel hybrid heat pipe solar collector/CHP system. The system was powered by solar and gas energy as well as the boiler waste heat to provide electricity and heating for residential buildings.

The research started from a review in relative to the several technical areas, including heat pipe technology and heat pipe thermal performance analysis, numerical methods of heat pipe heat transfer, heat pipe solar collectors, micro turbines and solar CHP technology. Technical progress in these areas was examined, and the innovative aspects of this research were identified compared to the current technical status.

The research investigated the thermal performance of a number of heat pipes, including micro/miniature heat pipes, normal circular and rectangular heat pipes, with/without wicks. An analytical model was developed to evaluate the heat transport capacity for the heat pipes. A parallelepiped miniature heat pipe with two sharp opposite corners was proposed. Variation of heat transport capacity for either micro/miniature or normal heat pipes with operation temperature, liquid fill level, inclination relative to horizon and channel geometry were investigated.

The research also investigated the operating characteristics of a number of heat pipes. A simplified numerical model was developed based on the analysis of the previous methods. Mathematical theory and numerical method used for modelling development were indicated. The operating characteristics of the selected heat pipes, e.g., two miniature and one mini heat pipes, and two normal heat pipes, were investigated using both the numerical technique and experimental testing.

The research further involved the design, modelling, construction and tests of two novel heat pipe solar collectors, i.e., the thin membrane heat pipe solar collector and the hybrid heat pipe solar/flue gas collector. A computer model was developed to analyse the heat transfer occurring in the collectors. Two collector efficiencies, η and η_1, were defined to evaluate their thermal performance, which were indicated as the function of a general

parameter $(t_{mean}-t_a)/I_n$. Effects of the top cover, manifold as well as flue gas temperature and flow rate (for hybrid collector only) on collector efficiencies were investigated using the computer model. Laboratory tests were carried out to validate modelling predictions and examine the thermal performance of the collectors. Comparison was made between the modelling and testing results, and the reasons for error formation were discussed. A correlation factor was determined to modify the theoretical predictions.

The research also investigated the performance of a micro impulse-reaction turbine. The structure configuration, coupling pattern with the generator as well as internal geometry contour of the turbine was described. The velocity, pressure and turbulent kinetic energy of the flow in the turbine were determined using numerical CFD prediction. In addition, experimental tests were carried out using a prototype system.

The research finally focused on the combined heat pipe solar collector, boiler and micro turbine system. The individual components, configurations and layout of the system were described. Theoretical analysis was carried out to investigate thermodynamic and heat transfer characteristics of the combined system, which was based on the assumption that the system operated on a typical Rankine cycle powered by both solar and gas energy. Tests for the prototype system was carried out to evaluate its real performance. The variation of refrigerant pressures and temperatures, hot water temperatures in the collector and boiler systems, as well as chill water temperatures were recorded. The results were used to estimate the heat from the boiler and the solar collectors, the electricity and hot water generation (indicated as kW energy) from the CHP operation as well as the gas consumption of the system. The modelling and experimental results were compared for the impulse-reaction turbine system, and a simple analysis of the energy and environmental benefits of the system was carried out.

8.2 Conclusions

Heat transport capacities of the selected heat pipes

The maximum heat transport capacity is the index evaluating heat transfer capability of a heat pipe, which is governed by six limits, i.e., the sonic limit, the entrainment limit, the boiling limit, the viscous limit, the capillary limit as well as the filled liquid mass limit. For the micro/miniature heat pipes investigated, heat transport capacity usually increases with the

increase of operation temperature, inclinations and channel cross-sectional area. The liquid fill level is recommended at the level of 1/4 to 1/3 of the evaporation length. The parallelepiped channel geometry is better in thermal performance than the circular channel geometry of the same cross-sectional area. The capillary limit is the dominant limit when operation temperature is below 80°C, but the entrainment limit would take the position when the temperature increases. For the normal heat pipes, heat transport capacity increases with the increase of operation temperature, inclinations and the channel cross-sectional area. The liquid fill level is the same as that for the micro/miniature heat pipes. A circular channel geometry is better in performance than the rectangular one of the same cross-sectional area. A wickless pipe is governed by the entrainment limit, and could achieve a higher level on heat transfer than the wicked one of the same cross-sectional area, which is governed by the capillary limit. However, since the wicked pipe is better at distributing liquid film evenly on the inner surface of the pipe, it would be the favourite choice if the pipe is installed at an inclination in relative to the horizontal.

Operating characteristics of the selected heat pipes

Cross-sectional area: For either a miniature or a normal heat pipe, the liquid cross-sectional area increases with height position above the filled liquid level in the evaporation section, decreases with the height in the condensation section, and remains the same in the adiabatic section. The vapour cross-sectional area varies at an opposite trend.

Axial and Radial Velocity: For a normal heat pipe, the axial vapour velocity varies in the cross section, which is higher in the central area, and lower in the periphery area. The variation of the velocity across radial direction is parabolic. Along the height position, the axial velocity increases slightly in the evaporation section, remains the same in the adiabatic section, and decreases in the condensation section.

Radial vapour velocity exists in a normal heat pipe. In the evaporation section, radial flow velocity is negative and its absolute value decreases gradually from the periphery to the centre area, which means an inward flow exists due to a constant injection from the interface of liquid/vapour phases. In the adiabatic section, radial flow velocity is zero, which means no radial flow exists due to absence of injection/ejection on the interface of liquid/vapour phases. In the condensation section, radial velocity becomes positive and its

absolute value increases gradually from the central area to the periphery, which means an outward flow exists due to a constant ejection on the interface of the liquid/vapour phases.

Pressures: For a miniature heat pipe, the total vapour-liquid pressure difference is an important factor affecting the operation of a heat pipe. The pressure difference is higher at the bottom of the evaporator section and this decreases with height position above the fill level. Increasing the width 'b' of the miniature heat pipe, with the cross-sectional area remaining the same, would reduce the flow resistance within the heat pipe, which results in reduced pressure differences.

For a normal heat pipe, the inner wall pressure is higher than the vapour pressure in the evaporation section, resulting in liquid vaporization, but lower than the vapour pressure in the condensation section, resulting in vapour condensation. The liquid pressure is much lower than vapour and inner wall pressures as part of its static pressure is converted into velocity pressure, causing flow of the fluid inside the heat pipe.

Temperatures: For either a miniature or a normal heat pipe, there are very small differences among vapour, liquid and wall temperatures, compared to the differences of vapour and heat/cool sources and heat conduction/convection mediums. This demonstrates that the heat pipes are excellent heat transfer devices, which could operate at an approximately constant temperature. The major heat resistances occurs in the heat conduction/convection mediums, resulting in remarkable temperature variation over these areas.

Comparisons between numerical predictions and testing results: The results from tests are in good agreement with numerical prediction when the test conditions are close to the simulation assumption. Although tests were constrained to temperature, the comparison carried out still supports the validity of the numerical model.

Heat Pipe Solar Collectors

Efficiencies: For a normal heat pipe solar collector, its performance was usually evaluated using efficiency η, which is defined as the ratio of heat taken from the manifold by cooling liquid and incident irradiation striking the collector absorber. However, for the hybrid heat pipe solar collector, another efficiency, η_1, was also employed for performance evaluation,

which is defined as the ratio of heat taken from the manifold by cooling liquid and the sum of incident irradiation striking the collector absorber and heat from exhaust gas. Either η or η_1 vary with the external conditions, e.g., global solar irradiation I_n, ambient temperature t_a, as well as cooling fluid inlet temperature t_0 and mass flow rate m, which are outlined by a general parameter $(t_{mean}-t_a)/I_n$. Overall, η (or η_1) decrease with the increase of $(t_{mean}-t_a)/I_n$. Their relationship could be expressed by second-order equations.

Top Covers and Manifolds: For either a normal heat pipe collector or a hybrid heat pipe collector, the top cover would impose a substantial impact onto collector performance. The evacuated cover condition was usually the best, but the 10mm thick thermo-clear polycarbonate cover may be more suitable for this application due to difficulty in creating an evacuated chamber in relation to the flat plate structure. Variation of the manifold structure, resulting in variations of heat transfer area and heat transfer coefficient, would bring about the variation of the collector heat output. Increasing contact area between collector and manifold would lead to an increased collector heat output.

Operation Modes: For the hybrid heat pipe solar collector, solar-exhaust flue gas combined operation would result in significant increase of the collector efficiency compared to solar-only operation. However, this operation would no longer perform well if a boiler is brought into operation. This is because the boiler increases collector inlet temperature, which results in a reduced temperature difference between the absorber and condenser, and consequently, a reduced heat output.

Testing and Modelling Results: Laboratory tests were carried out to validate modelling predictions and experimentally evaluate the collector performance. The test results were compared with the theoretical predictions, and it was found that the distinct differences existed between the theoretical and test values. For the thin membrane heat pipe solar collector, testing efficiencies were lower than the modelling predictions for the evacuated case, and higher than those for the case of the single glass cover with un-evacuated chamber. The reason is that the chamber was filled with an inert gas, argon, after being evacuated, resulting in a higher heat loss than the unevacuated case and a lower one than the evacuated case, but this was not taken into account in the model. For the hybrid heat pipe solar collector working at different operation modes, testing efficiencies were 10% to

20% less than the theoretical predictions. The reasons for this are mainly due to the several factors, including edge heat loss, unsatisfactory insulation, heat storage of the collector body itself and the simplified assumptions made in modelling setting-up. To enable the model to predict collector performance at a reasonable accuracy, a correlation factor was determined and brought into applications.

Micro Steam Turbine

Water is the best of the four working fluids investigated, including n-pentane, methanol, R141b and water, as it could produce a given electricity output at a lower mass flow rate and smaller flow area. Water is also found to be the only fluid that allowed a 6kW electricity to be produced for this application. However, If only 1.5kW electricity output were required, n-pentane, methanol, R141b and water would all be suitable working fluids. The higher the inlet pressure, the lower the mass flow rate and the smaller the required flow area if the electricity output and outlet pressure remain constant.

The results of CFD simulation and testing show good agreement. This indicates that CFD could be used as an effective tool for optimizing turbine geometry and determining operating conditions.

Hybrid Heat Pipe Solar Collector/CHP System

Modelling and Experimental Results: Experiemental results are far away from the theoretical predictions. The major reasons are that the real thermodynamic process was not a typical Rankine cycle, which caused an incomplete condensation in the condensers, and hence, a remarkably lower heat output. As a result, the heat input and energy consumption were reduced compared to an ideal Rankine cycle system. In addition, irreversibility existed in turbine, evaporation and condensation operations also contributed to energy losses, which increased this discrepancy as well.

System Performance: It was found that the turbo-alternator was too small for this system and affected its power output significantly. Work was therefore focused on the system using the micro impulse-reaction turbine. Testing showed that the majority of the heat required for impulse-reaction turbine operation came from the boiler (7.65kW), and very little (0.23kW) from the solar collector. The gas consumption was 8.5kW. Operation

resulted in an electricity output and domestic hot water generation of 1.34kW and 3.66kW, respectively. The electrical efficiency was 16% and the thermal efficiency was 43%, resulting in an overall efficiency of approximately 59%. This indicates that about 41% of the energy input was lost due to the resistances of mechanical movement and fluid flow, as well as heat loss due to unsatisfactory insulation of piping and equipment.

Increasing quantity of the collectors used would result in reduced heat output from the boiler. This would help to improve system performance and increase efficiencies. In this application, suitable quantity of collectors would be 4 as the flue gas flow rate could only provide 4 to 5 such collectors for heat recovery.

Energy and Environmental Effects: Use of the proposed system would save primary energy of approximately 3,150kWh per annum compared to conventional electricity and heating supply systems, and this would result in reduction of CO_2 emission of up to 1.5 tonnes. The running cost of the proposed system would also be lower. These results are an underestimate of the system's practical performance than the theoretical predictions as the turbine used was too small to achieve the desired efficiency. The system's performance would be improved by employing a more suitable turbine and developing an improved collector configuration to allow more efficient utilization of both solar energy and waste heat.

8.3 Further Work

Although substantial work has been carried out during this research, there are still quite a few opportunities to develop this project in order to improve the system's performance further. These may be indicated as follows:

System configuration

It was noticed that although the incomplete condensation led to a reduced heat output, it allowed the heat input to be reduced as well. As a result, the electricity, heat and overall efficiencies were increased compared to the completely condensed situation. This may be desirable at the situations where no much heat output was required. The reduced heat input may bring about another system consideration. In the system, a solar/exhaust gas collector, instead of the collector and boiler, may be used to produce refrigerant vapour. The turbine

may be driven by the vapour directly, rather than a vaporised second fluid generated via an additional heat exchanger. The condensation for the discharged vapour from the turbine could be carried out in a tiny heat exchanger, as an incomplete condensation occurs there and very little heat is extracted. Thus a more compact CHP device entirely driven by solar energy and waste heat would be produced.

Hybrid solar/gas collector

To develop the system, an 8kW heat capacity solar/exhaust gas collector capable of producing high pressure vapour (4-5bar) is required in order to operate the turbine. The collector may have the following features:

- A higher operation temperature, above 100°C, and a higher heat efficiency, 80% or more, are achievable. These could be realised by using following techniques, e.g., employing a thermo-clear top cover, creating an evacuated chamber, increasing solar flux to the absorber area, as well as enhancing heat transfer between flue gas and collector absorber. However, to ensure these techniques work with the system, a careful design would be necessary.
- A compact, light weight structure is desirable to allow it to be installed on the roof of a residential building,
- A concept to integrate the device into part of building structures, such as roof or chimney, is the highest priority.

Micro turbine

Another issue may be development of a suitable turbine configuration. A 0.25kW turbo-alternator has been tested, further work should aim to develop a large-scale prototype, which allows a 1.5kW electricity to be produced, in order to meet requirement of the novel system.

References

A

Abhat A. (1982) Performance investigation of a long, slender heat pipe for thermal energy storage application, J. Energy 6, pp. 6-16.

Alfred Ongiro Alfred et al (1996) Thermodynamic simulation and evaluation of a steam CHP plant using ASPEN plus, Applied Thermal Engineering Vol. 16, No. 3, pp. 263-271.

Armenante Piero M., Luo Changgen, Chou Chun-Chiao (1997) Velocity Profiles in a Closed, Unbaffled Vessel: Comparison between Experimental LDV Data and Numerical CFD Predictions, Chemical Engineering Science, Vol 52, No. 20, pp. 3483-3492

Attili Basem S. (1994) Numerical study of the vapour flow characteristics of a slender cylindrical heat pipe. Energy Convers, Mgmt Vol. 35, No. 11, pp. 999-1008.

B

Babin B. R., Peterson G. P., and Wu D. (1989) Analysis and Testing of a Micro Heat Pipe during Steady State Operation, American Society of Mechanical Enginners, New York, Paper 89-HT-17.

Babin B. R., Peterson G. P., and Wu D. (1990) Steady-state modeling and testing of a micro heat pipe, Journal of Heat Transfer 112, pp. 595-601.

Balzar A. et al. (1996) A solar cooker using vacuum-tube collectors with integrated heat pipes, Solar Energy **58**, pp. 63-68.

Bairamov R. and Toiliev K. (1981) Heat pipe in solar collectors. In Advances in Heat Pipe Technology, Ray D. A.(ED.), Pergamon Press, Oxford.

Bienert W. B. and Wolf D. A. (1976) Heat pipe applied to flat-plate solar collectors, Final Report COO/2604-76/1.

Blakemore F. B. et al (1995) Combined heat and power, economies of scale and option appraisal, Utilities Policy, Vol. 5, No. 3/4, pp. 167-174.

Bong T. Y. et al (1993) Thermal performance of a flat-plate heat pipe collector array, Solar Energy 50(6), pp. 491-498.

Bowman W. J. and Hitchcock J. E. (1988) Transient compressible heat pipe vapour dynamics, Transient compressible heat pipe vapour dynamics, 19888 National Heat Transfer Conference, Houston. TX, HTD-96, Vol. 1, pp. 329-337.

Butlin C. (1998) Personal Communication, Mobil Gas Marketing (UK) Ltd., 10 February 1998.

C

Cao Y. and Faghri A. (1990) Transient two-dimensional compressible analysis for high-temperature heat pipes with pulsed heat input, Numer. Heat Transfer, PART a 18, pp. 483-502.

Cao Y. and Faghri A. (1992) Analysis of high-temperature heat pipe startup from the frozen state, 1992 National Heat Pipe Conference, San Diego, CA, HTD-Vol. 206-3, Topics in Heat Transfer, pp. 89-97.

Chang W. S. and Colwell G. T. (1985) Mathematical modeling of the transient operating characteristics of a low-temperature heat pipe, Numer. Heat Transfer 8, pp. 169-186.

Chun W. et al (1999) An experimental study of the utilization of heat pipes for solar water heaters, Applied Thermal Engineering 19, pp. 807-817.

Church E. f. et al (1982) Steam Turbines, 3rd edition, McGRAW-Hill Book Company, Inc., New York, pp. 3-4.

Collier, J. C(1981) Convective Boiling and Condensation, McGraw-Hill, New York.

Colwell, G. T. and Modlin, J. M. (1992) Mathematical heat pipe models. Proceedings of the 8th International Heat pipe Confernece, Vol. 1, Beijing.

Colwell, G. T. and Chang, W. S. (1984) Measurement of the Transient Behavior of a Capillary Structure under Heavy Thermal Loading. International Journal of Heat and Mass Transfer, 27, pp. 541-551.

Cotter T. P. (1984) Principle and prospects of micro heat pipes, in: Proceedings of the 5th International Heat Pipe Conference, JaTech, Tokyo, pp. 328-335.

D

Deverall J. E., Kemme J. E. and Florschuetz L. W (1970) Sonic limitations and startup problems of heat pipes, Los Alamos Scientific Laboratory Report LA-4518 (accession number N71-18944), Los Alamos, NM.

DeVriers H. F. W., Kamminga W., and Franken J. C. (1980), Fluid circulation control in conventional and heat pipe planar solar collectors, Solar Energy 24, pp. 209-213.

Doster J. M. and Hall M. L. (1989) Numerical modeling of high-temperature liquid metal heat pipes, 1989 Joint ASME/A.I.Ch.E. National Heat Transfer Conference, Philadelphia, Pennsylvania, Vol. 89-HT-13, pp. 1-9.

Dunn P. D. and Reay D. A. (1982) Heat pipes, 3rd ed., Pergamon Press, New York.

E

El-nasr M. A. et al (1993) Performance of a wickless heat pipe solar collector, Energy Source 15, pp. 513-522.

Ernst D. M. (1981) Cost-effective solar collectors using heat pipes, Final Technical Report, DOE/CS/34099-4.

Evans R. D. (1990) Environmental and economic implication of small scale CHP. Energy amd Environment Paper No3. ETSU, Harwell Laboratory, Oxfordshire.

F

Faghri, A. (1995) Heat Pipe Science and Technology, Taylor & Francis, Washington, DC, pp. 11-110.

Faghri A. and Buchko M. (1991) Experimental and numerical analysis of low-temperature heat pipes with multiple heat sources, ASME J. Heat Transfer 113, pp. 728-734.

Faghri A. and Chen M. M. (1989) A numerical analysis of the effects of conjugateheat transfer, vapor compressibility, and viscous dissipation in heat pipes, Numer. Heat Transfer Part A 16, pp. 389-405.

FEW P. C. et al (1997) Modelling of a combined heat and power (CHP) plant incorporating a heat pump for domestic use, Energy Vol. 22, No. 7, pp. 651-659.

Fluent/UNS version 4.32, 1995.

Facão Jorge, Matos Joaquim, Oliveira Armando and Afonso Clito (2001) Computer Modelling of System Performance – Hybrid solar collector/CHP system, Progress report to European Commission, March 2001.

Franken R. D. (1979) Proc. ISES. New Delhi. pp. 885.

Fullarton David (2002) Personal Communication, Swep Limited, 7 March 2002.

G

Glanfranco Angelino Glanfranco et al (1998) Multicomponent working fluids for organic Rankine cycles (ORCs), Energy Vol. 23, No. 6, pp. 449-463.

Groll M. and Rosler S. (1992) Operation Principles and Performance of Heat Pipes and Closed Two-Phase Thermosyphons, J. Non-Equilib. Thermodyn. Vol. 17, pp. 91-151.

H

Hamworthy Heating Ltd (1997) Purewell Permanent Ignition, pp. 1-2.

Huang L., El-Genk M. S. and Tournier J.-M. (1993) Transient performance of an inclined water heat pipe with a screen wick, 1993 ASME National Heat Transfer Conference, Atlanta, GA, Heat pipes and Capillary Pumped Loops (Edited by A. Faghhi, A. J. Juhasz and T. Mahefkey), HTD-Vol. 236, pp. 87-92.

Hussein H. M. S. et al (1999) Optimisation of a wickless heat pipe flat plate solar collector. Energy Concers. Manage. **40**, pp. 1949-1961.

I

Incropera Frank P., De Witt David P. (1997) Fundamentals of heat and mass transfer, third edition, John Wiley & Sons, Inc, Singapore, pp. 502-503.

Ismail K. A. R. and Abogderah M. M. (1998) Performance of a heat pipe solar collector, Journal of solar energy engineering 120, pp. 51-59.

Ismail K. A. R. and Abogderah M. M. (1991) Comparative study between flat plate solar collector with heat pipes and commercial conventional unit, *IV congresso latino americano de transferencia de calor y material,* La Serena, Chile. pp. 229-332.

Ismail K. A. R. and Abogderah M. M. (1992[a]) Thermal and numerical analysis of heat pipe solar collector, Proceedings of the Second Renewable Energy Congress, Reading, U.K., Vol 2, pp. 862-866.

Ismail K. A. R. and Abogderah M. M. (1992[b]) Residential solar collector with heat pipes, 8[th] Heat Pipe Conference, Beijing, China, pp. 531-534.

Issacci F., Catton I. and Ghoniem N. M. (1991) Vapour dynamics of heat pipe startup. ASME J. Heat Transfer 113, pp. 985-994.

Ivanovsky M. N., Sorokin V. P. and Yagodkin I. V. (1982) The Physical Principles of Heat Pipes. Oxford University Press, New York.

J

Jennekens M. (1989) Learning from experiences with small-scale co-generation. Caddet Analysis Series No. 1, IEA/OCED.

K

KHALIL R.A.HAJ et al (1997) Optimization of solar pond electrical power generation system, Energy Conversation & Management Vol. 38 No. 8, pp. 787-798.

Kearton William J. (1972) Steam Turbine Theory and Practice, Pitman Publishing (Seventh Edition), Bath, pp. 1-5.

Kraus A. D. and Bar-Cohen A. (1983) Thermal Analysis and Control of Electronic Equipment, McGraw-Hill, New York.

L

Li M. et al (2002) Experiments of a solar flat plate hybrid system with heating and cooling, Applied Thermal Engineering 22, pp. 1445-1454.

Lin Song (2002) Hybrid CHP system, HP manufacture and performance tests, Internal report to project coordinator, March 2002.

London Electricity (1998) Electricity Prices for your business, Published by London Electricity Plc, April 1998

Lu W. D. and Guo H. F. (1984) Performance of a gravity assisted heat pipe solar collector, International Journal of Solar Energy 3, pp. 1-11.

M

Maidment G. G. and Tozer R. M (2002) Combined cooling, heat and power in supermarkets, Applied Thermal Engineering 22, pp. 653-665.

Mathioulakis E. et al (2002) A new heat-pipe type solar domestic hot water system, Solar Energy **72(1)**, pp. 13-20.

McNelis B. (1992) Photovoltaic refrigerator, Solar Air conditioning and Refrigeration. (Ed AAM Sayigh), Pergamon Press, pp. 268-289.

Merrigan M. A., Keddy E. S. and Sena J. T. (1986) Transient performance investigation of a space power system heat pipe, AIAA/ASME 4th Joinr Thermopfysis and Heat Transfer Conference, Boston, MA, paper AIAA-86-1273.

N

Naylor A.I. (1982) Photovoltaic Air conditioning System for Barbados. Sun at Work in Britain, No. 15, pp. 41-47.

O

Oliveira A. C. et al (2002) A combined heat and power system for buildings driven by solar energy and gas, Applied Thermal Engineering 22, pp. 587-593.

Olivier Le Corre et al (2002) Thermoeconomic analysis based on energy structure for the combined heat and power, Applied Thermal Engineering 22, pp. 561-566.

Ortabasi U. and Fehlner F. (1979) Cusp mirror-heat-pipe evacuated tubular solar thermal collector. Solar Energy **24**, pp. 477-489.

P

Pilavachi P. A. (2002) Mini- and micro-gas turbines for the combined heat and power, Applied Thermal Engineering 22, pp. 2003-2014.

Pilavachi P. A. (2002) Power generation with gas turbine system and combined heat and power, Applied Thermal Engineering 20, pp. 1421-1429.

Prosser G. T. & Maidment G. G. (1998) Investigation into the Viability of CHP in Cold Storage Facilities, International Institute of Refrigeration Conference, Refrigerated Transport, Storage & Display Conference.

R

Ramsey J. W. (1986) Experimental evaluation of a cylindrical parabolic solar collector, ASME paper 76-WA/HT-13 8.

Ransom V. H. and Chow H. (1987) ATHENA heat pipe transient model, In Trans. of 4th Symposium on Space Nuclear Power System, CONF-870102-Summs., (Edited by M. S. El-Genk and M.D.Hoover), pp. 389-392. ISNPS, UNM, Albuquerque, NM.

Riffat S. B., Zhao X. and Doherty P. S. (2000) Mathematical modeling of the membrane heat pipe solar absorber, EU Craft JOE3-CT98-7020, Task 2, Final report to the project coordinator.

Riffat S. B. (2000) European Commission, Energy, Environmental and Sustainable Development Programme, NNE5-1999-20114, Hybrid solar collector/CHP system.

Riffat S. B., Zhao X. and Doherty P. S. (2002) Analytical and numerical simulation of the thermal performance of 'mini' gravitational and 'micro' gravitational heat pipes, Applied Thermal Engineering 22, pp. 1047-1068.

Riffat S. B., Doherty P. S. and Abdel Aziz E. I. (2000) Performance testing of different types of liquid flat plate collectors, International Journal of Energy Research, 24, pp. 1203-1215.

Riffat S. B., Zhao X., Doherty P. S. (2002) Structure optimisation and performance simulation of a novel thin membrane heat pipe solar collector using a mathematical model, International Journal of Ambient Energy, V23, No. 1, pp. 3- 16.

Riffat S. B., Zhao. X., Doherty P. S. (2002) Investigation of the flow in an impulse micro turbine using numerical CFD predictions and laboratory testing, International Journal of Ambient Energy, V23, Number 4, pp. 171- 178.

Riffat S. B., Zhao X., Doherty P. S. and Boukhanouf Rabah (2002) Hybrid Solar Collector/CHP system: Two-full Scale Prototype System, University of Nottingham, Report to European Commission, October 2002.

Riffat S. B., Zhao X., Doherty P. S. and Boukhanouf Rabah (2003) Hybrid Solar Collector/CHP system: field-testing of the prototype system in the testing building, University of Nottingham, Report to European Commission, May 2003.

Riffat S. B., Minh Nguyen, Doherty P. S. (1999) An Integrated Hybrid Solar/Gas System for Building, Contract JOR3-CT97-0183, Laboratory/Field Testing of the Prototype Unit, Mid-term Assessment Report to European Commission, April 1999.

Ribot J. and McConnell R. D. (1983), Testing and analysis of a heat pipe solar collector, ASME journal of Solar Energy Engineering **105**, pp. 440-445.

Rommel Matthias (2000) Tests of the thin membrane heat pipe solar collector, Fraunhofer Institut Solare Energiesysteme, November 2000.

S

Sawyer S. L. (1991) Electricity generation from low temperature heat sources using organic Rankine cycle engine, Electric Energy Conf. Darwin, Australia, pp. 10-13.

Seo J. T. and El-Genk M. S. (1989) A transient model for liquid-metal heat pipes. In Space Nuclear Power Systems 1988 (Edited by M. S. El-Genk and M. D. Hoover), Vol. IX, pp. 405-418. Orbit, Malabar, FL.

Smith M. A. (1994) The economic and commercial feasibilty of domestic CHP, MSc thesis, University of Wales College of Cardiff.

Smith M. A. et al (1995) Technical and operational performance of a small-scale, combined heat-and-power (CHP) plant, Energy Vol. 20, No. 12, pp. 1205-1214.

Spencer L. C. (1989) A comprehensive review of small solar-powered heat engines: Part II. Research since 1950, Solar Energy, 43(4), pp. 197-210.

Sun Dawen (1997) Solar powered combined ejector-vapour compression cycle for air conditioning and refrigeration, Energy Conversation & Management Vol. 38, No. 5, pp. 479-491.

T

Takaoka M., Motai T., Sakaya M., Mochizuki M., Mashiko K., and Ito M. (1985) Development of long heat pipes and heat pipe products, Fujikura Technical Review, No. 14, Fujikura Ltd., Tokyo, Japan.

Terpstra M. and Van Veen J (1987) Heat pipes: construction and application. A study of Patents and Patent Applications, Elsevier Applied Science, New York.

Tilton D., Johnson J., Gottschlich J. and Iden S. (1986) Transient response of a liquid-metal heat pipe, Air Force Wright Aeronautical Laboratory Report AFWAL-TR-86-

2037, Wright Patterson AFB. OH.

U

Underwood C. P. (1995) Scenarios for the utilisation of power by HVAC plant from photovoltaic cladding on buildings, CIBSE National Conference, Eastbourne, UK, pp. 118-126.

University of Idaho (1996) Thermodynamic properties of fluids, Version 4.2, The center for Applied Thermodynamic Studies, College of Engineering, Moscow, Idaho.

X

Xu Feng et al (2000) A combined power/cooling cycle, Energy 25, pp. 233-246.

Y

Yagoub WKA (1999) A review of coating materials for a novel membrane heat pipe solar panel, Report to project coordinator, University of Nottingham, May 1999.

Yang S., Tao W. (1998) Heat Transfer, China High Education Press, pp. 162-165.

Z

Zanardi M. A. (1989) Numerical and experimental analysis of a cylindrical parabolic solar collector with a heat pipe, Ph. D dissertation, Dept of Mechanical Engineering, Campinas State University, Brazil.

Zhuang J. et al. (1989) Heat Pipe and Heat Pipe Heat Exchanger, first ed., The Press of Shanghai Jiaotong University, Shanghai, China, pp. 127-147.

Appendix

Heat transport capacity of the various heat pipes

Circular/wickless heat pipes
(length of evaporation section: 1.7m; adiabatic senction: 0.07m; condensation section: 0.2m)

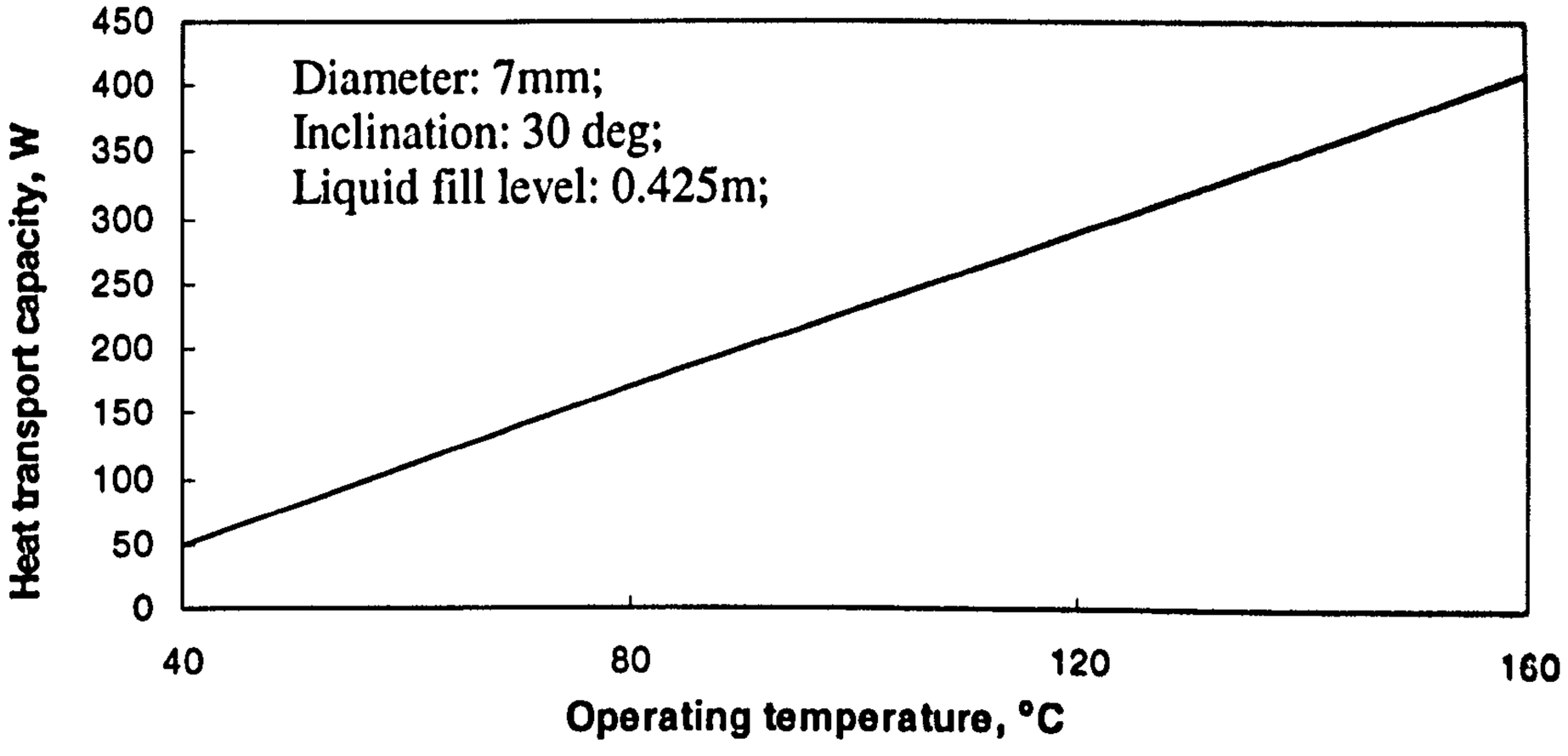

Figure A-1. Variation of heat transport capacity with operating temperature- Circular/wickless heat pipe

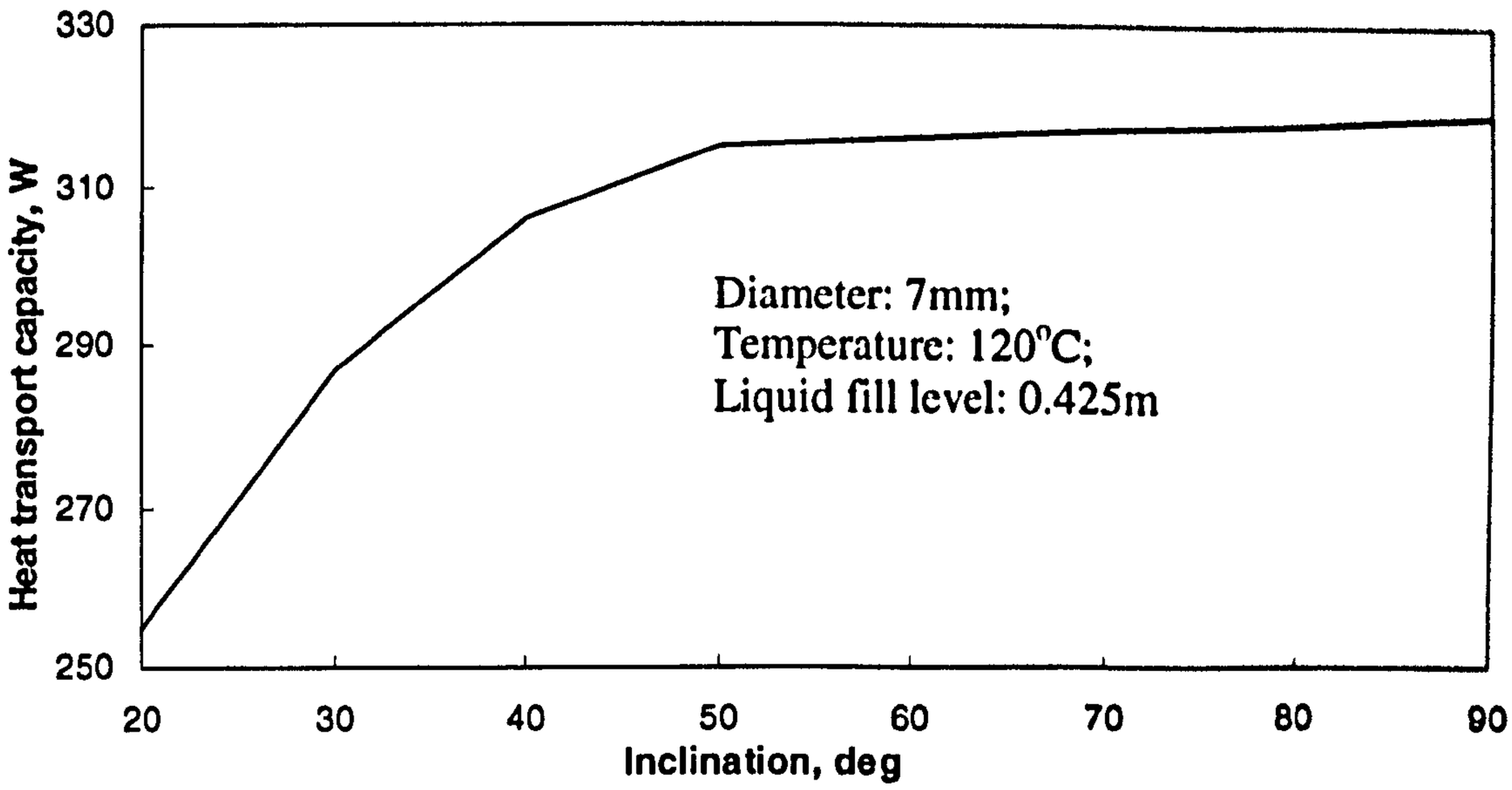

Figure A-2. Variation of heat transport capacity with inclination- Circular/wickless heat pipe

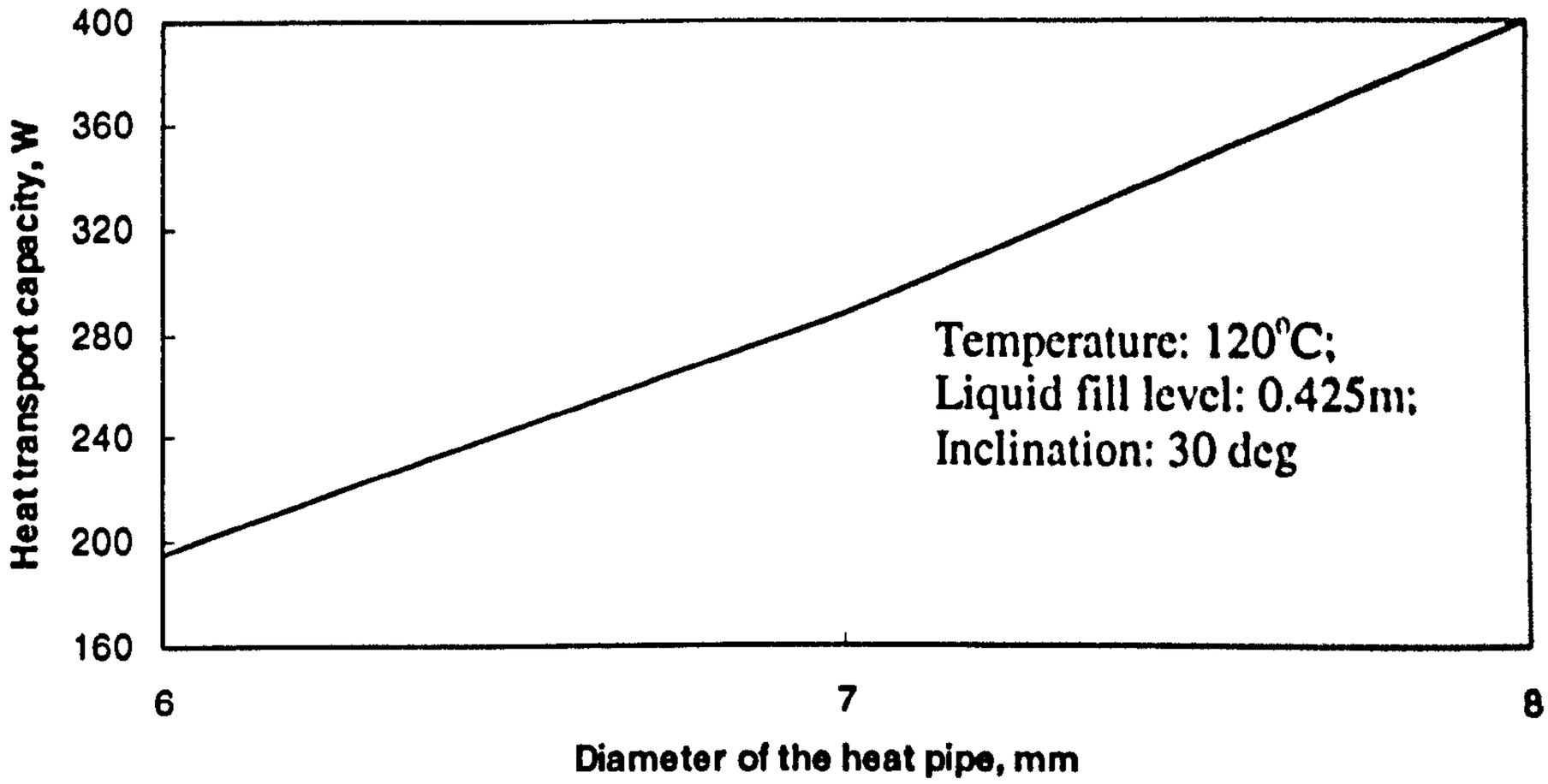

Figure A-3. Variation of heat transport capacity with diameter- Circular/wickless heat pipe

Circular/wicked heat pipes

(length of evaporation section: 1.7m; adiabatic senction: 0.07m; condensation section: 0.2m)

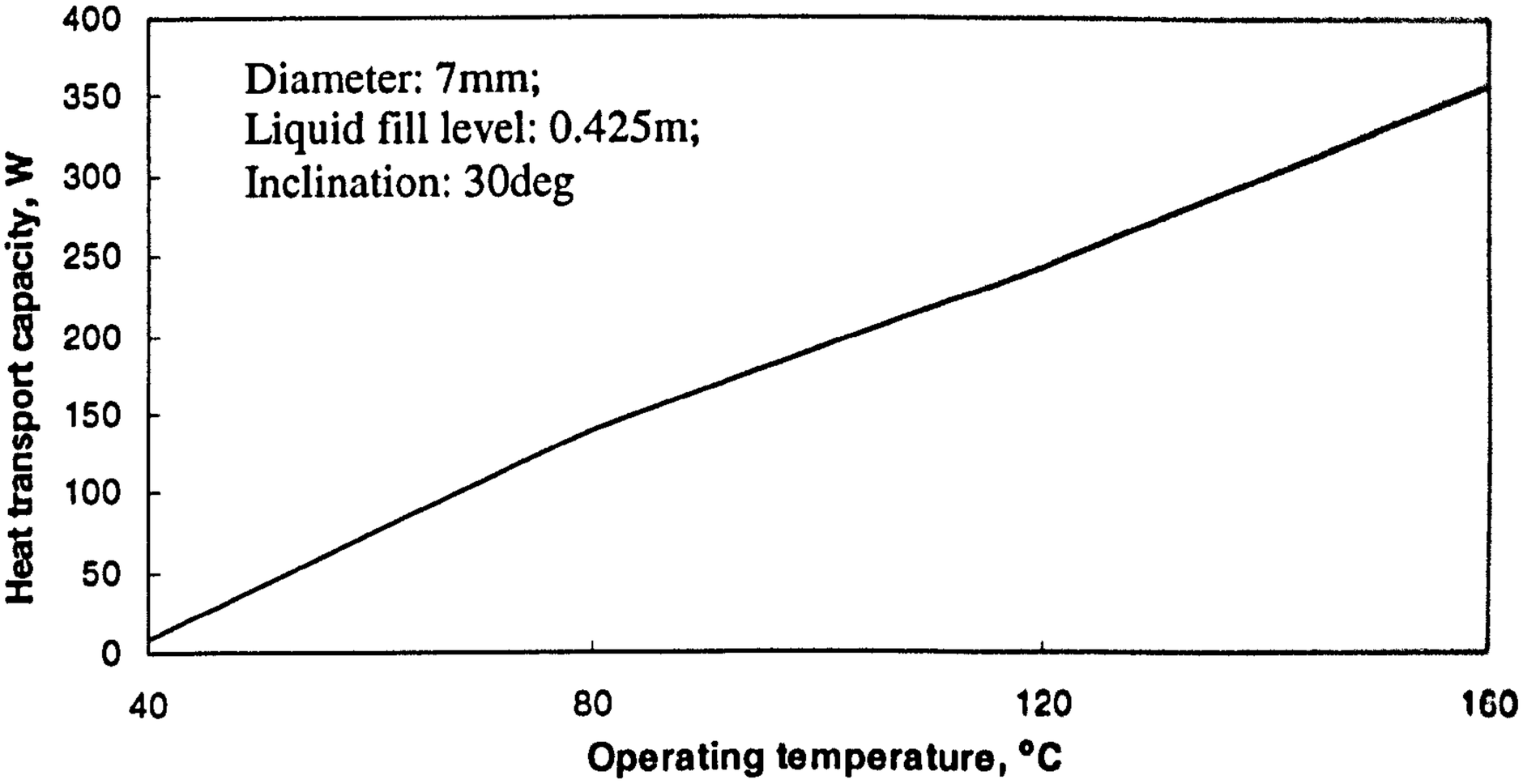

Figure A-4. Variation of heat transport capacity with operating temperature- Circular/wicked heat pipe

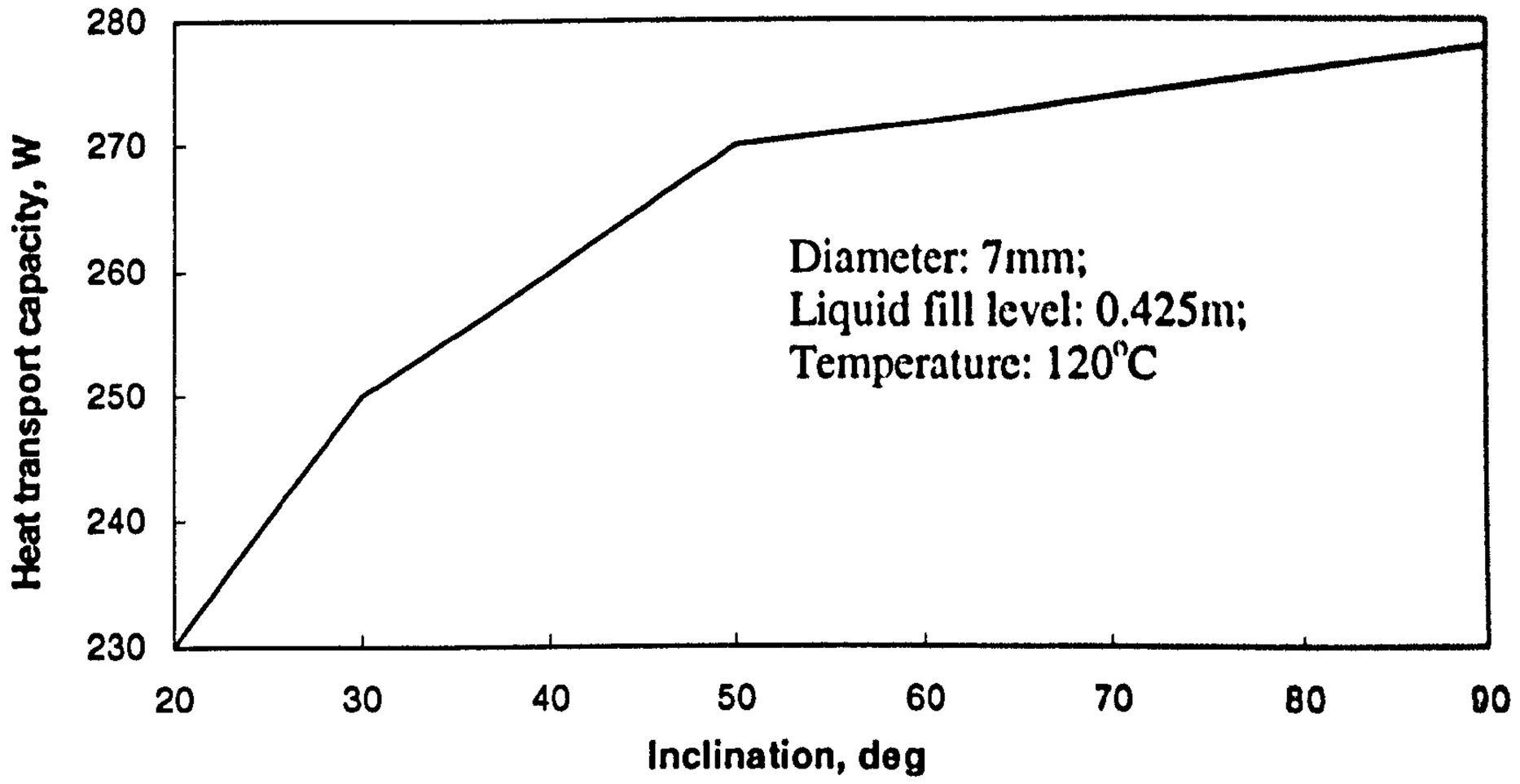

Figure A-5. Variation of heat transport capacity with inclination-Circular/wicked heat pipe

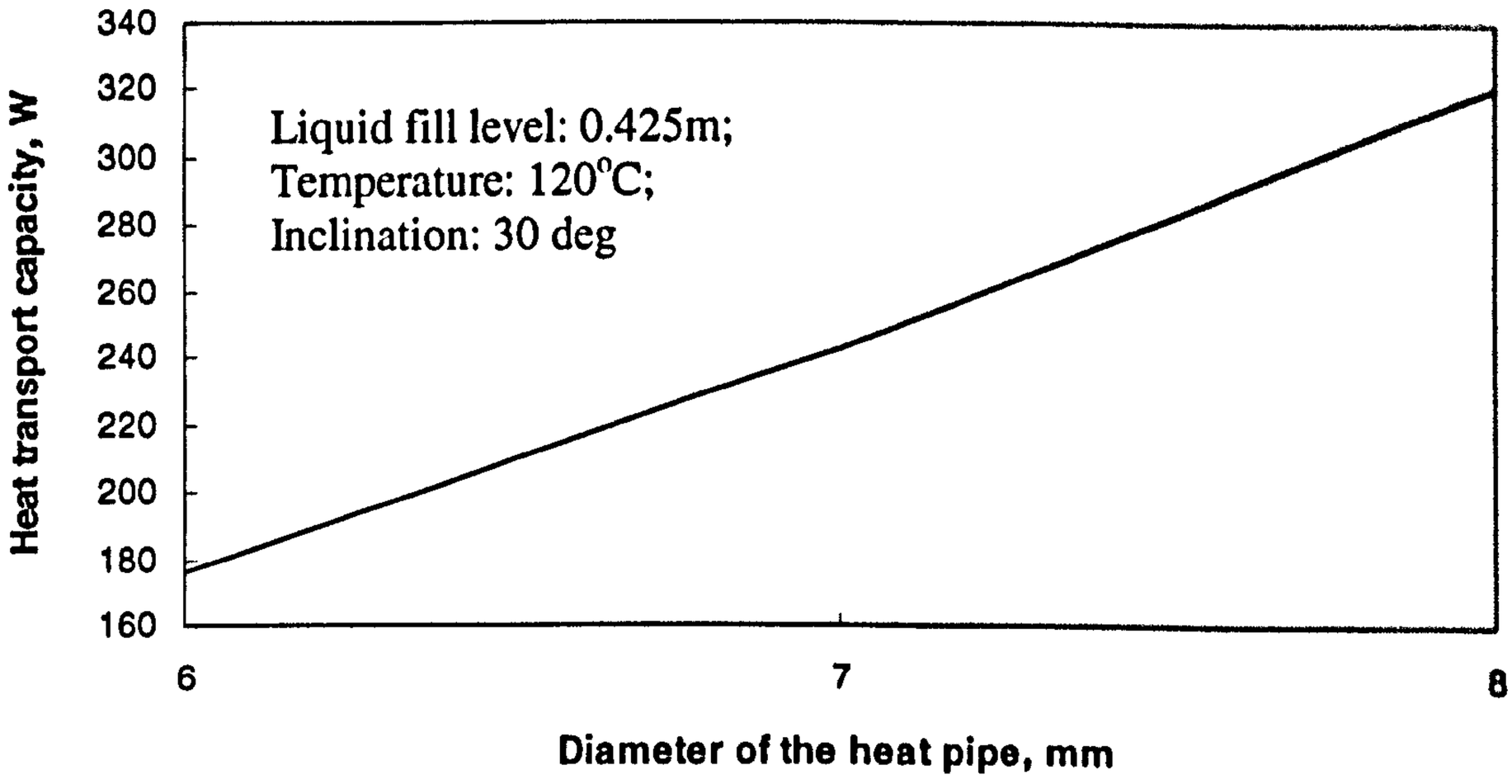

Figure A-6. Variation of heat transport capacity with diameter-Circular/wicked heat pipe

Rectangular/wickless heat pipe

(length of evaporation section: 1.7m; adiabatic senction: 0.07m; condensation section: 0.2m)

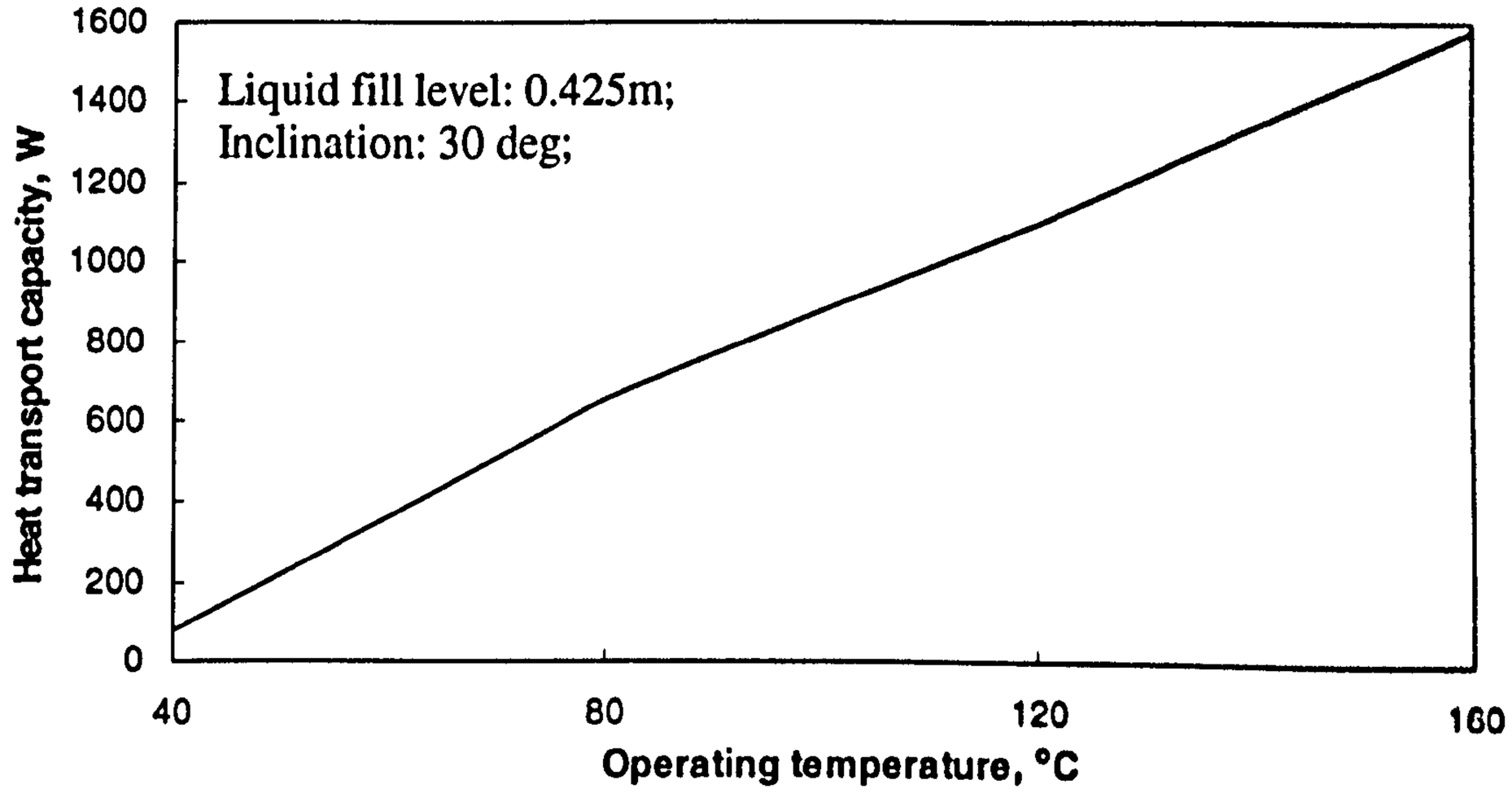

Figure A-7. Variation of heat transport capacity with operating temperature- Rectangular/wickless heat pipe (width: 25mm; height: 5mm)

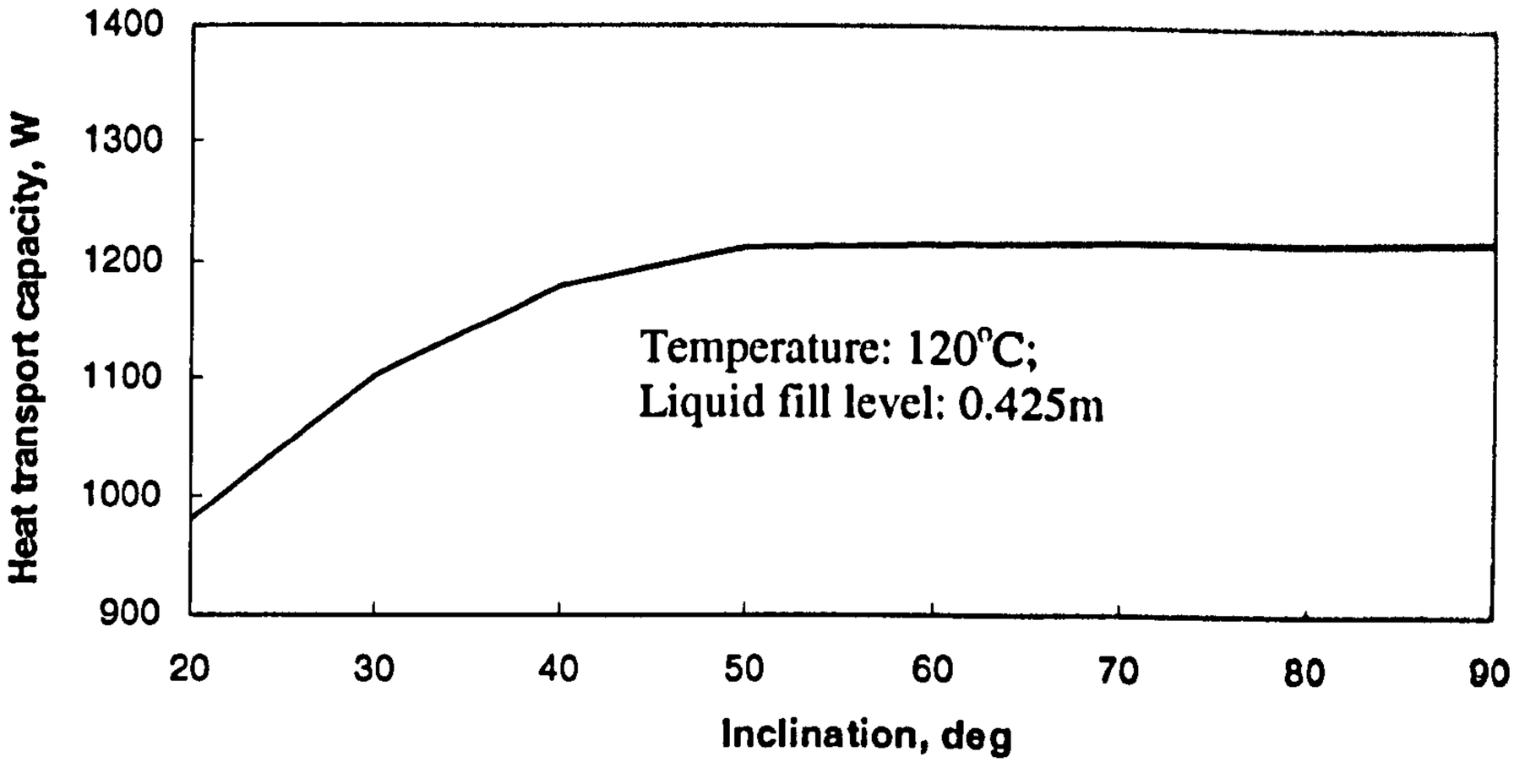

Figure A-8. Variation of heat transport capacity with inclination- Rectangular/wickless heat pipe (width: 25mm; height: 5mm)

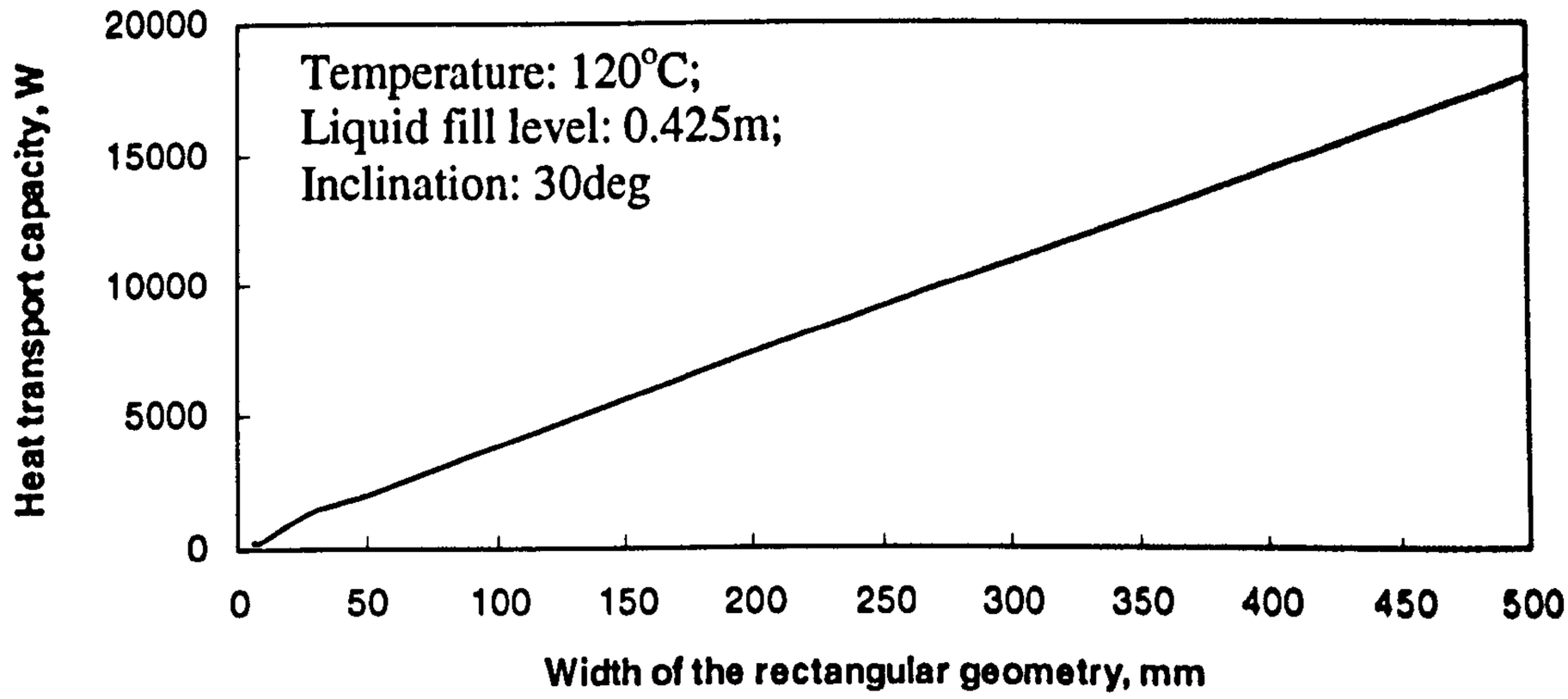

Figure A-9. Variation of heat transport capacity with width of the heat pipe- Rectangular/wickless heat pipe (height: 5mm)

Rectangular/wicked heat pipe

(length of evaporation section: 1.7m; adiabatic senction: 0.07m; condensation section: 0.2m)

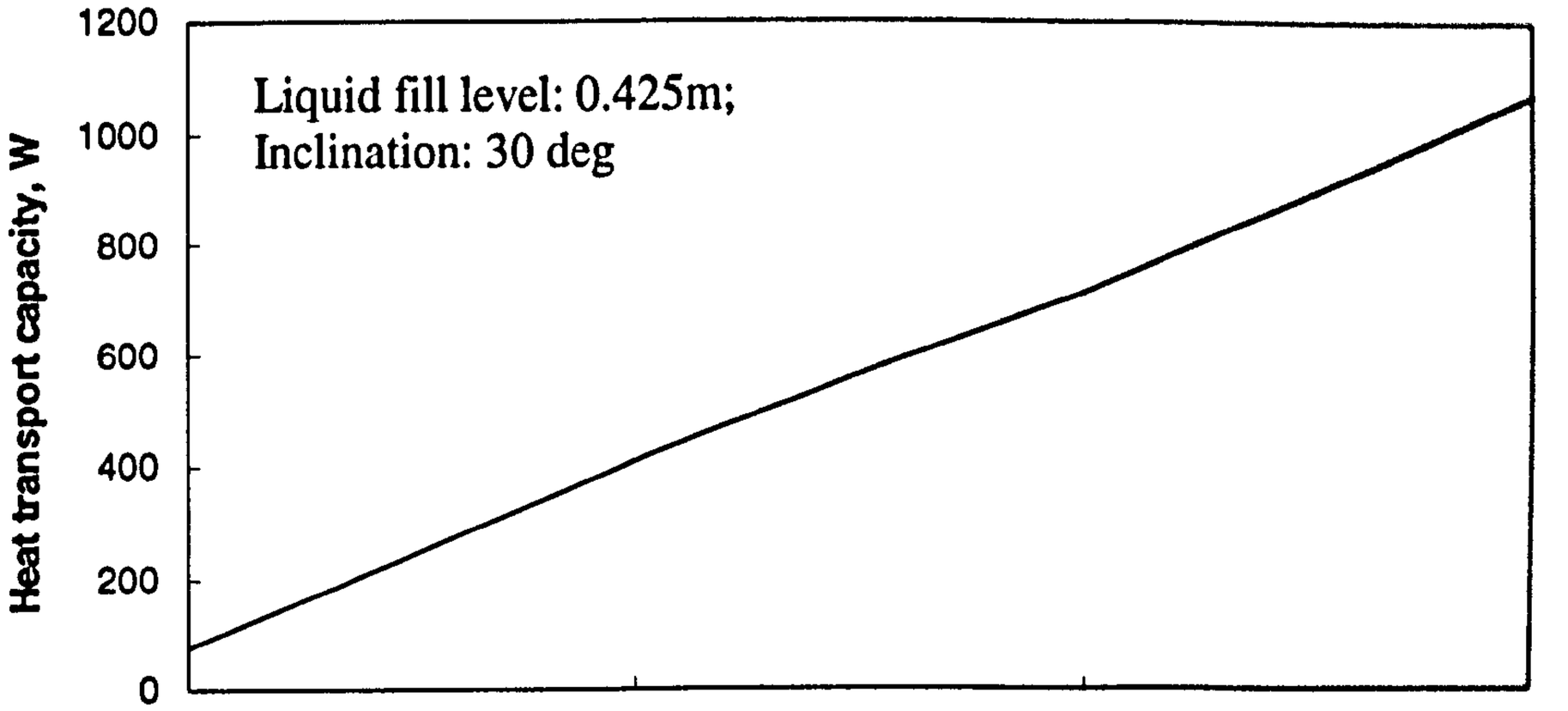

Figure A-10. Variation of heat transport capacity with operating temperature- Rectangular/wicked heat pipe (width: 25mm; height: 5mm)

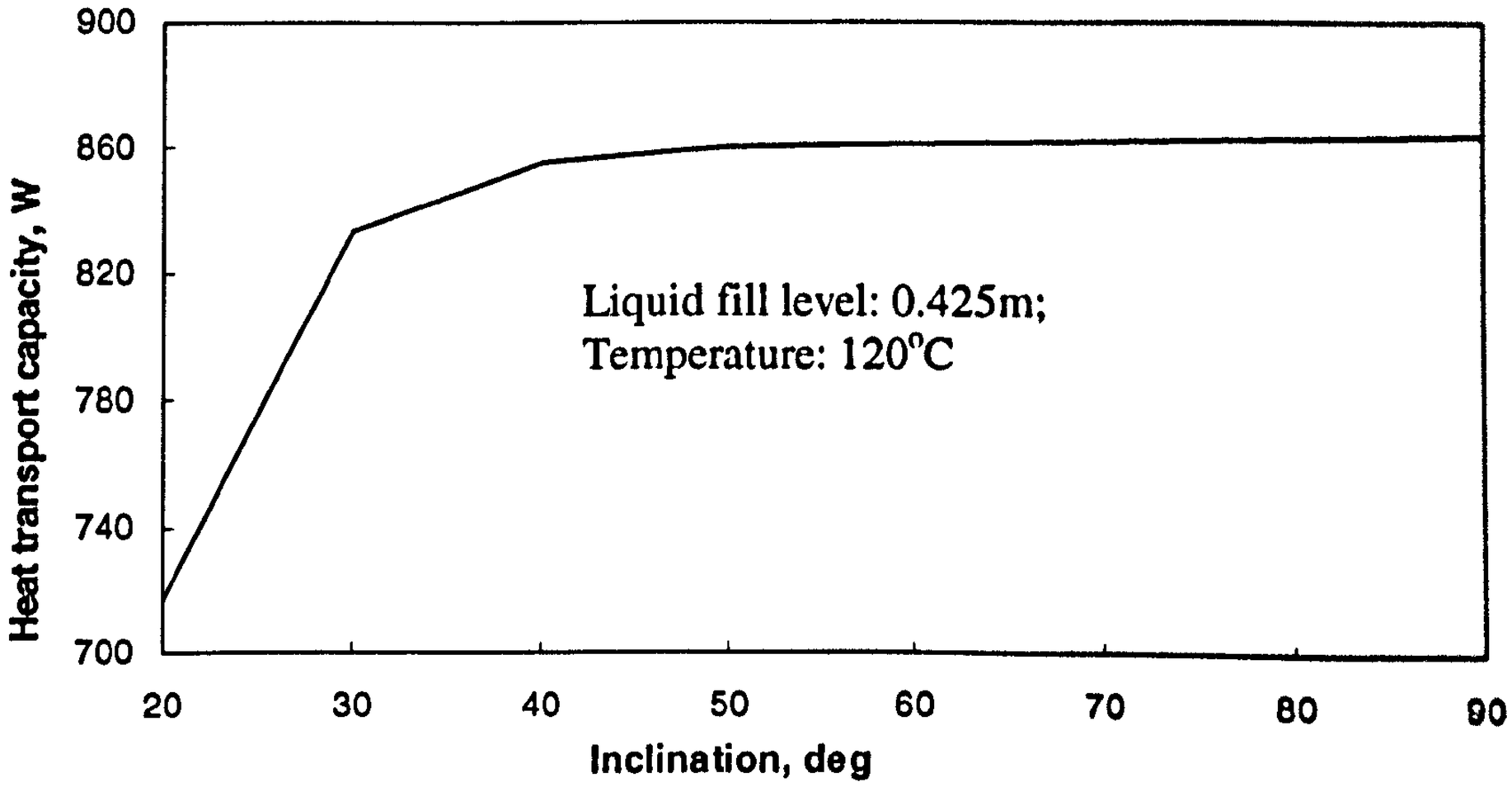

Figure A-11. Variation of heat transport capacity with operating inclination- Rectangular/wicked heat pipe (width: 25mm; height: 5mm)

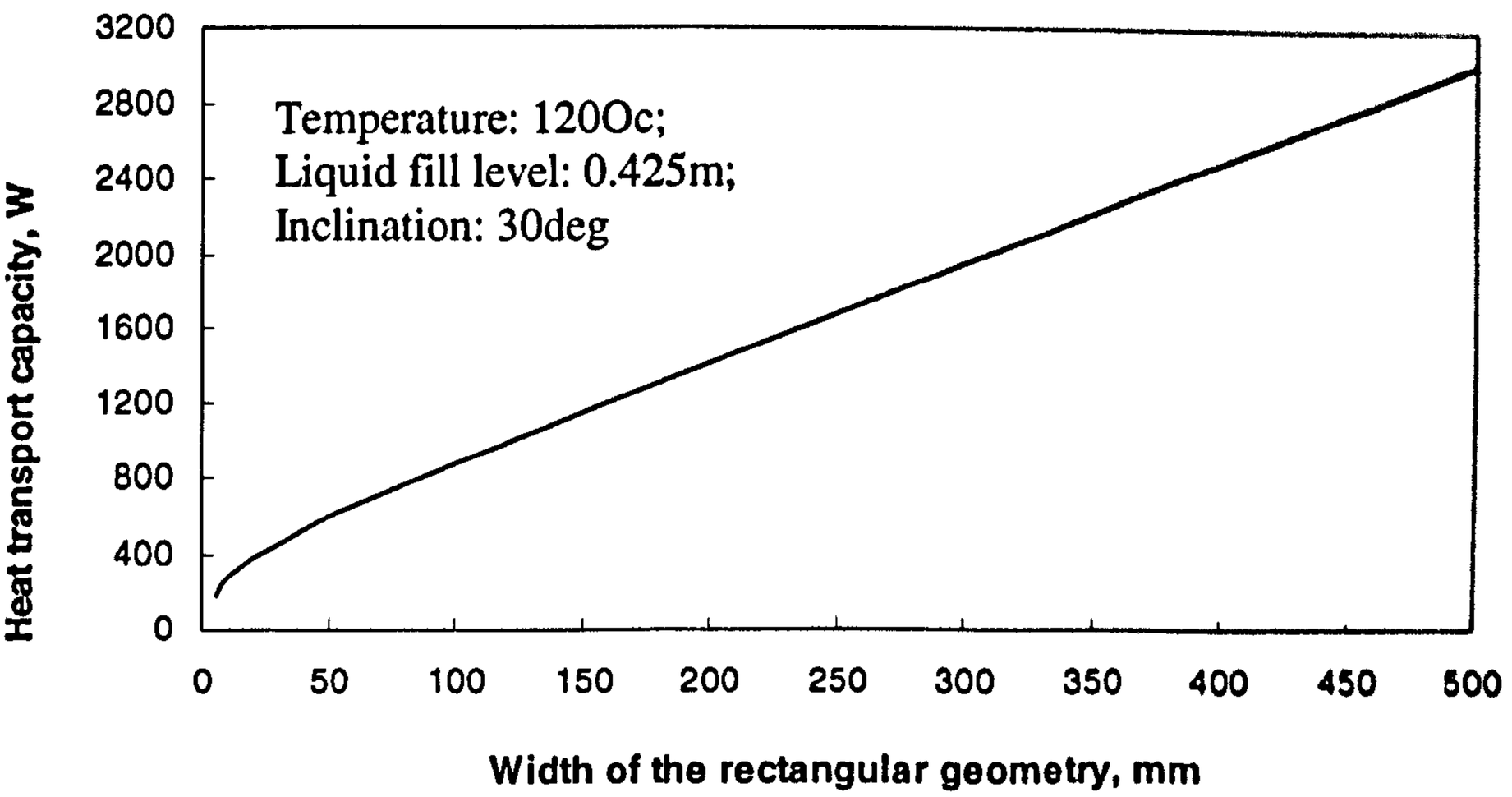

Figure A-12. Variation of heat transport capacity with width of the heat pipe- Rectangular/wicked heat pipe (height: 5mm)